Chiral Transition Metal Complexes under Resonance: Mechanism of a New Form of Chiral Raman Spectroscopy

by

Guojie Li

A thesis submitted in partial fulfillment of the requirements for the degree of

Doctor of Philosophy

Department of Chemistry

University of Alberta

Abstract

My PhD thesis primarily focuses on exploring chiroptical events and signatures of chiral transition metal complexes when they are under (near) resonance conditions. To achieve this goal, multiple chiroptical spectroscopic techniques were utilized, aided by theoretical calculations. These chiroptical techniques include Raman optical activity (ROA), vibrational circular dichroism (VCD), electronic circular dichroism (ECD), and a new form of chiral Raman spectroscopy which was discovered during the thesis research. We named this new form 'eCP-Raman' which is a combination of ECD (abbreviated as 'e' in the name) and circularly polarized Raman (CP-Raman) spectroscopy. The thesis encompasses the long discovery journey of uncovering the mechanism responsible for the large, induced chiral Raman signatures of solvents when the associated chiral solute is under resonance. The development of the eCP-Raman mechanism leads to the realization that resonance ROA (RROA) spectra measured in the present thesis work and in previous reports by others are (severely) contaminated by eCP-Raman contributions.

More specifically, Chapter 3 describes the observation of the strong, induced chiral Raman response of achiral solvent molecules when a chiral transition metal complex solute is under resonance condition and the eventual discovery of the eCP-Raman mechanism responsible for it. In Chapter 4, we examined the chiral Raman responses of three different chiral solutes under resonance and concluded that eCP-Raman contributes dominantly in all three cases, whereas RROA contributes negligibly. Importantly, the observed chiral Raman signatures of the solutes were correctly simulated by the proposed eCP-Raman mechanism. Chapter 5 describes the chiroptical characterization of two new chiral transition metal complexes, which are (near) resonance with the laser wavelength of the ROA spectrometer used. In chapter 6, an approach to

extract the true RROA spectrum of a chiral complex under resonance, based on the eCP-Raman mechanism, was proposed and applied. The comparison between the true RROA spectrum extracted and the preliminary simulation results, based on the latest theoretical RROA development, provides guidance for future development in this important direction.

Preface

The current thesis is submitted as the partial fulfillment of the requirements for obtaining the degree of Doctor of Philosophy in the University of Alberta. The work present in this thesis is based on my entire PhD study in the department of chemistry at the University of Alberta which started from September 2018 to July 2023 under the supervision of Prof. Yunjie Xu. Some of the works in the current thesis have been published, and the list of the author contributions are listed below.

Chapter 3 of my thesis is based on two published papers 1. "Transfer and Amplification of Chirality Within the "Ring of Fire" observed in Resonance Raman Optical Activity Experiments" G. Li, J. Kessler, J. Cheramy, T. Wu, M. P. Poopari, P. Bouř. Y. Xu, Angew. Chem. Int. Ed. **2019**, 58, 16495-16498. 2. "Two Spectroscopies in One: Interference of Circular Dichroism and Raman Optical Activity" T. Wu, G. Li, J. Kapitán, J. Kessler, Y. Xu, P. Bouř. Angew. Chem. Int. Ed. **2020**, 59. 21895-21898. In the 2019 published paper, I carried out the experimental Raman and ROA measurements, preliminary theoretical DFT calculations, data analysis and the initial manuscript writing. Dr. J. Kessler performed the Transition Polarization Model (TPM) calculations. J. Cheramy helped the chemicals preparation, instruments setting up and preparing the manuscript. Dr. T. Wu helped editing the manuscript. Dr. M. P. Poopari collected the preliminary experimental spectra. Prof P. Bouř and Prof. Y. Xu were the corresponding authors and were involved in the conceptualization, data analysis and manuscript reviewing-writing. In the 2020 published paper, Dr. T. Wu carried out the magnetic ROA experiments and the initial manuscript preparation. I measured the Raman and ROA spectra and helped the manuscript editing and the preparation of figures. Prof J. Kapitán helped with the magnetic ROA measurements. Dr. J. Kessler performed some initial theoretical simulations. Prof P. Bouř and

Prof. Y. Xu were the corresponding authors and were involved in the conceptualization, data analysis and manuscript reviewing-writing.

Chapter 4 of my thesis is based on the published paper "Can One Measure Resonance Raman Optical Activity?" G. Li, M. Alshalafeh, Y. Yang, J. R. Cheeseman, P. Bouř. Y. Xu, Angew. Chem. Int. Ed. **2021**, 60, 22004-22009. In this publication, I did all the experimental measurements, theoretical eCP-Raman calculations, data analysis and the initial manuscript writing. M. Alshalafeh synthesized the metal complex and helped with the manuscript preparation. Dr. Y. Yang provided the Python scripts for data analyses. Dr. J. R. Cheeseman performed all the finite lifetime calculations of RRaman and RROA. Prof. Y. Xu was the corresponding author who was involved in the conceptualization, data analysis, and manuscript reviewing-writing. Prof P. Bouř was also the corresponding author who was involved in the manuscript reviewing-writing.

Chapter 5 of my thesis is based on the published paper "Stereochemical Properties of Two Schiff-Base Transition Metal Complexes and Their Ligand by Using Multiple Chiroptical Spectroscopic Tools and DFT Calculations." G. Li, D. Li, M. Alshalafeh, J. Cheramy, H. Zhang, Y. Xu, Molecules **2023**, 28, 2571. In this published paper, I carried out the experimental measurements, theoretical calculations, data analysis and initial manuscript writing. Dr. D. Li did the preliminary experimental measurements and theoretical calculations. M. Alshalafeh did the synthesis and reviewed the manuscript. J. Cheramy helped reviewing and editing the manuscript. Prof. H. Zhang reviewed the manuscript. Prof. Y. Xu was the corresponding author and was involved in the conceptualization, data analysis and in manuscript reviewing-writing.

Chapter 6 of my thesis includes the experimental work I did to extract true RROA spectra and some preliminary simulation results from our theoretical collaborators. I did all the

experimental measurements, data analysis and the initial writing. M. Alshalafeh helped with the chemical synthesis and data collection. Dr. Q. Yang did the vibronic coupling simulations, while Dr. A. Baiardi and Prof J. Bloino developed the related theoretical calculation algorithm and computational scripts writing. Dr. J. R. Cheeseman did the simulations with the finite lifetime/vibronic coupling calculations. Prof Y. Xu was the supervisor and was involved in the conceptualization, data analysis and in manuscript reviewing-writing.

Acknowledgement

I would like to express my sincere gratitude to my supervisor Prof. Yunjie Xu, for her invaluable support and guidance throughout my research journey. Without her assistance, I would not have been able to make my progress in my work. I would like to thank all the group members of Xu and Jäger groups: Nate, Matthias, Leo, Jiao, Angelo, Amin, Joseph, Fan, Arsh, Moe, Bowei, Boyang, Yanqing, Haolu, Qian, Jiarui, Aran, Mutasem, Colton, Alex, Amanda and everyone else. I would like to thank Prof. Wolfgang Jäger for his insightful comments and questions in the group meetings. I would also like to thank all my supervisory committee members, Prof. Liang Li and Prof. John Klassen for their suggestions and comments for my candidacy exam and defense.

I am grateful to have had Dr. Mohammad Reza Poopari as my lab coordinator for Chemistry 37X. Our interactions and conversions have always been a source of joy, and I am truly appreciated all the support you have provided me.

Lastly, I would like to thank my friends and family for their support and love in the past five years with a special mention to my father. Their presence and encouragement are invaluable to me, and I am deeply grateful for their presence by my side.

Table of contents

Chapter 1. Introduction……1

1.1 Molecular Chirality and chiroptical spectroscopy ……...1

1.2 The applications of chiroptical spectroscopy in transition metal complexes ……...4

1.3 The history of Resonance ROA (RROA) and some puzzles ……5

1.4 Outline of this thesis…...……...8

Chapter 2. Experimental Chiroptical Methods and DFT Calculations……..…..…15

2.1 Overview ……15

2.2 Raman and ROA ……...17

2.2.1 The fundamentals of Raman and ROA ……....17

2.2.2 The history of ROA spectroscopy ……...……..…21

2.2.3 The ROA instrumentation ……....22

2.2.4 Some tips of Raman and ROA measurements……...…28

2.3 Vibrational Circular Dichroism (VCD) ……29

2.3.1 The fundamentals of VCD ……....……..…29

2.3.2 VCD instrumentation ……....30

2.4 Theoretical Calculations ……..…….33

Chapter 3. The Strong Induced Chiral Raman Signals of Solvents: Searching for the Mechanism ……..…40

3.1 Introduction ……40

3.2 Experimental Section ……41

3.3 Results and Discussions ……42

3.3.1 The Chiral Rayleigh Scattering Mechanism and “Ring of Fire” Model ……....42

3.3.2 The ECD Interference Mechanism ……....49

3.4 Conclusion ……54

Chapter 4. Can One Measure Resonance Raman Optical Activity? ……. 57

4.1 Introduction ……....57

4.2 Experimental Section ……60
4.3 Results and discussions ……..…62
4.4 Conclusions ……72

Chapter 5. Stereochemical Properties of Two Schiff Base Transition Metal Complexes and Their Ligand by Using Multiple Chiroptical Spectroscopic Tools and DFT Calculations ……. ……...……75
5.1 Introduction ……75
5.2 Results and Discussions ……..77
5.2.1 Systematic Conformational Searchers and Low-Energy Conformers of the Ligand and the Metal Complexes ……79
5.2.2 Experimental and Simulated IR, VCD, UV-Vis and ECD Spectra of the Salen-Chxn ligand ……85
5.2.3 Experimental and Simulated IR, VCD, UV-Vis and ECD Spectra of the Salen-Chxn-Ni(II) and Cu(II) Complexes ……...…91
5.2.4 Applications of the Exciton Chirality Method to the VCD and ECD Spectra of the Complexes ……..……...….101
5.2.5 Experimental and Simulated eCP-Raman Spectra of Salen-Chxn-Ni(II) and Salen-Chxn-Cu(II) ……103
5.3 Materials and Methods ……107
5.3.1 Experimental Section ...……107
5.3.2 Theoretical Section ……109
5.4 Conclusion ……...110

Chapter 6. Extraction of Pure Experimental RROA Data and Preliminary Theoretical Treatment ……...……... 116
6.1 Introduction ……...116
6.2 Experimental and General Theoretical Details ……..…119
6.3 Experimental Results and Discussion ……...120
6.4 Preliminary Theoretical Results and Discussion ……..…..……125
6.5 Conclusion ……...132

Chapter 7. Conclusions and future work …..…….... 137
7.1 Conclusions ……...137
7.2 future work ……....140

Bibliography…….…. 143

Appendix A. Supporting information for Chapter 3……...…. 156

Appendix B. Supporting information for Chapter 4……...……. 181

Appendix C. Supporting information for Chapter 5……..…….. 188

List of Tables

Table A1. Calculated (B3LYP/6-311++G**) spectral parameters of the five lowest-energy electronic transitions in the (R,R)-Ni complex …….....178

Table A2. Wavelength of five lowest-energy transitions (λ in nm) as calculated by different methods…….…….. 178

Table A3. Assignment of selected induced ROA solvent bands …….…….…….…..179

Table B1. The experimental and theoretical *CID* values of *R*-**Ni**, *R*-**Cu** and their $CHCl_3$ solvent and *S*-**BN** and its $CHCl_3$ and CH_3CN solvents. …….…….186

List of Figures (Chapters)

Figure 2.1. Four configurations of ROA…….....20

Figure 2.2. A picture of Chiral Raman-2X^{TM} spectrometer with SCP-ROA configuration…….22

Figure 2.3. A scheme of the optical components inside the Chiral-Raman 2X^{TM} spectrometer...23

Figure 2.4. Laser system control module. The red "ENABLE" light indicates the laser is on….24

Figure 2.5. Optical components in the scattered light pathway of the Chiral Raman 2X^{TM} spectrometer ……..25

Figure 2.6. Optical components in the scattered light pathway of the Chiral Raman 2X^{TM} spectrometer……...25

Figure 2.7. Sample cell mounter and holder. Left picture is the side view and right picture is the top view. ……...26

Figure 2.8. Optics in the light collection system.……...…….....27

Figure 2.9. A scheme of an FTIR-VCD instrument……...…….....31

Figure 3.1. Structure and electronic states of the (R, R)-bis(pyrrol-2-ylmethyleneamine) cyclohexane nickel(II) complex, (R,R)-Ni. A) Simplified scheme of the first four singlet electronic states with transition energies in vicinity of the 532 nm laser excitation. B) Structural formula of the complex. C) Dependence of the ROA tensors (sums of the diagonal elements of a, G', and A, in atomic units) on the excitation wavelength. The colored bars indicate the divergent regions. The CAM-B3LYP/6-311++G**/PCM/CHCl3 method was used in the computations…44

Figure 3.2. Experimental Raman ($I_R + I_L$) and ROA ($I_R - I_L$) spectra of the (R, R)- and (S, S)-Ni

complexes in CHCl3 and CDCl3 solutions (top left) and ROA spectra in nine other achiral organic solvents or their mixtures. The intensity is normalized to the strongest peak in each trace……45

Figure 3.3. Suggested enhancement mechanism with the Ni complex at the center and a bright shell of solvent molecules contributing most to the induced ROA signal. The relative absolute intensity as a function of the distance between the Ni atom and the center of mass of CHCl3 was calculated for five CHCl3 vibrational transitions ……47

Figure 3.4. Examples of simulated and experimental induced ROA spectra. (R, R)-Ni complex bands are marked by an asterisk (*). Note that absolute intensities cannot be measured; therefore, the experimental (detector counts) and computed (atomic units) scales are not related. ……49

Figure 3.5. Geometry of the ROA experiment. When the sample contains a compound differently absorbing left- and right circularly polarized light, additional chirality arises when the light is travelling through it...……50

Figure 3.6. The structure of Ni and Cu complexes..…….....52

Figure 3.7. ECD (Δε, L·mol^{-1}·cm^{-1} top) and ROA (Δ*I*, bottom, arbitrary units) spectra of **Ni** and **Cu** solutions in $CHCl_3$ within the region 0 to 1800 cm^{-1}, relative to the 532 nm laser, the asterisk marks the strongest band from the complex itself.……..53

Figure 4.1. The three chiral compounds discussed: (*R, R*)-bis (pyrrol-2-ylmethyleneamine)-cyclohexane nickel^{II} (*R*-**Ni**), *R*-bis-(trifluoroacetyl camphorato) copper^{II} (*R*-**Cu**), and atropisomeric naphthalenediimide derivative, *S*-nBu-NDI–BINAM (*S*-**BN)**, which consists of binaphthalenylamine (BINAM) and naphthalene (NDI).……...59

Figure 4.2. (a) Top: experimental Raman (I_R + I_L) spectrum of *R*-**Ni** in CH_2Cl_2 (blue) is compared with the simulated one (black); Bottom: experimental ROA (I_R – I_L) spectra of *R*-**Ni** in

CH_2Cl_2 (blue) and in $CHCl_3$ (red) are compared with simulated *eCP-Raman* contribution (black) and with simulated natural RROA spectrum (yellow). (b) Analogous results for *R*-**Cu**. Corresponding experimental and theoretical *solute* bands are numbered and asterisk (*) indicates the *solvent* bands. The calculated spectral intensities are displayed in units of [m^2 cm/sr] where m is meter and sr is steradian…..……..……...…...68

Figure 4.3. Comparison of the experimental (top) and simulated (bottom) I_R - I_L (*eCP-Raman*) spectra of the chiral solute *S*-**BN** whose bands are shown in the rectangle box and their intensities amplified by a factor of ten, and of achiral solvent $CHCl_3$ whose bands are outside the box. b) Parallel plots as in a) but with *S*-**BN** in CH_3CN solution……..……70

Figure 5.1. Possible conformations of salen-chxn: (1) the axial and equatorial conformations at cyclohexane; (2) the rotatable N-Chexane bonds are indicated by small arrows; (3) the OH orientation direction pointing to N=C (shown) or away (not shown); (4) the subtle staggered and eclipsed conformations of the tBu groups are also shown on the right side. The eclipsed CH3 groups are offset slightly for easy viewing. The tBu groups of the two aromatic branches can take on the staggered–staggered, staggered–eclipsed, and eclipsed–eclipsed conformations. …..…..81

Figure 5.2. Optimized geometries of the four low energy salen-chxn ligand conformers identified by the CREST search and optimized at the B3LYP-D3BJ/def2-TZVP level of theory with the PCM of CDCl3. The relative free energies in kJ mol^{-1} and the Boltzmann percentage abundances at 298 K are provided in the brackets....……...…82

Figure 5.3. The optimized geometries of the salen-chxn-Ni(II) and salen-chxn-Cu(II) conformers at the B3LYP-D3BJ/6-311++G(d,p) level of theory with the PCM of CDCl3 . The relative free energies in kJ mol−1 and the Boltzmann percentage abundances at 298 K are provided in the brackets..……....84

Figure 5.4. The simulated individual IR and VCD spectra of the four most stable salen-chxn conformers and the related Boltzmann averaged IR and VCD spectra at the B3LYP-D3BJ/def2-TZVP/PCM (CDCl3) level of theory at 298 K. The experimental and empirically weighted IR

and VCD spectra are also provided. The experimental units are on the right side. The main IR and VCD band features are labelled “a” to “t” to aid the comparison.……...…..……..87

Figure 5.5. The general assignment of the IR and VCD bands of salen-chxn. The main IR and VCD band features are labelled “a” to “t” to aid the comparison as in Figure 5.4.….……..88

Figure 5.6. Comparison of the experimental and theoretical UV-Vis and ECD spectra of salen-chxn in acetonitrile solution. The first 200 electronic states were included in the calculations at the two levels of theory indicated. For the empirically weighted spectra, we used the same weights derived from the IR and VCD comparison. The main UV-Vis and ECD bands are labelled as “1” to “6” to aid the comparison.……....90

Figure 5.7. (a) The IR spectrum of salen-chxn-Cu (II) in the 1700–1100 cm−1 region is divided into six parts from I to VI. (b) The molecular parts related to I to V are coloured. (c) The main vibrational modes of salen-chxn-Cu (II) in the 1450–1100 cm−1 region. The main IR bands in the 1100–1450 cm−1 region are labelled as “1” to “8” to aid the discussion……....92

Figure 5.8. Comparison of the experimental IR (top) and VCD (bottom) spectra of salen-chxn-Cu (II) with the corresponding calculated spectra in CDCl3 solution. The levels of theory used are B3LYP-D3BJ/6-311++G(d,p) and B3LYP-D3BJ/def2-TZVP+LANL2DZ(for Cu) with the PCM of chloroform. The simplified calculations were done by replacing tBu with an H atom...94

Figure 5.9. Comparison of the experimental IR (top) and VCD (bottom) spectra of salen-chxn-Ni (II) with the corresponding calculated spectra in CDCl3 solution. The levels of theory used are B3LYP-D3BJ/6-311++G(d,p) and B3LYP-D3BJ/def2-TZVP + LANL2DZ(for Ni) with the PCM of chloroform. The simplified calculations were done by replacing tBu with an H atom.. 96

Figure 5.10. Comparison of the experimental and simulated UV-Vis (top) and ECD (bottom) spectra of salen-chxn-Ni(II) and salen-chxn-Cu(II) at two different levels of theory. In total, 250 electronic states were included in the calculation. The main UV-Vis and ECD bands of salen-chxn-Ni(II) and salen-chxn-Cu(II) are labelled as “1” to “6” and “1” to “7”, respectively, to aid

the comparison.……...100

Figure 5.11. The two coupled C=N stretching transition dipole moments are indicated for the (R, R)- salen-chxn-Ni(II) and (S, S)-salen-chxn-Ni(II), providing the negative and positive exciton coupling couplets, respectively. …..……....103

Figure 5.12. (Top): experimental ECD spectra from 532 nm to 610 nm of salen-chxn-Ni(II) and salen-chxn-Cu(II). (Middle): experimental Raman spectra of the two metal complexes. (Bottom): the comparison of the experimental and simulated eCP-Raman spectra of the two metal complexes. The solute bands are indicated with asterisk…...…….105

Figure 6.1. The geometry formula of the RR-Ni (II) complex……...118

Figure 6.2. The UV-Vis and ECD spectra of RR-Ni (II) complex. The green line indicates 532 nm……121

Figure 6.3. (a) The raw $I_R - I_L$ spectrum (top) and the extracted pure RROA spectrum (bottom) of the RR-Ni (II) complex. (b) The raw Raman spectrum of the RR-Ni (II) complex. The solvent signal in the raw Raman and $I_R - I_L$ spectra was labelled by asterisk …….……...…….123

Figure 6.4. Calculated Raman, CP-Raman and ROA of RR-Ni(II) at 532 nm with different values for γ. Calculated $I_R + I_L$ and $I_R - I_L$ are displayed in units of [m^2 cm/sr] where m is meter and sr is steridian. CP-Raman was computed as $(I_R + I_L)$*DOC…….128

Figure 6.5. Calculated Raman, CP-Raman and ROA of *R*-**Ni** at 532 nm with two different basis sets. Calculated $I_R + I_L$ and $I_R - I_L$ are in m^2 cm/sr…….……..129

Figure 6.6. Comparison of the finite lifetime RRaman and RROA spectra of RR-Ni(II) at 532 nm with the experimental ones. The γ value was set at 880 cm^{-1}. …….…….130

List of Figures (Appendices)

Figure A1. CD (a,b) and absorption (c,d,e) spectra of the (*R,R*)-Ni complex. The TDDFT computations (a,c,d) were performed at the CAM-B3LYP/6-311++G**/PCM($CHCl_3$) level. The vibrational substructure of some bands in the absorption spectrum (d) was calculated at the harmonic level; for electronic bands with very different ground and excited state geometries, Gaussian profiles were used with a 30 nm full width at half maximum……..158

Figure A2. Boundary orbitals of the (*R,R*)-Ni complex at the B3LYP/6-311++G** level of theory……...159

Figure A3. A) Raw experimental Raman spectra of the (*R*,*R*)-Ni and (*S*,*S*)-Ni complex in $CDCl_3$ and in DCM (left $I_R + I_L$ axis) and Raman spectra of the pure solvents (right $I_R + I_L$ axis), measured at the 532 nm laser excitation. B) Raw experimental ROA spectra of the (*R*,*R*)-Ni and (*S*,*S*)-Ni complex in $CDCl_3$ and in DCM measured at the 532 nm laser excitation. C) Raman spectra of the (*R*,*R*)-Ni complex in $CDCl_3$ at the three excitation wavelengths: 532 nm (right $I_R + I_L$ axis), 633 nm and 785 nm (left $I_R + I_L$ axis). In the zoom-in window (right), the 532 nm spectrum is baseline corrected for easier comparison of the recorded spectral features.……160

Figure A4. A) Simulated Raman and ROA spectra of (*R*,*R*)-Ni for five excitation wavelengths, from the far-off resonance (1062 nm) to resonance at 532 nm conditions. Note the ~1000-fold increase of Raman and ROA intensities and sign changes of some ROA bands as the excitation wavelength approaches 532 nm. B) Comparison of the experimental Raman and ROA spectra of (*R*,*R*)-Ni at 532 nm in $CDCl_3$ with the simulations for the 540, 590 and 600 nm excitation. Asterisk (*) indicates a solvent band. ……161

Figure A5. From bottom to top: ROA spectra of neat 2-(*R*) and 2-(*S*)-butanol liquid, (*R*,*R*)-Ni in 2-(*R*)-butanol and 2-(*S*)-butanol, (*S*,*S*)-Ni in 2-(*R*)-butanol and 2-(*S*)-butanol, (*R*,*R*)-Ni and (*S*,*S*)-Ni in a mixture of 2-(*R*)-butanol:$CDCl_3$ (2:3), and 2-(*R*)-butanol with contributions of $CDCl_3$ and the Ni complex subtracted vs. (*R*,*R*)-Ni in a solvent mixture of 2-(*R*)-butanol:$CDCl_3$ (2:3)…..162

Figure A6. Experimental baseline-corrected ROA spectra of the (*R*,*R*)-Ni (blue) and (*S*,*S*)-Ni (green) complex in a mixture of 2-(*R*)-butanol:$CDCl_3$ (2:3) solvent, Raman spectra of neat $CDCl_3$ (orange) and 2-(*R*)-butanol (black), and ROA spectrum of 2-(*R*)-butanol (red). The strongest Ni complex bands at 1588 cm^{-1} are marked by an asterisk (*). The four rectangular boxes highlight the (*R*)-2-butanol ROA bands, which exhibit mirror-image quality for solutions containing the (*R*,*R*)-Ni and (*S*,*S*)-Ni complex. The induced chiral response of 2-butanol is completely dictated by the chirality of Ni complex.....……...…163

Figure A7. Raman (left) and ROA (right) spectra of the (*R*,*R*)-Ni complex in $CDCl_3$ (green) and in DCM (red). Raman spectra of pure solvents are also shown in both panels. The features related to $CDCl_3$ and DCM are marked with asterisks (*) in green and in red, respectively. The red square indicates that the corresponding DCM features are likely buried beneath those of the Ni complex……..…….163

Figure A8. The Transition Polarizability Model (TPM): at each particle, a local field ($\mathbf{F}_i$) of certain frequency induces a moment ($\mathbf{M}_i$) of the same (and for Raman scattering also of a different frequency). Fields from these moments are felt by other particles, where they induce additional moments, and so on. This system polarization is initiated by the excitation laser field ($\mathbf{F}_0$)……...164

Figure A9. Induced ROA spectra simulated for the (*R*,*R*)-Ni complex with a chloroform molecule for a random orientation (left), and when averaged over chloroform and complex rotational degrees of freedom (middle, right). As indicated, the simulations were done considering separately the electric dipole - electric dipole (α), electric dipole - magnetic dipole (G') and electric dipole - electric quadrupole (A) Rayleigh polarizabilities and/or their combinations……....169

Figure A10. Geometry of the backscattering SCP experiment, incoming unpolarized light of frequency ω enters with intensity I_0 at $l = 0$, the scattered light with intensity I^s and frequency ω' leaves. The incoming light is a sum of left- and right-circularly polarized components, $I_0(0) = I_R(0) + I_L(0)$, where $I_R(0) = I_L(0) = I(0)/2$…….……...…170

Figure A11. Intensities of the left- and right-circularly polarized light components as dependent on the path length *l*. ……...……..171

Figure B1. Calculated Raman, CP-Raman and ROA of *R*-**Ni** at 532 nm with different values for the damping parameter, γ. Calculated $I_R + I_L$ and $I_R - I_L$ are in m^2 cm/sr where m is meter and sr is steradian. …….…....181

Figure B2. Calculated Raman, CP-Raman and ROA of *R*-**Ni** at 532 nm with two different basis sets. Calculated $I_R + I_L$ and $I_R - I_L$ are in m^2 cm/sr……...182

Figure B3. Top: comparison of experimental IR + IL and IR - IL spectra of a) R-Ni and b) R-Cu in DCM (blue) and CHCl3 (red). The experimental IR + IL spectra (dotted line) of pure solvent DCM and CHCl3 are also provided for easy identification of the solvent bands. Bottom: simulated solute IR + IL (Raman) and IR - IL (eCP-Raman) spectra (pink) which are amplified by a factor of 5, and the related solvent spectra (black). The simulated IR + IL and IR - IL intensities are in m2 cm/sr and are scaled with the respective solvent or solute concentration and path length……183

Figure B4. Comparison of the simulated Raman, CP-Raman and ROA spectra of a) *R*-**Ni** and b) *R*-**Cu** without (γ=0) and with (γ=880 cm^{-1}) the finite-lifetime approach. The simulated $I_R + I_L$ and $I_R - I_L$ intensities are in m^2 cm/sr. For *R*-**Ni,** the optimized geometry and harmonic frequencies were computed at the B3LYP/aug-cc-pVTZ level of theory. …….……...…..…184

Figure C1. The QTAIM analysis of salen-chxn-I and -III with their bond critical points indicated: yellow = bond critical point, blue = ring critical point, and cyan = cage critical points. Salen-chxn-I has one more cage critical point than -III, stabilizing its geometry……..…188

Figure C2. The theoretical UV-Vis and ECD spectra of three salen-chxn ligand conformers in acetonitrile solution at the MN12L/def2-TZVP level. The first 200 electronic states were included in the calculations…….…….189

Figure C3. The simulated IR (top) and VCD (bottom) spectra of the three conformers of salen-chxn-Ni(II) and salen-chxn-Cu(II) at the B3LYP-D3BJ/6-311++G(d,p) level with the PCM of chloroform……190

Figure C4. a) Definition of the helicity-determining angle θ. For square planar, θ=0°, whereas θ=90° for tetrahedral. N_1 and O_1 are atoms of one aromatic branch, and N_2 and O_2 are atoms of the other branch. b) Illustration of the *M*-helicity in the near square planar metal complexes with the (R,R) ligand, viewing the coordination arrangement in a) from the right side. Note that N_2 and N_4 are connected by the cyclohexane ring. We use (R,R)-salen-chxn-Cu(II) as an example. Note that all other atoms are removed for clarity. ……190

Figure C5. The simulated UV-Vis (top) and ECD (bottom) spectra of salen-chxn-Ni(II) and salen-chxn-Cu(II) with the detailed contributions of individual electronic transitions indicated by sticks. The calculations were done at the B3LYP-D3BJ/6-311++G(d,p) and 250 electronic states were included in the calculation…….....191

Figure C6. The raw experimental VCD (top) and ECD (bottom) spectra of (R,R) and (S,S)-salen-chxn-Ni(II) and -Cu(II) …….....192

List of Symbols

λ	Wavelength
μ_{ind}	Induced dipole moment
a	electric dipole- electric dipole polarizability tensor
E	the electric field of the external radiation
Q_K	Specific normal mode K
ω_{jn}	Transition frequency
ω_0	Excitation frequency
I_R	Intensity of right circularly polarized light
I_L	Intensity of left circularly polarized light
G	Electric dipole- magnetic dipole polarizability tensor
A	Electric dipole- electric quadrupole polarizability tensor
Γ_j	Damping factor
γ	Damping parameter
$\hat{u}$	Electric dipole moment operator
$\hat{m}$	Magnetic dipole moment operator
$\hat{\theta}$	Electric quadruple moment operator
R_{ge}	Rotational strength of a given fundamental vibrational
ψ_e	Wavefunction of excited state
ψ_g	Wavefunction of ground state
$cos\theta$	The angle between the electric dipole and magnetic dipole transition moment vectors
ε	Molar absorptivity coefficient
$\Delta\varepsilon$	Differential molar absorptivity coefficient
ΔA	Differential absorption left and right circularly polarized light
A_L	Absorption of left circularly polarized light
A_R	Absorption of right circularly polarized light

List of Abbreviations

ECD	Electronic circular dichroism
VCD	Vibrational circular dichroism
ROA	Raman optical activity
CP-Raman	Circularly polarized Raman
eCP-Raman	Electronic circular dichroism-circularly polarized Raman
ORD	Optical rotatory dispersion
AC	Absolute configuration
VOA	Vibrational optical activity
CID	Circular intensity difference
RROA	Resonance Raman optical activity
SERROA	Surface enhanced Resonance Raman optical activity
SCP-ROA	Scattered circularly polarized Raman optical activity
SES	Single electronic state
RR	Resonance Raman
TES	Two electronic state
HF	Hartree-Fock
FFR	Far from resonance
TPM	Transition polarizability model
RR-Cu	RR-bis-(trifluoroacetylcamphorato) copper (II)
RR-Ni	RR-bis (pyrrol-2-ylmethyleneamine)-cyclohexane nickel (II)
S-BN	Atropisomeric naphthalenediimide derivative, *S*-nBu-NDI–BINAM
ECM	Exciton chirality method
ETDMs	Electric dipole transition moments
LCPL	Left circularly polarized light
RCPL	Right circularly polarized light
DFT	Density functional theory
TD-DFT	Time-dependent density functional theory
GDV	Gaussian Development Version

PCM	Polarizable continuum model
MCT	HgCdTe
PEM	Photoelastic modulator
AC	Alternating current
DC	Direct current
LIA	Lock-in-amplifier
CREST	Conformer-rotamer ensemble sampling tool
xTB	A semiempirical tight-binding quantum chemistry method
RMSD	Root-mean-square deviations
D3BJ	Grimme's dispersion correction with Becke Johnson damping
B3LYP	Becke, 3-parameter, Lee–Yang–Parr, Hybrid functional
QTAIM	A quantum theory of atoms in molecules

Chapter 1

Introduction

1.1 Molecular chirality and chiroptical spectroscopy

Molecular chirality was first discovered by the French chemist Louis Pasteur in 1848,[1] while conducting his investigations into the chemical and physical properties of tartaric acid. Pasteur observed that the two forms of tartaric acid exhibited distinct melting points and optical activities. This discovery marked a crucial milestone in the fields of stereochemistry and the study of three-dimensional structure of molecules. A molecule is chiral when its mirror image cannot be superimposed, similar to how the left hand is not superimposable on the right hand. Chirality is important since it can significantly influence the properties and interactions of molecules at the molecular level. In the pharmaceutical industry, for example, over half of the drugs on the market are chiral. Due to the prevalence of chirality in biological systems, one enantiomer of a drug can be effective while the other one is ineffective and even harmful to patient. One well-documented example is Thalidomide, which was used in 1950s to 1960s to treat morning sickness during pregnancy. The R enantiomer is an effective sedative and has soothing effect on anxiety, morning sickness and trouble sleeping, while the S enantiomer can cause severe birth defects for pregnant women. Furthermore, the R enantiomer can be easily converted to the S-enantiomer in the human body. Therefore, it is important to identify and separate the R and S enantiomers and study their chemical and biological properties individually to make sure the drug's safety and effectiveness.

To achieve this, several spectroscopic tools have been developed in the past decades,

such as X-ray crystallography,[2] electronic circular dichroism (ECD),[3] vibrational circular dichroism (VCD),[4,5] Raman optical activity (ROA)[5,6] and optical rotatory dispersion (ORD). Each of them has their own advantages and disadvantages. For example, X-ray crystallography provides high-resolution data at the atomic level, but it requires high quality single crystals, which may not be possible in some cases. ECD can distinguish the absolute configuration (AC) of a chiral molecule directly in solution although the broad nature of the observed bands often makes it challenging to interpret ECD spectra properly and extract the associated structural properties confidently.

In my studies, I have mainly used vibrational optical activity (VOA), which consists of VCD and ROA. The details of their instrumental designs and fundamentals are discussed in Chapter 2. Below, I will briefly introduce VCD and ROA, while the more specific backgrounds of VOA studies on chiral transition metal complexes and resonance ROA will be reviewed in 1.2 and 1.3, respectively.

VCD and ROA can be considered as the chiral version of IR and Raman spectroscopy, respectively. In the case of VCD, it measures the differential absorption of left versus right circularly polarized light in the mid-infrared region for certain vibrational transitions of chiral molecules. Using computational chemistry, researchers can obtain valuable information about functional groups, the nature of vibrational modes, and AC and conformations of chiral molecules in solution directly. One typical limitation of VCD measurements is that the intensity ratio of VCD to its parent IR is on the order of 10^{-4} to 10^{-6}. Due to the weakness of VCD signals, a fairly long measurement time is usually needed to obtain a reliable spectrum.

ROA serves as a complementary spectroscopic tool to VCD. While water strongly absorb the infrared radiation in the fingerprint region and is not considered a good solvent for VCD,

water is a weak scatterer and is routinely used as a solvent for many Raman and ROA studies of biomolecules.[7] Additionally, ROA can extend the measured spectral range down to very low wavenumber, as low as 50 cm^{-1} in some reports. Therefore, ROA can provide information about the low-wavenumber vibrational modes which are very difficult to access using a regular Fourier transformation VCD instrument. Like VCD spectroscopy, ROA measures the intensity difference between right- and left-circularly polarized light. However, the intensities of ROA signals are much weaker than its parent Raman. If one calculates the ratio of ROA intensities to the corresponding Raman intensities (i.e., circular intensity difference (CID)), it falls in the range of 10^{-3} to 10^{-6}. To overcome the weakness of ROA signals, ROA measurements typically require relatively long collection times and high concentration samples.

Based on the above descriptions, it is not surprising to conclude that utilizing both VCD and ROA in chiroptical research brings significant benefits. As will be elaborated in the later thesis chapters, the combined VCD and ROA studies are particularly advantageous when investigating solvent effects, conformational landscape, and chirality transfer events.[8]

In addition to the VOA spectroscopy, I also applied ECD spectroscopy to investigate the stereochemical properties of the chiral ligands and the associated chiral transition metal complexes. ECD commonly operates in the UV-Vis region and measures the differential absorption of left circularly polarized light (LCPL) and right circularly polarized light (RCPL) by a chiral molecule in the electronic transition region. This is in contrast to VCD which mainly focuses in the vibrational transition region and operates in the mid-IR region. The electronic transition information obtained from ECD are usually associated with the d-d (transition metal complexes) or π-π^* (organic chromophores) transitions.

1.2 The applications of chiroptical spectroscopy in transition metal complexes

Transition metal complexes have a wide range of applications in fields, such as asymmetric catalysis, [9] optoelectronics, [10] and medicine, [11] making them a crucial area of chemistry. Researchers have devoted significant attention to investigate the physical and chemical properties of these metal complexes, among which chirality is one of the most important. Chiroptical spectroscopic tools play a vital role in studying the absolute configuration of transition metal complexes. For instance, Enamullah et al. utilized the ECD spectroscopy to analyze the bis (naphthaldiminato) Nickel (II) complexes.[12] By comparing the simulated ECD spectra and the experimental spectra, the authors were able to determine the chirality of the metal center and the resulting helicity associated with the ligands. In a similar vein, Dezhahang et al. employed both ECD and VCD to investigate the ligand chirality, complex helicity, and coordination topology of five Schiff-base ligand transition metal complexes.[13] Their study also highlighted the usefulness of VCD in providing the insights into the conformational landscapes of the chiral molecules. In addition to determining chirality, VCD spectra also offer insight into the electron configuration and coordination number of transition metal complexes. For example, Merten et al. studied the effect of varying numbers of chelating ligands on the VCD patterns of NH_2 scissor mode.[14] They found that these patterns were highly dependent on both the number of unpaired electrons of metal center and the number of ligands chelating to it. This further demonstrates the potential of VCD spectroscopy in analyzing the three-dimensional structural properties of transition metal complexes.

Compared with ECD and VCD spectroscopies, ROA is less commonly used in coordination chemistry. This is partly because water, the most favorable solvent for ROA

measurements, is not suitable for most organometallic compounds. Furthermore, fluorescence can be a problem when studying chiral transition metal complexes because many of them are in resonance condition with the ROA source laser, making it challenging to obtain high-quality ROA spectra. On the other hand, there have been reports of ROA studies on transition metal complexes, including those presented in my thesis work. For example, Luber and Reiher simulated ROA spectra of several chiral metal complexes which were previously measured, demonstrating that one could extract the chirality information about these coordination compounds.[15]

1.3 The history of resonance ROA (RROA) and some intriguing new observations

The following text includes some paragraphs which are published in the paper titled "Electronic circular dichroism-circularly polarized Raman (eCP-Raman): a new form of chiral Raman spectroscopy" G. Li, M. Alshalalfeh, J. Kapitán, P. Bouř, Y. Xu, Chem. Eur. J. **2022,** e202104302. These are indicated with quotation marks.

The relatively weaker nature of ROA signals motivates researchers to enhance the signals by modifying their systems at the molecular level. One of the most common methods is called resonance ROA (RROA), a chiroptical version of resonance Raman spectroscopy. This resonance effect occurs when the laser excitation frequency matches one or several electronic transition(s) of the targeted molecules. Reliable ROA spectra with reasonable signal to noise ratio can be achieved under resonance conditions.

"In 1996, Nafie proposed the single electronic state (SES) theory[16] for RROA when only

a SES is in resonance with the excitation laser wavelength, formally establishing the linkage between ECD and ROA. Based on the SES theory, all RROA bands are monosignate, with a sign opposite to that of ECD of the resonance electronic state. This is commonly regarded as the hallmark of a RROA spectrum. In contrast, multi-signate spectra are common for off-resonance ROA measurements." Two years later, the first experimental monosignate RROA spectra have been reported for naproxen and its derivatives by Vargek et al.[17] The RROA bands show the same relative intensities as those in the parent resonance Raman (RR) spectra. Additionally, the magnitude of the RROA to RR ratio is comparable to the dissymmetric factor of the ECD band to the corresponding UV-vis band, although the RROA and ECD have opposite signs. Their observations appear to be consistent with the SES theory advanced by Nafie.

In 2010, Merten et al. studied a europium (III) complex and reported the first experimental example of RROA in transition metal complexes.[18] Later on, the SES theory was extended to the two electronic state (TES) theory,[19] to account for the two electronic states which are both in resonance and affect the RROA spectral patterns and to explain the bisignate RROA spectrum observed.

More recently, RROA has been reported for several biomolecules, such as aggregated carotenoids,[20] human serum transferrin,[21] imidazole–myoglobin complex,[22] and a photoreceptor protein.[23] These authors also utilized the SES theory to explain the observation although no detailed spectral simulations were reported because of the complexity of the systems investigated. In addition, a few reports of surface enhanced ROA and surface enhanced RROA have also published.[24,25]

Although considerable progresses have been made in both experimental and theoretical RROA, it is still very difficult to reproduce the previously reported RROA spectra theoretically.

During the course of this thesis research, some doubts were raised about whether the RROA spectra reported are indeed true RROA spectra, a central point of my thesis study. Below, I briefly describe some fascinating yet puzzling observations encountered in the ROA experiments of several transition complexes.

"In 2014, while working on a series of transition metal complexes with the Schiff-base ligand (R,R) and (S,S)-bis(pyrrol-2-ylmethyleneamine)-cyclohexane, members of our research group observed a greatly enhanced intensity for the $I_R - I_L$ spectra with Ni and Cu. The $I_R - I_L$ signals appeared in a few minutes rather than a few hours as typically expected. The elevated Raman baselines indicated that Ni and Cu were under (or near) resonance, leading to the initial speculation that these are RROA features."

At the time as it is now, density functional theory (DFT) of ROA was widely implemented in many electronic structure calculation packages. Ruud et al. successfully presented the first DFT calculations of ROA by using the hybrid functional B3LYP of non-resonance organic molecules such as methyloxirane, a-pinene, and trans-pinene.[26] The DFT method has shown considerable improvements in prediction of vibrational frequencies and ROA signs compared to the earlier Hartree-fock (HF) method calculations. However, modelling a resonating system and treating the electronic states in the resonance regime pose significant challenges. For example, Luber et al. reported that how the consideration of a second electronic excited state can lead to significant changes in the RROA spectral patterns.[27] Additionally, while damping factors in the polarizability tensors are negligible under the far from resonance (FFR) approximation (i.e., the usual ROA measurement condition), they play a vital role in RROA intensity calculations. To address these complications, several approaches such as sum over state formalism,[27] time-depend density functional theory[28] and finite life-time approach[28, 29] have been

developed.

We applied some of these theoretical ROA treatments in collaborations with several theorists. None of the calculations generated any ROA patterns which resemble the experimental one. I carried out some subsequent experiments with a range of solvents and realized that the strong ($I_R - I_L$) bands observed actually belong to the achiral solvents, rather than the chiral solute we focused on.

The huge induced solvent chiral signatures were both exciting and puzzling to us. Our research group has considerable experience in spectroscopic characterizing non-covalent interactions associated with chiral molecules in the gas phase,[30] in the cold rare gas matrices,[31] in solution,[32] and at interfaces.[33] "Specific non-covalent intermolecular interactions, for example hydrogen-bonding, between a chiral solute and achiral solvent molecules, have been reported to produce the induced (chirality transferred) solvent VCD bands.[34] However, extensive modeling of the specific Ni-solvent adducts showed no sign of any enhancement or any ROA patterns which remotely resemble the experimental observation."

The discovery journey to uncover the mechanisms of these induced chiral Raman solvent bands and the associated chiral solute bands is described in the result chapters of the thesis, Chapter 3 and 4. The search for other transition metal complexes with similar resonance properties and the approach to extract true RROA spectra are discussed in Chapter 5 and 6, respectively.

1.4 Outline of this thesis

In chapter 2, I introduce the fundamentals and instrumentation of Raman, ROA, and VCD spectroscopies in detail. The working principles and design of major optical components in ROA

and VCD spectrometer are explained. Furthermore, some tips for routine Raman and ROA measurements are provided. In the last section, the density functional theory (DFT) calculations of Raman and ROA spectra are also discussed.

Chapter 3 summarizes the results from three publications. In chapter 3, I studied the phenomena of chirality transfer from the resonating (R, R)-bis (pyrrol-2-ylmethyleneamine)-cyclohexane nickel (II) complex (RR-Ni) to achiral solvent molecules. A through-space solvent-solute interaction mechanism, "ring of fire", was initially proposed to explain the observation. The transition polarization model (TPM) was utilized to reproduce the chiral Raman ($I_R - I_L$) spectral features of solvent molecules. With the combination of theoretical calculations and several parallel experimental measurements, we successfully ruled out any specific intermolecular interaction mechanism for this unique chiral transfer effect.

On the other hand, the "ring of fire" model failed to explain the observed ($I_R - I_L$) spectral patterns of a second transition metal complex which is also under resonance. The consideration of all possible light-matter interaction events under the usual ROA measurement condition led to the discovery of a new form of chiral Raman spectroscopy which we called eCP-Raman. The detailed mechanism and the associated equation of this new form of chiral Raman spectroscopy are presented. Furthermore, we discuss the nature of the chiral Raman signals detected and estimate the contributions by different mechanisms both experimentally and theoretically.

Chapter 4 focuses on the chiral Raman signals detected for the solute molecules, RR-Ni and R-Cu, instead of the solvent molecules. Both transition metal complexes are under (near) resonance with the laser excitation frequency of the ROA spectrometer used. It was unclear before hand whether the observed chiral Raman signals correspond to their true RROA spectra or not. Quiet surprisingly, the simulated eCP-Raman spectra of these two metal complexes, based

on the mechanisms and equation presented in Chapter 3, show excellent agreement with the experimental data, whereas the RROA contributions are negligible. Neglecting the eCP-Raman contribution may lead to misinterpretation of the observed chiral Raman data and incorrect conclusions. Importantly, we point out that the RROA spectra reported in previous literatures may be severely contaminated.

In Chapter 5, I used VCD, ECD and chiral Raman spectroscopy to investigate the stereochemical properties of two Schiff-based transition metal complexes (salen-chxn-Ni (II) and salen-chxn-Cu (II)) and its ligand. One underlying purpose is to expand the chiral Raman research to a large set of chiral transition metal complexes which are under resonance. Interestingly, minor changes in the ligand conformation may lead to noticeable different VCD features, allowing exploration of the ligand's conformational landscape. Furthermore, the applications of exciton chirality method were discussed. This project demonstrated the advantages of employing multiple chiroptical spectroscopic tools in conjunction with theoretical modelling to study conformational landscapes, ligand chirality and helicity of transition metal complexes in solution.

Chapter 6 centers on extracting true RROA of the chiral transition metal complex, RR-Ni. An experimental approach to extract RROA was proposed which utilized experimental ECD and CP-Raman measurements, as well as the eCP-Raman equation derived in Chapter 3. The chapter describes the trail measurements conducted to minimize the contributions of eCP-Raman in the experimental chiral Raman spectrum of the RR-Ni (II) complex and presents the true RROA spectrum obtained. The true experimental RROA spectrum is compared to preliminary results of the latest theoretical simulations using several different approaches. Comments about the

theoretical challenges in capturing the RROA features of a system under near resonance condition are provided.

In the final chapter, I provide a general conclusion of all my work in each chapter, and some future work and potential projects are proposed to further enhance our understanding on the interpretation of RROA spectra. Lastly, the bibliography and several appendices are included at the end of the thesis, which contain supporting information of each research chapter.

References

[1] L. Pasteur, Ann, Chim. Phys. **1848**, 24, 442-459.

[2] (a) Y.G. Shi, Cell, **2014**, 159, 995-1014. (b) L. Maveyraud, L. Mourey, Molecules, **2020**, 25, 1030. (b) N. K. Thakral, R. L. Zanon, R. C. Kelly S. Thakral, J. of Pharm. Sci. **2018**, 107, 2969-2982.

[3] (a) N. Berova, L.D. Bari, G. Pescitelli, Chem. Soc. Rev. **2007**, 36, 914-931. (b) G. Pescitelli, T. Bruhn, Chirality, **2016**, 28, 466-474.

[4] A. S. Perera, J. Thomas, M. R. Poopari, Y. Xu, Front. Chem. **2016**, 4.

[5] L. A. Nafie, Vibrational Optical Activity: Principles and Applications, John Wiley & Sons, Ltd., UK, **2011.**

[6] L. D. Barron, Molecular light scattering and optical activity, 2nd edn. Cambridge, **2004**.

[7] R. Sgammato, W. Herrebout, C. Johannessen, J. Raman Spectrosc. **2019**, 50, 1905-1913.

[8] (a) A.S. Pererea, J. Cheramy, C. Merten, J. Thomas, Y. Xu, ChemPhysChem. **2018**, 19, 2234-224; (b) Y. Yang, J. Cheramy, M. Brehm, Y. Xu, ChemPhysChem. **2022**, doi.org/10.1002/cphc.202200161; c) M. R. Poopari, Z. Dezhahang, Y. Xu, Spectrochim. Acta Mol. Biomol. Spectrosc. **2013**, *136*, 131–140; (c) G. Li, D. Li, M. Alshalalfeh, J. Cheramy, H. Zhang, Y. Xu, Molecules **2023**, 28, 2571.

[9] S. Bellemin-Laponnaz, S. Dagorne, Chem. Rev. **2014**, 114, 8747-8774.

[10] V. W. W. Yam, A. S. Y. Law, Coord. Chem. Rev. **2018**, 367, 127-162.

[11] J. Karges, Angew. Chem. Int. Ed. **2022**, 61, e202112236.

[12] M. Enamullah, M. A. Quddus, M. R. Hasan, G. Pescitelli, R. Berardozzi, G. Makhloufi, V. Vasylyeva, C. Janiak, Dalton Trans. **2016**, 45, 667-680.

[13] Z. Dezhahang, M. R. Poopari, J. Cheramy, Y. Xu, Inorg. Chem. **2015**, 54, 4539-4549.

[14] C. Merten, K. Hiller, Y. Xu, Phys. Chem. Chem. Phys. **2012**, 14, 12884-12891.

[15] S. Luber, M. Reiher, Chem. Phys. **2008**, 346, 212-223.

[16] L. Nafie, Chem. Phys. **1996**, 205, 309-322.

[17] M. Vargek, T. B. Freedman, E. Lee, L. A. Nafie, Chem. Phys. Lett. **1998**, 287, 359-364.

[18] C. Mertem. H. Li, X. Lu, A. Hartwig, L. A. Nafie, J. Raman Spec. **2010**, 41, 1563-1565.

[19] C. Merten, H. Li, L. A. Nafie, J. Phys. Chem. A. **2012**, 116, 7329-7336.

[20] M. Dudek, E. Machalska, T. Oleszkiewicz, E. Grzebelus, R. Baranski, P. Szczśnisk, J. Mlynarski, G. Zajac, A. Kaczor, M. Baranska, Angew. Chem. Int. Ed. **2019**, 58, 8383-8388.

[21] J. Bogaerts, C. Johannessen, J. Raman Spec. **2019**, 50, 641-646.

[22] R. Sgammato, W. Herrebout, C. Johannessen, J. Raman Spectrosc. **2019**, 50, 1905 – 1913.

[23] S. Haraguchi, M. Hara, T. Shingae, M. Kumauchi, W. D. Hoff, M. Unno, Angew. Chem. Int. Ed. **2015**, 54, 11555 – 11558.

[24] (a) S. Abdali, E. W. Blanch, Chem. Soc. Rev. **2008**, 37, 980 – 992; (b) S. O. Pouř, S. E. J. Bell, E. W. Blanch, Chem. Commun. **2011**, 47, 4754 – 4756; (c) S. O. Pouř, L. Rocks, K. Faulds, D. Graham, V. Parchaňský, P. Bouř, E. W. Blanch, Nat. Chem. **2015**, 7, 591 – 596.

[25] S. Abdali, C. Johannessen, J. Nygaard, T. Nørbygaard, J. Phys. Condens. Matter **2007**, 19, 285205.

[26] K. Ruud, T. Helgaker, P. Bour. J. Phys. Chem. A. **2002**, 106, 7449-7455.

[27] S. Luber, J. Neugebauer, M. Reiher, J. Chem. Phys. **2010**, 132, 044113.

[28] L. Jensen, J. Autschbach, M. Krykunov, G. C. Schatz, J. Chem. Phys. **2007**, 127, 134101.

[29] T. Helgaker, S. Coriani, P. Jørgensen, K. Kristensen, J. Olsen, K. Ruud, Chem. Rev. **2012**, 112, 543-631.

[30] (a) F. Xie, N. A. Seifert, A. S. Hazrah, W. Jäger, Y. Xu, ChemPhysChem **2021**, 22, 455-460; (b) J. Thomas, O. Sukhorukov, W. Jäger, Y. Xu, Angew. Chem. Int. Ed. **2013**, 52, 4402-4405

[31] C. Merten, Y. Xu, Angew. Chem. Int. Ed. **2013**, 52, 2073−2076.

[32] (a) G. Yang, Y. Xu, Phys. Chem. Chem. Phys. **2008**, 10, 6787−6795; (b) M. R. Poopari, Z. Dezhahang, G. Yang, Y. Xu, ChemPhysChem **2012**, 13, 2310−2321.

[33] Y. Yang, X. Sun, M. R. Poopari, C. Jian, H. Zeng, T. Tang, Y. Xu, ChemPhysChem **2022**, doi.org/10.1002/cphc.202200608.

[34] (a) G. Yang, Y. Xu, J. Chem. Phys. **2009**, 130, 164506/1-9; (b) A. S. Perera, J. Cheramy, C. Merten, J. Thomas, Y. Xu, ChemPhysChem, **2018**, 19, 2234-2242.

Chapter 2

Experimental Chiroptical Methods and DFT Calculations

2.1 Overview

As indicated in the introduction chapter, multiple spectroscopic techniques have been utilized in my PhD research. These included conventional Raman, IR and UV-Vis spectroscopies as well as their chiral counterparts, Raman optical activity (ROA), VCD, and ECD spectroscopies. While the formers are commonly applied to provide general chemical information such as the functional groups involved, geometric and electronic properties of the systems of interest in solution, the associated linewidths in solution are usually fairly broad and generally do not provide enough specificity to distinguish different conformers of the targeted molecular systems. For example, in several recent spectroscopic studies of transition metal complexes and their ligands[1] and monosaccharides,[2] the predicted Raman and IR bands are very similar among different conformers and therefore could not be used to identify conformational species. The chiroptical spectroscopic counterparts, especially ROA and VCD, exhibit chiroptical spectral features which are exquisitely sensitive to conformational differences, in addition to chirality, thus providing rich stereochemical including conformational information about these chiral species in solution directly.

ROA and VCD spectroscopies also powerful tools for deciphering solvent effect and non-covalent interactions,[3] two related subjects of intense current interesting. This is because ROA

and VCD not only offer the same advantage as their parent Raman and IR often with a range of vibrational bands in the fingerprint region, they further demonstrated excellent sensitivity to non-covalent interactions with solvent and solute molecules. The non-covalent interactions often result in only small frequency shifts in the Raman and IR fingerprint region, making it difficult to extract conclusive information about the interactions. The associated ROA and VCD spectral features, on the other hand, tend to exhibit clear pattern changes when both sign and intensity of a band can be altered or some new bands may appear.[4] For example, the induced solvent VCD bands have been reported at the water bending region for a number of simple chiral molecules in aqueous solution.[4(a)] This induced solvent chiroptical signature mechanism was initially explored to explain the observed solvent $I_R - I_L$ chiral Raman features of several transition metal complexes discussed in the latter chapters of my thesis.

In this chapter, I will first briefly review the fundamentals of Raman/circularly polarized Raman/ ROA, and IR/VCD, spectroscopies. Since the basic theories of them are covered in many review papers and textbooks,[5] the readers are referred to them for the detailed derivations and descriptions. I will only introduce some terms which are important to follow the results in the current thesis. In addition, during my PhD study, I have used three main chiral optical spectroscopic instruments which include a chiral Raman spectrometer, a FT-IR/VCD spectrometer, and an UV-Vis/ECD spectrometer to investigate stereochemical properties of a series of Schiff-base chiral transition metal complexes and their ligands. Brief descriptions of these instruments will be provided. In particular, the optical components in the chiral Raman 2X^{TM} spectrometry will be described in detail since it is the main spectroscopic tool used.

Finally, to interpret the experimental chiroptical data and to extract the sought after

information, it is necessary to simulate the corresponding chiroptical spectra. In my thesis study, these theoretical tasks were performed using density functional theory (DFT) calculations. In general, the approach includes multiple steps: (1) search for all possible conformations of the targeted chiral molecular systems using a fast inexpensive semi-empirical quantum chemical tool; (2) optimize the candidates at a cheap DFT level, allowing one to reliably select the relevant low energy geometries; (3) reoptimize the geometries of the candidates in (2) at a suitable DFT level and simulate their IR/VCD, Ramam/ROA and UV-Vis/ECD as required. Some relevant details about the choice of conformational searching tool and levels of theory will be briefly explained at the end of this chapter.

2.2 Raman and ROA

2.2.1 The fundamentals of Raman and ROA

Raman scattering is an inelastic scattering process where the monochromatic incident light interacts with molecules and causes them to experience a vibrational and/or rotational transition to a different energy level. This light-matter interaction causes the frequency of scattered photons to be different with the frequency of incident photons. Such shift in frequency (or energy) of the scattered photon is called Raman shift, which can provide us structural information to identify molecules. Raman intensity is proportional to the square of induced electric dipole moment[6] and the induced electric dipole can be represented as equation (2.1)

$$\mu_{ind} = \alpha E = (\frac{\partial a}{\partial Q_K})_0 Q_K E \quad (2.1)$$

Where α is the electric dipole- electric dipole polarizability tensor, a property of the molecule, and E is the electric field of the external radiation. According to equation (2.1), a change in the

polarizability of the molecule with respect to the specific normal mode Q_K is necessary for the detection of Raman scattering by the external electric field (E).

The electric dipole-electric dipole polarizability tensor can be further described by equation (2.2).[5]

$$\tilde{\alpha}_{\alpha\beta}(\omega_0) = \frac{1}{\hbar}\sum_{j\neq m,n}\left[\frac{\langle\tilde{m}|\widehat{\mu_\alpha}|\tilde{j}\rangle\langle\tilde{j}|\widehat{\mu_\beta}|\tilde{n}\rangle}{\omega_{jn}-\omega_0-i\Gamma_j}+\frac{\langle\tilde{m}|\widehat{\mu_\beta}|\tilde{j}\rangle\langle\tilde{j}|\widehat{\mu_\alpha}|\tilde{n}\rangle}{\omega_{jn}+\omega_R+i\Gamma_j}\right] \quad (2.2)$$

Here, $\tilde{m}$, $\tilde{J}$ and $\tilde{n}$ represent the wave function for initial state, intermediate states, and final state. $\widehat{\mu_\alpha}$ and $\widehat{\mu_\beta}$ are the electric dipole- electric dipole operator. ω_{jn} is the transition frequency between intermediate states and final state. Γ_j is the damping factor.

In equation 2.2, the first term in the bracket is called the resonance term, where the frequency denominator will be extremely small if the transition frequency ω_{jn} is very close to the excitation frequency ω_0. Therefore, when the molecules are in resonance with the laser excitation frequency, the resonance term dominates and greatly enhances the Raman intensities.

One can carry out our Raman scattering experiments using a randomly polarized light source, a linearly polarized light or a circularly polarized light source. Circularly polarized Raman (CP-Raman), which is explained below, differs from conventional Raman in that it employs circularly polarized light as the incident radiation. In CP-Raman spectra, the intensity difference of the two circularly polarized light ($I_R - I_L$) signals is recorded as a function of frequency. These signals are bisignate, even for achiral molecules such as chloroform.[7] The CP-Raman process only involves the electric dipole-electric dipole polarizability tensor, which is the same as that in Raman spectroscopy, Therefore, the intensities of CP-Raman are comparable to those in Raman and are much stronger than the ROA signals. The CP-Raman signals can also be collected by the current Chiral Raman spectrometry and severely interfere the desired ROA signals.[8] In the results

chapters of this thesis, I will demonstrate the long journey how we recognized this CP-Raman event during resonance ROA (RROA) measurements and our efforts to distinguish them in the final $I_R - I_L$ spectra. We want to point out that CP-Raman plays an important role in the discovery of a new type of chiral Raman spectroscopy[8,9] in which our contribution is described in the result chapters of this thesis.

The chiral version of Raman scattering, i.e., ROA, measures the small intensity difference of scattered right circular polarized light (RCPL) versus the left circular polarized light (LCPL)[5(a)]. Based on the polarization status of incident light and scattered light, ROA can be distinguished into four configurations (Figure 2.1). The first configuration is called incident circular polarization (ICP) ROA where the incident light is right and left circularly polarized and the collected scattered light is unpolarized. The second configuration, which is now commercially available and widely used for research purpose is called scattered circular polarization (SCP) ROA. In this configuration, unpolarized incident light is required and the circularly polarized portions of right and left scattered light are captured to determine the intensity differences ($I_R - I_L$). The remaining two configurations are both called dual circular polarization (DCP) ROA and one can further distinguish them as in-phase and out-phase forms. The common part is that both the incident and scattered light are circularly polarized while in the case of in-phase DCP the polarization statuses of incident and scattered radiation are switched synchronously and in out-phase DCP, the polarization statuses are switched oppositely. Besides the polarization status of incident and scattered light, ROA can also be defined by using scattering geometries such as forward scattering, right angle scattering and back scattering.

It is noticeable that the experimental ROA signals are typically 10^{-3}~10^{-6} times less intense than their corresponding Raman signals. Since only one photon in a million photons can

experience Raman scattering and ROA is a much weaker process than Raman, it generates a few limitations to capture ROA signals. Longer collection time and relatively high concentrations of samples are required. Therefore, several efforts have been made to amplify the ROA intensities such as resonance ROA (RROA)[10,11] , surfaced enhanced ROA (SEROA)[12,13] and a combination of these two techniques surface enhanced resonance ROA (SERROA)[14].

To calculate the ROA intensities, in addition to the electric dipole- electric dipole polarizability tensor used in Raman scattering, one also needs to consider two additional polarizability tensors, namely the electric dipole-magnetic dipole (shown in equation 2.3)[5] and electric dipole-electric quadrupole (shown in equation 2.4)[5].

$$\tilde{G}_{\alpha\beta}(\omega_0) = \frac{1}{\hbar}\sum_{j\neq m,n}\left[\frac{\langle\tilde{m}|\widehat{\mu_a}|\tilde{j}\rangle\langle\tilde{j}|\widehat{m_\beta}|\tilde{n}\rangle}{\omega_{jn}-\omega_0-i\Gamma_j} + \frac{\langle\tilde{m}|\widehat{m_\beta}|\tilde{j}\rangle\langle\tilde{j}|\widehat{\mu_a}|\tilde{n}\rangle}{\omega_{jn}+\omega_R+i\Gamma_j}\right] \quad (2.3)$$

Here, $\widehat{m_\beta}$ is the electric dipole- magnetic dipole operator and the other parameters are explained in equation 2.2.

$$\tilde{A}_{\alpha\beta\gamma}(\omega_0) = \frac{1}{\hbar}\sum_{j\neq m,n}\left[\frac{\langle\tilde{m}|\widehat{\mu_a}|\tilde{j}\rangle\langle\tilde{j}|\widehat{\theta_{\beta\gamma}}|\tilde{n}\rangle}{\omega_{jn}-\omega_0-i\Gamma_j} + \frac{\langle\tilde{m}|\widehat{\theta_{\beta\gamma}}|\tilde{j}\rangle\langle\tilde{j}|\widehat{\mu_a}|\tilde{n}\rangle}{\omega_{jn}+\omega_R+i\Gamma_j}\right] \quad (2.4)$$

Here, $\widehat{\theta_{\beta\gamma}}$ is the electric dipole- electric quadrupole operator and the other parameters are explained in equation 2.2.

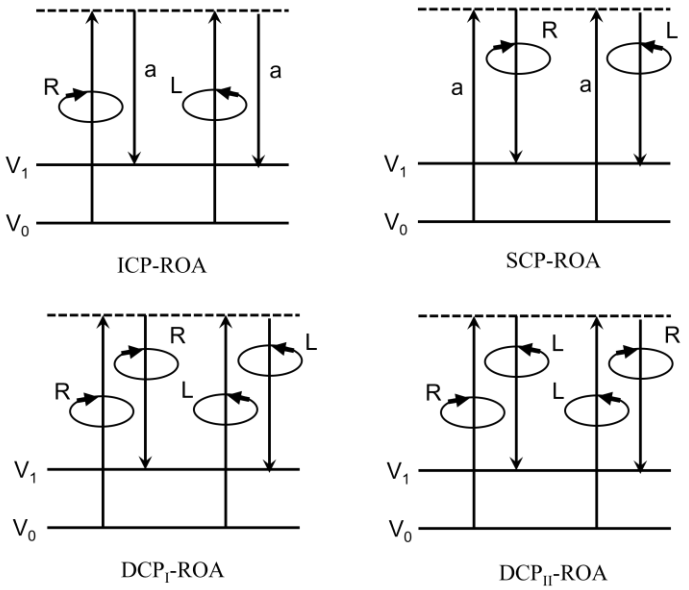

Figure 2.1. Four configurations of ROA. R represents Right circularly polarized light. L represents Left circularly polarized light. α represents randomly polarized light.

2.2.2 The History of ROA spectroscopy

In 1971, Barron and Buckingham theoretically predicted the ROA effect of optically active or chiral molecules[15]. Two years later, still from Barron's work, the first vibrational optical activity of chiral a-phenylethylamine[16] was successfully observed by using the ICP-ROA configuration with right-angle (90 degrees) geometry. Other parallel ROA measurements were carried out by Hug et al. and the first complete ROA spectra of d- (+)-a-phenylethylamine and (-)-a-pinene were obtained[17]. (-)-a-pinene is now a common standard for ROA instrument testing and calibration. In early days, it was challenging to achieve a good quality ROA spectrum. Hence, considerable efforts were made in the past decades to modify the instrumental configurations and improve the performance. For instance, Hug and Surbeck added an analyzer in the light pathway to allow the spectrograph can collect the scattered light in both parallel and perpendicular directions[18] and one can recognize and eliminate more easily eliminate optical artefacts. Barron et al. made a breakthrough in the layout of the ROA instrument and introduced the backscattering (180 degrees) geometry[19] in place of the usual right-angle (90 degrees) geometry. The dual circular polarization (DCP)-ROA configuration[20,21] proposed by L. A. Nafie also provided a tremendous improvement for the quality of ROA spectra. The most significant innovations of the ROA instrument come from Hug's group. In 1999, Hug and his colleges initially developed the dual-channel design coupled with high output spectrograph[22] and four years later, they introduced the concept of creating virtual enantiomer[23] via a half waveplate to correct the

artifacts and offsets from any optical components. These two major works established a solid foundation for the design of the modern commercialized SCP-ROA (or chiral Raman) spectrometer manufactured by Bio tools company.

2.2.3 The ROA instrumentation

In this thesis, all the Raman and corresponding chiral Raman spectra were measured on a commercial chiral-Raman 2X™ spectrometer (Figure 2.2). It measures the intensity differentials between left and right circularly polarized scattered light from chiral systems by using the scattered circular polarization (SCP)-ROA configuration. The details of SCP-ROA configuration are fully discussed in ref 22 and 23. This spectrometer uses back-scattering geometry to minimize artifacts and other optical offset. Therefore, only the scattered light whose propagation direction is 180 degrees to the incident radiation, will be captured by the charge coupled detector (CCD). Here, I will briefly introduce the key optical components inside this chiral-Raman instrument. For the sake of simplicity, I will follow the sequence of how the light pass through them as shown in Figure 2.3.

Figure 2.2. A picture of Chiral Raman-2X™ spectrometer with SCP-ROA configuration[24] (picture was taken by J. Cheramy)

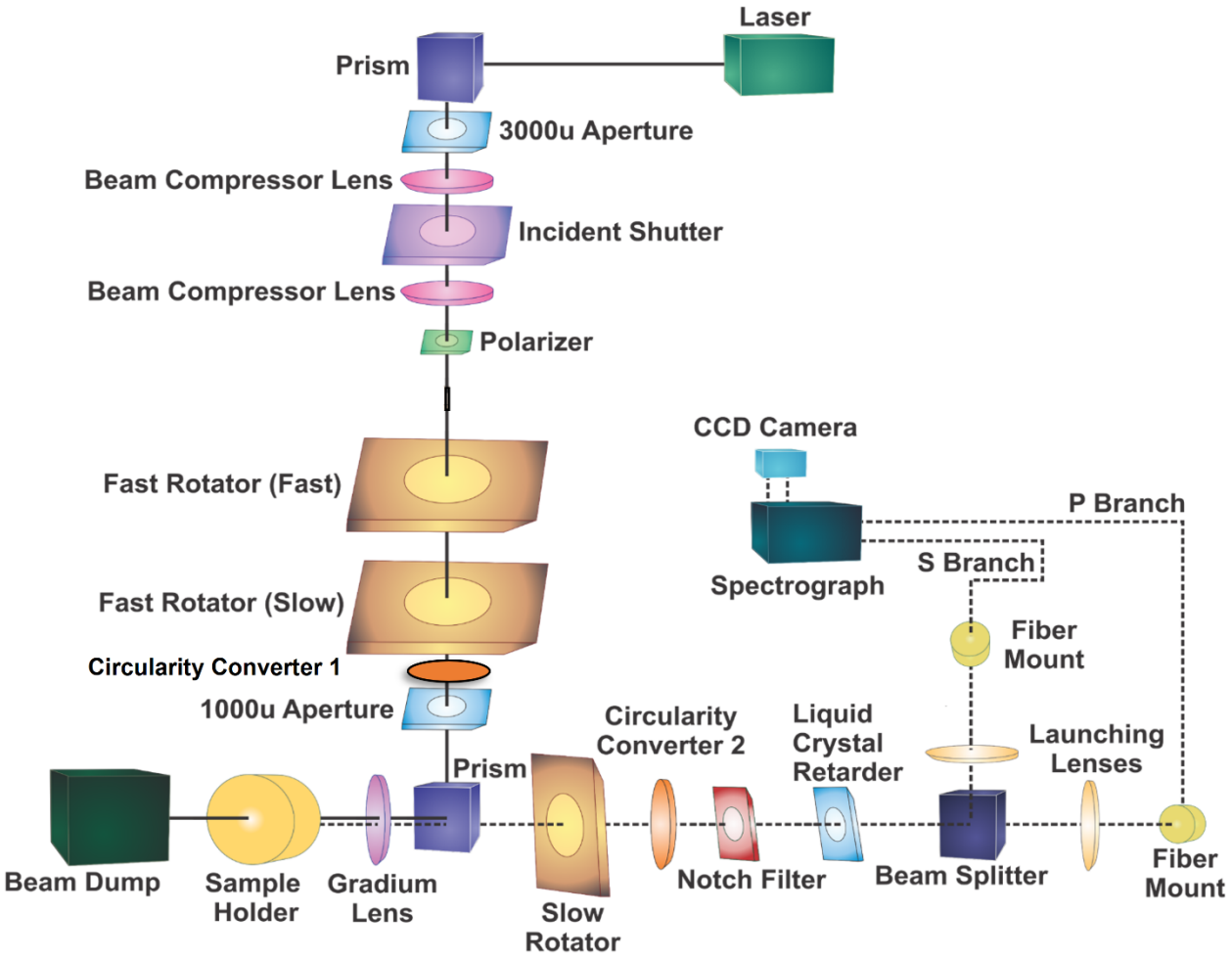

Figure 2.3. A scheme of the optical components inside the Chiral-Raman 2X™ spectrometer (adapted from Bio tools user manual)

Laser: An OPUS 532 laser generates a continuous wave of coherent green light with a wavelength of 532nm. The power can be adjusted from 0W to 2W with horizontal polarization. The laser control system is shown in Figure 2.4 and includes a key and enable button to control the laser status on or off. The rotating knob is used to adjust the laser power.

Figure 2.4. Laser system control module. The red "ENABLE" light indicates the laser is on.

Incident shutter: Allowing the required radiation to pass through.

Polarizer: Eliminating any unwanted circularly polarized components of the incident beam

A set of fast rotators: composed of two half wavelength plates with opposite rotating directions to create all orientations of linearly polarized light and make sure the incident beam is pure randomly polarized light.

Circularity converter 1 (CC1): A half wavelength plate which can convert the left circularly polarized light to right circularly polarized light and vice versa. It is moved in and out during measurements to correct any unwanted circularly polarized contaminations in the incident pathway.

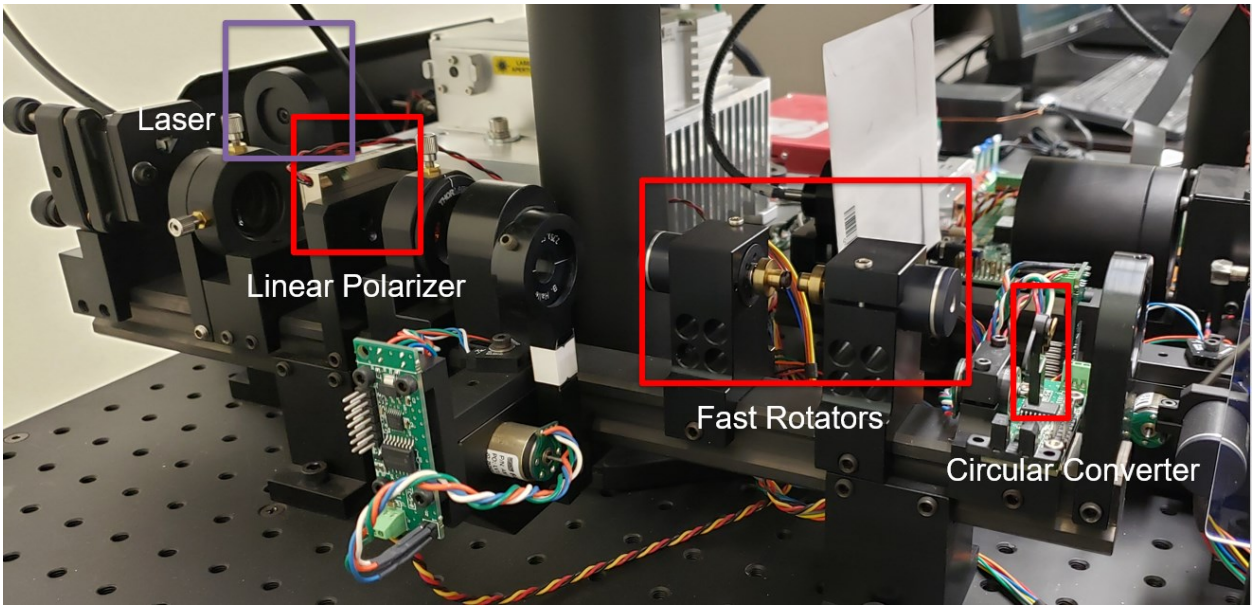

Figure 2.5. Optical components in the incident light pathway of the Chiral Raman 2X™ spectrometer

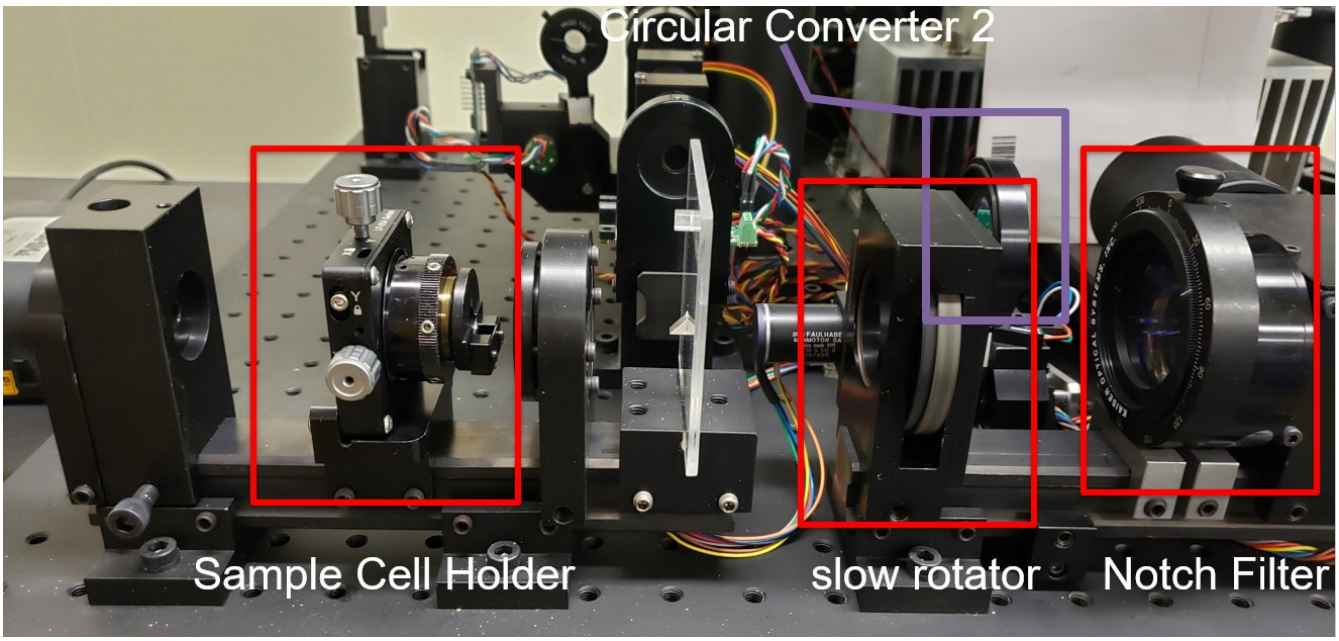

Figure 2.6. Optical components in the scattered light pathway of the Chiral Raman 2X™

spectrometer

Prism: used to refract the incident beam towards to the sample cell and allow the scattered light to pass through it

Sample holder: A mounting bracket holds the silica cells. A double cell design is presented in Figure 2.7, which allows the study of two systems without chemical interaction, for instance, resonating achiral molecules plus chiral molecules without any chemical interaction. The cell positions can be adjusted in three dimensions with two screws in X and Y direction and one rotating metal ring in the Z direction.

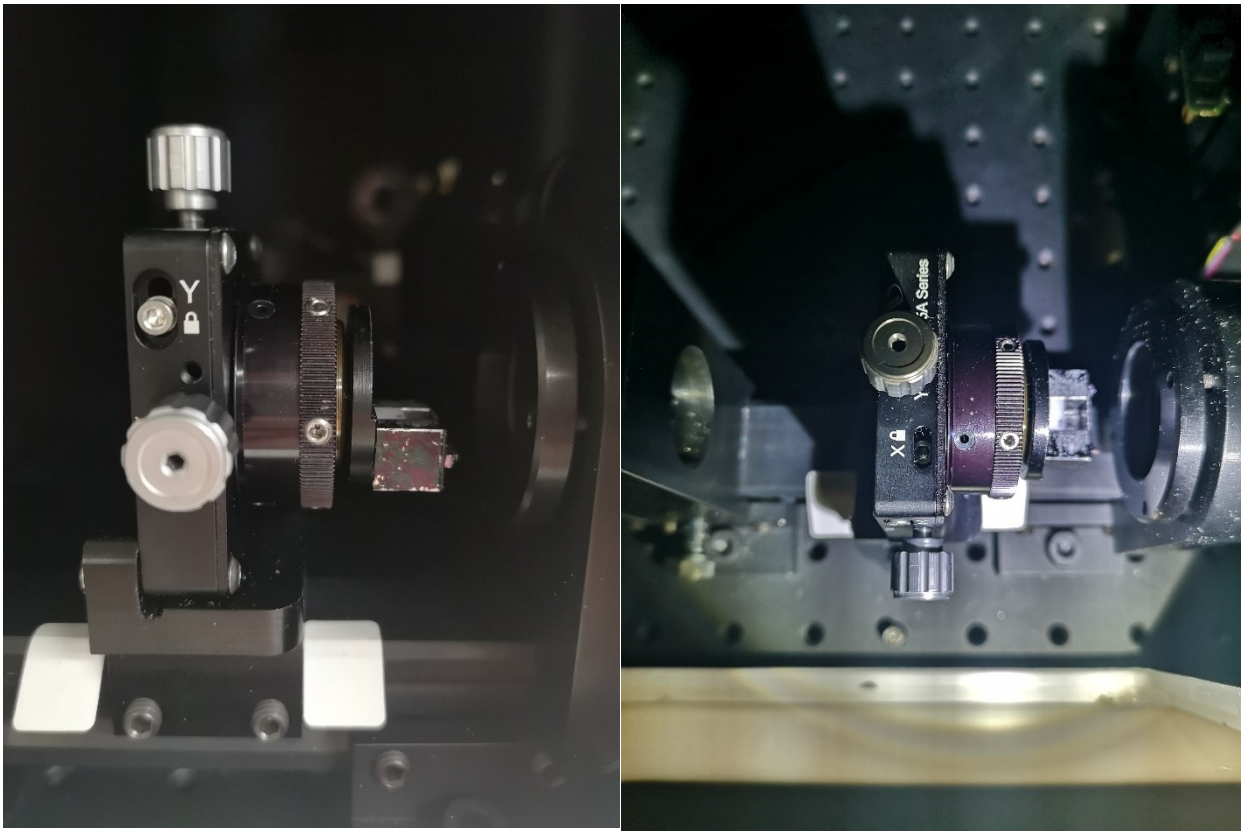

Figure 2.7. Sample cell mounter and holder. Left picture is the side view and right picture is the top view.

Slow rotator: A half wavelength plate is used to correct any linearly polarized residue due

to the preceding optical components.

Circular converter 2 (CC2): A half wavelength plate is used to create the "virtual enantiomer". The concept of virtual enantiomer was developed by W. Hug and discussed in the ref 18. Since systematic instrumental offsets cannot be eliminated by increasing the collection time and be determined by the comparison of either standard or subsequent measurements[23], circular converter 2 provides us a way to optically generate the enantiomer. By subtracting the measurements, we can obtain the offset-free spectrum of our interest. CC2 moves in and out the scattered pathway hundreds of thousands of times during one single measurement. Therefore, the ball bearings connected to the mechanical arm with the electric motor can easily wear out after a few years. Regular checkups and replacements are highly recommended.

Notch filter: Eliminating the large Rayleigh scattering of our system is a crucial step for Raman and other chiral Raman measurements, as only one in millions photon (10^6~10^7) will have a Raman scattering effect, while the remaining photons experience Rayleigh scattering.

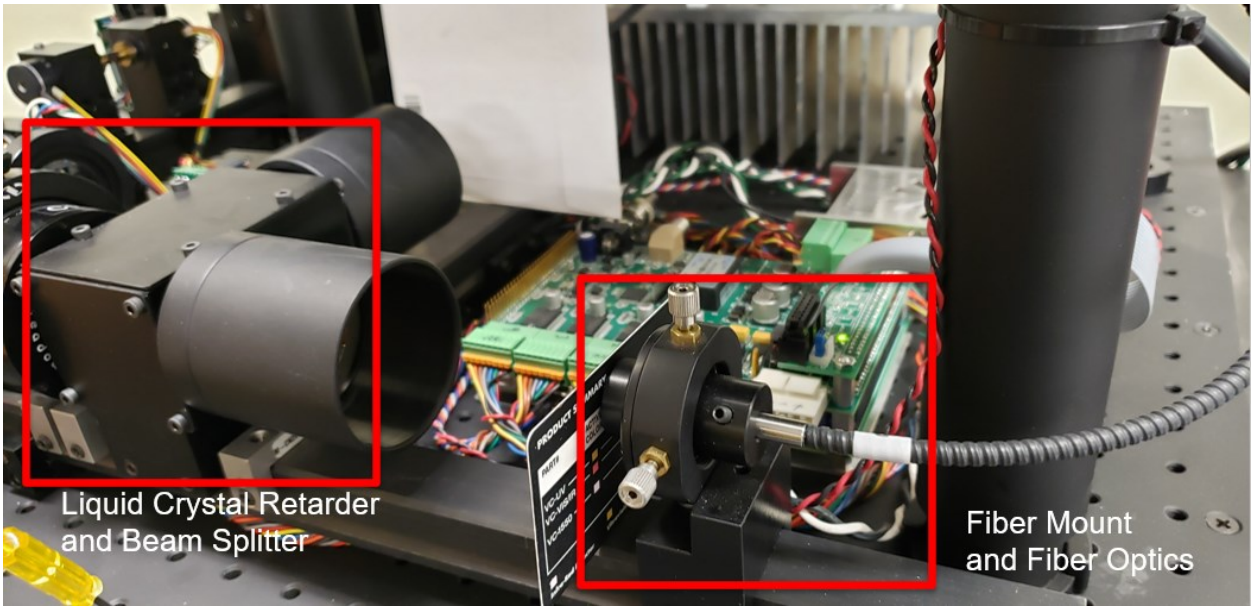

Figure 2.8. Optics in the light collection system.

Liquid crystal retarder: A quarter wavelength plate converts left and right circularly polarized light to p-type or s-type linearly polarized light. The fast and slow axis of this waveplate keeps orientating to control the conversion during measurements.

Beam splitter: Splitting the p-type and s-type linearly polarized light from the proceeding liquid crystal retarder and passing them to the fiber optic branch.

Fiber optic branches (bundles): Collecting the scattered photons from one end and are spread out as S and P branch at the other end lined up with the silt of the spectrograph.

Spectrograph: dispersing the collected scattered light by using a volume-phase holographic transmission grating.

CCD camera: A 1024x256 pixel array back-thinned camera, and the array is divided into two parts horizontally. Each part captures the scattered light from one fiber optic branch (i.e., S or P).

2.2.4 Some tips of Raman and ROA measurements

One of the biggest challenges of Raman and ROA measurements is the fluorescence effect, which is commonly observed when the sample and/or some other contaminations are in resonance with the incident radiation. A few famous examples are biological chromophores[25] which have a few conjugate systems, self-assembly and aggregation supramolecules[26] and transition metal complexes[27]. In my routine measurements, severe fluorescence effect is usually raised by fluorescent impurities from the raw materials. One option is to use high laser power to burn them off. To do this, one can open the incident timing shutter and set the laser power at 300-500mw, which is much higher than in a typical resonance Raman or chiral Raman measurement and expose the samples to the incident laser for 10-20 minutes. However, for transition metal

complexes, this method rarely works since it will cause the metal complexes to decompose due to their thermal stabilities.

Another difficulty is achieving the focus point of the incident laser on the silica cell. As mentioned before, the sample holder can be adjusted in all three directions. If the cell position is not optimized (either the cell is too close to or too far from the laser focus point), the Rayleigh and Raman scattering generated by the silica cell itself can overwrite the signals of the interests. This effect is even stronger when one tries to carry out a double cell measurement, making the cell position optimization more important. Therefore, it is highly recommended to run the (a)-pinene standard measurement before any sample measurements to determine the optimized cell position.

2.3 Vibrational Circular Dichroism (VCD)

2.3.1 The fundamentals of VCD

VCD spectroscopy is the chiral version of IR spectroscopy, and it measures the differential absorption of left versus right circularly polarized light of a chiral molecule, accompanying its vibrational transitions. This can be written as equation 2.6 here.

$$\Delta A = A_L - A_R \quad (2.6)$$

In addition to that, a new parameter called rotational strength can also be used to describe the sign and magnitude of VCD signals. Equation 2.7 gives us detailed information about rotational strength.

$$R_{ge} = Im\{\langle\psi_g|\hat{\mu}|\psi_e\rangle \cdot \langle\psi_e|\hat{m}|\psi_g\rangle\} \quad (2.7)$$

Where $\hat{\mu}$ is the electric dipole moment operator and $\hat{m}$ is the magnetic dipole moment operator. $\langle\psi_g|\hat{\mu}\,|\psi_e\rangle$ is defined as electric transition dipole moment and $\langle\psi_e|\hat{m}\,|\psi_g\rangle$ is defined as

magnetic transition dipole moment. Equation 2.7 can also be rewritten as $R = |\mu| \cdot |m| \cdot cos\theta$, which is a dot product of two vectors, μ and m, where $|\mu|$ is the magnitude of electric dipole transition moment and $|m|$ is the magnitude of magnetic dipole transition moment. The angle θ is the angle between the electric and magnetic transition dipole moment vectors. If the angle is larger than -90 degrees but is smaller than 90 degrees, the VCD signal will have a positive sign. If it is equal to 90 degrees or 270 degrees, the VCD response will be zero. If it is larger than 90 degrees but is smaller than 270 degrees, a negative VCD signal is expected. Similar to its complementary ROA spectroscopy, VCD signals are also very weak and the intensities ratio of VCD to the corresponding IR is typically in the order of 10^{-4} to 10^{-6}, making it challenging to do VCD measurements.

2.3.2 VCD instrumentation

In this thesis, all the IR and VCD spectra were measured on an FTIR-VCD module manufactured by the Bruker company. There are two major components in this module namely, a FTIR spectrometer (Vertex 70) and a VCD module (PMA 50). For the purpose of this thesis, I will only focus on the VCD module and Figure 2.9. shows a scheme of the FTIR-VCD instrument.

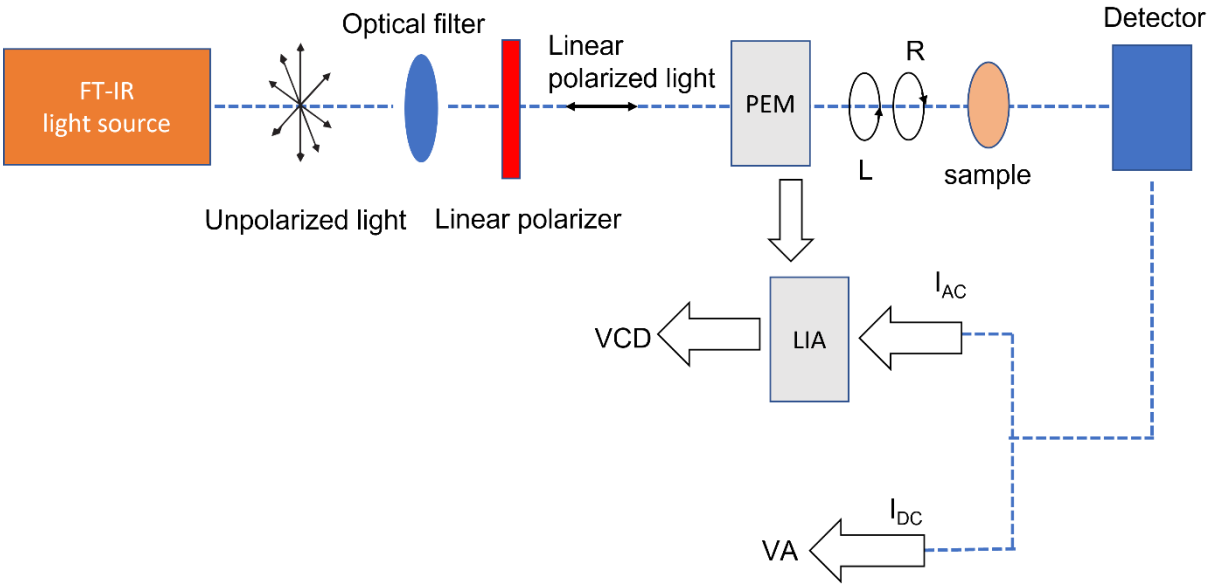

Figure 2.9. A scheme of an FTIR-VCD instrument

For a VCD measurement, the light source from the proceeding FTIR spectrometer is directed into the VCD compartment. The unpolarized light first passes through an optical filter to cut off the undesired frequency. In my measurements, I mainly focus on the 800cm^{-1} to 1800cm^{-1} since it is the fingerprint region of the bending, wagging, and stretching modes, which is commonly used to identify a bunch of unknown samples. A wire grid linear polarizer is used after that to convert the unpolarized light to the linearly polarized light at horizontal direction. The photoelastic modulator (PEM) is the heart part of VCD instrument. PEM consists of a rectangular transparent solid bar and a piezoelectric transducer, and it can be viewed as a optical retarders to modulate the polarized light. The design of PEM is based on the photoelastic effect and birefringence can be induced to the transparent solid bar with suitable materials such as silica by stress. The transducer is turned to the resonance frequency of the transparent silica bar and an alternative current (AC) will be sent through the transducer to stretch and compress the transparent silica bar. As a result, the birefringence of the transparent silica bar changes and it

can retarder one of the parallel or perpendicular component of linearly polarized light to generate the left or right circularly polarized light.

In our VCD instrument, the linearly polarized light is aligned 45 degrees to the modulator axis of the PEM. The linearly polarized light can be divided into two individual orthogonal components, one with vertical oscillating electric field and the other with horizontal oscillating electric field with respect to the modulate axis of PEM. As the transparent silica bar is stretched or compressed, the refractive index of the transparent silica bar along the vertical or the horizontal axis will be changed as well. Therefore, a phase difference can be created between the vertical and horizontal electric field. This phase difference is oscillating as a function of time to allow the PEM act as an oscillating quarter wavelength plate and convert the polarization status of the incident linearly polarized light to left and right circularly polarized light (LCPL and RCPL). After being absorbed by the chiral samples in the sample holder, the LCPL and RCPL will be captured by a HgCdTe (MCT) detector, cooled by liquid nitrogen during measurements. The liquid nitrogen should be refilled every 6 hours. MCT detector will convert the optical signal to the electrical signal, and it has two components. One is the high frequency alternative current (AC) signal which corresponds to the VCD spectrum and can be obtained by passing through the high pass filter. The other is the low frequency direct current (DC) signal, which is associated with the IR spectrum and is obtained by passing through the low pass filter.

Another key component of VCD module is the lock in amplifier (LIA). As previously mentioned, VCD measures the absorption differential between LCPL and RCPL which is typically 10^{-4} to 10^{-6} weaker than its parent IR intensity. Therefore, the LIA is used to extract the weaker VCD signals. The high frequency AC signals are sent to the LIA, which is referenced to the PEM resonance (modulation) frequency of 50 kHz. In the LIA, a synchronous demodulation

process occurs to demodulate the high frequency AC signals. Afterwards, the demodulated AC signals and DC signals are converted to the frequency domain AC and DC spectra through Fourier transform. The final VCD spectrum is achieved by taking the ratio between frequency domain AC and DC spectra.

In addition to the more standard solution measurements, our laboratory is also equipped with a matrix isolation (MI) set-up[28] where one can carry out MI-VCD investigation of organic molecules and their aggregates with much narrow bandwidth than in solution.

2.4 Theoretical calculations

As mentioned at the beginning of this chapter, three main calculation steps are needed in order to produce a final simulated chiroptical spectrum to compare with the experimental one. Below I will go through these main steps and explain why certain tools were chosen for each step.

To ensure a systematic conformational search of the chiral molecular target, I utilized a program named Conformer–Rotamer Ensemble Sampling Tool (CREST) developed by Grimme and co-workers.[29] The program offers an efficient scheme to sample the conformational space of a molecule by utilizing the semiempirical tight-binding methods combined with a meta-dynamics driven search algorithm.[29] Our research group has successfully used CREST in high resolution rotational spectroscopic studies of a wide range of organic molecules and their non-covalently bonded complexes.[30] It is worthwhile to point out that with the resolution in the tens of kHz routinely available, rotational spectroscopy is extremely sensitive to small structure differences that even those with different OH pointing directions can be easily distinguish from one to

another.[31] Furthermore, with its typical high sensitivity, one can routinely measure ^{34}S, ^{13}C, and even ^{18}O isotopologues of organic molecules in natural abundances to establish the heavy atom frame geometry experimentally.[32] As a result, one can use rotational spectroscopic studies to benchmark the reliability of CREST in conformational searches, whereas it is very difficult to use solution studies for the same purpose because spectral features for different conformers are rarely so well separated.

Since CREST search tend to generate a great number of possible conformations,[33] a multitier approach was developed reduce the computational cost. This approach[33(c)] typically includes a few additional steps, for example, an optimization with a relaxed convergence criteria at the revPBE-D3/def2-SVP[34] level, with the empirical D3 dispersion correction[35,36] and then a single-point energy evaluation at the B3LYP-D3/def2-TZVP level using Molpro.[37] These in-between steps were shown to provide energetic ranking of the CREST candidates in good agreement with the high level DFT calculations and therefore allow one to confidently reduce the number of candidates for the final DFT calculations without losing any important conformers. The final geometry optimizations and harmonic frequency calculations are performed by using Gaussian 16 package.[38]

Another advantage with CREST is that it is possible to include an implicit solvent environment during the conformation searches. For example, an implicit solvation model available with CREST is GFN2-xTB GBSA[39] where GBSA stands for the generalized Born (GB) model with surface area (SA) contributions.[40] In our experience, CREST searches with and without a solvent environment may generate very different conformational candidates.[41]

In the final step, higher level DFT calculations are performed for geometry optimizations and other necessary calculations. I used the hybrid functional B3LYP (Becke three-parameter

Lee-Yang-Parr)[42] and its two variants, CAM-B3LYP[43] and B3LYP-D3BJ[44]. CAM-B3LYP attenuates the electron-electron repulsion term in the coulomb operator and leads to more accurate description of the long-range electron interactions. In addition, D3BJ, i.e., the dispersion correction (D3) with the Becke-Johnson damping (BJ) factor, was employed to account for the long-range van der Waals interactions. This popular hybrid functional has generated good geometry predictions based on a large number of rotational spectroscopic investigations and has also been demonstrated in many VOA studies for providing good agreement between the experimental and theoretical VOA spectra of many chiral systems including transition metal complexes and the organic ligands.[45]

Moreover, the selection of suitable basis sets is also very important to predict Raman/ROA and IR/VCD spectra. Although large basis sets can usually improve the agreement between the experimental results and theoretical predictions, the computational costs also need to be considered to some extent. For some transition metal complexes which have nearly a hundred atoms, it appeared to be more efficient to first do geometry optimizations with a small basis set such as 6-31G(d). After the preliminary calculation is done, one can carry out a further simulation with a large basis set by using the optimized structure from the initial run. In my studies, I tested a range of different basis sets, for instance, the split-valence basis sets developed by Pople and co-workers, such as 6-311++G(d,p), 6-311++G(2d,p) and 6-311++G(2df,2pd).[46] All of them have additional polarization and diffusion functions to improve the accuracy of basis functions. The correlation-consistent basis set[47] cc-pVTZ and its augmented version aug-cc-pVTZ and the Karlsruhe basis set[48] def2-TZVP were also employed in my calculations. For the studies of transition metal complexes, the effective core potentials[49] LanL2DZ was also used for the transition metal center.

References

[1] G. Li, D. Li, M. Alshalalfeh, J. Cheramy, H. Zhang, Y. Xu, Molecules **2023**, 28, 2571. https://doi.org/10.3390/molecules28062571.

[2] A. S. Perera, C. D. Carlson, J. Cheramy, Y. Xu, Chirality **2023**, 1-14. DOI: 10.1002/chir.23576.

[3] (a) A. S. Perera, J. Cheramy, M. R. Poopari, Y. Xu, Phys. Chem. Chem. Phys. **2019**, 21, 3574-3584. (b) Y. Yang, J. Cheramy, M. Brehm, Y. Xu, ChemPhysChem. **2022**, doi.org/10.1002/-cphc.202200161.

[4] (a) M. Losada, P. Nguyen, Y. Xu, J. Phys. Chem. A **2008**, 112, 5621−5627. (b) M. R. Poopari, P. Zhu, Z. Dezhahang, Y. Xu, J. Chem. Phys. **2012**, 137, 194308/1−7.

[5] (a) L. A. Nafie, Vibrational Optical Activity: Principles and Applications, John Wiley & Sons, Ltd., UK, **2011**; (b) L. D. Barron, Molecular light scattering and optical activity, 2nd edn. Cambridge, **2004**. (c) L. A. Nafie, T. B. Freedman, R. K. Dukor, "Vibrational Circular Dichroism", In Handbook of Vibrational Spectroscopy, John Wiley & Sons, Ltd., UK, **2002**. (d) R. K. Dukor, L. A. Nafie, "Vibrational Optical activity of pharmaceuticals and biomolecules", In Encyclopedia of Analytical Chemistry, John Wiley & Sons, Ltd., UK, **2000**. (e) G. E. Tranter, "Protein Structure Analysis by CD, FTIR, and Raman Spectroscopies", In Encyclopedia of Spectroscopy and Spectrometry, Oxford: Academic Press. UK, **2017**. (f) H. G. Kuball "Chiroptical Analysis" In Encyclopedia of Analytical Science, Elsevier Ltd. NL, **2005**. (g) N. Harada, N. Berova, "Separations and Analysis" In Comprehensive Chirality, Elsevier Ltd. NL, **2012**.

[6] D. L. Long, The Raman Effect: A Unified Treatment of the Theory of Raman Scattering by Molecules. John Wiley & Sons, Ltd., UK, **2002**.

[7] R. Clark, S. R. Jeyes, A. J. McCaffery, R. A. Shatwell, J. Am. Chem. Soc. **1974**, 96, 5586-5588.

[8] (a) G. Li, M. Alshalalfeh, J. Kapitán, P. Bouř, Y. Xu, Chem. Eur. J. **2022**, e202104302; (b) G.Li, M. Alshalalfeh, Y. Yang, J. Cheeseman, P. Bouř, Y. Xu, Angew. Chem. Int. Ed. **2021**, 60, 22004-22009; (c) T. Wu, G. Li, J. Kapitán, J. Kessler, Y. Xu, P. Bouř, Angew. Chem. Int. Ed. **2020**, 59, 21895-21898.

[9] E. Machalska, G. Zajac, A. J. Wierzba, J. Kapitán, T. Andruniow, M. Spegel, D. Gryko, P. Bouř, M. Baranska, Angew. Chem. Int. Ed. **2021**, 60, 21205-21210.

[10] M. Vargek, T. B. Freedman, E. Lee. L. A. Nafie, Chem. Phys. Lett**. 1998**, 287, 359-364.

[11] C. Merten, H. Li, L. A. Nafie, J. Phys. Chem. A **2012**, 116, 7329-7336.

[12] S. Abdali, E. W. Blanch, Chem. Soc. Rev. **2008**, 3, 980-992.

[13] S. O. Pour, S. E. J. Bell, E. W. Blanch, Chem. Comm. **2011**, 47, 4754-4756.

[14] S. Abdali, C. Johannessen, J. Nygaard, T. Nørbygaard, J. Phys.: Condens. Matter **2007**,19, 285205.

[15] L. D. Barron, A. D. Buckingham, Mol. Phys. **1971,** 20, 1111-1119.

[16] L. D. Barron, M. P. Bogaard, A. D. Buckingham, J. Am. Chem. Soc. **1973**, 95, 603-605.

[17] W. Hug, S. Kint, G. F. Bailey, J. R. Scherer, J. Am. Chem. Soc. **1975**, 97, 5589-5590.

[18] W. Hug, H. Surbeck, Chem. Phys. Lett. **1979**, 60, 186-192.

[19] L. D. Barron, L. Hecht, W. Hug, M. J. Maclntosh, J. Am. Chem. Soc. **1989**, 111, 8731-8732.

[20] L. A. Nafie, T. B. Freedman, Chem. Phys. Lett. **1989**, 154, 260-266.

[21] D. Che, L. Hecht, L. A. Nafie, Chem. Phys. Lett. **1991**, 180, 182-190.

[22] W. Hug, G. Hangartner, J. Raman Spectrosc. **1999**, 30, 841-852.

[23] W. Hug, Appl. Spectrosc. **2003**, 57, 1-13.

[24] J. Cheramy, Master Thesis. **2016**.

[25] R. Sgammato, W. Herrebout, C. Johannessen, J. Raman Spectrosc. **2019**, 50, 1905-1913.

[26] (a) G. Zajac, A. Kaczor, A. P. Zazo, J. Mlynarski, M. Dudek, M. Baranska, J. Phys. Chem. B **2016**, 120, 4028-4033. (b) M. Dudek, G. Zajac, A. Kaczor, M. Baranska, J. Raman, Spectrosc. **2017**, 48, 673-679. (c) G. Zajac, J. Lasota, M. Dudek. A. Kaczor, M. Baranska, Spectrochim. Acta A Mol. Biomol. Spectrosc. **2017**, 173, 356-360.

[27] (a) G. Li, J. Kessler, J. Cheramy, T. Wu, M. R. Poopari, P. Bouř, Y. Xu, Angew. Chem. Int. Ed. **2019**, 58, 16495-16498. (b) T. Wu, J. Kapitán, P. Bouř, J. Phys. Chem. Lett. **2022**, 13, 3873-3877.

[28] C. Merten, Y. Xu, ChemPhysChem **2013**,14, 213−219.

[29] P. Pracht, F. Bohle, S. Grimme, Phys. Chem. Chem. Phys., 2020,22, 7169-7192.

[30] (a) E. G. Schnitzler, N. A. Seifert, S. Ghosh, J. Thomas, Y. Xu, W. Jäger, Phys. Chem. Chem. Phys. **2017**, 19, 4440-4446; (b) N. A. Seifert, J. Thomas, W. Jäger, Y. Xu, Phys. Chem. Chem. Phys. **2018**, 20, 27630-27637; (c) M. D. Marshall, H. O. Leung, S. R.

Domingos, A. Krin, M. Schnell, N. A. Seifert, Y. Xu, W. Jäger, Phys. Chem. Chem. Phys. **2022**, 24, 28495-28505; (d) J. Thomas, I. Peña, C. Carlson, Y. Yang, W. Jäger, Y. Xu, Phys. Chem. Chem. Phys. **2020**, 22, 23019-23027.

[31] (a) Z. Su, Y. Xu, Angew. Chem. Int. Ed. **2007**, 46, 6163−6166. (b) J. Thomas, X. Liu, W. Jäger, Y. Xu, Angew. Chem. Int. Ed. **2015**, 54, 11711-11715.

[32] (a) N. Borho, Y. Xu, Phys. Chem. Chem. Phys. **2007**, 9, 1324−1328; (b) J. Thomas, J. Yiu, J. Rebling, W. Jäger, Y. Xu, J. Phys. Chem. A. **2013**, 117, 13249−13254.

[33] (a) A. N. Mort, F. Xie, A. S. Hazrah, C. D. Carlson, Y. Xu, Phys. Chem. Chem. Phys. **2023**, 25, 16264-16272; (b) B. Wu, N. A. Seifert, A. Insausti, J. Ma, S. Oswald, W. Jäger, Y. Xu, Phys. Chem. Chem. Phys. **2022**, 24, 14975-14984; (c) H. Wang, M. Heger, M. H. Al-Jabiri, Y. Xu, Molecules, **2022**, 27, 38/1-19. https://doi.org/10.3390/molecules27010038.

[34] Weigend, F.; Ahlrichs, R. Phys. Chem. Chem. Phys. **2005**, 7, 3297-3305.

[35] Grimme, S.; Antony, J.; Ehrlich, S.; Krieg, H. J. Chem. Phys. **2010**, 132, 154104.

[36] Smith, D.G.A.; Burns, L.A.; Patkowski, K.; Sherrill, C.D. J. Phys. Chem. Lett. **2016**, 7, 2197-2203.

[37] Werner, H.-J.; Knowles, P.J.; Knizia, G.; Manby, F.R.; Schütz, M. Molpro: Wires Comput. Mol. Sci. **2012**, 2, 242-253.

[38] Frisch, M.J.; Trucks, G.W.; Schlegel, H.B.; Scuseria, G.E.; Robb, M.A.; Cheeseman, J.R.; Scalmani, G.; Barone, V.; Petersson, G.A.; Nakatsuji, H.; et al. Gaussian 16, Revision C.03; Gaussian, Inc.: Wallingford, CT, **2019**.

[39] Bannwarth, C.; Caldeweyher, E.; Ehlert, S.; Hansen, A.; Pracht, P.; Seibert, J.; Spicher, S.; Grimme, S. WIREs Comput. Mol. Sci. **2021**, 11, e1493.

[40] Onufriev, A.V.; Case, D.A. Annu. Rev. Biophys. **2019**, 48, 275−296.

[41] M. Alshalalfeh, N. Sun, A. H. Moraes, A. P. A. Utani, Y. Xu, Molecules **2023**, 28, 4013. https://doi.org/10.3390/molecules28104013.

[42] (a) A. D. Becke, J. Chem. Phys. **1993**, 98, 5648-5652. (b) C. Lee, W. Yang, R. G. Parr, Phys. Rev. B. **1988**, 37, 785.

[43] T. Yanai, D. P. Tew, N. C. Handy, Chem. Phys. Lett. **2004**, 393, 51-57.

[44] A.D. Becke and E.R. Johnson, J. Chem. Phys. **2005**, 123, 154101.

[45] (a) Z. Dezhahang, M. R. Poopari, F. E. Hernández, C. Diaz, Y. Xu Phys. Chem. Chem. Phys. **2014**, 16, 12959−12967; (b) C. Merten, Y. Xu, Dalton Trans. **2013**, 42, 10572−10578. (c) J. Tomeček, P. Bouř, J. Chem. Theory Comput. **2020**, 16, 2627-2634.

[46] (a) R. Ditchfield, W. J. Hehre, J. A. Pople, J. Chem. Phys. **1971**, 54, 724-728. (b) R. Krishnan, J. S. Binkley, R. Seeger, J. A. Pople, J. Chem. Phys. **1980**, 72, 650-654.

[47] T. M. Dunning, J. Chem. Phys. **1989**, 90, 1007-1023.

[48] (a) F. Weigend, F. Furche, R. Ahlrichs, J. Chem. Phys. **2003**, 119, 12753-12762. (b) F. Weigend, R. Ahlrichs, Phys. Chem. Chem. Phys. **2005**, 7, 3297-3305.

[49] (a) P. J. Hay, W. R. Wadt, J. Chem. Phys. **1985**, 82, 270-283. (b) S. Chiodo, N. Russo, E. Sicilia, J. Chem. Phys. **2006**, 125, 104107.

Chapter 3

The Strong Induced Chiral Raman Signals of Solvents: Searching for the Mechanism

"This chapter is modified based on the following published papers."

1. G. Li, J. Kessler, J. Cheramy, T. Wu, M. R. Poopari, P. Bouř, Y. Xu. "Transfer and Amplification of Chirality within the "Ring of Fire" Observed in Resonance Raman Optical Activity Experiments" Angew. Chem. Int. Ed. **2019,** 58, 16495-16498.

2. T. Wu, G. Li, J. Kapitán, J. Kessler, Y. Xu, P. Bouř. "Two Spectroscopies in One: Interference of Circular Dichroism and Raman Optical Activity" Angew. Chem. Int. Ed. **2020,** 59. 21895-21898.

3.1 Introduction

Most important molecules found in living organisms are chiral and are sensitive to circularly polarized light. This sensitivity was first explored by Pasteur,[1] while he examined the chemical and optical properties of a group of compounds known as tartrates. Since then, an amazing variety of chiroptical methods has been developed for fundamental studies and practical applications.[2] One of the youngest and most dynamically evolving tools is Raman optical activity (ROA).[3] It can provide rich stereochemical information because of the wealth of vibrational bands usually exhibited by chiral molecules, and is applicable directly in solutions. On the other hand, the ROA effect is weak, and a large amount of sample is usually needed for the analysis.

This has prompted vigorous search for enhancement techniques, utilizing, for example, molecular resonance, [4] nanoplasmons (resonating metallic nanoparticles), [5] and molecular aggregation.[6]

When one molecular sample is under resonance, some fascinating phenomena have been reported for Raman and related spectroscopies. For example, the induction of large ROA signals in achiral reporter molecules in the presence of nanoplasmons or a solvent-signal enhancement under hyper-Raman scattering have been observed.[5(a)] [7] Even though many properties of nanoplasmons can be explained by established electromagnetic and chemical theories,[8] the ROA enhancement and chirality transfer effects have so far resisted detailed interpretation. In general, "chirality transfer" phenomena when chiral molecules make non-chiral ones optically active has attracted much attention. The chirality induction provides a detailed insight into molecular interactions[9] and is of interesting for nanotechnology industry and analytical chemistry.[10]

In this context, we believe that the strong chirality transfer under resonance conditions described in this work significantly contributes to the understanding of molecular interactions with chiral light. We report strong ROA of a range of solvents induced by a chiral nickel complex under resonance conditions. Contrary to common belief, the chirality transfer appears quite general, and the induced ROA signals were even stronger than those of the Ni complex itself. For 2- butanol, a chiral solvent, the induced ROA intensity was stronger than the natural one.

3.2 Experimental Section

Raman and ROA spectra were measured using a ChiralRaman-2X^{TM} spectrometer (BioTools) operating with 532 nm laser excitation source. For a typical experiment, about 0.04m

or a saturated solution of the complex was used, with laser power at the source set to 30-50 mW and an accumulation time of 25 h. Measurements with 633 nm and 785 nm excitation wavelengths were done on an inVia confocal Raman microscope (Renishaw).

DFT calculations were performed with the Gaussian16 software package,[11] using the B3LYP and CAM-B3LYP functionals and the 6-311 ++ G(2df,2pd) basis set.[12] The observed dependence on functional and basis set was consistent with previous studies.[13] The solvent was modeled using the polarizable continuum model (PCM).[14] In some computations, the LanL2DZ[15] effective core potential basis set were used for Ni and People basis set 6-311 ++ G(2df,2pd) were used for C, N, H atoms. Since the Ni atom has a significant number of inner shell electrons, we used the LanL2DZ basis set with an effective core potential (ECP) to represent these inner-shell electrons i.e., reducing the number of explicit electrons in the calculation, and therefore reduced computational cost. The B3LYP/6-311++ G(2df,2pd)/PCM ROA polarizabilities (tensors a, G', and A, see Ref. [2]) were used as input parameters for the Transition Polarizability Model (TPM) as described in Figure A8. Further experimental and computational details can be found in the appendix.

3.3 Results and Discussions

3.3.1 The Chiral Rayleigh Scattering Mechanism and "Ring of Fire" Model

The resonance-ROA phenomenon itself, an area of intense experimental and theoretical interest, can be rationalized only in simple cases.[4(a),16] None of them, however, is applicable to the observations presented here. Based on extensive experimental data and model calculations, we show that the effect is not caused by specific chemical bonding, p–p stacking, and/or

hydrogen bonding, but rather based on through-space solvent–solute interactions, a concept utilized for describing, for example, chirality transfer in the presence of nanoplasmons.[5(a)]

This outcome is surprising because the Ni complex molecule is much smaller than nanoparticles. However, in resonance with laser radiation, its polarizability significantly increases. The results thus can be linked to so-called quantum plasmons,[17] a term used to describe plasmonic behavior at the molecular limit. One may therefore expect further fundamental and practical explorations in this area.[18]

The Ni complex itself (Figure 3.1) was previously investigated by UV/Vis and IR absorption spectroscopy, electronic and vibrational circular dichroism (ECD, VCD), and density functional theory (DFT).[19] The UV/Vis and ECD spectra contain several bands and can be reasonably well explained on the basis of time dependent DFT (Figure A1, Supporting Information). Interestingly, the first three lowest-energy transitions with a strong participation of nickel d-orbitals ($S_0 \rightarrow S_1$, $S_0 \rightarrow S_2$, and $S_0 \rightarrow S_3$) show relatively high dissymmetry factors g (CD-to-absorption ratio, up to g = 0.0762, see also Table A1 and A2 (appendix), and Figures 3.1A and A2). These g-values are about 100 times larger than those for common chiral molecules.

As schematically shown in Figure 3.1A, the equilibrium geometries of the three lowest-energy excited electronic states differ significantly from that of the ground state. Therefore, the ground-state vibrational wavefunction overlaps with a large number of excited vibrational states. The vibrational sub-structure of the electronic bands is not resolvable, which is consistent with the experimental UV/Vis and ECD spectra.[19] When the excitation light is in resonance with these electronic transitions, molecular polarizabilities (and their derivatives determining Raman and ROA intensities) sharply increase. A typical dependence of the polarizability tensors a, G', and $A^{2,3}$ on the wavelength can be seen in Figure 1 C. Raman and ROA measurements also confirm

the enhancement at 532 nm (resonance) when compared to laser excitations at 633 and 785 nm (non-resonance; Figure A3) and can be qualitatively reproduced by DFT computations (Figure A4). Minor inconsistencies are due to the limited accuracy of DFT[20] and the pre-resonance approximation.[3(a)]

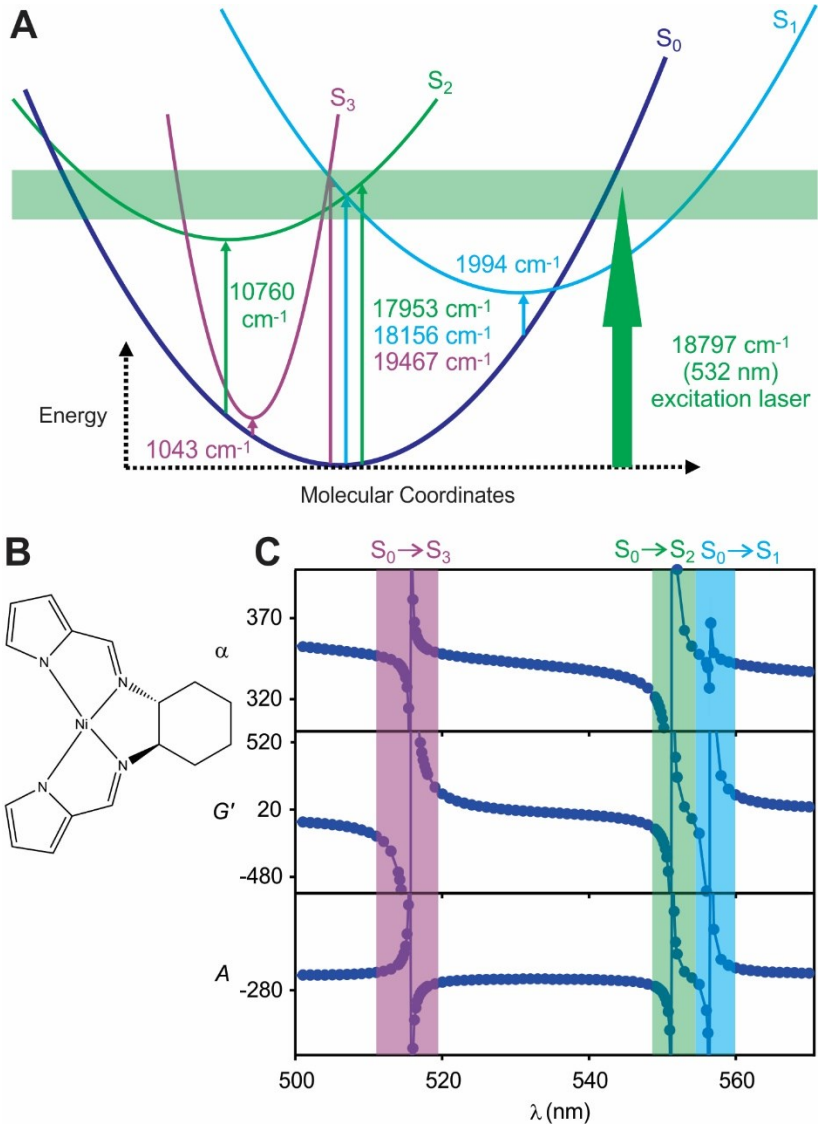

Figure 3.1. Structure and electronic states of the (R, R)-bis(pyrrol-2-ylmethyleneamine) cyclohexane nickel(II) complex, (R,R)-Ni. A) Simplified scheme of the first four singlet

electronic states with transition energies in vicinity of the 532 nm laser excitation. B) Structural formula of the complex. C) Dependence of the ROA tensors (sums of the diagonal elements of a, G', and A, in atomic units) on the excitation wavelength. The colored bars indicate the divergent regions. The CAM-B3LYP/6-311++G**/PCM/CHCl3 method was used in the computations.

While the behavior of the Ni complex fits into established theories, the accompanying huge ROA signal of the solvents was unexpected. Figure 2 shows the effect for CHCl3 /CDCl3, DCM, dimethyl sulfoxide (DMSO and DMSO-d_6), and mixtures containing benzene, acetone, methanol (MeOH and MeOH-d_4), carbon tetrachloride (CCl4), and acetonitrile (ACN-d_3). This variety of polar/nonpolar, hydrogen-bond donor/acceptor, and chlorinated solvents was chosen to test if the formation of long-lived chiral solute–solvent clusters[21] was responsible for the chirality transfer.[22] Despite significant differences in physical and chemical properties, such as polarity, dielectric constant, hydrogen- or p-bonding capabilities, the effect was observed in all solvents. The solvent response is approximately linear so that the signal from a solvent mixture is a sum of the individual solvent components.

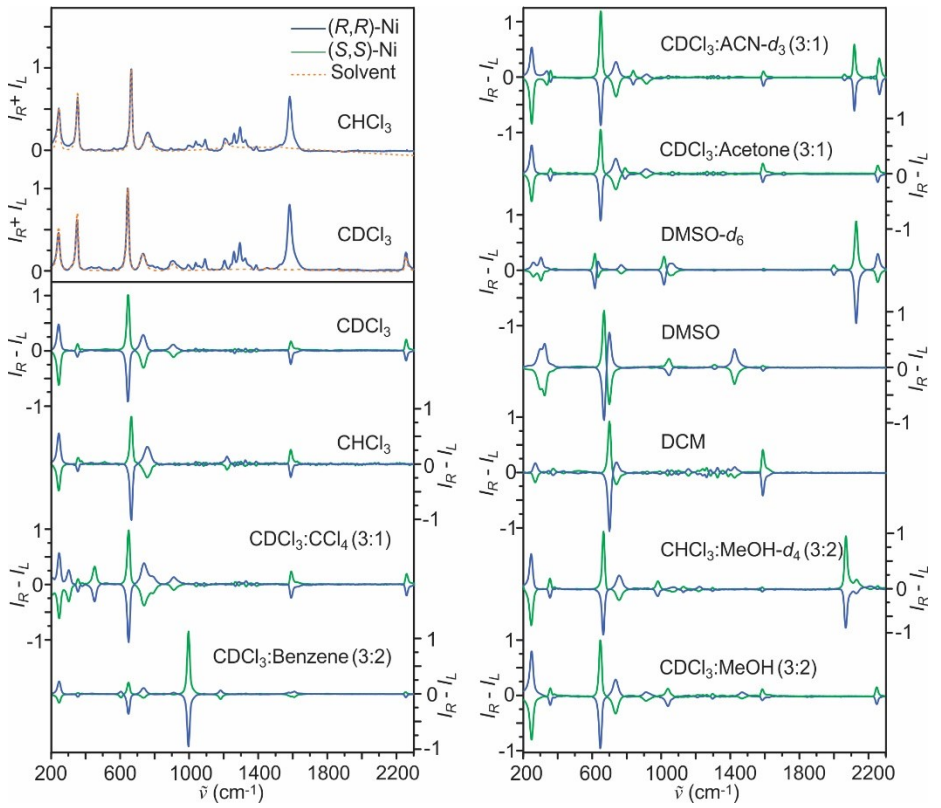

Figure 3.2. Experimental Raman ($I_R + I_L$) and ROA ($I_R - I_L$) spectra of the (R, R)- and (S, S)-Ni complexes in CHCl3 and CDCl3 solutions (top left) and ROA spectra in nine other achiral organic solvents or their mixtures. The intensity is normalized to the strongest peak in each trace, the circular intensity difference (ratio of ROA and Raman intensities) varied from 10^{-3} to 10^{-2}.

(R)- and (S)-2-butanol were investigated as solvents possessing natural (permanent) chirality. Despite the low solubility in 2-butanol, the addition of a small amount of the Ni complex altered the ROA spectra noticeably (Figure A5). The competition between induced and natural chirality is clearly visible, even though none of the Ni-complex ROA bands are apparent (Figure A5). In a 2-butanol/CDCl3 solvent mixture, the complex is more soluble and its ROA bands, including the strongest one at 1588 cm^{-1}, become visible. More importantly, the (R)-2-butanol ROA bands exhibit the mirror-image symmetry for solutions containing the (R, R)-Ni and (S, S)-

Ni complexes (Figure A6). Under such conditions, the induced chirality dominates and the natural one becomes immeasurably small.

Raman and ROA bands of the Ni complex in $CDCl_3$ and DCM are essentially unchanged by the solvent variation (Figure A7). This is probably also true for other solvents, although the Ni complex bands are often weak and difficult to identify because of experimental noise and interference with the strong induced solvent bands.

DFT simulations of non-resonance and resonance ROA spectra of a large number of clusters consisting of the Ni complex and a few solvent molecules predicted a much smaller induced ROA than in case of the isolated Ni complex (not shown), which is in contrast to experimental findings. Thus, an electromagnetic mechanism is more probable in which the resonating Ni complex behaves in a similar fashion to plasmonic metal nanoparticles used in surface-enhanced Raman scattering (SERS). Indeed, a transition-polarizability model (TPM, Figure A8)[23] based on through-space solute– solvent interactions rationalize the observed solvent-chirality induction in the vicinity of the resonating molecule to a big extent. Similar to SERS, the effective polarizability of a molecular solvent–solute pair is much larger than the sum of the polarizabilities of the individual molecules.[2,23c, 24] Interestingly, for the complex in resonance, the maximum effective (total) polarizability occurs at distances larger than the smallest solute–solvent separation. Solvent molecules in this "ring of fire" (Figure 3.3) contribute most to the measured ROA spectra. The quantum plasmon—the Ni complex with large polarizabilities—thereby affects the properties of distant solvent molecules. Although the optimal distance cannot be computed accurately at the moment (a factor of 100 was assumed for the effective polarizabilities in Figure 3.3, compared to a non-resonance), it is clear that the volume around the solute and therefore the number of affected solvent molecules grows quite quickly with the distance ($\approx R^3$), and a strong spectroscopic response can be produced.

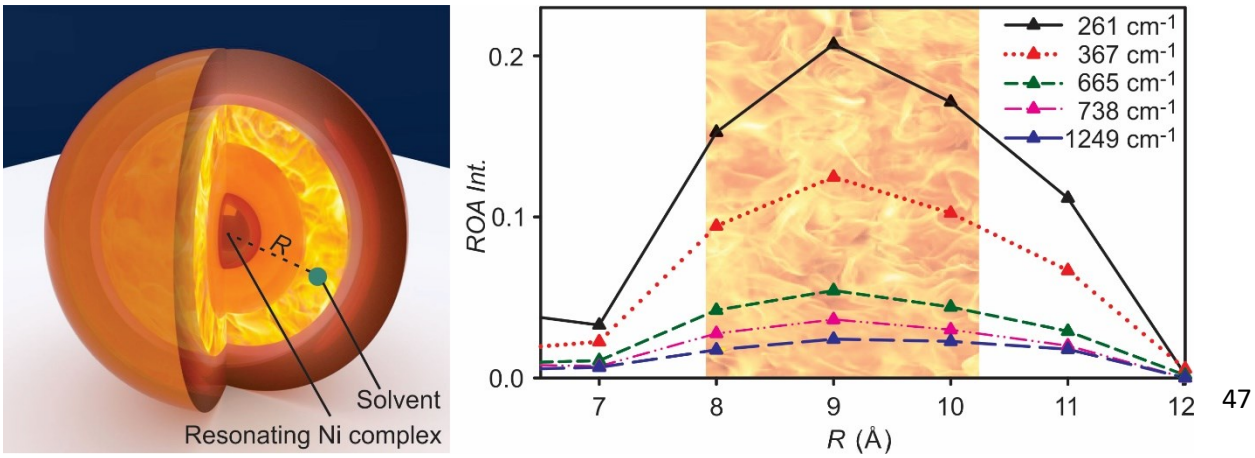

Figure 3.3. Suggested enhancement mechanism with the Ni complex at the center and a bright shell of solvent molecules contributing most to the induced ROA signal. The relative absolute intensity as a function of the distance between the Ni atom and the center of mass of CHCl3 was calculated for five CHCl3 vibrational transitions.

In Figure 3.4, we see a detailed comparison of the experimental and simulated induced ROA spectra of the solvents CHCl3, DCM, and DMSO in the presence of the (R, R)-Ni complex. Positions and assignments of the strongest bands for these and other solvents are listed in Table A3. In general, the TPM model reproduces the experimental sign patterns and major trends in relative induced ROA intensities. For DCM, for example, bands 1–3 are easily assigned, while bands 4–7 in the region of the Ni-complex signal can be identified based on the comparison done in Figure A7. Experimental signs and relative intensities of bands 4, 5, and 7 also agree with the simulation, whereas band 6 overlaps severely with a Ni-complex band. For DMSO and DMSO-d6, some predicted ROA signals with frequencies near band 5 and below band 1 are not observed experimentally. However, the model cannot explain the observed high ROA/Raman ratios, probably caused by additional factors such as vibrational coherence or spin polarization.

Regarding the theoretical foundations of ROA, another surprising observation is that the electric-dipole/electric-quadrupole Rayleigh polarizability (A) is primarily responsible for the induced ROA event (Figure A9). As expected, the “ordinary” (achiral) a polarizability gives a zero contribution except for the anisotropic non-averaged case. But also, the contribution of the G’ tensor, which quite often dominates ROA spectra, is rather negligible when compared with A, confirming that the chirality-transfer mechanism here is different from regular molecular ROA.[3a, 25]

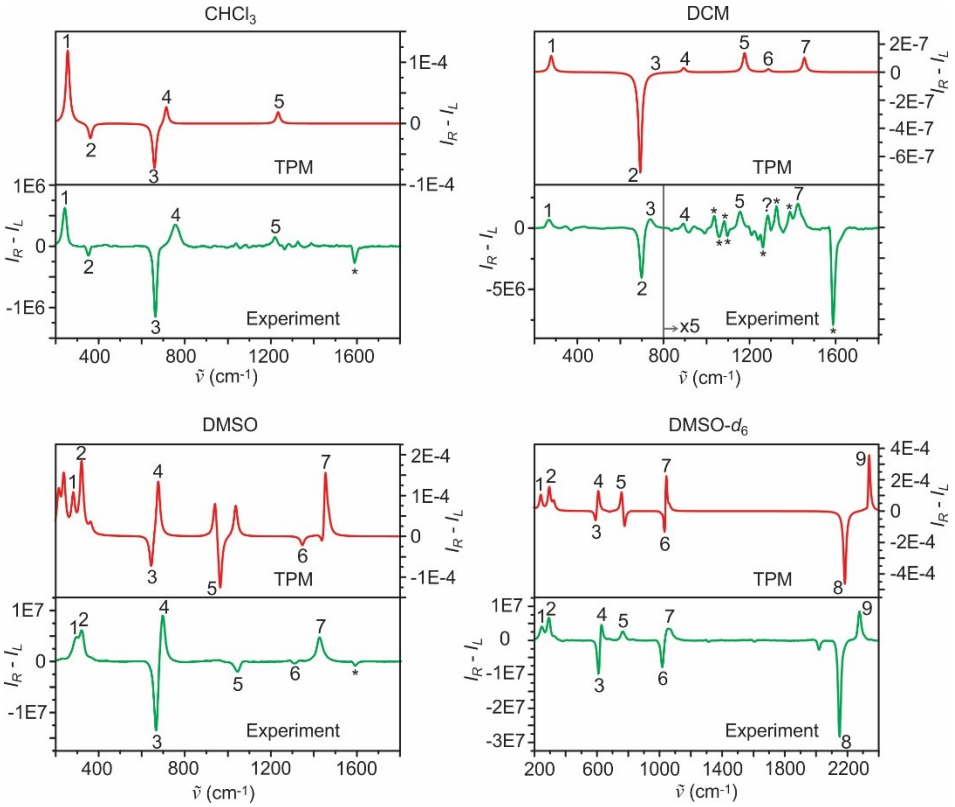

Figure 3.4. Examples of simulated and experimental induced ROA spectra. (R, R)-Ni complex bands are marked by an asterisk (*). Note that absolute intensities cannot be measured; therefore, the experimental (detector counts) and computed (atomic units) scales are not related.

Although the proposed "ring of fire" model can explain most of the observed ROA band signs, but the magnitudes are not well captured. In particular, the predicted ROA to Raman signal ratio (so called circular intensity difference, CID) was too small. To explain this inconsistency, a second mechanism, which considers the interference of circular dichroism when measuring RROA spectra was discovered.

3.3.2 The ECD Interference Mechanism

In a resonance/ pre-resonance ROA experiment (where frequency of the laser light is close to that of an electronic transition) these complexes also lead to a strong electronic circular dichroism (ECD, differential absorption of left- and right-circularly polarized light, CPL). This left/right CPL imbalance can be ultimately detected as an additional component of ROA (difference in intensities of right- and left-CPL during Raman scattering).

Let us examine a common scattered circular polarized (SCP) backscattering ROA experiment[26] in detail. The light enters the sample, and the polarization difference is detected in the scattered light (Figure 3.5, also Figures A10 and A11 in the appendix). However, when the sample exhibits ECD, the incoming light polarizes even before (and also after) being scattered, for example, in a volume element schematically labeled dl in the Figure. Recorded ROA signal thus gains additional, sometime dominant component from ECD absorption. We believe that this event has been ignored in previous literature.

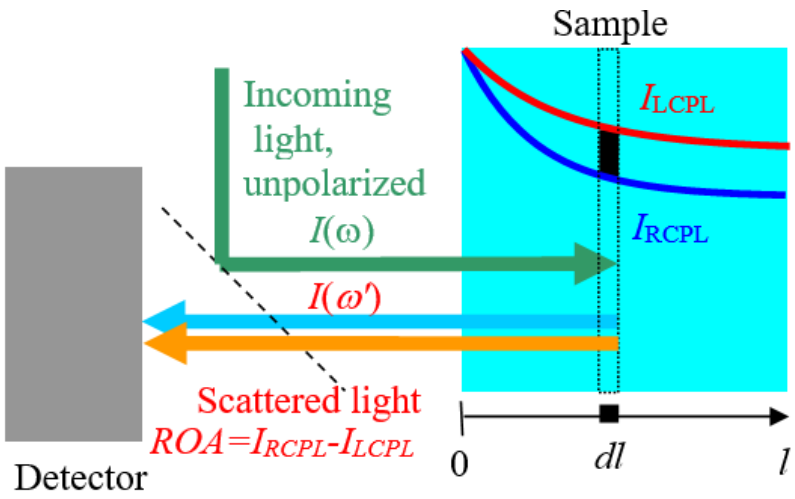

Figure 3.5. Geometry of the ROA experiment. When the sample contains a compound differently absorbing left- and right circularly polarized light, additional chirality arises when the light is travelling through it.

The interference of ECD with ROA is in practice a complicated event. The scattering occurs in a tiny volume (typically < 60 mL). The laser is focused on an even smaller spot and most volume does not participate in the scattering. Samples absorbing the laser light may decompose, exhibit strong resonance Raman signal and fluorescence. Temperature-induced variation of the refractive index can cause a "thermal lensing". The light polarized through ECD passes through the solution, undergoes Raman-scattering and further depolarizes.

Nevertheless, theoretical considerations do allow to estimate the extent of mixing of the ECD and ROA phenomena. Observed ratio of the ROA and Raman signals can be obtained as

$$CID = \frac{I_R - I_L}{I_R + I_L} = \frac{\Delta\varepsilon' + DOC\Delta\varepsilon}{4} \text{ cL} \quad (3.1)$$

where $\Delta\varepsilon$ and $\Delta\varepsilon'$ are differential absorption indices of the excitation and scattered light, respectively, determining ECD intensity, I_R and I_L are detected intensities of right and left CPL, c is the concentration, L is optical path length, and DOC is the degree of circularity of each vibrational transition of the solvent. [2]

From (3.1) we see that CID has the potential to be relatively large compared to usual ROA experiments. Whereas typical CIDs for organic molecules is about 10^{-4}, the ECD "dissymmetry ratio, $\Delta\varepsilon/\varepsilon$, is about 10^{-3}. For d-d and f-f transitions of transition metal complexes, this quantity can even approach one.[27, 28, 29] The solvent thus enters formula (3.1) through the DOC parameter, which says how the scattered molecule "remembers" the initial circular

polarization. DOC is also connected to Raman scattering depolarization ratios, or just to molecular polarizability changes under a particular vibration.

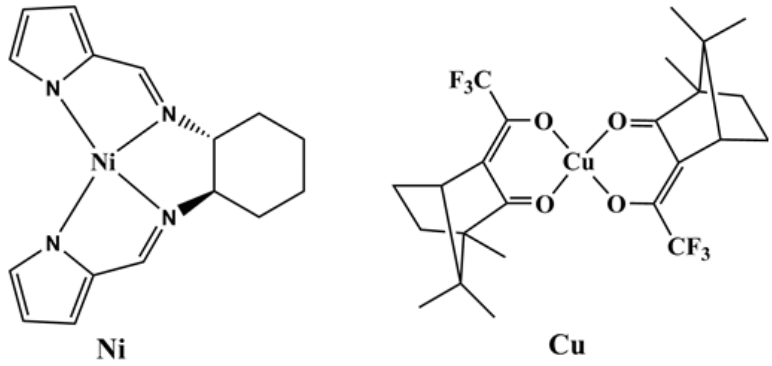

Figure 3.6. The structure of Ni and Cu complexes.

To verify the interference of ECD and ROA, we analyzed ROA spectra for model nickel and copper complexes, structures of which are plotted in Figure 3.6. Chloroform solutions of the Ni and Cu compounds provide ECD and ROA spectra plotted in Figure 3.7. As discussed before, the strongest ROA bands belong to the chloroform solvent. However, the two complexes behave differently. ECD signal of Ni is maximal at the excitation 532 nm wavelength, and it quickly diminishes within the scattered wavenumber range, i.e., $|\Delta\varepsilon'| < |\Delta\varepsilon|$. From formula (3.1) we see that the degree of circularity multiplying $\Delta\varepsilon$ will be most important in this case. Indeed, simulated signs and relative band intensities nearly copy the DOC values (Table A4), and in general agree with the experiment.

On the other hand, for Cu the ECD intensity is about constant ($\Delta\varepsilon' \sim \Delta\varepsilon$) in the scattering range, which results in single-sign ROA. The (RR)-Cu complex gives negative ECD and induced chloroform ROA of the same sign.

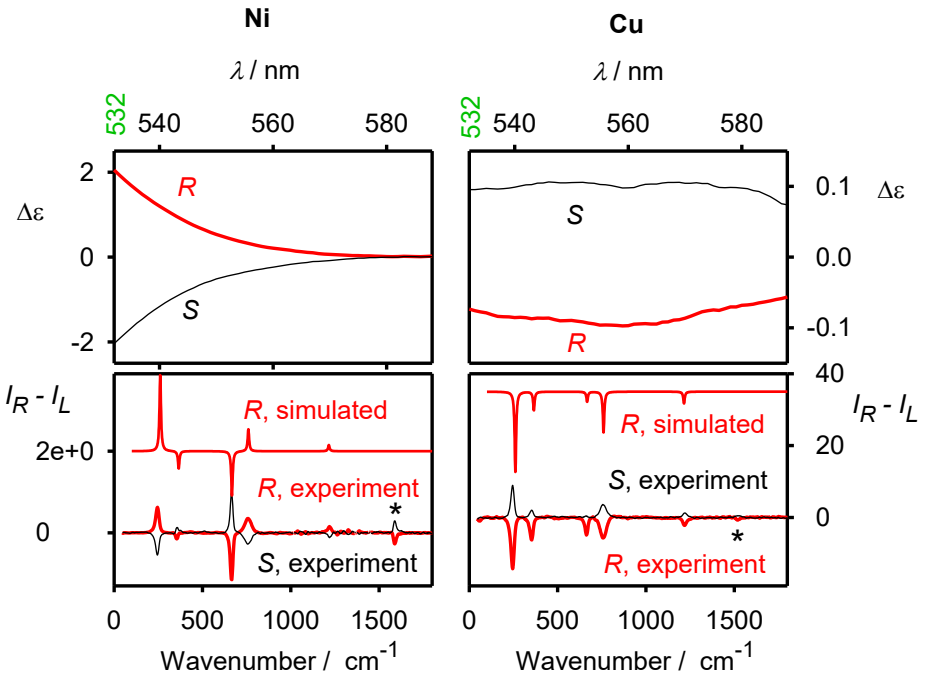

Figure 3.7. ECD (Δε, L·mol^{-1}·cm^{-1} top) and ROA (Δ*I*, bottom, arbitrary units) spectra of **Ni** and **Cu** solutions in $CHCl_3$ within the region 0 to 1800 cm^{-1}, relative to the 532 nm laser, the asterisk marks the strongest band from the complex itself.

Circular dichroism of the chiral complexes thus appears as the dominating factor leading to the "transfer" of their chirality to the solvents. In our previous study,[27] we wrongly proposed chiral resonance Rayleigh scattering as the main mechanism. The Rayleigh scattering is present but cannot explain the strength of measured ROA intensities. In both cases, chiral Rayleigh scattering and ECD, the excitation light is made chiral by the metal complex/dye, and further Raman-scattered by the solvent. Therefore, the former Rayleigh "ring of fire" model could correctly explain ROA band signs in case of the Ni complex.

3.4 Conclusion

In conclusion, we have conducted several experiments showing that extremely strong induced solvent chiral signals were collected in the chiral Raman spectra under resonance condition. After analyzing the origin of the chiral transfer effect in resonance ROA measurements, two mechanisms were proposed. The first chiral Rayleigh scattering mechanism, or “ring of fire” model can reproduce the sign but not the magnitude of our experimental observations. Therefore, a second mechanism due to the intertwining of ROA and ECD effects is explored and can be readily used to predict both the observed signs and intensities. We find it important to recognize this phenomenon in chiral spectroscopic techniques, where it can produce unwanted artifacts. On the other hand, we believe that the effect itself has the potential to be used in many applications, such as in analytical chemistry, where the strength can conveniently overcome sensitivity limitations traditionally hampering chiral analysis.

References

[1] L. Pasteur, Théses de chimie et de physique, Bachelier, Paris, **1847**.

[2] L. D. Barron, Molecular Light Scattering and Optical Activity, Cambridge University Press, Cambridge, UK, **2004**.

[3] (a) L. Nafie, Vibrational optical activity: Principles and applications, Wiley, Chichester, **2011**; (b) J. Haesler, I. Schindelholz, E. Riguet, C. G. Bochet, W. Hug, Nature **2007**, 446, 526-529.

[4] (a) A. Baiardi, J. Bloino, V. Barone, J. Chem. Theory Comput. **2018**, 14, 6370-6390; (b) J. Šebestík, J. Kapitán, O. Pačes, P. Bouř, Angew. Chem. Int. Ed. **2016**, 55, 3504-3508.

[5] (a) S. O. Pour, L. Rocks, K. Faulds, D. Graham, V. Parchanˇsky´, P. Bourˇ, E. W. Blanch, Nat. Chem. **2015**, 7, 591 – 596; (b) K. Osin´ska, M. Pecul, A. Kudelski, Chem. Phys. Lett. **2010**, 496, 86 – 90; (c) C. Johannessen, P. C. White, S. Abdali, J. Phys. Chem. A **2007**, 111, 7771 – 7776.

[6] M. Dudek, G. Zajac, A. Kaczor, M. Baranska, J. Phys. Chem. B **2016**, 120, 7807 – 7814.

[7] R. Shimada, H. Kano, H. Hamaguchi, J. Chem. Phys. **2008**, 140, 204506.

[8] (a) K. A. Willets, R. P. VanDuyne, Annu. Rev. Phys. Chem. **2007**, 58, 267 – 297; (b) S. Y. Ding, E. M. You, Z. Q. Tian, M. Moskovits, Chem. Soc. Rev. **2017**, 46, 4042 – 4076.

[9] Y. Liu, G. Yang, M. Losada, Y. Xu, J. Chem. Phys. **2010**, 132, 234513/1-11.

[10] Z. Liu, J. Ai, P. Kumar, E. You, X. Zhou, X. Liu, Z. Tian, P. Bouř, Y. Duan, L. Han, N. Kotov, S. Ding, S. Che, Angew. Chem. Int. Ed. **2020**, 59, 15226-15231.

[11] M. J. Frisch, et al., Gaussian 16, Wallingford, CT, **2016.**

[12] (a) A. D. Becke, J. Chem. Phys. 1993, 98, 5648 – 5652; (b) T. Yanai, D. Tew, N. C. Handy, Chem. Phys. Lett. **2004**, 393, 51 – 57.

[13] J. R. Cheeseman, M. J. Frisch, J. Chem. Theory Comput. **2011**, 7, 3323 – 3334.

[14] J. B. Foresman, T. A. Keith, K. B. Wiberg, J. Snoonian, M. J. Frisch, J. Phys. Chem. **1996**, 100, 16098 – 16104.

[15] P. J. Hay, W. R. Wadt, J. Chem. Phys. 1985, 82, 299 – 310.

[16] (a) C. Merten, H. Li, L. A. Nafie, J. Phys. Chem. A **2012**, 116, 7329 – 7336; (b) L. N. Vidal, T. Giovannini, C. Cappelli, J. Phys. Chem. Lett. **2016**, 7, 3585 – 3590; (c) L. A. Nafie, Chem. Phys. **1996**, 205, 309 – 322.

[17] K. D. Chapkin, L. Bursi, G. J. Stec, A. Lauchner, N. J. Hogan, Y. Cui, P. Nordlander, N. J. Halas, Proc. Natl. Acad. Sci. USA **2018**, 115, 9134 – 9139.

[18] C. Zong, M. Xu, L. J. Xu, T. Wei, X. Ma, X. S. Zheng, R. Hu, B. Ren, Chem. Rev. **2018**, 118, 4946 – 4980.

[19] Z. Dezhahang, M. R. Poopari, J. Cheramy, Y. Xu, Inorg. Chem. **2015**, 54, 4539 – 4549.

[20] (a) A. D. Laurent, D. Jacquemin, Int. J. Quantum Chem. **2013**, 113, 2019 – 2039; (b) H. H. Falden, K. R. Falster-Hansen, K. L. Bak, S. Rettrup, S. P. A. Sauer, J. Phys. Chem. A **2009**, 113, 11995 – 12012.

[21] A. S. Perera, J. Thomas, M. R. Poopari, Y. Xu, Front. Chem. **2016**, 4, 9.

[22] (a) Y. Zhang, M. R. Poopari, X. Cai, A. Savin, Z. Dezhahang, J. Cheramy, Y. Xu, J. Nat. Prod. **2016**, 79, 1012 – 1023; (b) E. Debie, L. Jaspers, P. Bultinck, W. Herrebout, B. V. D. Veken, Chem. Phys. Lett. **2008**, 450, 426 – 430.

[23] (a) S. Yamamoto, P. Bouř, J. Comput. Chem. **2013**, 34, 2152-2158; b) V. Novák, M. Dendisová, P. Matějka, P. Bouř, J. Phys. Chem. C **2016**, 120, 18275-18280; c) V. Novák, J. Šebestík, P. Bouř, J. Chem. Theory Comput. **2012**, 8, 1714-1720.

[24] (a) P. Bourˇ, J. Chem. Phys. **2007**, 127, 136101; (b) B. G. Janesko, G. E. Scuseria, J. Chem. Phys. **2006**, 125, 124704.

[25] S. Luber, C. Herrmann, M. Reiher, J. Phys. Chem. B **2008**, 112, 2218 – 2232.

[26] W. Hug, G. Hangartner, J. Raman Spectrosc. **1999**, 30, 841 – 852.

[27] G. Li, J. Kessler, J. Cheramy, T. Wu, M. R. Poopari, P. Bouř, Y. Xu, Angew. Chem. Int. Ed. **2019**, 58, 16495 – 16498.

[28] J. Tomeček, P. Bouř, J. Chem. Theor. Comput. **2020**, 16, 2627-2634.

[29] (a) T. Wu, J. Kapitán, V. Mašek, P. Bouř, Angew. Chem. Int. Ed. **2015**, 54, 14933–14936; (b) J. L. Lunkley, D. Shirotani, K. Yamanari, S. Kaizaki, G. Muller, J. Am. Chem. Soc. **2008**, 130, 13814-13815.

Chapter 4

Can One Measure Resonance Raman Optical Activity?

"This chapter is copied from the following published paper."

G. Li, M. Alshalalfeh, Y. Yang, J. R. Cheeseman, P. Bouř, Y. Xu. "Can One Measure Resonance Raman Optical Activity?" Angew. Chem. Int. Ed. **2021,** 60, 22004-22009.

4.1 Introduction

Raman spectroscopy is a powerful spectroscopic tool for elucidating structural information. The chiral version of Raman spectroscopy, Raman optical activity (ROA), [1] has been utilized substantially to characterize absolute configurations and conformational distribution dynamics of many biomolecules[2] and (in)organic molecules.[3] A known experimental limitation is the weakness of the Raman signal. This is even more severe for ROA intensity of which is typically only 10^{-3} –10^{-4} of that of Raman.[1b] Researchers have been therefore exploring the resonance regime when the excitation laser frequency is in (near) resonance with one or multiple electronic transitions of a chiral molecule to enhance its ROA intensity. Such resonance ROA (RROA) enhancements have been reported for naproxen and its derivatives,[4] transition metal complexes,[5] carotenoid aggregation,[6] and biological systems.[7] Also following the advances of surface enhanced Raman spectroscopy (SERS) development, some exciting works on surface enhanced ROA (SEROA)

have appeared.[8] The combination of these two methods, that is, surface enhanced RROA (SERROA), has also been reported, for example, for myoglobin.[9]

Another significant challenge is how to interpret the observed chiral Raman spectra under resonance conditions. These spectral patterns often do not show any resemblance to the corresponding far-off resonance spectra that can be predicted pretty reliably with DFT calculations.[10] In the case when only a single electronic state (SES) is in resonance with the excitation laser wavelength, the SES theory pioneered by Nafie predicts that the ratio of RROA to resonance Raman (RRaman) in the most common SCP experiment equals to -1/2 times the ratio of electronic circular dichroism (ECD) to absorption.[11] As a result, the mono-signate ROA feature is often regarded as a hallmark of RROA and has been utilized to interpret experimental ROA results in many subsequent publications when (near) resonance is present.[5,7] For example, S. Haraguchi et al.[7] reported an RROA spectrum of a photoreceptor protein in resonance with the laser excitation at 532 nm and showing a mono-sign, opposite to that of the singlet resonant state, as anticipated. Very recently, a monosignate RROA was reported for a chiral naphthalenediimide derivative (abbreviated as BN in Figure 4.1).[12] A perplexing observation was that the experimental RROA sign of BN is the same as the ECD of the corresponding (near) resonance electronic transition, contrary to the SES prediction. To explain this observation, the authors proposed two BN conformers with (near) resonance electronic transitions having opposite ECD signs, and that one conformer dominates the ground and the other the excited state. The SES theory was then invoked to explain the surprising RROA sign-switching based on the conformer in the excited electronic state.

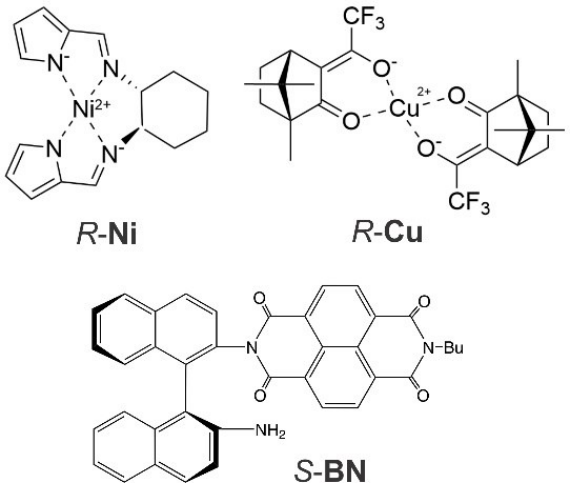

Figure 4.1. The three chiral compounds discussed: (*R, R*)-bis (pyrrol-2-ylmethyleneamine)-cyclohexane nickel^{II} (*R*-**Ni**), *R*-bis-(trifluoroacetyl camphorato) copper^{II} (*R*-**Cu**), and atropisomeric naphthalenediimide derivative, *S*-nBu-NDI–BINAM (*S*-**BN)**, which consists of binaphthalenylamine (BINAM) and naphthalene (NDI).

More recent theoretical developments show that by considering excited state interference and Herzberg–Teller effects, a multi-signate RROA showing intensity enhancement in RROA spectra can be produced.[13] Other approaches to treat RROA, such as using time-dependent (TD) formulation and real time propagation TDDFT, have also been developed.[14] DFT calculations have been compared to the experimental RROA of medium-size organic molecules such as naproxen sodium, quinidine and 2-Br-hexahelicen, as well as some transition metal complexes.[14c, 15]

When a chiral molecule is under (near) resonance in an ROA experiment, several light-matter interaction events can occur at the same time. These include absorption, ECD, and Rayleigh and

Raman scattering as well as their polarized forms. These complications have not been addressed before or have been commonly ignored in the RROA research literature. Herein, we show that a new form of resonance Raman spectroscopy of natural chirality can be carried out using a ROA instrument under (near) resonance condition. This new spectroscopy can be regarded as a combination of ECD and circularly polarized-Raman[1] (CP-Raman). We abbreviate it as eCP-Raman, in a similar fashion that magnetic-chiral dichroism (MChD) can be regarded as a product of ECD and magnetic CD.[16] Using three chiral compounds as examples, we demonstrate that in these cases, natural RROA is completely masked by this effect. The recently developed finite-lifetime approach for resonance (see Computational Details in the appendix) provides good agreement with the experimental observations. Finally, we comment on the possibility of detecting the true RROA experimentally, which we find to be a crucial point in the development of current RROA methodology.

4.2 Experimental Section

Experimental Details

The Raman and ROA spectra were measured on a ChiralRaman-2X^{TM} spectrometer of BioTools. The concentration of the solutes *R*-**Ni** and *R*-**Cu** was 0.037M and 0.09M respectively. The collection time for *R*-**Ni** was 25 hours and for *R*-**Cu** 17 hours. The laser power used was from 30 to 50 mW at excitation wavelength of 532nm for all experiments. The optical cell length is 0.5 cm and the focal point was approximately at the center of the cell.

ECD spectra of *R*-**Ni** (0.003M) and *R*-**Cu** (0.012M) were collected using an Olis DSM 17 CD spectrophotometer and the region presented is from 532 nm to 590 nm in Figure A. The path length used is 0.1 cm. *R*- and *S*-**Cu** and -**Ni** were synthesized and purified following the

procedures described in Refs. [17],[18]

For the *CID* calculations based on Eq. (1), we use L = 0.25 cm in all cases. This is because, the full length of the ROA cell is 0.50 cm and for simplicity, we assume that the laser light is focused at the center of the cell where scattering happens and the absorption path length is taken as half of the cell length.

For the *CID* values of *R*-**Ni** and *R*-**Cu**, we use [**Ni**] = 0.037 M, [**Cu**] = 0.073 M, L= 0.25 cm and the $\Delta\varepsilon$ and $\Delta\varepsilon'$ values are taken from the spectra presented in Figure A, SI. For the final I_R - I_L spectral simulations of *R*-**Ni** and *R*-**Cu** in $CHCl_3$, we use [**Ni**] = 0.037 M, [**Cu**] = 0.073 M, [$CHCl_3$] = 12.48 M, L= 0.15 cm and the above *CID* values.

For the *CID* values of ***S*-BN** in CH_3CN and in $CHCl_3$, we use [**BN**] = 0.003 M, L= 0.25 cm and the $\Delta\varepsilon$ and $\Delta\varepsilon'$ values are taken from Ref. 11. For the final I_R - I_L spectral simulations of *S*-**BN** in CH_3CN and in $CHCl_3$, we have [**BN**] = 0.003 M, [CH_3CN] = 18.90 M, and [$CHCl_3$] = 12.48 M, and L = 0.15 cm.

Computational Details

DFT calculations including geometry optimization, harmonic frequency, Raman, CP-Raman and ROA calculations for *R*-**Ni** and *R*-**Cu** were performed using the Gaussian Development Version (GDV) package.[19] Raman, DOC, and ROA polarizability tensors were calculated at 532 nm using the finite-lifetime (or damped response) approach. The calculated I_R + I_L and I_R - I_L intensities are displayed in units of [m^2 cm/sr] where m is meter and sr is steridian. A value of γ = 880 cm^{-1} was used for the final spectral simulations.

For *R*-**Ni,** the optimized geometry and harmonic frequencies were computed at the B3LYP/aug-cc-pVTZ level of theory.

For *R*-**Cu,** the optimized geometry, harmonic frequencies, Raman and ROA polarizability tensors (532nm) were computed at the uM11Plus/6-311++G(2d,p) level of theory. M11Plus is a range-separated hybrid meta functional which incorporates nonlocal rung-3.5 correlation. This functional predicted Raman which matched the experimental **Cu** Raman well, especially the relative intensity of the two main Raman bands in the 1500-1800 cm^{-1} region. Other functionals predicted a much stronger band around 1700 cm^{-1} than at ~1550 cm^{-1}, in contrast the experiment, as shown in Ref. 5.

For *S*-**BN,** the optimized geometry, harmonic frequencies, Raman and ROA polarizability tensors (532nm) were computed at the CAM-B3LYP/Def2-TZVP level of theory using the Gaussian 16 software package.[20] Solvent effects were modelled by polarizable continuum model (PCM).

4.3 Results and Discussion

Strong induced solvent ROA patterns were observed in recent studies of chirality transfer from a chiral solute under resonance to a series of achiral solvents.[5,21, 22] Several chirality induction mechanisms were proposed, such as solvent-chiral solute interactions, similar to those used to explain induced solvent vibrational circular dichroism features,[23] or an ad hoc "ring of fire" mechanism[21] where chiral Rayleigh scattering appears to contribute significantly. Some noticeable discrepancies between experiment and theory remained between these two proposals. Later on, it was recognized the induced solvent ROA patterns could be satisfactorily interpreted by ECD and polarized Raman scattering.[22]

In light of these findings, we focus on interpretation of experimental I_R - I_L features of three chiral solutes (shown in Figure 4.1) under resonance, which were previously regarded as RROA. These are two transition metal complexes, R-Ni[24] and R-Cu,[5] and one organic molecule, S-BN.[12] These systems show both multi-signate and mono-signate I_R - I_L patterns. Although some interpretations were presented before, based on the SES theory,[5,12] no theoretical simulations of the spectra were reported.

To detect a RROA spectrum, a chiral target needs to be in (near) resonance with the incident laser light, at 532 nm for the current study. One well-known experimental challenge is the interference of the fluorescence with the Raman scattering. In addition, UV/Vis absorption may be too strong, leaving little light for Raman scattering. It is generally assumed that good-quality mirror-image ROA spectra for a pair of chiral solute enantiomers are proof of true RROA. Unfortunately, such an assumption oversimplifies the real situation. We noticed this first in the Ni system, where the metal centers provide extremely large magnetic dipole moments in the d-d electronic transitions. Therefore, the ratio of ECD to UV/Vis absorption is high.[21] Consequently, even though by absorbance at 532 nm only a few percent of the light is lost, a strong ECD causes noticeable imbalance of the right versus left circularly polarized light (RCPL/LCPL). This imbalance in RCPL/LCPL then leads to CP-Raman scattering.[1] as previously reported by Clark et al. in 1974[25]and by others.[26] By recording I_R - I_L using 100% LCPL for the excitation, these authors obtained a multi-signate CP-Raman of several common solvents such as chloroform.[25] The CP-Raman intensity and sign can be predicted using only components of the electric-dipole–electric-dipole polarizability tensor, as in the case of Raman.[1,26]

Nowadays, the majority of ROA measurements utilize the scattered circular polarized (SCP) backscattering setup,[27] where a randomly polarized light shines on a chiral sample and the

I_R - I_L signal is registered. Under resonance, the imbalance in I_R - I_L, produced by ECD of the chiral solute, leads to CP-Raman intensity, which is collected in the same spectrum as natural RROA. In addition, the out-going Raman scattering is again subjected to the ECD process. Therefore, an RROA signal thus measured is generally contaminated by eCP-Raman. In other words, the I_R - I_L signal thus collected contains both RROA and eCP-Raman contributions. For eCP-Raman, Equation (1) was derived:[22]

$$CID = \frac{I_R - I_L}{I_R + I_L} = = \frac{ln10}{4}\, cL\, \Delta\varepsilon \left(\frac{\Delta\varepsilon'}{\Delta\varepsilon} + DOC \right) \qquad (1)$$

Here $\Delta\varepsilon$ and $\Delta\varepsilon'$ are differential absorption indices for the excitation and scattered light, that is at 532 nm ($\Delta\varepsilon$) and at each Raman band ($\Delta\varepsilon'$). c is the concentration of the chiral solute, L is the optical path length, and *DOC* is the degree of circularity[1] of each vibrational transition of either the solute or solvent. I_R and I_L are the intensities of scattered RCPL and LCPL registered at the ROA instrument, respectively. We will use Eq. (1) to evaluate *eCP-Raman* contributions of both achiral solvents and chiral solutes in the three examples considered.

It is important to point out that simulations of I_R - I_L signals of achiral solvents generally do not involve any resonance calculations as they are transparent at 532 nm. Since achiral solvents do not have their own ROA intensity, the solvent I_R – I_L signals contain only *eCP-Raman* contributions and can be evaluated based on Eq. (1). While the solvent *DOC* curves can be obtained by ratioing the solvent CP-Raman and Raman spectra calculated using the usual far-off resonance calculations, the chiral solute contributions, i.e., $\Delta\varepsilon$ value at 532 nm and $\Delta\varepsilon'$ curve can be taken directly from the experimental measurements. Such evaluations were demonstrated in Ref.[22].

Simulating the I_R - I_L signal of a chiral solute under resonance, on the other hand, is more complicated, as it may contain variable contributions from both RROA and *eCP-Raman*.

Furthermore, (near) resonance effects may be significant and need to be properly accounted for in the calculations of Raman, CP-Raman, and RROA. We applied the finite-lifetime (or damped response) approach, similar to that described previously[28] to treat the resonance effect in its Raman, CP-Raman and ROA spectra, using the Gaussian Development Version (GDV) package.[19] The simulation of CP-Raman requires only the same polarizability tensors (α) as for Raman and not the additional electric dipole – magnetic dipole and electric dipole – electric quadrupole polarizabilites (G' and A, respectively) as needed for ROA. In this approach, an imaginary phenomenological damping parameter, γ, is added to the incident frequency ω, where γ is related to the lifetime of the excited states and to the widths of the absorption (or dispersion) peaks. While previous implementations were numerical (i.e. numerically differentiating the polarizabilities, G' and A tensors with respect to nuclear coordinates, generally requiring substaintial computational time), the current fully analytic derivative implementation in GDV additionally includes magnetic field dependent basis functions (GIAOs) which ensure gauge origin-independent results and typically takes about 1.5 to 2 times longer than a normal Raman and ROA calculation with G16.[20]

Geometry optimizations, harmonic frequency, Raman, CP-Raman and ROA calculations at 532 nm for *R*-**Ni** and *R*-**Cu** were performed using the GDV package.[19] *eCP-Raman* spectrum of *R*-**Ni** (or *R*-**Cu**) under (near) resonance was simulated by multiplying its simulated RRaman spectrum with *CID* from Eq. (1). *Experimental* $\Delta\varepsilon$ at 532 nm and $\Delta\varepsilon'$ curve in the range from 532 nm to 590 nm (corresponding to 0 ~ 1850 cm^{-1} on the Raman scale) were used, while *DOC* was obtained from DFT. While it is possible to evaluate $\Delta\varepsilon$ and $\Delta\varepsilon'$ based on ab initio calculations as well, the accuracy of the current ECD calculations is not yet sufficient to yield reliable *eCP-Raman* predictions.

For the damping parameter, γ = 880 cm^{-1}, as suggested by others[28], was used. We also tested the sensitivity of simulated Raman, CP-Raman and RROA spectra of *R*-**Ni** to this damping parameter, by using γ = 988 cm^{-1}, 880 cm^{-1} and 550 cm^{-1}. The comparisons are summarized in the Appendix. (Figure B1) As one can see, the three values give more or less the same results for Raman and CP-Raman, which are directly relevant to the current *eCP-Raman* simulations, while some small differences appear for RROA in the lower cm^{-1} region.

For *R*-**Ni,** the optimized geometry and harmonic frequencies were computed at the B3LYP/aug-cc-pVTZ level of theory. We also tested the sensitivity of the simulated Raman, CP-Raman and RROA spectrum of *R*-**Ni** to different basis sets such as aug(sp)-cc-pVDZ and aug-cc-pVDZ. The results with the additional basis sets are provided in Figure B2 in the Appendix. As can be seen in Figure B2, essentially identical spectra were predicted with all basis sets tried.

Other parameters used to simulate the *eCP-Raman* and RROA spectra are provided in "Experimental Section" . For example, the concentration of *R*-**Ni** was 0.037 M and the path length 0.25 cm for the evaluation of *CID*. Note that this concentration would be too low for a non-resonant ROA experiment. The path length corresponds to half of the cell length since the laser focal point was approximately at the center of the cell. The *DOC* curve was simulated by taking the ratio of the associated CP-Raman versus Raman spectra of *R*-**Ni** extracted from the DFT calculations with the finite-lifetime approach. Finally, the *eCP-Raman* spectrum of *R*-**Ni** was calculated as Raman × *CID* from Eq. (1). An analogous procedure was used for *eCP-Raman* of *R*-**Cu**.

In Figure 4.2, simulated $I_R + I_L$ (Raman) and $I_R - I_L$ (*eCP-Raman*) spectra of *R*-**Ni** and *R*-**Cu** based on Eq. (1) are compared with experimental spectra of *R*-**Ni** in CH_2Cl_2 (DCM) and $CHCl_3$ and of *R*-**Cu** in DCM and $CHCl_3$, respectively. Calculated natural RROA spectra of both

chiral solutes at 532 nm are also provided. Several important observations can be made about Figure 4.2. First, the I_R+I_L (Raman) experimental spectral patterns of both **Ni** and **Cu** are well reproduced by the simulations. Second, the $I_R - I_L$ experimental spectral patterns of *R*-**Ni** are essentially the same in both solvents, and the same can be said for *R*-**Cu**. In other words, there are no explicit solute-solvent interactions or formations of specific solute-solvent complexes to be concerned about. Third, somewhat surprisingly, the simulated $I_R - I_L$ spectra based on Eq. (1) are in very good agreement with the experimental $I_R - I_L$ spectra for both **Ni** and **Cu**. The positive experimental $I_R - I_L$ **Ni** feature near 1570 cm^{-1} looks less prominent than that in the simulated bi-signate features. This can be attributed to slightly broader experimental bands where the symmetric and asymmetric C=N stretching modes overlap. Fourth, the simulated *CID* magnitude is in the order of 10^{-3} for **Ni** and 10^{-4} for **Cu**, in good agreement with the related experimental magnitudes, capturing the difference between **Ni** and **Cu**. Indeed, the experimental I_R - I_L signal of **Ni** emerged in a few minutes rather than 2-3 hours in the case of **Cu**. Fifth, the simulated natural RROA is drastically different from the experimental $I_R - I_L$ spectral patterns for both **Ni** and **Cu**.

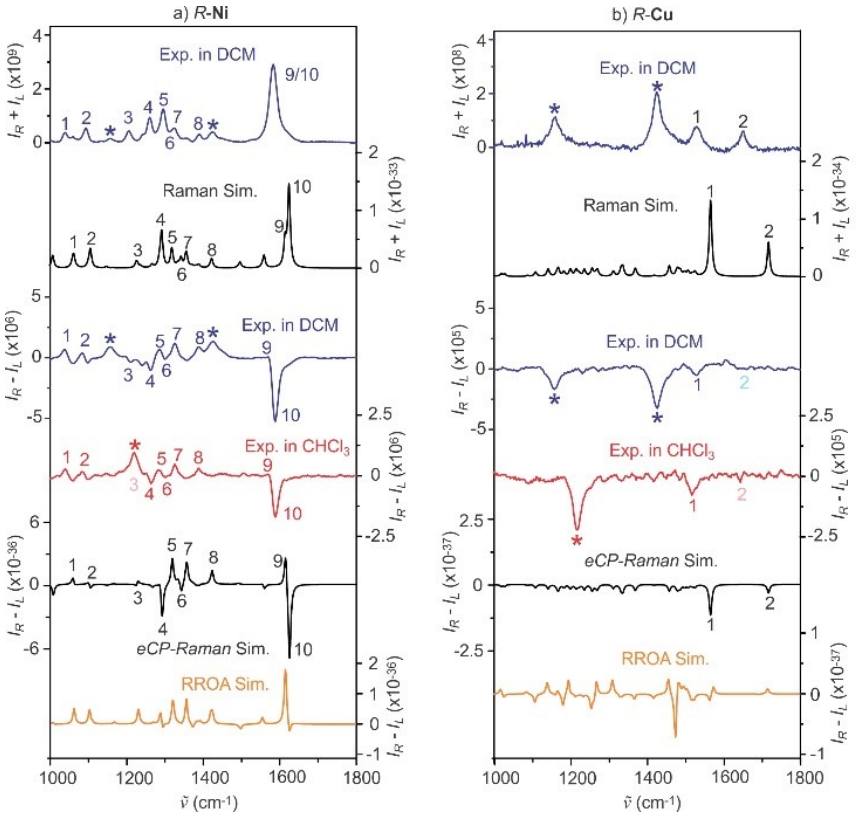

Figure 4.2. (a) Top: experimental Raman ($I_R + I_L$) spectrum of *R*-**Ni** in CH_2Cl_2 (blue) is compared with the simulated one (black); Bottom: experimental ROA ($I_R - I_L$) spectra of *R*-**Ni** in CH_2Cl_2 (blue) and in $CHCl_3$ (red) are compared with simulated *eCP-Raman* contribution (black) and with simulated natural RROA spectrum (yellow). (b) Analogous results for *R*-**Cu**. Corresponding experimental and theoretical *solute* bands are numbered and asterisk (*) indicates the *solvent* bands. The calculated spectral intensities are displayed in units of [m^2 cm/sr] where m is meter and sr is steradian.

The simulated $I_R + I_L$ (Raman) and $I_R - I_L$ (*eCP-Raman*) spectra of both solvent and solute in the 250-2250 cm^{-1} region are depicted in Figure B3, in the appendix for *R*-**Ni** and *R*-**Cu**, showing good agreement with the experimental data. Furthermore, the relative intensity of solvent to solute appears to be well reproduced for both $I_R + I_L$ and $I_R - I_L$ for *R*-**Cu**. For both $I_R + I_L$ (Raman) and $I_R - I_L$ (*eCP-Raman*) of *R*-**Ni**, the experimental *R*-**Ni** intensity relative to the

respective solvent is ~4 times of the simulated ones, suggesting that the (near) resonance enhancement of Raman intensity of *R*-**Ni** is a bit overestimated theoretically.

Overall, the good agreement between simulated and experimental $I_R + I_L$ (Raman) and $I_R - I_L$ (*eCP-Raman*) spectra in Figure 4.2 and Figure B3 strongly supports the conclusion that the *eCP-Raman* mechanism proposed for Eq. (1) is the dominant contributor in these systems. The simulated natural RROA spectral patterns of the solutes, on the other hand, look different from the experimental ones. This, together with the strong solvent I_R - I_L bands facilitated only by *eCP-Raman*, indicates that the natural RROA mechanism plays a negligible role in the experimental I_R - I_L spectra observed in both **Ni** and **Cu** cases.

The third example, *S*-**BN**, is an organic molecule with axial chirality. Using experimental ECD profiles in two different solvents, $CHCl_3$ and CH_3CN, and the experimental concentration information reported in Ref. [12], we performed similar calculations as for **Ni** and **Cu**. The final I_R - I_L simulations of *S*-**BN** in $CHCl_3$ and CH_3CN are summarized in Figure 4.3, for comparison to the experimental data. In Figure 4.3, we see a similar situation for **Ni** and **Cu**. First, the negative I_R - I_L feature of the main *S*-**BN** band observed experimentally is correctly predicted by *eCP-Raman*. Second, the experimental I_R - I_L spectral features of $CHCl_3$ and CH_3CN are also captured by the simulations, including the positive I_R - I_L band of CH_3CN at 2256 cm^{-1}. Third, the strong experimental I_R - I_L bands of $CHCl_3$ and CH_3CN are about ten times stronger than the main band of *S*-**BN**. This ratio is captured by the simulations. The comparisons shown in Figure 4.3 clearly demonstrate that one can explain the experimental observation reported in Ref. [12] satisfactorily with the *eCP-Raman* mechanism, and not by natural RROA.

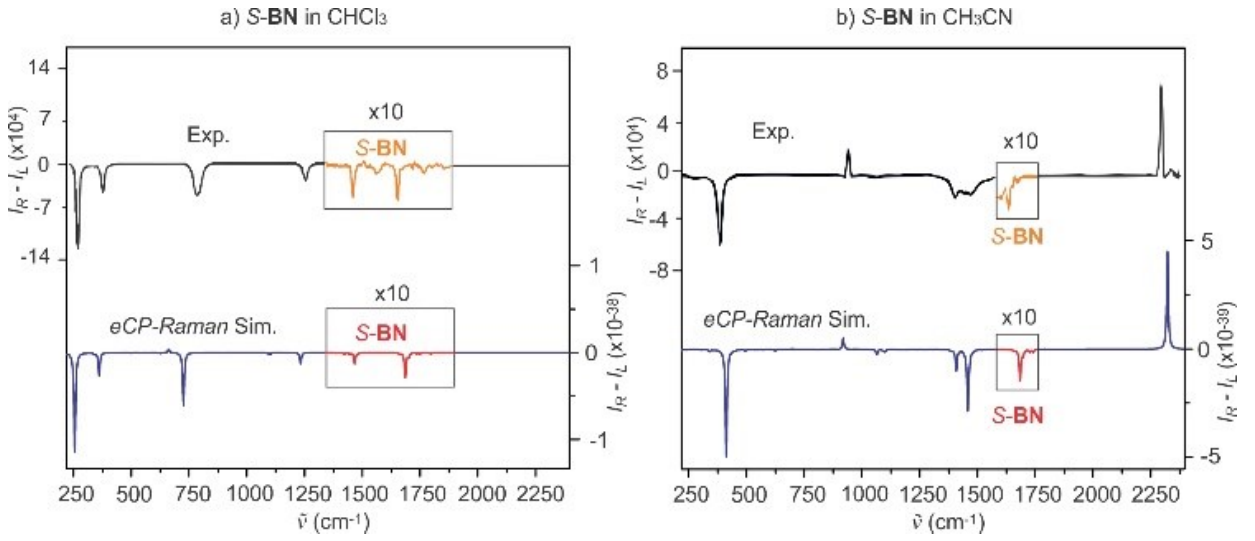

Figure 4.3. a) Comparison of the experimental[12] (top) and simulated (bottom) I_R - I_L (*eCP-Raman*) spectra of the chiral solute *S*-**BN** whose bands are shown in the rectangle box and their intensities amplified by a factor of ten, and of achiral solvent $CHCl_3$ whose bands are outside the box. b) Parallel plots as in a) but with *S*-**BN** in CH_3CN solution

From Eq. (1), one can see that sign of *CID* depends on the sign of $\Delta\varepsilon$, i.e., ECD sign at 532 nm, and that of the term ($\Delta\varepsilon'/\Delta\varepsilon$ +*DOC*). Since -1 ≤ *DOC* ≤ 5/7,[1b] if the $\Delta\varepsilon'/\Delta\varepsilon$ ratio is larger than or near 1, it controls the sign of the ($\Delta\varepsilon'/\Delta\varepsilon$ +*DOC*) term. This leads to a mono-signate $I_R - I_L$ spectrum, the same sign as that of $\Delta\varepsilon$ at 532 nm, such as in the case of *R*-**Cu**. Appearance of mono-signate $I_R - I_L$ can also result from a more delicate interplay between $\Delta\varepsilon'/\Delta\varepsilon$ versus *DOC* as in the case of *S*-**BN**. Therefore, for *eCP-Raman*, single sign $I_R - I_L$ can be observed, as in the case of SES with true molecular RROA.[1,11,28 b] However, the mechanisms are different. A mono signate $I_R - I_L$ spectrum does not imply that a SES is in resonance or that the $I_R - I_L$ sign should be opposite to that of ECD.

As shown in Table B1, the *CID* values of the chiral solutes and of the solvents based on Eq. (1) generally agree with the experimental *CID*s in the three cases discussed. For example, the experimental *CID* values are -2.6×10^{-3} for the *R*-**Ni** band at ~1588 cm^{-1} and -5.7×10^{-4} for the *R*-**Cu** band at 1520 cm^{-1}, in agreement with the simulated *CID* values of -4.8×10^{-3} and -8.9×10^{-4}, respectively.

In Figure B4, we compare Raman, CP-Raman and RROA of *R*-**Ni** and *R*-**Cu** calculated at 532 nm with and without the finite-lifetime approach. Clearly, the finite-lifetime approach is crucial for reproducing the experimental $I_R - I_L$ spectrum of *R*-**Ni**. For *R*-**Cu**, on the other hand, the differences are minor. This is consistent with the experimental observation that *R*-**Ni** is the nearest resonance case, then *R*-**Cu**, and finally *S*-**BN**. Not surprisingly, the simulations of *S*-**BN** without the finite-lifetime in Figure 4.3 already agrees well with the experiment.

In all three examples discussed, the *eCP-Raman* contribution appears to dominate the experimental $I_R - I_L$ observation. Can one detect *true* RROA of a chiral solute? This may be possible if the *CID* of true RROA is significantly larger than of *eCP-Raman* given by Eq. (1). Such a condition may be achieved by changing the concentration of the chiral solute. Among the three examples, *R*-**Ni** is the most promising one since it is closest to resonance. Nevertheless, several attempts were made to lower *R*-**Ni** concentration to seek RROA without success. In Figure 4.2, the theoretical RROA intensities predicted at 532 nm are ~3 times smaller than the simulated $I_R - I_L$ (*eCP-Raman*) intensities for **Ni**.

On the other hand, RROA intensity depends drastically on the excitation and transition energies, the latter of which are difficult to accurately predict theoretically. Indeed, different levels of theory can give very different RROA. Improvements in instrumentation can be helpful. If one is able to tune the excitation laser wavelength (technically not yet realized at the present

time), one may set it to a zero ECD crossing point to mostly avoid ECD interference at the excitation wavelength. However, outgoing Raman scattered light is expected to be still affected by ECD. If a system is very near resonance, the chance to detect true RROA is higher in principle, but this can cause other experimental complications such as stronger absorption and fluorescence.

The current study shows that if there is measurable ECD of a chiral solute at 532 nm at the concentration used for the RROA measurement, the contribution from *eCP-Raman* cannot be ignored. Strong I_R - I_L achiral solvent bands can be regarded as a hallmark of *eCP-Raman*, although they may not be visible for weak scatters such as water. It is likely that *eCP-Raman* contributed in many of the previously reported RROA or even SERROA experimental studies, and their conclusions may need to be re-examined.

4.4 Conclusion

In summary, we have analyzed I_R - I_L spectra of three typical chiral molecules under (near) resonance in Raman scattering experiments. These resonant I_R - I_L features could be satisfactorily explained by a new form of chiral Raman spectroscopy, *eCP-Raman,* without detectable contribution from the *true*, *natural* RROA. We think that it is of crucial importance to recognize this mechanism when interpreting RROA data, otherwise misleading conclusions about molecular behavior may be drawn. The current study opens the way for a new form of chiral Raman spectroscopy under resonance which is sensitive to natural chirality and structures of chiral molecules. The results also underline the significance of further theoretical development of RROA as a complex and largely unexplored phenomenon.

References

[1] (a) L. D. Barron, Molecular Light Scattering and Optical Activity, Cambridge University Press, Cambridge, UK, **2004**; (b) L. A. Nafie, Vibrational optical activity: Principles and applications, Wiley, Chichester, **2011**.

[2] L. D. Barron, Biomed. Spectrosc. Imaging **2015**, 4, 223 – 253.

[3] M. Krupová, J. Kessler, P. Bourˇ, ChemPlusChem **2020**, 85, 561 – 575.

[4] M. Vargek, T. B. Freedman, E. Lee, L. A. Nafie, Chem. Phys. Lett. **1998**, 287, 359 – 364.

[5] C. Merten, H. Li, L. A. Nafie, J. Phys. Chem. A **2012**, 116, 7329 – 7336.

[6] M. Dudek, E. Machalska, T. Oleszkiewicz, E. Grzebelus, R. Baranski, P. Szczesniak, J. Mlynarski, G. Zajac, A. Kaczor, M. Baranska, Angew. Chem. Int. Ed. **2019**, 58, 8383 – 8388.

[7] (a) S. Haraguchi, M. Hara, T. Shingae, M. Kumauchi, W. D. Hoff, M. Unno, Angew. Chem. Int. Ed. **2015**, 54, 11555 – 11558. (b) R. Sgammato, W. Herrebout, C. Johannessen, J. Raman Spectrosc. **2019**, 50, 1905 – 1913; (c) J. Bogaerts, C. Johannessen, J. Raman Spectrosc. **2019**, 50, 641 – 646.

[8] (a) S. Abdali, E. W. Blanch, Chem. Soc. Rev. **2008**, 37, 980 – 992; (b) S. O. Pouř, S. E. J. Bell, E. W. Blanch, Chem. Commun. **2011**, 47, 4754 – 4756; (c) S. O. Pouř, L. Rocks, K. Faulds, D. Graham, V. Parchaňský, P. Bouř, E. W. Blanch, Nat. Chem. **2015**, 7, 591 – 596.

[9] S. Abdali, C. Johannessen, J. Nygaard, T. Nørbygaard, J. Phys. Condens. Matter **2007**, 19, 285205.

[10] J. R. Cheeseman, M. J. Frisch, J. Chem. Theory Comput. **2011**, 7, 3323 – 3334.

[11] L. Nafie, Chem. Phys. **1996**, 205, 309 – 322.

[12] E. Machalska, G. Zajac, M. Baranska, D. Kaczorek, R. Kawęcki, P. F. J. Lipiński, J. E. Rode, J. Dobrowolski, Chem. Sci. **2021**, 12, 911 – 916.

[13] L. N. Vidal, T. Giovannini, C. Cappelli, J. Phys. Chem. Lett. **2016**, 7, 3585 – 3590.

[14] (a) S. Luber, J. Neugebauer, M. Reiher, J. Chem. Phys. **2010**, 132, 044113; (b) A. Baiardi, J. Bloino, V. Barone, J. Chem. Theory Comput. **2018**, 14, 6370 – 6390; (c) J. Mattiat, S. Luber, J. Chem. Phys. **2019**, 151, 234110/1 – 16.

[15] (a) S. Luber, M. Reiher, ChemPhysChem **2010**, 11, 1876 – 1887; (b) F. Krausbeck, J. Autschbach, M. Reiher, J. Phys. Chem. A **2016**, 120, 9740 – 9748; (c) L. Abella, H. D. Ludowieg, J. Autschbach, Chirality **2020**, 32, 741 – 752.

[16] G. L. J. A. Rikken, E. Raupach, Nature **1997**, 390, 493 – 494.

[17] K. M. Nicholas, Inorg. Chim. Acta **1976**, 20, L42.

[18] X. F. Shan, D. H. Wang, C. H. Tung, L. Z. Wu, Tetrahedron **2008**, 64, 5577-5582.

[19] M. J. Frisch, et al., Gaussian development version, Gaussian, Inc., Wallingford, CT, **2020**. See Appendix for the full reference.

[20] M. J. Frisch, et al., Gaussian 16, Revision C.01, Gaussian, Inc., Wallingford, CT, **2016**. See Appendix for the full reference.

[21] G. Li, J. Kessler, J. Cheramy, T. Wu, M. R. Poopari, P. Bouř, Y. Xu, Angew. Chem. Int. Ed. **2019**, 58, 16495 – 16498.

[22] T. Wu, G. Li, J. Kapitán, J. Kessler, Y. Xu, P. Bouř, Angew. Chem. Int. Ed. **2020**, 59, 21895 – 21898. Note a factor of ln10 was missing in the original derivation.

[23] (a) J. Sadlej, J. C. Dobrowolski, J. E. Rode, Chem. Soc. Rev. **2010**, 39, 1478 – 1488; (b) M. Losada, Y. Xu, Phys. Chem. Chem. Phys. **2007**, 9, 3127 – 3135; (c) A. S. Perera, J. Thomas, M. R. Poopari, Y. Xu, Front. Chem. **2016**, 4, 9; d) T. Wu, J. Kessler, P. Bouř, Phys. Chem. Chem. Phys. **2016**, 18, 23803 – 23811.

[24] Z. Dezhahang, M. Poopari, J. Cheramy, Y. Xu, Inorg. Chem. **2015**, 54, 4539-4549.

[25] R. Clark, S.R. Jeyes, A. J. McCaffery, R. A. Shatwell, J. Am. Chem. Soc. **1974**, 96, 5586-5588.

[26] W. Hug, G. Zuber, A. de Meijere, A. F. Khlebnikov, H.-J. Hansen, *Helv. Chim. Acta* **2001**, 84, 1-21.

[27] W. Hug, G. Hangartner, J. Raman Spectrosc. **1999**, 30, 841-852.

[28] (a) L. Jensen, J. Autschbach, M. Krykunovc, G. C. Schatz, J. Chem. Phys. **2007**, 127, 134101; (b) L. A. Nafie, *Theor.* Chem. Account, **2008**, *119*, 39-55; (c) T. Helgaker, S. Coriani, P. Jørgensen, K. Kristensen, J. Olsen, K. Ruud, Chem. Rev. **2012**, 112, 543-631.

Chapter 5

Stereochemical Properties of Two Schiff-Base Transition Metal Complexes and Their Ligand by Using Multiple Chiroptical Spectroscopic Tools and DFT Calculations

"This chapter is copied from the following published paper."

G. Li, D. Li, M. Alshalalfeh, J. Cheramy, H. Zhang, Y. Xu, Stereochemical Properties of Two Schiff-Base Transition Metal Complexes and Their Ligand by Using Multiple Chiroptical Spectroscopic Tools and DFT Calculations Molecules **2023,** 28, 2571.

5.1 Introduction

Schiff base ligands have attracted much attention in fields ranging from coordination chemistry to organic synthesis to pharmaceutical.[1,2] These ligands are imines with a general formula of R-CH=N- R′ where R and R′ are linear/cyclic alkyl or aryl groups.[3] Thanks to their selectivity and stability, Schiff bases and their transition metal complexes have been increasingly utilized as enantioselective catalysts,[4] chiral fluorescent sensors[5] and liquid crystal display devices.[6] A well-designed Schiff base has been considered "a privileged ligand" since it can be easily prepared and used to coordinate with a wide range of different metal centers of various oxidation states.[3]

Not only can stereogenic centers or other chirality elements (axes or planes) be introduced into a metal salen complex, the ligands' backbone and the metal centers can be easily varied and finely tuned in designing a synthesis, including catalytic routes.[7] Moreover, the salen metal complexes themselves can also serve as ligands to further coordinate to a second metal or self-assemble into an oligomer through coordination chromophore and metal substrate.[8,9]

Detailed stereochemical properties, such as conformational distribution, ligand chirality and absolute configuration of the metal centers, are of significant importance for further exploration of this fascinating class of chiral molecular systems. Historically, such chirality related information has been typically obtained using X-ray crystallography, where a high-quality single crystal is needed.[10,11] However, to extract the stereochemical properties of these systems directly in solution, chiral spectroscopic methods, such as electronic circular dichroism (ECD),[12] vibrational circular dichroism (VCD),[13, 14, 15, 16] and vibrational Raman optical activity (ROA)[17] have been utilized. In particular, VCD and ROA, which both exhibit many well-resolved vibrational bands, can provide detailed information not only about the absolute configuration of the system but also about the conformational distributions and intermolecular interactions with solvents[18, 19, 20] and with the solute itself,[21] with the aid of DFT calculations.[22]

In this paper, we focus on a chiral tetradentate Schiff-base ligand, (R, R) and (S, S)-N, N′-Bis(3,5-di-tert-butylsalicylidene)-1,2-cyclohexanediamine (salen-chxn) and its complexes with Ni(II) and Cu(II). First, a series of chiroptical spectroscopic measurements were carried out, which include IR, VCD, UV-Vis, ECD, Raman and the newly discovered ECD-circularly polarized Raman, i.e., eCP-Raman.[23, 24, 25, 26] Very recently, eCP-Raman spectroscopy was used to probe chirality recognition by a stereodynamic vanadium probe[27] and to study a series of atropisomeric naphthalenediimides.[28] Therefore, it is of great interest to further explore

applications of eCP- Raman spectroscopy with the current systems. Second, applying the recently developed fast conformer-rotamer ensemble sampling tool, CREST,[29] systematic conformational searches were performed for both the ligand and the metal complexes. Third, we conducted extensive simulations of the related IR, VCD, UV-Vis, ECD, Raman and eCP-Raman spectra of the ligand and the complexes using the DFT and time-dependent DFT (TDDFT) calculations. As a result, excellent agreements between the experimental and theoretical VCD features were achieved, allowing one to confidently extract stereochemical information about the systems, including ligand conformations and absolute configurations of the center metal and ligands. We also paid attention to the more subtle effects, such as the conformational preference of the tertbutyl (tBu) groups and how they influence the VCD and ECD features. The exciton chirality method, or the coupled oscillator model,[30] has been extensively used by chemists to assign absolute configurations based on ECD without any calculations. Its application criteria were very recently reviewed.[31] The coupled oscillator approach has recently been extended to VCD analyses of carbohydrates[32] and peptides.[33] In the current study, the exciton chirality method was applied to both VCD and ECD spectra. We provided some comments about its performance based on the comparison with the associated DFT and TDDFT simulations.

5.2 Results and Discussions

The structural formulas of the Schiff base ligand and its two transition metal complexes are shown in Scheme 5.1. In the following, we describe the systematic conformational searches of the ligand and the metal complexes and the DFT geometry optimizations done for each compound in Section 5.2.1. Subsequently, we simulated the IR, VCD, UV-Vis and ECD spectra of the low-energy conformers of salen-chxn. Next, we experimentally compared the final

averaged and experimental spectra to extract the preferred conformations in Section 5.2.2. Then, in Section 5.2.3, we examined the experimental IR, VCD, UV-Vis and ECD spectra of the salen-chxn-Ni(II) and –Cu(II) complexes and compared them with the simulated ones to extract the helicity of the respective metal complexes. The more subtle effects of the conformations of the tBu groups are also discussed. Overall, the excellent agreements between experiment and theory allow one to conclusively identify the main conformers in the solution. Next, the applications of the exciton chirality model to the VCD and ECD spectra of the ligand and the metal complexes are discussed, and some comments are provided on the applicability of the model in each case in Section 5.2.4. Finally, in Section 5.2.5, we describe the eCP-Raman experiments of the two metal complexes under (near) resonance, the analyses of the observed solvent chiral Raman spectra, and the potential applications of eCP-Raman.

While the (R, R) and (S, S) enantiomers of the ligand were purchased directly from Sigma-Aldrich, the Ni(II) and Cu(II) complexes were synthesized according to the procedure described in Section 5.3.1. Therefore, for simplicity, unless otherwise specified, we use the (R, R)-enantiomer of the ligand and the complexes for all the geometry presentations and spectral simulations in this paper.

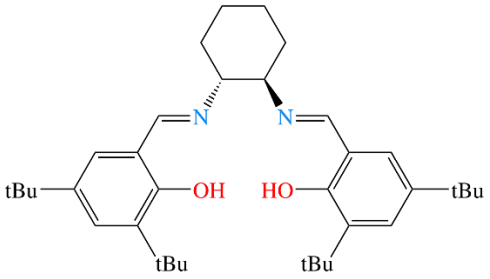

salen-chxn

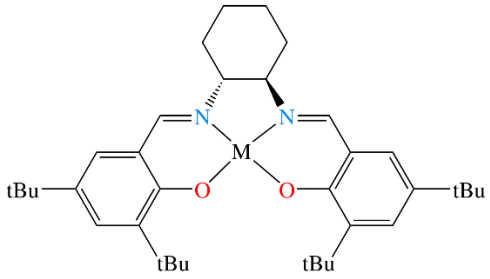

salen-chxn-M
M = Ni(II), Cu(II)

Scheme 5.1. The molecular formula of the (R, R)-N, N′-Bis(3,5-di-tert-butylsalicylidene)-1,2-cyclohexanediamine (salen-chxn) ligand and its Ni(II) and Cu(II) complexes, denoted as salen-chxn-Ni(II) and salen-chxn-Cu(II), respectively. tBu indicates the tertbutyl group.

5.2.1 Systematic Conformational Searches and Low-Energy Conformers of the Ligand and the Metal Complexes

Based on its chemical formula, the salen-chxn ligand may exhibit a range of conformational flexibilities, as shown in Figure 5.1. These are associated with the cyclohexane ring conformations, the axial and equatorial positions of the two large substituents, the rotatable motions about the N-C_{hexane} bonds, the OH pointing direction, and finally, the staggered and eclipsed conformations of the two tBu groups in each substituent. Based on the previous VCD studies[14, 34] of several related salen ligands with the 1,2-cyclohexanediamine subunit, one would expect the chair conformation of the cyclohexane ring to be significantly more stable than the boat one, while both the axial and equatorial positions support stable conformers. Rather than manually going through these potential ligand conformations, we used the Conformer–Rotamer Ensemble Sampling Tool, i.e., CREST, by Grimme and co-workers[29] for systematic conformational searches. The capability of CREST to generate a nearly complete set of relevant conformations has been extensively benchmarked by gas phase spectroscopic investigations, such as rotational spectroscopic studies of a wide range of molecules and non-covalently bonded clusters[35,36,37] and IR chirality recognition studies of protonated amino acid binary aggregates.[38] For example, CREST was used to identify drastically different binary aggregates of tetrahydro-2-furoic acid observed in a jet-cooled rotational spectroscopic[39] and in a matrix-isolation VCD[40] where very different binary conformers were identified from those in solution.[41] One exception

reported recently is the weakly bound heterochiral trimer of propylene oxide,[42] where the most stable geometry established experimentally is not a minimum in CREST. Another advantage of CREST is the readily available implicit solvation models for many solvents, which can be used during a conformational search. This capability was utilized in a very recent VCD study of steroids.[43]

The details of the CREST program and the multitiered approach developed before[38] are described in Section 5.3, Materials and Methods. In total, 91 ligand geometries were generated after the initial CREST search. The low-level geometry optimization and the subsequent single point energy calculation (see Section 5.3.2 for details) reduced the number to 48 geometries within an energy window of 20 kJ mol−1. Further geometry optimizations were carried out at several different levels of theory, including B3LYP[44,45]/6-31G(d)[46], B3LYP-D3BJ/6-311++G(d,p), and B3LYP-D3BJ/def2-TZVP[47] with the polarizable continuum model (PCM)[48] of CDCl3. In addition, the D3 dispersion correction[49.50] with the Becke–Johnson (BJ) damping function[51] was used. The DFT optimization generated four ligand conformers within an energy window of ~15 kJ mol−1. The corresponding optimized geometries are depicted in Figure 5.2, with their relative free energies and their Boltzmann percentage abundances at 298 K.

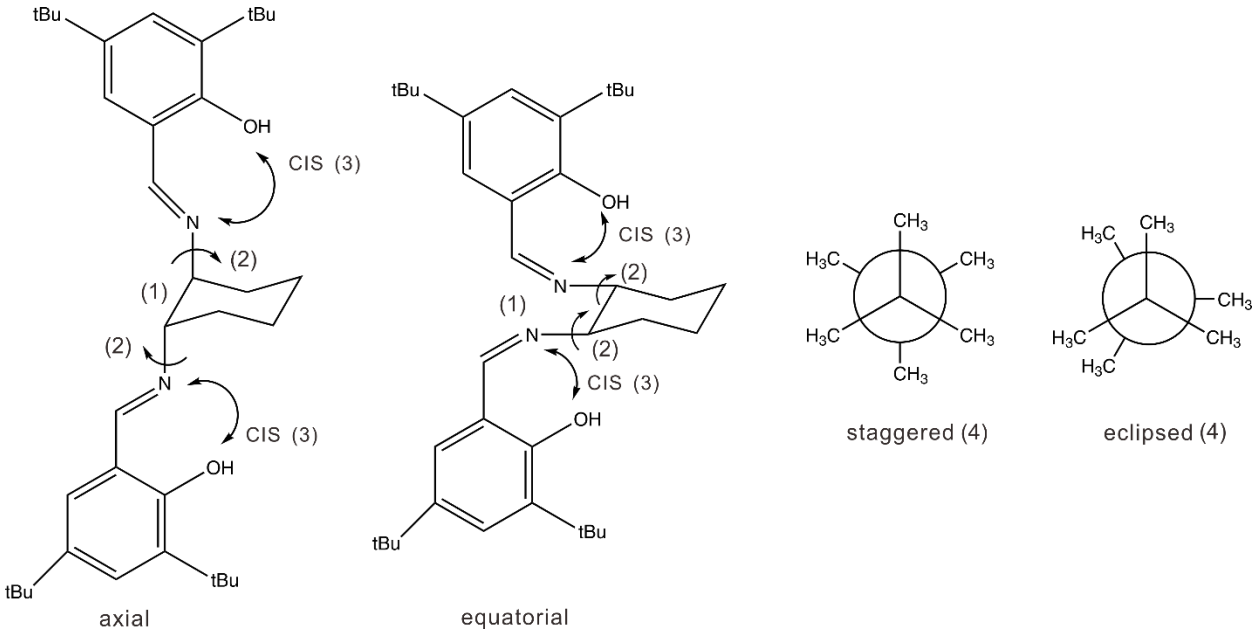

Figure 5.1. Possible conformations of salen-chxn: (1) the axial and equatorial conformations at cyclohexane; (2) the rotatable N-Chexane bonds are indicated by small arrows; (3) the OH orientation direction pointing to N=C (shown) or away (not shown); (4) the subtle staggered and eclipsed conformations of the tBu groups are also shown on the right side. The eclipsed CH3 groups are offset slightly for easy viewing. The tBu groups of the two aromatic branches can take on the staggered–staggered, staggered–eclipsed, and eclipsed–eclipsed conformations.

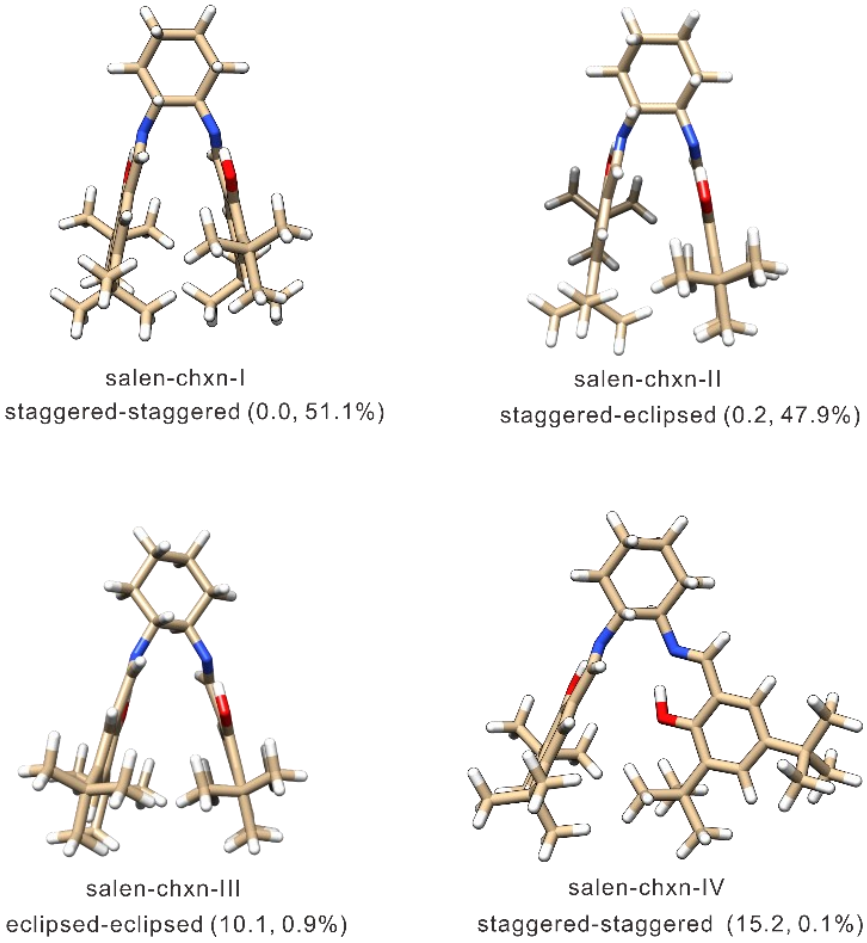

Figure 5.2. Optimized geometries of the four low energy salen-chxn ligand conformers identified by the CREST search and optimized at the B3LYP-D3BJ/def2-TZVP level of theory with the PCM of CDCl3. The relative free energies in kJ mol^{-1} and the Boltzmann percentage abundances at 298 K are provided in the brackets. The blue and red colors represent the nitrogen and oxygen atoms, respectively, whereas the white color is for the hydrogen atoms, and the carbon frame is in the ginger color.

It is interesting to note that no conformers with the substituents in the axial position were

identified by CREST. Even if one constructed an axial conformer as an initial input geometry, the DFT geometry optimization also turned it into an equatorial conformer. Clearly, the axial position does not support a stable conformer. This is different from other related ligands studied before [14], possibly because the substituents in salen-chxn are considerably bulkier. Additionally, only conformers with the OH groups pointing to N=C to form intramolecular H-bonds were identified by CREST within an energy window of 20 kJ mol^{-1}. The six-membered H-bonded and benzene rings form a planar structure, bestowing structural rigidity to the main frame of the salen-chxn ligand. As seen in Figure 5.2, the relative orientation of these two planar substituent structures leads to different types of conformers. The most stable type (Type I) has these two planar substituents stretching out with the OH group up in one substituent and down in the other. In contrast, other relative orientations, for example, with the two planes roughly perpendicular to each other (Type II), are more than 15 kJ mol^{-1} less stable. Overall, the three most stable Type I conformers take on the staggered–staggered (global minimum), staggered–eclipsed, and eclipsed–eclipsed tBu arrangements, while the next less stable conformer is Type II with the staggered–staggered tBu arrangement (see Figure 5.2)

For the salen-chxn-Ni(II) and salen-chxn-Cu(II) complexes, the same conformational searches as described above were conducted. However, the coordination with the metal centers makes these systems more rigid than the salen-chxn ligand, and only nine candidates were identified. The geometry optimizations were performed at the B3LYP-D3BJ/6- 311++G(d,p) level and the combined B3LYP-D3BJ/def2-TZVP (for all atoms except the metal atom) + LANL2DZ (Los Alamos National Laboratory 2 double-ζ,[52] for Ni and Cu) level. The DFT calculations led to three conformers associated with the different tBu arrangements. Consistent results were obtained at both levels of theory. The optimized geometries of the three conformers

for Ni and three for Cu obtained are summarized in Figure 5.3, with their free energies and Boltzmann factors at 298 K.

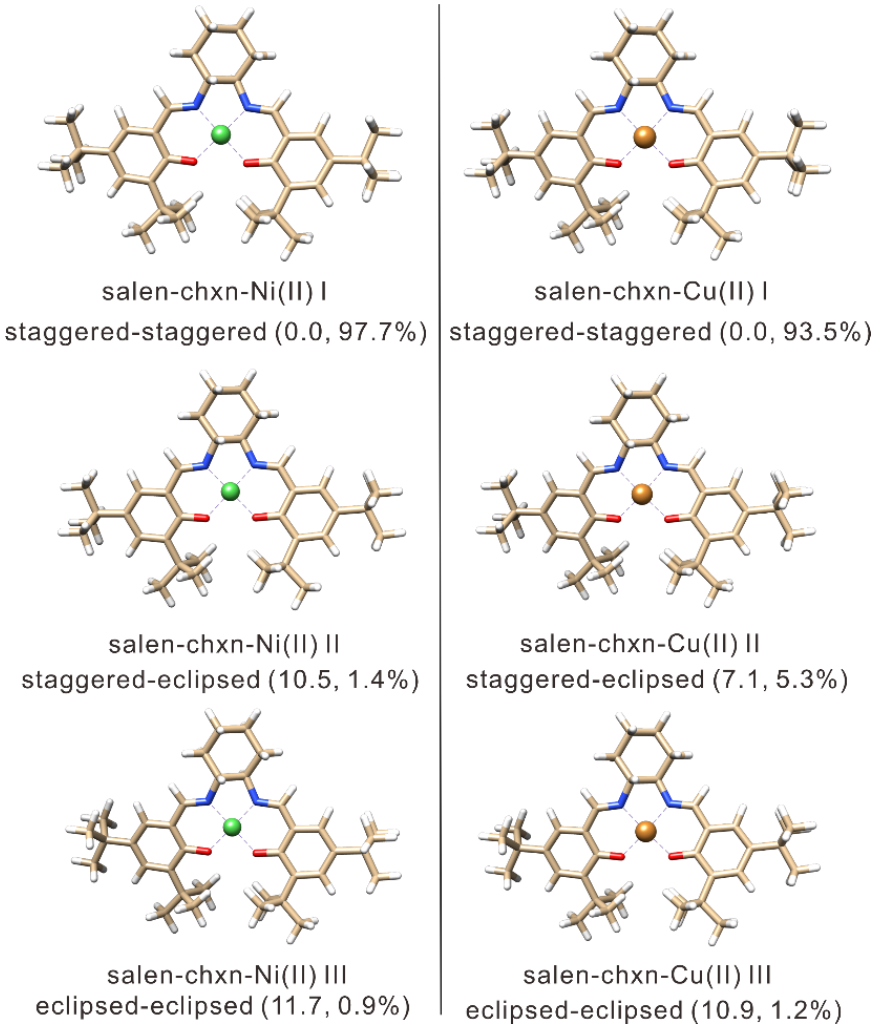

Figure 5.3. The optimized geometries of the salen-chxn-Ni(II) and salen-chxn-Cu(II) conformers at the B3LYP-D3BJ/6-311++G(d,p) level of theory with the PCM of CDCl3 . The relative free energies in kJ mol−1 and the Boltzmann percentage abundances at 298 K are provided in the brackets. The blue and red colors represent the nitrogen and oxygen atoms, respectively, whereas the white color is for the hydrogen atoms, and the carbon frame is in the ginger color. The green and gold colors represent the nickel and copper atoms, respectively.

5.2.2. Experimental and Simulated IR, VCD, UV-Vis and ECD Spectra of the Salen-Chxn Ligand

The individual conformer IR and VCD spectra of the four most stable salen-chxn conformers are depicted in Figure 5.4, together with the Boltzmann averaged and the experimental IR and VCD spectra of the ligand in CDCl3 solution. In terms of the IR spectra, those of salen-chxn-I (staggered–staggered) and -II (staggered–eclipsed) look almost identical, whereas those of salen-chxn-III (eclipsed–eclipsed) and -IV (Type II staggered–staggered) demonstrate some noticeable differences. In general, it is easy to correlate the experimental IR bands with the calculated ones, and all the visible features are labelled with letters “a” to “t” for easy recognition. For example, the highest wavenumber bands of salen-chxn-III, i.e., those labelled as a (antisymmetric) and a’ (symmetric) for the C=N stretching modes, are blue-shifted by ~7 cm^{-1} compared to those of -I and -II, and the relative intensity of b of -III is somewhat weaker than those of -I and -II. For salen-chxn-IV, the C=N and aromatic ring C=C stretching region exhibits a much different pattern in terms of spacing and relative intensity when compared to those of -I, -II and -III. To facilitate vibrational discussion, the experimental IR band assignments are provided in Figure 5.5, based mainly on the calculated IR spectrum of the dominant conformer, salen-chxn-III and -I (vide infra). As mentioned above, band a and a’ correspond to the antisymmetric and symmetric C=N stretches, respectively. While the unresolved b band contains the symmetric and antisymmetric aromatic ring C=C stretching bands, the c and c’ are the symmetric and antisymmetric wagging motions of the CHs of the aromatic ring coupled with the OHs, respectively.

As in the case of their IR spectra, the VCD spectra of salen-chxn-I and -II are very similar, except in the 1420–1500 cm−1 region (bands d to f) where some minor differences are noted,

mostly related to the C-H wagging motions from the tBu groups and the benzene rings. While salen-chxn-III and -IV offer similar main VCD features in the region below 1580 cm^{-1}, they exhibit drastically different VCD spectra from those of -I and -II in the above 1580 cm−1 region. Compared to the experimental VCD features, it is obvious that only salen-chxn-III shows the negative/positive VCD signs (high to low cm^{-1}) of the C=N stretching bands a and a' in the ~1635 cm−1 region, which matches the experimental ones. Salen-chxn-I, -II and -IV, on the other hand, all offer wrong VCD sign patterns. In the 1245 cm−1 region, salen-chxn-III exhibits a strong positive VCD feature, which matches the experimental band m intensity. In contrast, the other three conformers offer a relatively weak VCD feature at this position or not at all. Overall, salen-chxn-III offers the best agreement with the experimental IR and VCD features, especially in the above 1580 cm−1 region and around 1250 cm^{-1}. At the same time, salen-chxn-I and -II provide somewhat better agreements in the 1300 cm−1 region centered on feature i and in the 1100 cm−1 region centered on feature r. In general, the predicted VCD features of salen-chxn-IV do not offer any good agreement with the experimental ones in all the main regions discussed above. Clearly, a combination of substantial salen-chxn-III and some amount of salen-chxn-I and -II would be needed to account for the observed IR and VCD features. Therefore, we also included the empirically weighted IR and VCD spectra in Figure 5.4, where empirical percentage abundances of 60%, 20% and 20% were assigned to salen-chxn-III, -I and -II, respectively. The empirical abundances are somewhat different from the theoretical Boltzmann percentages, which overly emphasize the contribution of salen-chxn-I and -II and downplay the importance of salen-

chxn-III. Nevertheless, based on the good agreement between the experimental and empirically weighted theoretical IR and especially VCD spectra, we can conclude that salen-chxn-I, -II and -III are all important conformers in solution, with -III being the most abundant one.

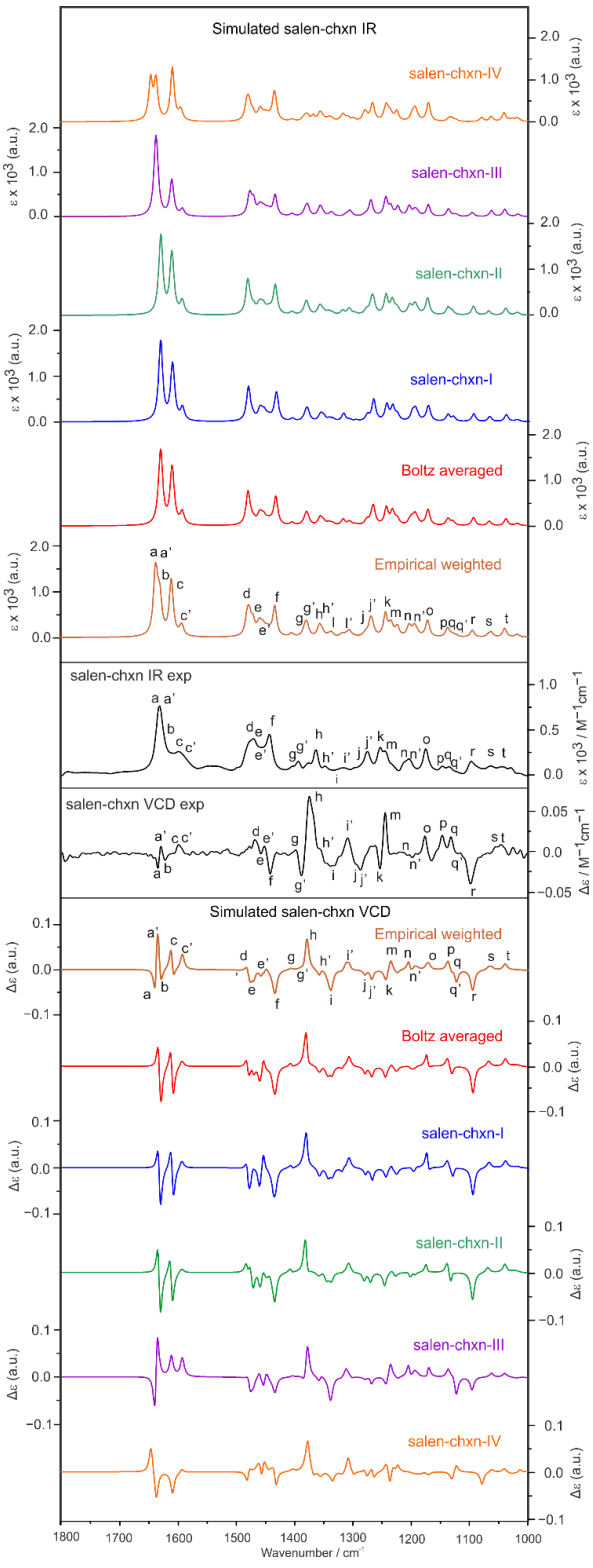

Figure 5.4. The simulated individual IR and VCD spectra of the four most stable salen-chxn conformers and the related Boltzmann averaged IR and VCD spectra at the B3LYP-D3BJ/def2-TZVP/PCM (CDCl3) level of theory at 298 K. The experimental and empirically weighted IR and VCD spectra are also provided. The experimental units are on the right side. The main IR and VCD band features are labelled "a" to "t" to aid the comparison.

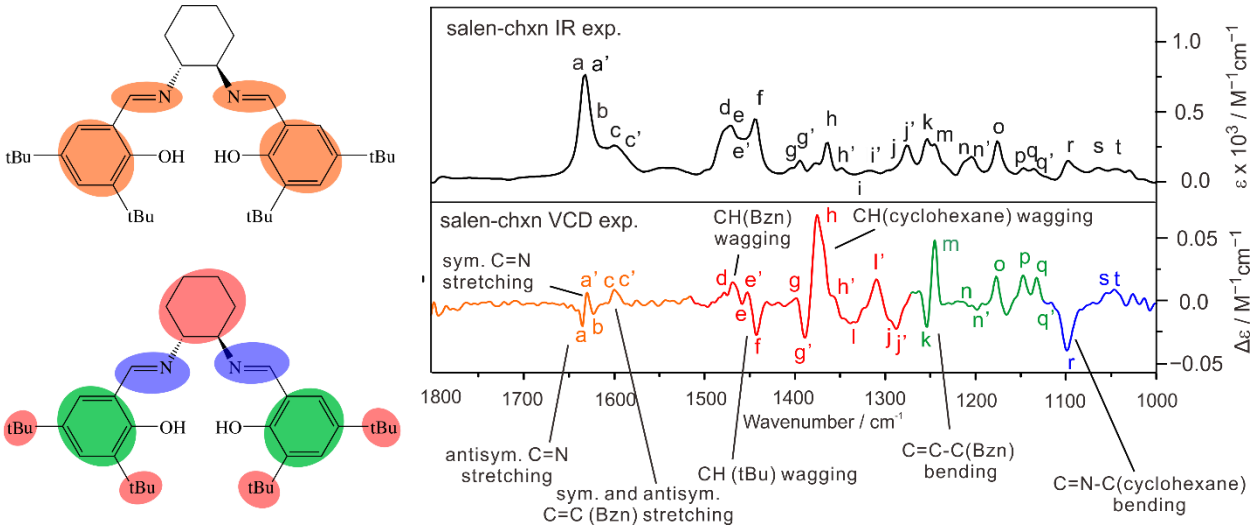

Figure 5.5. The general assignment of the IR and VCD bands of salen-chxn. The main IR and VCD band features are labelled "a" to "t" to aid the comparison as in Figure 5.4.

With regard to the three tBu conformations, one may initially assume that the staggered arrangement would be noticeably more stable than the eclipsed one because of the Newman projections shown in Figure 5.2. But a closer examination reveals that the two tBu groups are so far apart that the closest H···H distance is still over 3.6 Å, very unlikely to make a noticeable difference in their relative free energy. Actually, the closest H··H distances are those between the tBu group and the aromatic ring. They are about 2.1 Å, again not likely to make much difference in the relative energy. Indeed, the DFT free energy difference for salen-chxn-I (staggered–

staggered) and -II (staggered–eclipsed) is quite small, i.e., <0.2 kJ mol^{-1}. It was puzzling initially why salen-chxn-III (eclipsed–eclipsed) is so much less stable than salen-chxn-II (staggered–eclipsed) or salen-chxn-I (staggered–staggered). A further examination revealed that to accommodate the eclipsed–eclipsed tBu arrangement, the tBu groups in one aromatic branch become too close to the tBu groups in another branch, generating much steric tension and pushing the two aromatic branches a bit further apart. This change, although subtle, can be seen visually in the changes of IR and VCD bands above 1400 cm^{-1}, especially those associated with the C=N stretches and aromatic ring C=C stretches. This is also reflected strongly in the relative free energies with salen-chxn-III predicted to be ~10 kJ mol−1 less stable.

Figure C1 (appendix) provides the bond critical points related to the non-covalent interactions based on the Quantum Theory of Atoms in Molecules (QTAIM)[53] analysis. As one can see, salen-chxn-I has one more cage critical point than -III, further stabilizing -I. On the other hand, comparing the experimental IR and, in particular, the VCD features with the simulated ones strongly indicates that all three conformers, i.e., salen-chxn-I, -II and -III, are all present dominantly in the solution. Therefore, one may speculate that the additional cage critical point in salen-chxn-I may limit its interactions with the solvent. In salen-chxn-III, on the other hand, the aromatic rings may be more ready to accommodate some solvent molecules, making it more stable in the solution through some explicit solute–solvent interactions. We also note that the single point energy calculations at the DLPNO-CCSD(T)[54]/cc-pVDZ level using ORCA[55] reduce the relative free energy difference between salen-chxn-I and -III to 7.1 kJ mol^{-1}, suggesting that the true energy difference may be overestimated at the DFT level. Please note that the relative Gibbs energy corrections were taken directly from the DFT calculations, and the PCM of CDCl3 was included in the single point calculations.

The experimental UV-Vis and ECD spectra of salen-chxn in acetonitrile (ACN) are provided in Figure 5.6. The UV-Vis and ECD spectra of the three dominant conformers derived from the IR and VCD analyses discussed above were calculated at two different levels of theory: B3LYP-D3BJ/def2-TZVP which was used for the IR and VCD calculations above, and MN12L/def2-TZVP. The individual UV-Vis and ECD spectra of salen-chxn-I, -II and -III are provided in Figure C2, while the related Boltzmann weighted spectra are also depicted in Figure 5.6. In addition, the empirically weighted UV-Vis and ECD spectra using the percentage abundances obtained from the IR and VCD analyses are also shown in Figure 5.6.

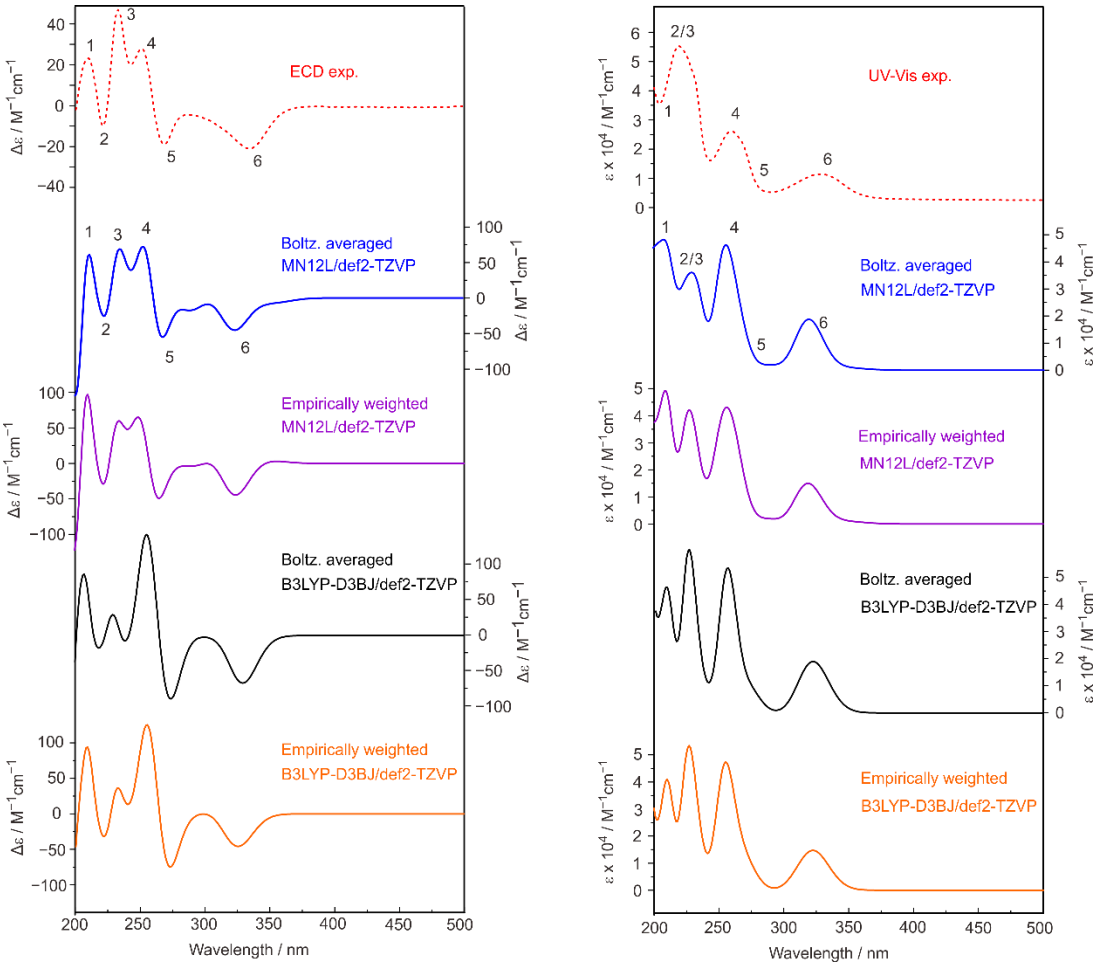

Figure 5.6. Comparison of the experimental and theoretical UV-Vis and ECD spectra of salen-

chxn in acetonitrile solution. The first 200 electronic states were included in the calculations at the two levels of theory indicated. For the empirically weighted spectra, we used the same weights derived from the IR and VCD comparison. The main UV-Vis and ECD bands are labelled as "1" to "6" to aid the comparison.

It is clear that the UV-Vis and ECD spectra of these three conformers look very similar. Not surprisingly, the Boltzmann and empirically weighted UV-Vis and ECD spectra look very similar because the UV-Vis and ECD features are much less sensitive to the subtle tBu conformations. Taking advantage of better resolution with ECD, the experimental peaks at 209 nm, 221 nm, 233 nm, 250 nm, 266 nm and 330 nm can be tentatively assigned to the calculated ones labelled 1 to 6. Overall, the simulated UV-Vis and ECD spectra at the MN12L level provide a better agreement with the experimental ones than the B3LYP level.

5.2.3. Experimental and Simulated IR, VCD, UV-Vis and ECD Spectra of the Salen-Chxn-Ni(II) and Cu(II) Complexes

Since the IR features of these two complexes are quite similar, we first focus on the IR band assignment and the comparison of the IR bands of the complexes with the ligand, using salen-chxn-Cu (II) as an example. One goal here is to facilitate an in-depth understanding of the appearance of several strong bisignate VCD couplets compared to the ligand. The band assignments are given in Figure 5.7, based on the theoretical simulation (vide infra). The region of interest is roughly divided into six regions, namely I-VI, associated with the vibrational motions centered at different parts of the complex, as shown in Figure 5.7

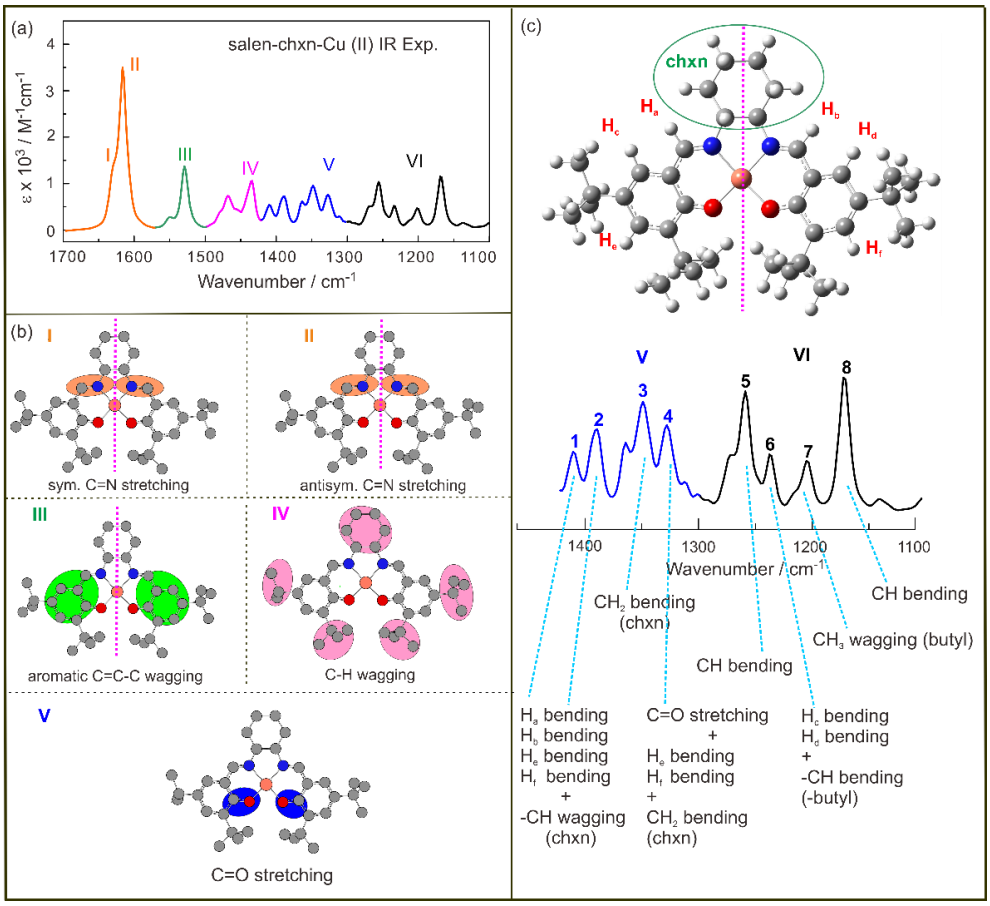

Figure 5.7. (a) The IR spectrum of salen-chxn-Cu (II) in the 1700–1100 cm−1 region is divided into six parts from I to VI. (b) The molecular parts related to I to V are coloured. (c) The main vibrational modes of salen-chxn-Cu (II) in the 1450–1100 cm−1 region. The main IR bands in the 1100–1450 cm−1 region are labelled as "1" to "8" to aid the discussion.

The shoulder I is mainly associated with the C=N symmetric stretch, while II is dominated by the C=N antisymmetric stretch with considerable contributions from the aromatic ring C=C stretches. In comparison to the ligand, the antisymmetric C=N stretch is red-shifted, whereas the aromatic ring C=C stretches appear to be slightly blue-shifted. Region III contains mostly aromatic ring C-H wagging motions, demonstrating a noticeably strong intensity

compared to the somewhat related vibrational modes in the ligand, i.e., band c and c', which are of much lower intensity and blue-shifted greatly. While region IV is mainly related to the cyclohexane CH2 and tBu CH3 motions, region V contains the symmetric and antisymmetric C-O stretches. The rest of the low wavenumber features are grouped into VI, and their more detailed assignments are provided in Figure 5.7.

As described in Section 5.2.1, three low-energy conformers were identified for each metal complex. The Boltzmann weighted simulated IR and VCD spectra of salen-chxn-Cu (II) at the B3LYP-D3BJ/6-311++G(d,p) and B3LYP-D3BJ/def2-TZVP+LANL2DZ(for Cu) levels are compared with the experimental ones in Figure 5.8. The associated individual conformer IR and VCD spectra at the B3LYP-D3BJ/6-311++G(d,p) level are shown in Figure C3. It is interesting to note that both IR and VCD spectra of these three conformers look very similar, unlike in the case of the ligand itself. This means that the IR and VCD spectra do not offer discrimination among these tBu conformers. Generally, excellent agreements were achieved between the experimental and theoretical IR and VCD spectra of salen-chxn-Cu (II). We note that all visible IR and VCD experimental features are reproduced theoretically. The strongest VCD features in the Cu (II) complex are the negative/positive (from low to high cm^{-1}) bisignate features in Molecules 2023, 28, 2571 11 of 22 regions I and II. These bisignate features are associated with the antisymmetric and symmetric C=N stretches in the Cu (II) complex based on the simulation, a point which will be further explored in Section 5.2.4. On the other hand, the two aromatic rings C=C stretches in region II are not strongly coupled. In fact, the GaussView visualization shows them as mainly located at the right and the left branches separately. This situation leads to an overall negative VCD which is not well resolved from the negative wing of the aforementioned bisignate feature.

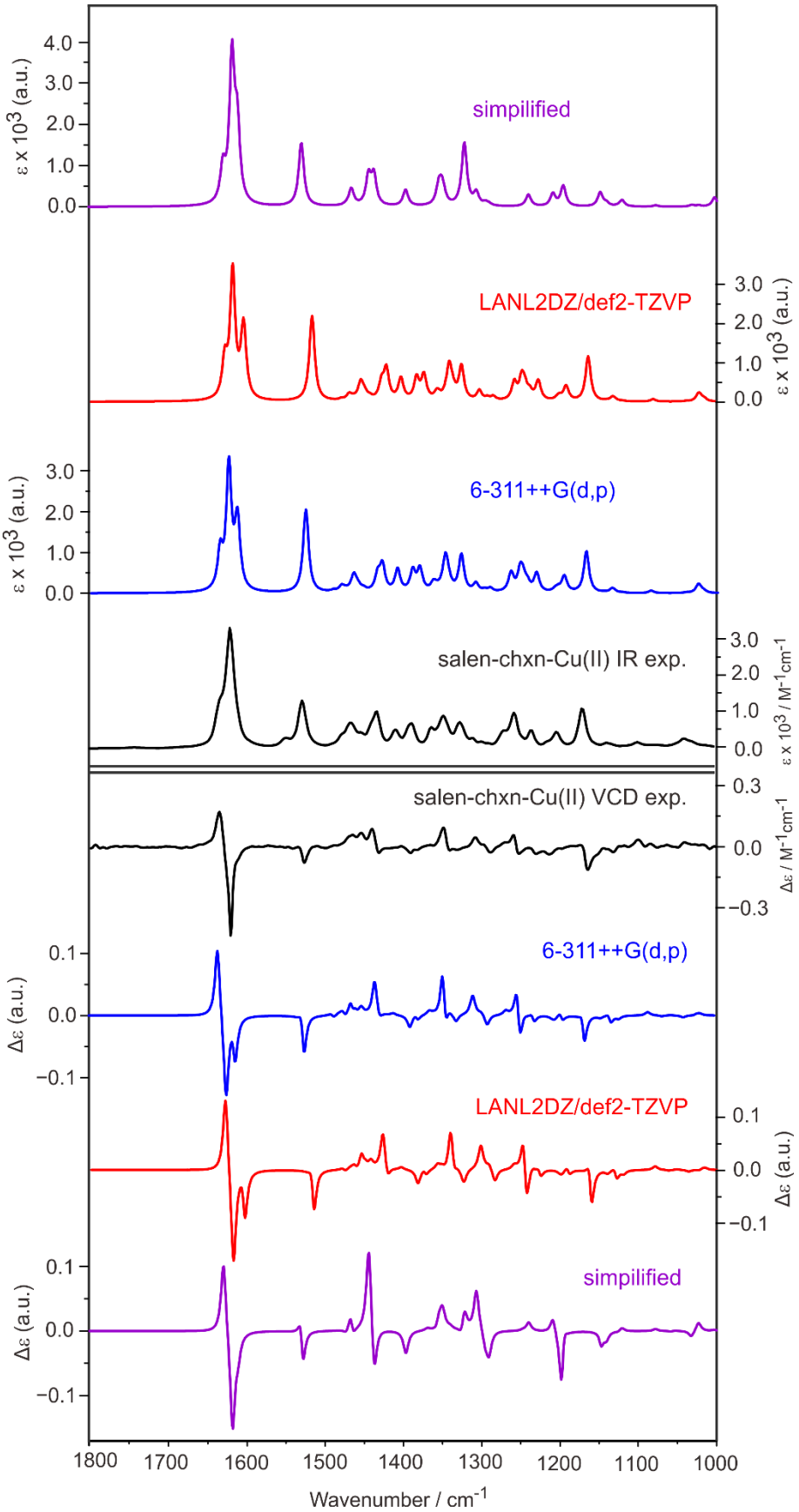
simpilified
LANL2DZ/def2-TZVP
6-311++G(d,p)
salen-chxn-Cu(II) IR exp.
salen-chxn-Cu(II) VCD exp.
6-311++G(d,p)
LANL2DZ/def2-TZVP
simpilified
ε x 10^3 (a.u.)
ε x 10^3 / M^-1cm^-1
Δε / M^-1cm^-1
Δε (a.u.)
Wavenumber / cm^-1
1800
1700
1600
1500
1400
1300
1200
1100
1000

Figure 5.8. Comparison of the experimental IR (top) and VCD (bottom) spectra of salen-chxn-Cu (II) with the corresponding calculated spectra in CDCl3 solution. The levels of theory used are B3LYP-D3BJ/6-311++G(d,p) and B3LYP-D3BJ/def2-TZVP+LANL2DZ(for Cu) with the PCM of chloroform. The simplified calculations were done by replacing tBu with an H atom.

Parallel calculations and comparisons were also performed for the salen-chxn-Ni(II) complex. While the Boltzmann-weighted simulated IR and VCD spectra of salen-chxn-Ni(II) are compared with the experimental ones in Figure 5.9, the associated individual conformer IR and VCD spectra are also shown in Figure C3 (appendix). Again, excellent agreements between theory and experiment have been achieved, and neither IR nor VCD features are sensitive to the different conformations due to the tBu arrangements.

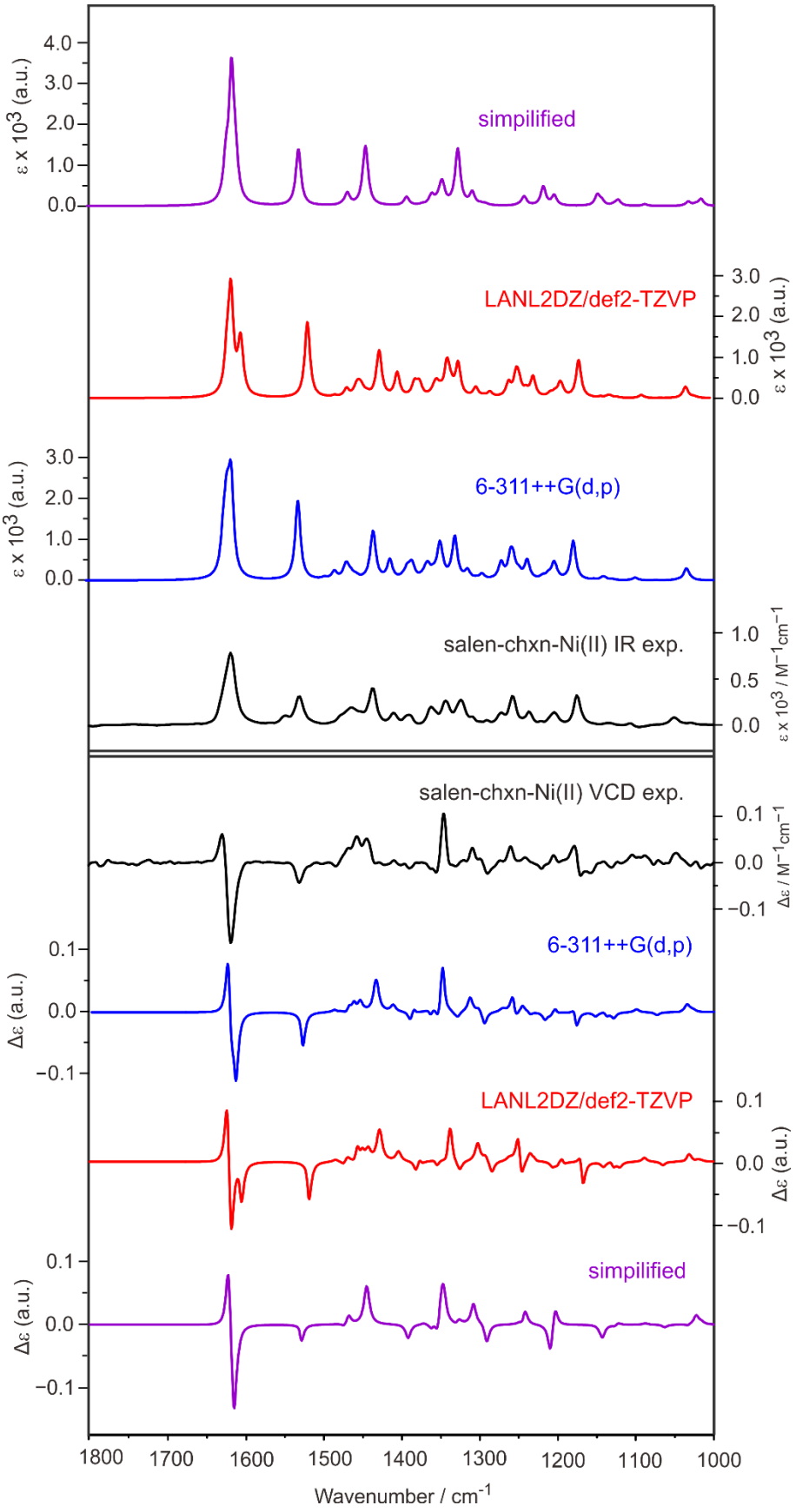
simpilified
LANL2DZ/def2-TZVP
6-311++G(d,p)
salen-chxn-Ni(II) IR exp.
salen-chxn-Ni(II) VCD exp.
6-311++G(d,p)
LANL2DZ/def2-TZVP
simpilified
ε x 10^3 (a.u.)
ε x 10^3 / M^-1cm^-1
Δε (a.u.)
Δε / M^-1cm^-1
Wavenumber / cm^-1
1800
1700
1600
1500
1400
1300
1200
1100
1000

Figure 5.9. Comparison of the experimental IR (top) and VCD (bottom) spectra of salen-chxn-Ni (II) with the corresponding calculated spectra in CDCl3 solution. The levels of theory used are B3LYP-D3BJ/6-311++G(d,p) and B3LYP-D3BJ/def2-TZVP + LANL2DZ(for Ni) with the PCM of chloroform. The simplified calculations were done by replacing tBu with an H atom.

As discussed above, the simulated IR and VCD spectra agree very well with the experimental features for both the Ni(II) and Cu (II) complexes, supporting that the most stable conformation predicted for each complex (see Figure 5.3) is the main species in solution. In contrast to the ligand case where the staggered–staggered (20%), staggered–eclipsed (20%), and eclipsed–eclipsed (60%) salen-chxn conformers all contribute significantly to the observed spectra, the staggered–staggered conformation prevails with ~97% and 93% abundances for the salen-chxn-Ni(II) and -Cu (II) complexes in solution, respectively. We do acknowledge that the IR and VCD features are not very sensitive to the tBu conformations, unlike in the case of the ligand. Another goal of the current study is to explore the possibility of speeding up the calculations by replacing each tBu group with an H atom and verifying if the simplified calculations can theoretically capture all major experimental IR and VCD features. The simplified calculation was performed at the B3LYP-D3BJ/6-31G(d,p) (for C and H atoms) + 6-311++G(2d,p) (for Ni or Cu, N and O atoms) level. The results are also presented in Figures 5.8 and 5.9 for the Cu (II) and Ni(II) complexes, respectively. It is interesting to note that major IR and VCD features in the above 1500 cm−1 region were well reproduced. In contrast, those medium strength bands in the below 1500 cm−1 region for the Ni (II) and Cu(II) complexes were not captured accurately. This is not surprising because these specific bands below 1500 cm−1

can be largely assigned to the CH3 motions of the tBu functional groups as well as the CHs associated with the cyclohexane ring.

Therefore, if one's main focus is the absolute configuration of the metal complexes, it is enough to do simplified calculations. On the other hand, the complete calculations allow detailed assignment of all visible vibrational and VCD bands, greatly boosting the confidence of conformational identification.

Another key point of interest is the absolute configuration of the chiral metal centers, i.e., the helicity of the metal complexes.[14] The dihedral angle θ which defines the specific helicity preference, is the dihedral angle between the O1-Metal-N1 and the O2-Metal-N2 planes shown in Figure C4 (appendix), where O1 and N1 belong to one aromatic branch, and O2 and N2 belong to another. These angle values are 3.7 and 9.0 degrees for the Ni(II) and Cu (II) complexes, respectively. Since these two metal complexes exhibit nearly square planar geometries, one may speculate that the M or P helicity would be possible because only a small change in the dihedral angle to the opposite direction would be enough for the helicity switch. In a previous study of several Ni(II) complexes which are in a distorted square planar N2O2-coordination sphere, a diastereomeric equilibrium was detected, with a strong preference of the Λ (i.e., M) over Δ (i.e., P) metal chirality for the R-ligands.[56] The preference for Δ or Λ was shown to be tunable by using different solvents in the case of a tris(diamine)nickel (II) complex.[57] Interestingly, the situation is quite different for the nearly square planar Ni(II) and Cu(II) complexes with the salen-chxn ligands. No P helicity geometry candidates were identified in the CREST searches within an energy window as high as 60 kJ mol^{-1}. To further confirm the absence of stable P helicity geometries, we also constructed several Ni(II) geometries with the P helicity as the starting geometries. All of them reverted to the M helicity with the DFT geometry

optimization. It appears that the cyclohexane ring, which connects the two nitrogen atoms of the ligand, strongly influences the outcome of the possible diastereomers with the (R, R) ligands, i.e., only the M helicity diastereomers are stable.

for the (R, R)-salen-chxn-Ni(II) and Cu(II) complexes. This calculation result, combined with the excellent agreement between the experimental and theoretical IR and VCD of the (R, R)-salen-chxn-Ni(II) and Cu(II) complexes, allows one to unequivocally state that the dominant conformers are with the M metal chirality. This conclusion is similar to that drawn for other nearly square planar Schiff base transition metal complexes with similar ligands, for example, the bis(pyrrol-2-ylmethyleneamine)-cyclohexane-Ni(II), Cu(II), Pd (II) and Pt(II) complexes reported previously.[14]

The experimental UV-Vis and ECD spectra of the salen-chxn-Ni(II) and salen-chxn-Cu(II) are depicted in Figure 5.10. From the IR and VCD analyses, we know that, by far, the dominant conformation is staggered–staggered. Therefore, we carried out TDDFT calculations for the most stable salen-chxn-Ni(II) and salen-chxn-Cu(II) conformers with 97% and 93% abundances, respectively. The resulting UV-Vis and ECD spectra are summarized in Figure 5.10 as well. To facilitate the comparison, noticeable experimental UV-Vis and ECD bands are numbered 1 to 6 or 7, and the corresponding band assignments in the calculated spectra are also numbered accordingly. Because of the broad nature of the spectral features in the UV-Vis region, the assignments are less conclusive in comparison to the IR and VCD assignments. At the same time, the calculated UV-Vis and ECD spectra at the two different levels of theory differ noticeably, highlighting the challenges in modelling transition metal complexes. Interestingly, the B3LYP-D3BJ/6-311++G(d,p) provides considerably better agreement with the experiment for both metal complexes than MN12L/6-311++G(d,p). It is known that the performance of

different combinations of DFT functionals and basis sets usually need to be tested for the excited state calculations of transition metal complexes because of the associated challenges.[15] The good agreement provided by the B3LYP-D3BJ/6-311++G(d,p) calculations allowed one to assign most of the major features observed. Overall, one could confidently state that the helicity of the metal centers, i.e., Ni(II) and Cu(II), are indeed M based on the ECD analyses, the same conclusion derived from the corresponding VCD analyses.

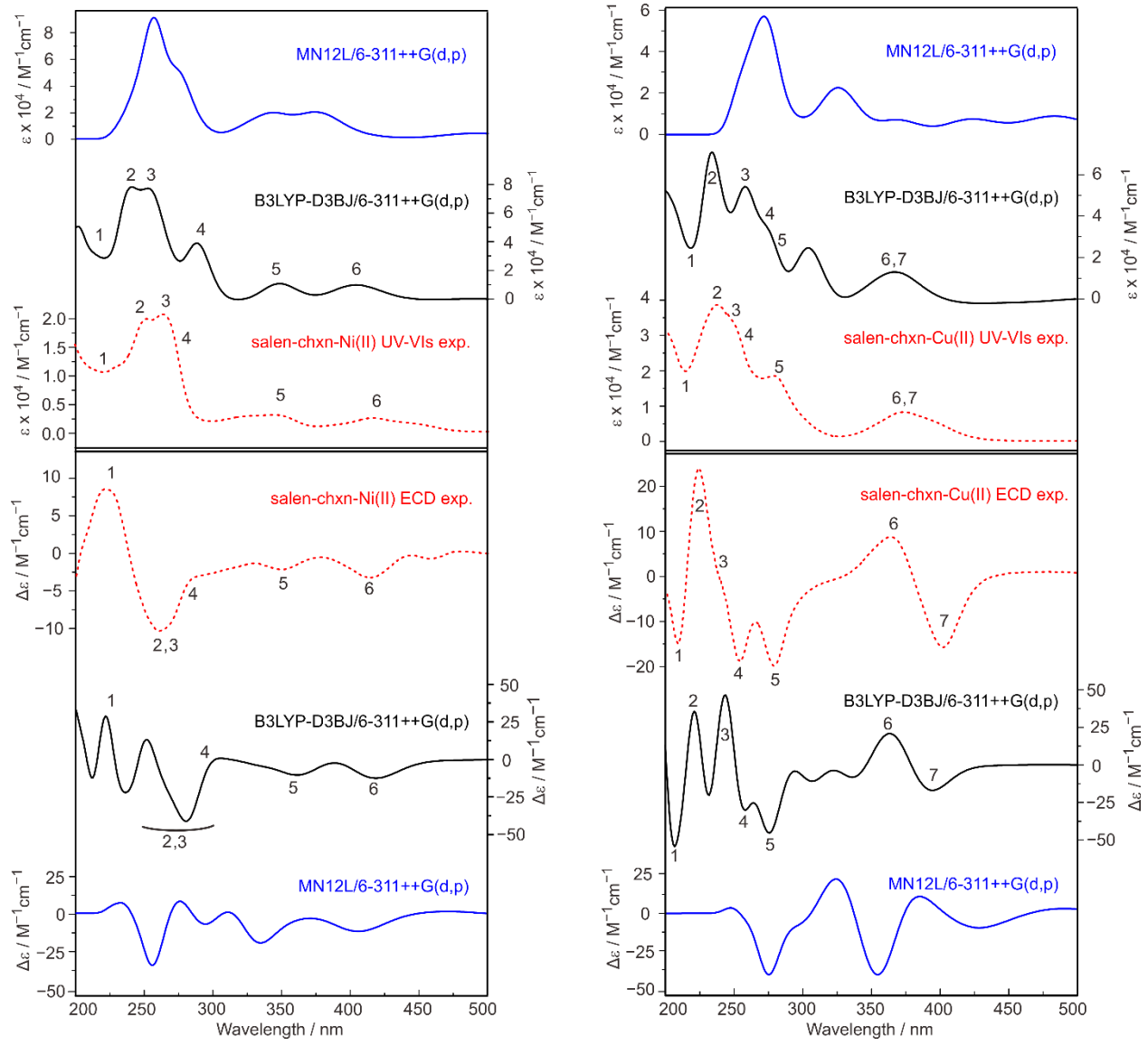

Figure 5.10. Comparison of the experimental and simulated UV-Vis (top) and ECD (bottom)

spectra of salen-chxn-Ni(II) and salen-chxn-Cu(II) at two different levels of theory. In total, 250 electronic states were included in the calculation. The main UV-Vis and ECD bands of salen-chxn-Ni(II) and salen-chxn-Cu(II) are labelled as "1" to "6" and "1" to "7", respectively, to aid the comparison.

5.2.4. Applications of the Exciton Chirality Method to the VCD and ECD Spectra of the Complexes

The exciton chirality method for ECD spectroscopy was recently comprehensively reviewed by Pescitelli.[31] The author outlined three main prerequisites for correctly applying the exciton chirality method. These include: (i) knowing the conformational distribution of the molecular target; (ii) knowing the corresponding direction of the electric transition moments; and (iii) assuming the observed ECD signals to be dominated by the exciton coupling mechanism. Below we first discuss whether it is suitable to apply the exciton chirality method to the ECD spectra of the ligand and the two complexes and use the theoretical calculations in the current study to rationalize the conclusion. Second, we extend the exciton chirality method application to the VCD spectra of the three compounds studies.

For the salen-chxn ligand, it is unsuitable for applying the exciton chirality method to interpret the resulting ECD features because the system does not fulfil criteria (ii) and (iii). There are multiple chromophores in the UV-Vis region, and most bands appear to be severely overlapped, making it difficult to identify the exciton couplets. The situation for the two metal complexes seems somewhat promising at first. In the experimental ECD spectrum salen-chxn-Ni(II), one strong negative Cotton couplet is in the region below 300 nm. A clear negative Cotton couplet centered at about 385 nm is present in the salen-chxn-Cu (II) ECD spectrum. On the

other hand, as one can see in Figure 5.10, the ECD spectra of these two metal complexes look very different even though they share many similarities (although Cu (II) is an open shell and Ni(II) is a closed shell), making it difficult to fulfill requirement (ii). To illustrate this difficulty, the contributions of the individual electronic transitions to the UV-Vis and ECD spectra are provided in Figure C5 (appendix). It is clear that the negative Cotton couplet contains some obvious contributions by multiple electronic transitions rather than an obvious pair of coupled transitions. Salen-chxn-Cu (II) suffers a similar issue. Some of these difficulties associated with applying the exciton chirality method to the salen Ni(II) complexes were also alluded to in a previous publication.[58]

For the salen-chxn ligand, applying the exciton chirality method to interpret the resulting VCD features is unsuitable because none of the three criteria are fulfilled. While salen-chxn-I, -II and -III all have similar arrangements of the two aromatic branches, the resulting VCD features are sensitive to more subtle differences, such as the orientations of the tBu groups. Second, there are no obvious observed VCD features dominated by the exciton coupling mechanism. The situation improves with the two metal complexes. First of all, both of their observed experimental VCD features are dominated by a negative VCD couplet in the above 1580 cm−1 region where the lower wavenumber band shows a negative sign. Second, the bisignate VCD couplets of salen-chxn-Ni (II) and -Cu (II) are related to the symmetric and antisymmetric C=N stretches, whose vibrational electric transition moment directions are well defined, as shown in Figure 5.11. Second, only one main conformer was identified for each metal complex, or at least the minor tBu arrangements do not affect the relative orientation of the two aromatic branches, thanks to the rigidity introduced by the coordination bonding to a central metal atom. Following the VCD exciton chirality method proposed by Taniguchi and Monde,[59] the method indeed

predicted a negative Cotton effect for (R, R)-salen-chxn-Ni(II) (Figure 5.11), marked by a counter-clockwise rotation of the C=N groups. The same scheme can be applied to salen-chxn-Cu(II).

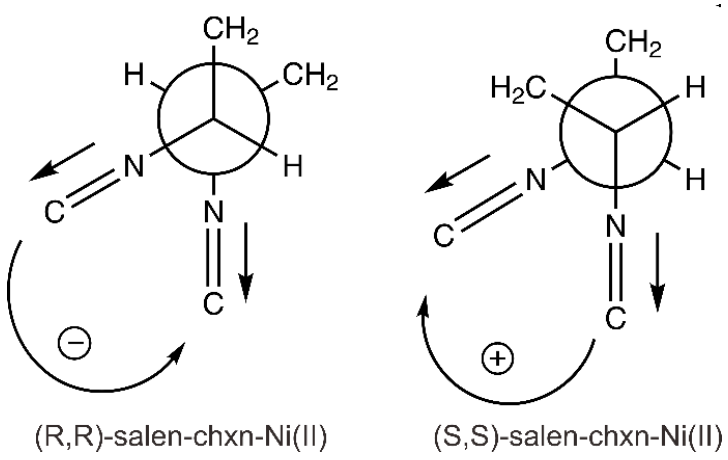

Figure 5.11. The two coupled C=N stretching transition dipole moments are indicated for the (R, R)- salen-chxn-Ni(II) and (S, S)-salen-chxn-Ni(II), providing the negative and positive exciton coupling couplets, respectively.

5.2.5. Experimental and Simulated eCP-Raman Spectra of Salen-Chxn-Ni(II) and Salen-Chxn-Cu(II)

Recently, it was discovered that when a chiral compound, such as a transition metal complex, is under (near) resonance, the chiral Raman measurement carried out using a ROA spectrometer may contain significant eCP-Raman contributions in addition to resonance ROA features. However, since there have been very few examples reported of the newly discovered eCP-Raman spectroscopy, we conducted further Raman and eCP-Raman studies of salen-chxn-Ni(II) and salen-chxn-Cu(II). In a typical ROA experiment, a randomly polarized light passes through a chiral sample, and the chiral Raman response is measured by the small intensity difference of the

back-scattered right circularly polarized light (I_R) versus left circularly polarized light (I_L) using the scattered circularly polarized (SCP)-ROA.[60] For systems under (near) resonance, it was reported recently that the $I_R - I_L$ signals contain two important contributions: resonance ROA and eCP-Raman. eCP-Raman occurs because the randomly polarized light becomes circularly polarized when it passes through a chiral sample under resonance and is absorbed differentially. The resulting circularly polarized light interacts with the chiral solute and solvent and generates circularly polarized Raman responses ($I_R - I_L$) by both the chiral solute and (achiral) solvent. We emphasize that both chiral or achiral systems may produce eCP-Raman features, and the IR − IL responses are measured in the usual channel with a regular SCP-ROA instrument. One hallmark of eCP-Raman is the huge I_R—I_L bands of (achiral) solvent, i.e., the chirality of the chiral solute is now imprinted onto the eCP-Raman response of the achiral solvent. Experimental Raman and $I_R - I_L$ spectra of salen-chxn-Ni(II) and salen-chxn-Cu (II) are provided in Figure 5.12. It is immediately obvious that both Raman and $I_R - I_L$ spectra are dominated by the solvent CDCl3 bands, whereas the bands of the Ni(II) and Cu (II) complexes are fairly weak. Similar observations were reported in recent publications.[23,24,25,61] The huge $I_R - I_L$ responses of CDCl3 indicate that the chiral Raman contribution is largely dominated by the eCP-Raman effect, as discussed above.

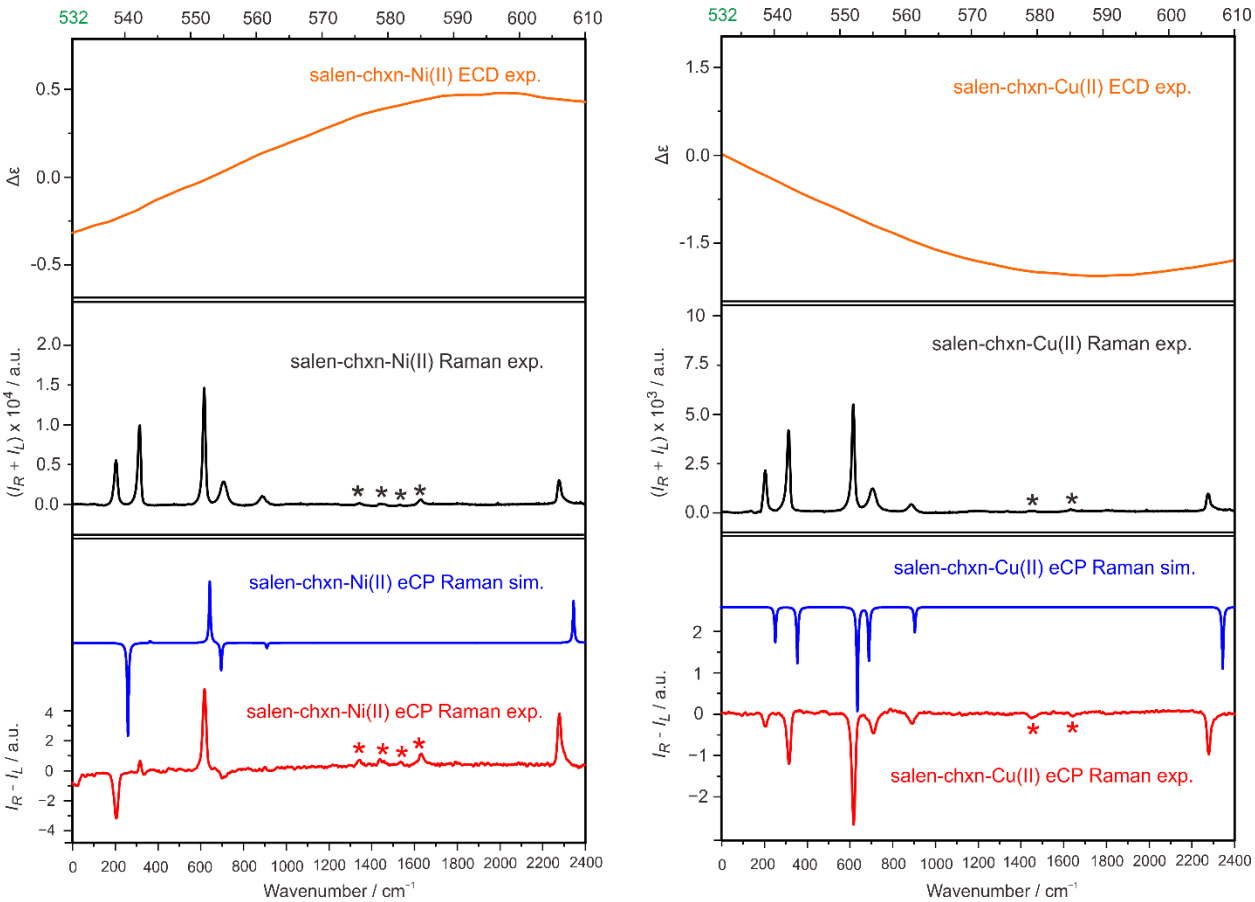

Figure 5.12. (Top): experimental ECD spectra from 532 nm to 610 nm of salen-chxn-Ni(II) and salen-chxn-Cu(II). (Middle): experimental Raman spectra of the two metal complexes. (Bottom): the comparison of the experimental and simulated eCP-Raman spectra of the two metal complexes. The solute bands are indicated with asterisk.

The eCP-Raman contribution can be described using the following expression[23,25]

$$CID = \frac{I_R - I_L}{I_R + I_L} = \frac{ln10}{4} cL\Delta\varepsilon\left(\frac{\Delta\varepsilon'}{\Delta\varepsilon} + DOC\right) \qquad (5.1)$$

Here CID, the normalized circular intensity difference, is defined as $(I_R - I_L)/(I_R + I_L)$ where $I_R + I_L$ corresponds to Raman and $I_R - I_L$ to eCP-Raman. $\Delta\varepsilon$ and $\Delta\varepsilon'$ are decadic, differential absorption coefficients of the chiral solute for the excitation light at 532 nm and the scattered light at each Raman band, respectively. C is the concentration of the chiral solute, L is the optical path length, and DOC is the normalized degree of circularity of the vibrational transition of interest. By applying Equation (5.1), one can simulate eCP-Raman using CID times Raman.

While c and L are experimental parameters, one can, in principle, calculate $\Delta\varepsilon$ and $\Delta\varepsilon'$ as well as DOC. On the other hand, theoretically, it is currently still extremely challenging to capture the $\Delta\varepsilon$ and $\Delta\varepsilon'$ magnitudes in the weak tail regions of the ECD bands of the transition metal complexes. Therefore, we decided to utilize the experimental ECD measurements of Ni(II) and Cu(II) in the tail regions, which are included in the top panels of Figure 5.12. It is interesting to point out that even though the ECD intensities are very low in the region beyond 532 nm for these two complexes, the zoom-in graphs in Figure 5.12 show that the spectral patterns look very different in salen-chxn Ni(II) versus Cu(II). If one re-examines the CID equation above, it is obvious that $\Delta\varepsilon$ and $\Delta\varepsilon'$ play a significant role in determining the signs and relative intensities of eCP-Raman bands. Therefore, one can expect drastically different eCP-Raman spectral patterns of salen-chxn-Ni(II) versus Cu(II), even though only the transition metal centers are different in these two salen-chxn metal complexes. Quantum mechanically, DOC, corresponding to the intensity and sign of CP-Raman signals, can be calculated using the same electric dipole–electric dipole polarizability tensors as for Raman scattering.[62] In the bottom panel of Figure 5.12, we compare the simulated and experimental results. As one can see, with the combined experimental and theoretical inputs, all the strong $I_R - I_L$ solvent bands are fully captured using the eCP-Raman

calculations, confirming the dominant nature of the light–matter interactions through the eCP-Raman mechanism. From the above eCP-Raman discussions of the two metal complexes, one can see that the chirality information of the metal complexes is now imprinted onto the $I_R - I_L$ solvent bands. These bands are generally much stronger than the corresponding ones of the metal complexes themselves because the solvent Raman bands have higher intensities than the metal complexes thanks to their large concentrations, a condition which is true in almost all solution experiments. This offers an opportunity to monitor the chirality of the complexes with only a small amount of chiral samples. By combining the high chiral sensitivity of ECD with the high-resolution capability of Raman spectroscopy, eCP-Raman is a promising new tool for absolute configuration determination and for probing excited state phenomena with the aid of improved theoretical simulations of ECD.

5.3 Materials and Methods

5.3.1 Experimental Section

The (R,R) and (S,S) salen-chxn ligands (98%) were purchased from Sigma-Aldrich, Milwaukee, USA and used without further purification. The salen-chxn-Ni(II) and -Cu(II) complexes were synthesized based on the previous literature procedures.[63] Briefly, the salen-chxn ligand was dissolved in absolute ethanol, and then the solution was heated to reflux (almost boiling). The perchlorate hexahydrate salt of Ni (or Cu) in absolute ethanol was added into the ligand solution and refluxed for 3 h. The solution mixture was concentrated using a rotavapor, and the residue was again dissolved in CH2Cl2 and ethyl acetate. The resulting solution was filtered under suction filtration to remove unreacted ligands. After that, the solvent was removed from the filtered solution using a rotavap to collect the remaining solid powder, which was further

recrystallized using dichloromethane. The resulting crystals of the Ni(II) and Cu(II) complexes were collected. All IR and VCD spectra were collected using an FTIR spectrometer (Bruker Vertex 70, Milton, Canada) coupled to a VCD model (PMA 50).[64] The photoelastic modulator (PEM) was set at 1400 cm−1 for all measurements. The liquid nitrogen-cooled mercury cadmium telluride (MCT) detector was used, and the resolution was set at 4 cm^{-1}.The CDCl3 solutions of the salen ligand and the salen-chxn-Ni(II) and salen-chxn-Cu (II) complexes were prepared in concentrations of 0.060 M, 0.060 M and 0.060 M, respectively. A demountable BaF2 cell was used for all measurements. For sale-chxn, salen-chxn-Ni(II) and salen-chxn-Cu (II), a 0.1 mm, 0.1 mm, and 0.05 mm Teflon spacer were used, collection time was one, one, and two hours, respectively. The final IR spectra were baseline corrected by the subtraction of the solvent spectrum measured under the same conditions, while the VCD spectra were obtained using the usual (R-S)/2 method.

The UV-Vis and ECD spectra of the salen-chxn ligand in acetonitrile were measured using a JASCO-810 ECD spectrometer with a concentration of 1 mM and a path length of 0.2 mm. The UV-Vis and ECD spectra of the salen-chxn-Ni(II) and -Cu(II) complexes in acetonitrile were collected using a Jasco-1700 spectrometer. The concentration was 1 mM (5 mM), and the path length of sample cell was 1 mm. The mass spectrometry and NMR data of the two metal complexes are reported in Point C1, appendix. The expected mass weights of the two complexes were confirmed, and the NMR data are consistent, with the Ni(II) complex being diamagnetic and the Cu(II) complex being paramagnetic with broad NMR lines. The raw VCD and ECD spectra of the (R,R) and (S,S)-salen-chxn-Ni(II) and -Cu(II) complexes studies are also presented in Point S1. The eCP-Raman spectra were measured using a Biotools (Jupiter, USA) chiral Raman spectrometer in the backward scattered circular polarized (SCP) scheme. The collection

time for salen-chxn-Ni(II) and salen-chxn-Cu(II) was 5 and 25 h, respectively. CDCl3 was used as the solvent, and the concentration was 10 mM and 5 mM for the Ni(II) and Cu(II) complexes, respectively.

5.3.2 Theoretical Section

To systematically explore the possible conformers of the ligand and the complexes, we utilized the CREST code,[29] including the generalized Born (GB) based GBSA implicit solvation model, using CDCl3 as the solvent. Built upon the previous semiempirical tight-binding (TB) quantum chemistry method, GFN-xTB,[65] the CREST code offers fast and reliable exploration and screening of the conformational space of mid- to large-sized molecules. A multitiered approach developed before[39] was applied to ensure fast and complete conformational searches. This includes several steps: (1) use CREST to generate candidates; (2) apply DFT optimizations of the CREST candidates with relaxed convergence criteria at the revPBE-D3/def2-SVP[47] level, with the empirical D3 dispersion correction; (3) do a single-point energy evaluation at the B3LYP-D3/def2-TZVP level of the optimized structures in step (2); Step 2 and (3) were done using Molpro[66] (4) perform the final geometry optimizations and harmonic frequency calculations using the Gaussian 16 package.[67] In the current study, the step (4) calculations were carried out at the B3LYP-D3BJ/def2- TZVP level for the ligand, at the B3LYP/6-311++G(d,p) level and the B3LYP-D3BJ/def2- TZVP (for all atoms except Ni and Cu) + LANL2DZ(for Ni and Cu) for the metal complexes. To account for the bulk solvent environment, the implicit solvent ($\varepsilon = 4.81$ for CDCl3) was included using the integral equation formalism (IEF) version of the PCM [48]. A Lorentzian band shape with a half-width at half-height (HWHH) of 4 cm−1 was applied to the simulations of IR and VCD spectra. In order to improve the frequency accuracy of the simulated

spectra, a linear correlation method, as described in ref 68,[68] was utilized to scale the simulated frequencies in the current study. The TDDFT calculations were employed to calculate the excited state energies, oscillator strength and optical rotation dispersion calculations at the B3LYP-D3BJ/6-311++G (d,p) and MN12L/6-311++G(d,p) levels of theory with the PCM of acetonitrile (ε = 35.688). The first 200 and 250 electronic states were taken into account for the ligand and the two metal complexes in simulating their UV-Vis and ECD spectra, respectively. A Gaussian line shape with an HWHH of 0.15 eV was used for the simulations of UV−Vis and ECD spectra.

5.4 Conclusion

The stereochemistry properties of a flexible salen-chxn ligand and two salen transition metal complexes, salen-chxn-Ni(II) and salen-chxn-Cu(II), were investigated using a combined experimental and theoretical approach with a series of chiroptical tools: UV-Vis and ECD, IR and VCD, and Raman and eCP-Raman. While many conformational candidates were generated with the systematic CREST conformational searches, the main low-energy conformations for the three molecular systems studied are associated with the different tBu arrangements. The excellent agreement between the experimental and simulated IR and VCD spectra of salen-chxn demonstrated that there are three main conformational species in solution with an estimated abundance of 60% salen-chxn-III and 20% each of salen-chxn-I and -II, also supported by the UV-Vis and ECD study. The complexation with Ni(II) and Cu(II) leads to a strong preference for the staggered–staggered ligand conformation with a nearly squared planar coordination geometry and, at the same time, induces an absolute configuration of the metal center, i.e., the helicity of the complexes. We were able to confirm the structural preference and determine the helicity of the metal complexes to be M for (R,R)-salen-chxn ligand based on the good agreement between

the observed and simulated chiroptical spectra. We also showed that the salen-chxn-Ni(II) and -Cu(II) are under (near) resonance with the Raman laser at 532 nm and measured the corresponding eCP-Raman spectra of them, which are dominated by the induced solvent chiral Raman bands. These observed chiral Raman solvent bands agree well with the simulated ones, demonstrating that the mechanism is well understood and highlighting eCP-Raman as a promising new tool for absolute configuration determination. Moreover, we extended the application of the exciton chirality method to the metal complexes and extracted their helicity information from the observed VCD spectra. Interestingly, it was found that the excitation chirality method did not work for the ECD interpretation of all three systems. Using the calculation results, we highlighted the important criteria for properly applying the excitation chirality method and discussed the reasons for its failure in the case of ECD interpretation of the three compounds studied. The current work demonstrates the advantages of applying multiple chiroptical spectroscopic techniques in a combination of theoretical modelling in order to explore conformational landscapes, ligand chirality, and helicity of transition metal complexes in solution.

References

[1] J. L. Segura, M. J. Mancheño, F. Zamora, Chem. Soc. Rev. **2016**, 45, 5635-5671.

[2] M. N. Uddin, S. S. Ahmed, S. M. Rahatul Alam, J. Coord. Chem. **2020**, 73, 3109-3149.

[3] M. S. More, P.G. Joshi, Y. K. Mishra, P. K. Khanna, Mater. Today Chem. **2019**, 14 100195.

[4] S. De, A. Jain, P. Barman, ChemistrySelect **2022**, 7, e202104334.

[5] M. K. Goshisht, G. K. Patra, N. Tripathi, Mater. Adv. **2022**, 3, 2612-2669.

[6] F. S. Alamro, S. M. Gomha, M. Shaban, A. S. Altowyan, T. Z. Abolibda, H. A. Ahmed, Sci. Rep. **2021**, 11, 15046. https://doi.org/10.1038/s41598-021-94533-6

[7] S. N. Shariff, S. Saravu, D. Ramakrishna, IntechOpen, London, **2022**. DOI: http://dx.doi.org/10.5772/intechopen.107904.

[8] A. Gualandi, F. Calogero, S. Potenti, P. G. Cozzi, Molecules, **2019**, 24, 1716.

[9] Z.-W. Li, X. Wang, L.-Q. Wei, I. Ivanović-Burmazović, G.-F. Liu, J. Am. Chem. Soc. **2020**, 142, 7283-7288.

[10] R. Mazzoni, F. Roncaglia, L. Rigamonti, Crystals **2021**, 11, 483.

[11] A. Trujillo, M. Fuentealba, D. Carrillo, C. Manzur, J. R. Hamon, J. Organomet. Chem. **2009**, 694, 1435–1440.

[12] G. Pescitelli, L.D. Bari, N. Berova, Chem. Soc. Rev. **2011**, 40, 4603–4625.

[13] C. Merten, K. Hiller, Y. Xu, Phys. Chem. Chem. Phys. **2012**, 14, 12884–12891.

[14] D. Dezhahang, M. R. Poopari, J. Cheramy, Y. Xu, Inorg. Chem. **2015**, 54, 4539–4549.

[15] G. Pescitelli, S. Lüdeke, A. C. Chamayou, M. Marolt, V. Justus, M. Górecki, L. Arrico, L. Di Bari, M. A. Islam, I. Gruber, Inorg. Chem. **2018**, 57, 13397–13408.

[16] M. Górecki, M. Enamullah, M. A. Islam, M. K. Islam, S. P. Höfert, D. Woschko, C. Janiak, G. Pescitelli, Inorg. Chem. **2021**, 60, 14116–14131

[17] T. Wu, X. Z. You, P. Bouř. Coord. Chem. Rev. **2015**, 284, 1–18.

[18] P. Zhu, G. Yang, M. R. Poopari, Z. Bie, Y. Xu, ChemPhysChem **2012**, 13, 1272–1281.

[19] Y. Zhang, M. P. Poopari, X. Cai, A. Savin, Z. Dezhahang, J. Cheramy, Y. Xu, J. Nat. Prod. **2016**, 79, 1012–1023

[20] A. C. Chamayou, G. Makhloufi, L. A. Nafie, C. Janiak, S. Lüdeke, Inorg. Chem. **2015**, 54, 2193–2203.

[21] C. Merten, C.J. Berger, R. McDonald, Y. Xu, Angew. Chem. Int. Ed. **2014**, 53, 9940–9943.

[22] G. Yang, Y. Xu, Top. Curr. Chem. **2011**, 298, 189–236.

[23] G. Li, M. Alshalalfeh, J. Kapitán, P. Bouř, Y. Xu, Chem. Eur. J. **2022**, 28, e202104302**.**

[24] G. Li, M. Alshalalfeh, Y. Yang, J. R. Cheeseman, P. Bouř, Y. Xu, Angew. Chem. Int. Ed. **2021**, 60, 22004–22009.

[25] T. Wu, G. Li, J. Kapitán, J. Kessler, Y. Xu, P. Bouř, Angew. Chem. Int. Ed. **2020**, 59, 21895–21898.

[26] E. Machalska, G. Zajac, A. J. Wierzba, J. Kapitán, T. Andruniow, M. Spiegel, D. Gryko, P. Bouř, M. Baranska, Angew. Chem. Int. Ed. **2021**, 60, 21205–21210.

[27] E. Machalska, N. Hachlica, G. Zajac, D. Carraro, M. Baranska, G. Licini, P. Bouř, C. Zonta, A. Kaczor, Phys. Chem. Chem. Phys. **2021**, 23, 23336–23340.

[28] E. Machalska, G. Zajac, M. Baranska, P. Bouř, D. Kaczorek, R. Kawecki, J. E. Rode, K. Lyczko, J. C. Dobrowolski, Chem. Comm. **2022**, 58, 4524.

[29] P. Pracht, F. Bohle, S. Grimme, Phys. Chem. Chem. Phys. **2020**, *22*, 7169-7192.

[30] N. Harada, K. Nakanishi, Univ Science Books: Mill Valley, CA, USA, **1983**.

[31] G. Pescitelli, Chirality **2022**, 34, 333–365.

[32] T. Taniguchi, D. Manai, M. Shibata, Y. Itabashi, K. Monde, J. Am. Chem. Soc. **2015**, 137, 12191–12194.

[33] M. A. J. Koenis, L. Visscher, W. J. Buma, V. P. Nicu, J. Phys. Chem. B **2020**, 124, 1665–1677.

[34] Z. Dezhahang, M. R. Poopari, Y. Xu. Chem. Asian J. **2013**, 8, 1205–1212.

[35] F. Xie, N. A. Seifert, M. Heger, J. Thomas, W. Jäger, Y. Xu, Phys. Chem. Chem. Phys. **2019**, 21, 15408–15416.

[36] S. Oswald, N. A. Seifert, F. Bohle, M. Gawrilow, S. Grimme, W. Jäger, Y. Xu, M. A. Suhm, Angew. Chem. Int. Ed. **2019**, 58, 5080–5084.

[37] C.D. Carlson, A. S. Hazrah, D. Mason, Q. Yang, N. A. Seifert, Y. Xu. J. Phys. Chem. A **2022**, 126, 7250–7260.

[38] H. Wang, M. Heger, M. H. Al-Jabiri, Y. Xu, Molecules **2022**, 27, 38.

[39] F. Xie, N. A. Seifert, W. Jäger, Y. Xu, Angew. Chem. Int. Ed. **2020**, 59, 15703–15710.

[40] Y. Yang, J. Cheramy, Y. Xu, ChemPhysChem **2021**, 22, 1336–1343.

[41] T. Kuppens, W. Herrebout, B. Veken, P. Bultinck, J. Phys. Chem. A **2006**, 110, 10191–10200.

[42] F. Xie, M. Fusè, A.S. Hazrah, W. Jäger, V. Barone, Y. Xu, Angew. Chem. **2020**, 132, 22613–22616.

[43] Y. Yang, A. Krin, X. Cai, M. R. Poopari, Y. Zhang, J. R. Cheeseman, Y. Xu, Molecules **2023**, 28, 771.

[44] A. Becke, Phys. Rev. A **1988**, 38, 3098–3100.

[45] C. Lee, W. Yang, R. Parr, Phys. Rev. B **1988**, 37, 785–789.

[46] M. J. Frisch, J. A. Pople, J. Chem. Phys. **1984**, 80, 3265.

[47] F. Weigend, R. Ahlrichs, Phys. Chem. Chem. Phys. **2005**, 7, 3297–3305.

[48] B. Mennucci, J. Tomasi, R. Cammi, J. R. Cheeseman, M. J. Frisch, F. J. Devlin, S. Gabriel, P. J. Stephens, J. Phys. Chem. A **2002**, 106, 6102–6113.

[49] S. Grimme, J. Antony, S. Ehrlich, H. J. Krieg, Chem. Phys. **2010**, 132, 154104

[50] D. G. A. Smith, L. A. Burns, K. Patkowski, C.D. Sherrill, J. Phys. Chem. Lett. **2016**, 7, 2197–2203.

[51] A. D. Becke, A. D. Johnson, J. Chem. Phys. **2005**, 123, 154101.

[52] P. J. Hay, W. R. Wadt, J. Chem. Phys. **1985**, 82, 299–310.

[53] R. F. W. Bader, Chem. Rev. **1991**, *91*, 893-928.

[54] C. Riplinger, P. Pinski, U. Becker, E. F. Valeev, F. Neese, J. Chem. Phys. **2016**, 144, 024109

[55] F. Neese, Software Update: The ORCA Program System—Version 5.0. WIREs Comput. Mol. Sci. **2022**, 12, e1606.

[56] M. Enamullah, M. A. Quddus, M. R. Hasan, G. Pescitelli, R. Berardozzi, G. Makhloufi, V. Vasylyeva, C. Janiak, Dalton Trans. **2016**, 45, 667–680.

[57] C. Merten, R. McDonald, Y. Xu, Inorg. Chem. **2014**, 53, 3177–3182.

[58] H. Zhang, L.-L. Zeng, Y.-K. Wang, S. Cao, D. Guo, D. Li, X.-M. Fang, L.-R. Lin, Acta Phys.-Chim. Sin. **2015**, 31, 2229–2250.

[59] T. Taniguchi, K. Monde, J. Am. Chem. Soc. **2012**, 134, 3695–3698.

[60] Hug, W. Virtual enantiomers as the solution of optical activity's deterministic offset problem. Appl. Spectrosc. **2003**, 57, 1–13.

[61] G. Li, J. Kessler, J. Cheramy, T. Wu, M. R. Poopari, P. Bouř, Y. Xu, Angew. Chem. Int. Ed. **2019**, 58, 16495–16498.

[62] L.A. Nafie, Vibrational Optical Activity: Principles and Applications; Wiley: Chichester, UK, **2011**.

[63] A. Haikarainen, J. Sipilä, P. Pietikäinen, A. Pajunen, I. Mutikainen, J. Chem. Soc. Dalton Trans. **2001**, 991–995.

[64] M. Losada, H. Tran, Y. Xu, J. Chem. Phys. **2008**, 128, 014508.

[65] S. Grimme, C. Bannwarth, P. Shushkov, J. Chem. Theory Comput. **2017**, 13, 1989–2009.

[66] H. J. Werner, P. J. Knowles, G. Knizia, F. R. Manby, M. Schütz, Wires Comput. Mol. Sci. **2012**, 2, 242–253.

[67] M. J. Frisch, G.W. Trucks, H.B. Schlegel, G. E. Scuseria, M. A. Robb, J. R. Cheeseman, G. Scalmani, V. Barone, G. A. Petersson, H. Nakatsuji, Gaussian 16; Revision, C.03; Gaussian, Inc.: Wallingford, CT, USA, **2019**.

[68] M. Katari, E. Nicol, V. Steinmetz, G. van der Rest, D. Carmichael, G. Frison, Chem. Eur. J. **2017**, 23, 8414–8423.

Chapter 6

Extraction of Pure Experimental RROA Data and Preliminary Theoretical Treatment

6.1 Introduction

Raman optical activity (ROA) measures the small intensity difference in the Raman scattering of right and left circularly polarized light from optical active molecules. As elaborated in the previous chapters, ROA measurements are often quite challenging because of the weak signals. Only one photon in a million experiences Raman scattering process. Moreover, the intensity ratio of ROA over Raman, also called circular intensity difference (CID), is typically in the order of 10^{-3}~10^{-4}.[1] To overcome the weakness of ROA signals, high concentration samples, long exposure time and instrumental optimization are required to obtain high quality ROA spectra. The necessity of large amounts of samples and long measuring time is undesirable or unachievable in some situation, and much research effort has been devoted to increase ROA signal intensity.

Despite significant improvements of instrumentation,[2] Researchers have continuously worked on developing new strategies to enhance the ROA signals. One effective approach to increase the intensity of its parent spectroscopy, i.e., Raman spectroscopy, is to operate the measurements in the resonance regime where the incident laser frequency is matches the electronic transition frequency of target molecules. The first resonance Raman experiment was carried out by Harrand and Lennuier in 1946[3] where the authors noticed a strong Raman

enhancement of a dichloronitrobenzene solution if the excitation wavelength was chosen to be in resonance with an absorption band. The phenomenon was extensively investigated both experimentally and theoretically in the following years, especially after the invention of laser. Nowadays, resonance Raman spectroscopy is a powerful tool for the study of metal-containing biological molecules, such as heme proteins.[4] Two significant advances of resonance Raman spectroscopy are its sensitivity and selectivity. For example, in the case of heme proteins, one can selectively excite the porphyrin group using laser excitation at 410 nm, and observe the associated Raman band with minimum interference of other functional groups since the others are off-resonance. To apply the same resonance Raman approach to the ROA measurements is technically challenge because of the complexity of an ROA instrument. Only a few wavelengths have been reported to be utilized successfully for ROA measurements[5] and the most common one is at 532 nm which is the one available in our research group.

In early 2010s, our research group investigated several transition metal complexes utilizing multiple chiroptical spectroscopic techniques.[6,7] While their vibrational circular dichroism spectra could be well simulated theoretically, providing rich stereochemical information including conformational distributions of these metal complexes in solution, one particular group of transition metal complexes[7] with a chiral pyrrol-2-yl Schiff-base ligand exhibits unusual 'ROA' enhancement and band patterns.[8] We will refer the chiral signals using a ROA spectrometer as $I_R - I_L$ to avoid any confusion. Very interestingly, strong $I_R - I_L$ signals originating from both the chiral solute and achiral solvent molecules were present simultaneously in the spectra. Subsequently, we re-examined all possible light-matter interactions and discovered a form of chiral Raman spectroscopy, which we called eCP-Raman.[9] This is the combination of electronic circular dichroism (ECD) and circularly polarized (CP) Raman. Upon

comparing our observation with the theoretical calculations, we found that the experimental $I_R - I_L$ spectral patterns can be fully explained by the eCP-Raman mechanism whereas the contribution by the natural resonance ROA (RROA) mechanism is negligible.[9a] Clearly, the inherent RROA signals of the chiral resonating complex are severely masked by the dominating eCP-Raman signals.

Can one extract true RROA spectra from a regular chiral Raman measurement using an ROA spectrometer? This is the main question I will address in this chapter using an example transition metal complex, (R, R)-bis(pyrrol-2-ylmethyleneamine) cyclohexane nickel(II) complex, abbreviated as RR-Ni (II) (shown in Figure 6.1). Parallel to the experimental RROA research, there have been significant theoretical efforts aiming at developing models to simulate RROA spectra adequately.[10] One difficulty is that many of the previously reported experimental RROA spectra may be contaminated with eCP-Raman contributions and erroneous conclusions might be drawn when comparing simulations to those experiments. In this chapter, some recent theoretical efforts to simulate the experimental resonance Raman and RROA spectra reported[11] here will also be discussed.

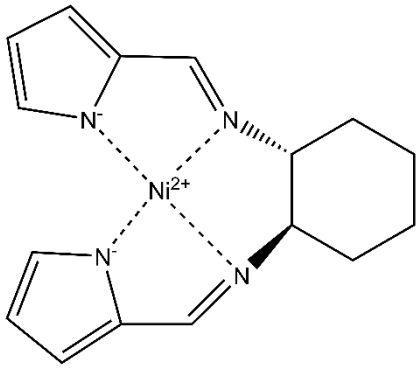

Figure 6.1. The geometry formula of the RR-Ni (II) complex.

6.2 Experimental and General Theoretical Details

Synthesis: The RR-Ni (II) complex (shown in Figure 1) was synthesized and purified based on the procedures described in Ref.[12] . All the reactant compounds were purchased from Sigma-Aldrich and used without the need for purification. The chiral ligand was synthesized by combing 2-pyrrole aldehyde and 1,2-diamino cyclohexane. Subsequently, the nickel salt was added to form the Ni (II) complex. The reaction duration is more than 7 hours to ensure its completion. Both the starting materials, ligand and final complex are air-stable. To confirm the purity of final products, mass spectrometry analysis was conducted.

Spectroscopic measurements: The Raman and ROA spectra were measured using Chiral Raman-2X^{TM} spectrometer manufactured by Bio tools company operating with a 532 nm laser excitation source. The laser power was set at 10 mW to prevent sample decomposition. The total collection time for the spectra was 50 hours. A solution of 1.0 mg of Ni complex dissolved in 1 mL of $CHCl_3$ was prepared, providing a concentration of 0.00307 M. The cell mount was adjusted 2 mm away from the laser focusing point to minimize the optical pathlength and reduce the eCP-Raman signals.

The UV-Vis and ECD spectra were obtained using a Jasco-1500 spectrometer. The concentration used was the same as the ROA measurement for the region from 400-700 nm and the path length of the sample cell was 1 mm.

Theoretical calculations: As discussed in Chapter 4, the I_R - I_L signal of a chiral solute under resonance contains two both RROA and *eCP-Raman* contributions and (near) resonance effects may significantly influence the Raman, CP-Raman, and RROA simulations. To treat the resonance effects in the Raman, CP-Raman and ROA spectra, we applied the finite-lifetime (or

damped response) approach developed and implemented by Dr. Cheeseman in the Gaussian Development Version (GDV) package.[13] While the simulations of Raman and CP-Raman require only the (electric dipole – electric dipole) polarizability tensors, α, additional electric dipole – magnetic dipole and electric dipole – electric quadrupole polarizabilities (G' and A, respectively) are needed for ROA. The fully analytic derivative implementation in the GDV include not only the differentiating the α, G' and A polarizability tensors with respect to nuclear coordinates but also as well as magnetic field dependent basis functions (GIAOs) which insure gauge origin-independent result. Overall, the analytical derivative finite-lifetime approach typically takes only about 1.5 to 2 times longer than a normal Raman and ROA calculation with Gaussian16.[14] We note that the existing finite lifetime approach still cannot fully reproduce the current experimental results. Further preliminary theoretical developments are described in the result session 6.4. Theoretical Results and Discussion.

6.3 Experimental Results and Discussion

The experimental UV-Vis and ECD spectra of the RR-Ni (II) complex are provided in Figure 6.2 The ECD spectra in the relevant region of 400-700 nm (Figure 6.2 (b)), the broad UV-Vis and ECD spectra exhibit multiple electronic transitions with (at least) three visible bands: for example, below 450 nm, negative ECD bands were observed, while at 480 nm, positive ECD bands merged. Additionally, beyond 500 nm, a rapid decay in ECD absorption is observed and ECD absorption

nears the baseline beyond 550 nm. Notably, the laser excitation frequency of 532 nm falls within the tail region of the electronic transition at 480 nm. This positioning makes the RR-Ni (II) complex a promising candidate for the extraction the RROA signals.

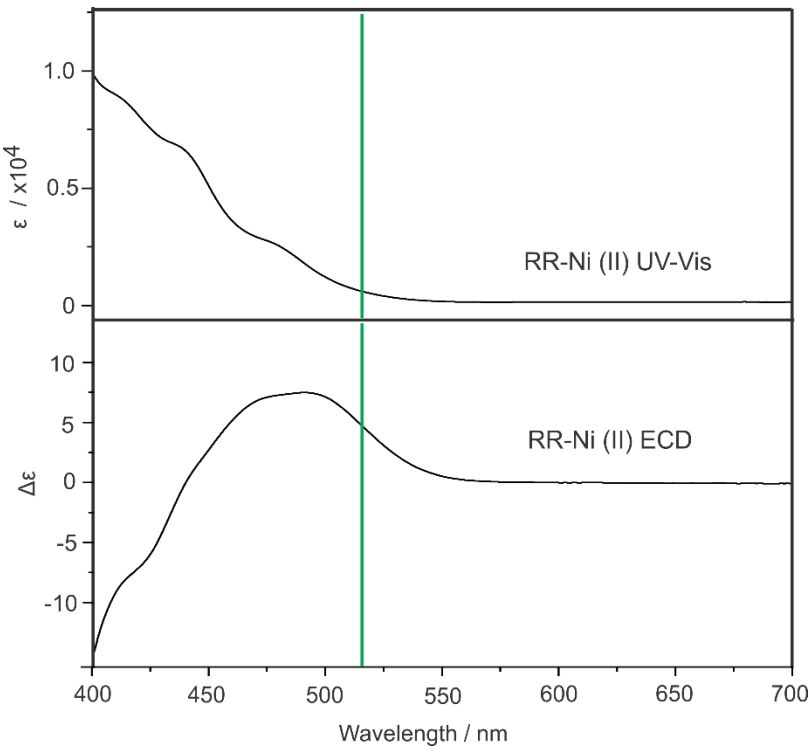

Figure 6.2. The UV-Vis and ECD spectra of RR-Ni (II) complex. The green line indicates 532 nm.

For the eCP-Raman contribution, the related CID value which is the ratio of the intensity of eCP-Raman over Raman can be calculated using equation 6.1.[8(b),9(a)]

$$CID = \frac{I_R - I_L}{I_R + I_L} = = \frac{ln10}{4}\, cL\, \Delta\varepsilon \left(\frac{\Delta\varepsilon'}{\Delta\varepsilon} + DOC \right) \qquad (6.1)$$

Here, $\Delta\varepsilon$ and $\Delta\varepsilon'$ are decadic, differential absorption coefficients for the excitation light at 532 nm and for the scattered light at each Raman band, respectively. c is the concentration of the chiral solute, L is the optical path length, DOC is the degree of circularity of the vibrational transition of interests, and I_R and I_L are the intensities of scattered RCPL and LCPL registered at the ROA instrument, respectively.

It is interesting to point out that the eCP-Raman CID of RR-Ni(II) depends on the concentration of RR-Ni(II) and also the experimental pathlength used. Since the other terms in equation 6.1 are either constants or terms associated with the molecular properties and cannot be changed easily, we focus on c and L. The aforementioned eCP-Raman CID behaves differently compared to the RROA CID which depends on the molecular properties but not the concentration of RR-Ni(II) or the pathlength. Therefore, to decrease the eCP-Raman CID and therefore the contribution of eCP-Raman relative to RROA, one needs to use as low concentration and as short pathlength as possible. On the other hand, a low concentration will lead to very low Raman, eCP-Raman and RROA intensity and one may not obtain good quality Raman and I_R -I_L spectra. The same can be said about the pathlength.

Many different concentrations and pathlength combinations were tested. The best results are given in Figure 6.3 with the raw Raman and $I_R - I_L$ spectra of RR-Ni(II) in $CHCl_3$. Some experimental details are provided in section 6.2. The optimized spectra were obtained at the concentration of 0.00307M with 2mm optical pathlength and averaging collection time is 50hrs with 10mw irradiation power. In the raw Raman spectrum, there in only one medium strength band belong to $CHCl_3$, which is marked with *. As mentioned before, the $I_R - I_L$ spectrum of RR-Ni(II) encompasses a mixture of eCP-Raman and RROA signals of RR-Ni. One therefore needs to remove the eCP-Raman contribution.

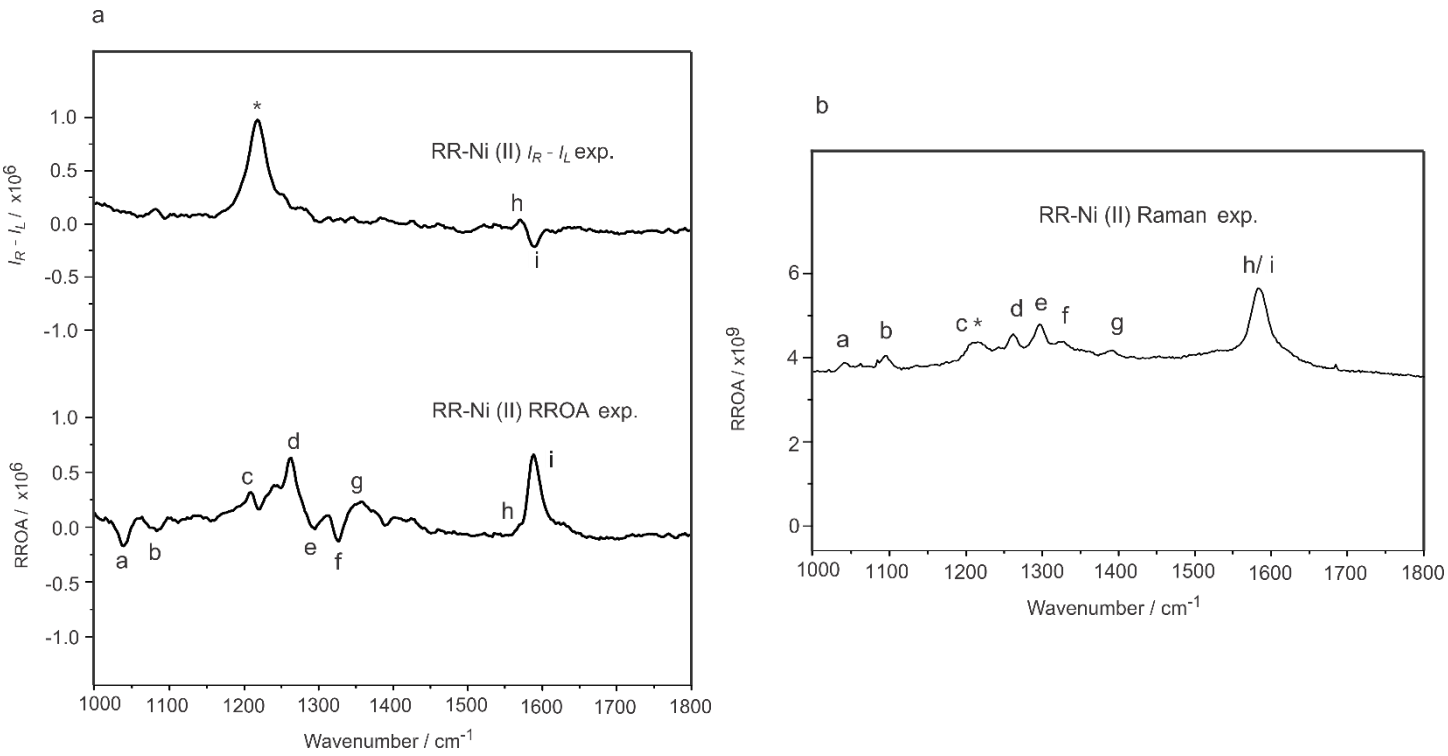

Figure 6.3. (a) The raw $I_R - I_L$ spectrum (top) and the extracted pure RROA spectrum (bottom) of the RR-Ni (II) complex. (b) The raw Raman spectrum of the RR-Ni (II) complex. The solvent signal in the raw Raman and $I_R - I_L$ spectra was labelled by asterisk.

The equation 6.1 provides a blueprint for the procedure. While it is possible to calculate the eCP-Raman CID directly using equation 6.1, the accuracy of the current theoretical modelling is simply not good enough for extracting the true RROA spectrum meaningfully. Rather, we opted to use a full experimental procedure: a) use the experimental ECD spectrum to obtain $\Delta\varepsilon$ and $\Delta\varepsilon'$ directly. The $\Delta\varepsilon$ value at 532 nm and the $\Delta\varepsilon'$ curve in the range from 532 nm to 590 nm (corresponding to 0 ~ 1850 cm^{-1} on the Raman scale) were used; b) the *DOC* plot was obtained by taking the ratio of the experimental CP-Raman and Raman spectra which were

measured directly using the ROA spectrometer; and c) the experimental concentration c and L are 0.00307 M and 0.2 cm, respectively. The experimental eCP-Raman was then obtained by multiplying the experimental Raman and the experimental eCP-Raman CID obtained. Finally, the true RROA spectrum was extracted by removing the eCP-Raman contribution from the raw $I_R - I_L$ spectrum of RR-Ni(II) in $CHCl_3$. The pure RROA spectrum is also presented in Figure 6.3. We note that a similar pure RROA spectrum of RR-Ni(II) in dichloromethane using the same subtraction procedure. The procedure employed here is also similar to that used in a recent publication.[15]

In the raw $I_R - I_L$ spectrum, the most intense band observed belong to the solvent $CHCl_3$ which is labeled with an asterisk. The only visible $I_R - I_L$ feature of the RR-Ni (II) complex is the bi-signate pattern observed at the C=O stretching region, around 1600 cm^{-1}, labelled as h and i. After removing the eCP-Raman contributions, the pure RROA spectrum reveals additional bands belonging to RR-Ni(II) and are labelled as 'a' to 'g' The spectral patterns of $I_R - I_L$ and RROA exhibit notable differences, demonstrating the significant contributions from the eCP-Raman mechanism in the raw $I_R - I_L$ spectrum, even though significant effort was made to minimize eCP-Raman contribution in the experiment. This is consistent with the conclusions draw in Chapter 4 that a typical raw $I_R - I_L$ spectrum observed for this molecular system under the usual experimental condition is dominated by eCP-Raman.[9]

There are several important points one can make about the true RROA spectrum extracted. First, this RROA spectrum contains bands of different signs, i.e., does not exhibit a mono-signate spectral feature. Based on the single electronic state (SES) theory[16] proposed by L. A. Nafie, one would expect a mono-signate RROA spectrum if the chiral system is under resonance with one electronic state. Second, the RROA CID value, i.e., the intensity ratio of

RROA versus Raman for the strongest band which corresponds to the C=N stretching at ~1600 cm^{-1} is positive, while the the dissymmetric factor g, i.e., the ratio of ECD versus UV-Vis absorption, at 532nm and 532-590nm is also positive. Based on the SES theory, one would expect the RROA CID to be $-\frac{g}{2}$, clearly the current observation is in direct contrast to this expectation.

From the experimental UV-Vis and ECD measurements, it is clear that the RR-Ni(II) complex is under resonance or near resonance at 532 nm. One may hypothesize that the invalidity of the SES theory in this context is because multiple electronic states of RR-Ni(II) are under near resonance condition at 532 nm. Indeed, a previous TDDFT calculation predicted that there are multiple electronic states which are near resonance at 532 nm.[8(a)] Currently, there are no theoretical programs which can simulate RROA spectra under the condition described accurately. In the next section, we describe some preliminary theoretical results obtained in collaboration with Drs. J. R. Cheeseman, Qin Yang, Alberto Baiardi, and Julien Bloino.

6.4 Preliminary Theoretical Results and Discussion

Another goal of this project is to utilize the existing state-of-the-art theoretical DFT calculations and verify if they can reproduce the experimental RRaman and RROA spectra of RR-Ni(II). A further goal is to explore potential new theoretical treatments in collaboration with theorists to capture the main RROA features observed experimentally.

Back in 2014, some preliminary DFT calculations of RR-Ni(II) were performed in our group using the G09 and later G16 packages. The simulated RRaman and RROA spectra patterns, i.e., both intensities and signs of bands, varied drastically as one approached resonance, at 532 nm. As it turned out, the existing DFT calculations in these packages could not deal with the

(near) resonance situation. Indeed, the resonance regime is highly challenging, especially with regard to ROA simulations. Besides the early SES theory by Nafie and others,[16,18] over the past few years, some new theoretical approaches have been reported. One hall-mark of the SES RROA is that the RROA spectrum is mono-signated, i.e., all Raman bands have the same ROA sign. Questions were raised about the possibility of multi-signated RROA when two or more electronic states are under (near) resonance conditions. For example, in the ROA study of a chiral transition metal complex, bis-(trifluoroacetylcamphorato) copper (II), abbreviated $Cu(tfc)_2$,[17] the authors reported multi-signated ROA spectrum and proposed that this was caused by having two resonance electronic states (TES), a phenomenon they termed TES-RROA, in contrast to SES. In the $Cu(tfc)_2$ case, it turned out that the observed $I_R - I_L$ spectrum is dominated by the eCP-Raman contribution, rather than by the RROA contribution.[9] In terms of theoretical developments, L. N. Vidal et al. used a fully quantum mechanical methodology to consider the excited state interference and Herzberg-Teller effects. The authors showed that such consideration allows one to produce the sign alternation and intensity enhancement in RROA spectra[18] that was not possible with the SES theory.[16] We also note that many previously reported RROA spectra are likely contaminated by the eCP-Raman contribution. This perhaps has hindered the RROA theory development, for lacking true RROA experimental spectra for comparison and guidance.

Below, we first applied the analytical derivative, finite lifetime approach implemented by Cheeseman[9a] to account for the resonance effect in Raman and ROA. As described in the previous literature,[19] the Raman polarizability and derivative terms are evaluated using equations 6.4.1 and 6.4.2. In the finite-lifetime approach, an imaginary phenomenological damping parameter γ is added to the incident frequency ω, where γ is related to the lifetime of the excited

states and to the widths of the absorption (or dispersion) peaks.

$$a_{\alpha\beta} = \frac{1}{\hbar}\sum_{m}\left[\frac{\langle g|\widehat{\mu_a}|m\rangle\langle m|\widehat{\mu_\beta}|g\rangle}{\omega_m - (\omega_I + i\gamma)} + \frac{\langle g|\widehat{\mu_\beta}|m\rangle\langle m|\widehat{\mu_a}|g\rangle}{\omega_m + (\omega_I + i\gamma)}\right] \quad (6.4.1)$$

$$\tilde{\alpha}_{\alpha\beta} = \frac{\partial a_{\alpha\beta}}{\partial R} = \frac{\partial\left\{\frac{1}{\hbar}\sum_m\left[\frac{\langle g|\widehat{\mu_a}|m\rangle\langle m|\widehat{\mu_\beta}|g\rangle}{\omega_m - (\omega_I + i\gamma)} + \frac{\langle g|\widehat{\mu_\beta}|m\rangle\langle m|\widehat{\mu_a}|g\rangle}{\omega_m + (\omega_I + i\gamma)}\right]\right\}}{\partial R} \quad (6.4.2)$$

where g represents the groud state and m is the intermediate state. γ is the damping factor. ω_m is the transition frequency of ground state and excited states. ω_I is the frequency of incident radiation.

The DFT calculations including geometry optimization, harmonic frequency, Raman, CP-Raman and ROA calculations for RR-Ni(II) were performed using the Gaussian Development Version (GDV) package.[13] Raman, DOC, and ROA polarizability tensors were calculated at 532 nm using the finite-lifetime (or damped response) approach mentioned above. The fully analytic derivative implementation in GDV includes magnetic field dependent basis functions (GIAOs). The optimized geometry and harmonic frequencies of RR-Ni(II) were computed at the B3LYP/aug-cc-pVTZ level of theory. The Raman and ROA polarizability tensors (532nm) were computed at the B3LYP/ aug(sp)-cc-pVDZ level of theory. First, we tested the sensitivity of the results to the value of the damping parameter, γ. The calculations were performed with three different γ values at 988 cm^{-1}, 880 cm^{-1}, and 550 cm^{-1} and the results are summarized below in

Figure 6.4. The three different γ values give more or less the same results for Raman and CP-Raman, while some differences are noted for ROA, especially in the lower wavenumber region.

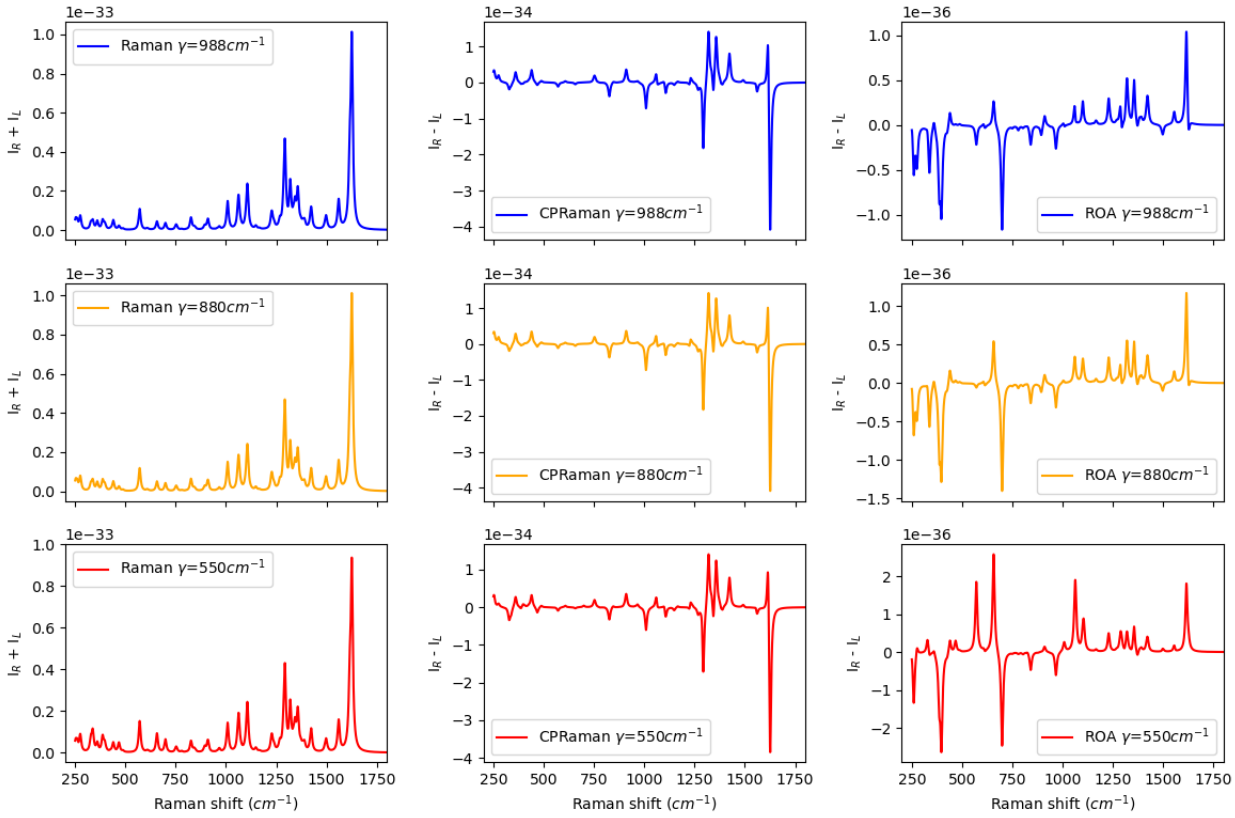

Figure 6.4. Calculated Raman, CP-Raman and ROA of RR-Ni(II) at 532 nm with different values for γ. Calculated $I_R + I_L$ and $I_R - I_L$ are displayed in units of [m^2 cm/sr] where m is meter and sr is steridian. CP-Raman was computed as $(I_R + I_L)$*DOC.

We note that a γ value of 880 cm^{-1} was suggested by others[19] for such calculations and among the three γ values used, γ = 880 cm^{-1} gives the closest agreement to the RROA experiment. Another level of theory, B3LYP/aug-cc-pVDZ, was also applied for the calculations of the Raman and

ROA polarizability tensors (532 nm). As can be seen in Figure 6.5, these two basis sets predict essentially identical spectra.

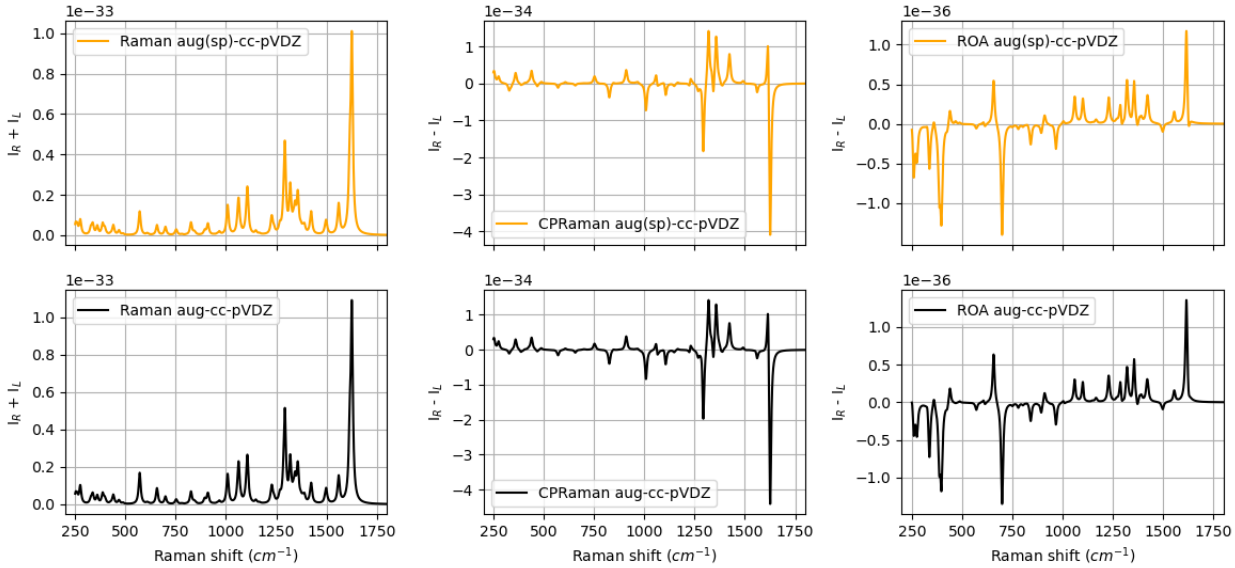

Figure 6.5. Calculated Raman, CP-Raman and ROA of *R*-**Ni** at 532 nm with two different basis sets. Calculated $I_R + I_L$ and $I_R - I_L$ are in m^2 cm/sr.

Figure 6.6 presents a comparison between the experimental RRaman and RROA spectra and the corresponding simulated spectra using the finite lifetime approach. The finite lifetime calculation provides satisfactory agreement with the experimental RRaman spectrum. For the RROA spectrum, the positive and most intense feature at 1600 cm^{-1} was reproduced, as well as several other features like bands d and g. On the other hand, several bands at lower wavenumber region such as a to c exhibit the opposite sign compared to the experimental observation. These bands are mostly associated to the C-H wagging and C-H scissoring from the five-member pyrrole ring.

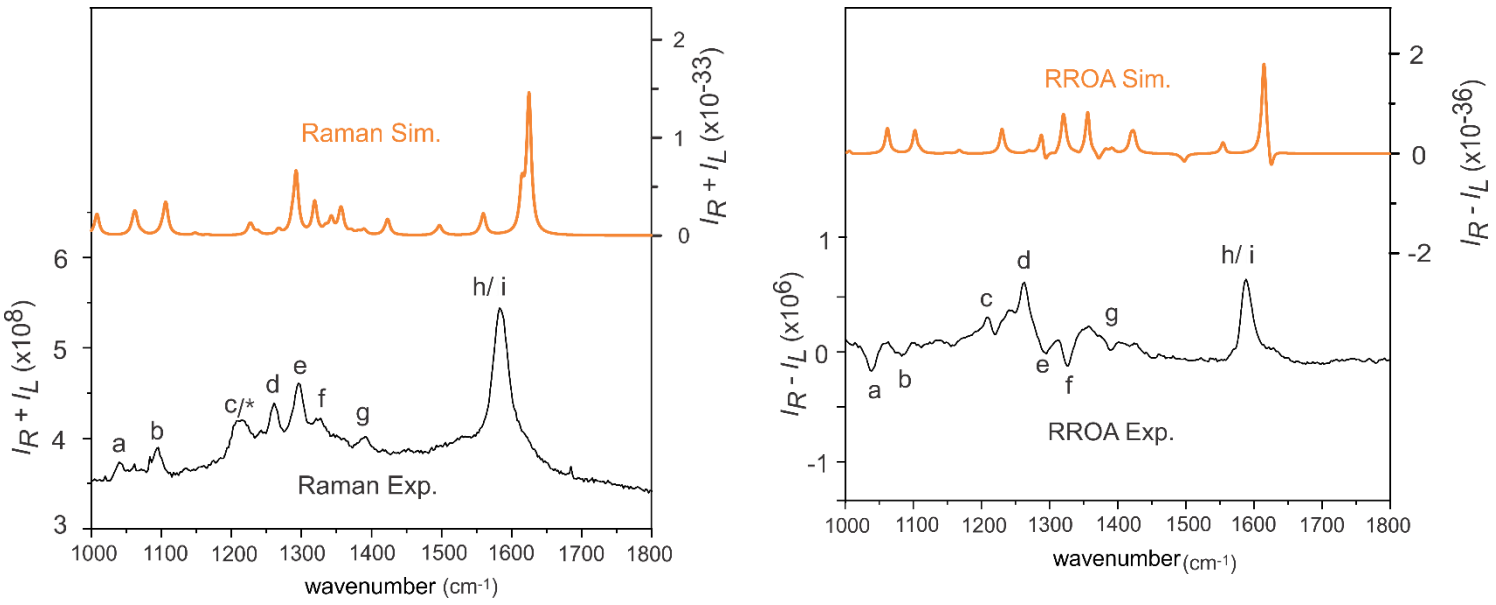

Figure 6.6. Comparison of the finite lifetime RRaman and RROA spectra of RR-Ni(II) at 532 nm with the experimental ones. The γ value was set at 880 cm^{-1}.

In the finite lifetime approach used above, the excited state vibrational contributions for state(s) in strong resonance is missing. To include the vibrational levels of the ground and excited state(s) m for under strong resonance conditions, we turn to another method known as vibronic coupling approach.[20,21,22] The formalism of the Raman polarizability in vibronic coupling approach is provided in equation (6.4.3)

$$\tilde{\alpha}_{\alpha\beta} = \frac{1}{\hbar}\sum_{ev}\left[\frac{\langle\psi_{g1}|\langle g|\widehat{\mu_a}|e\rangle|\psi_{ev}\rangle\langle\psi_{ev}|\langle e|\widehat{\mu_\beta}|g\rangle|\psi_{g0}\rangle}{\omega_{ev,g0} - (\omega_0 + i\gamma_{ev})}\right.$$

$$\left. + \frac{\langle\psi_{g1}|\langle g|\widehat{\mu_\beta}|e\rangle|\psi_{ev}\rangle\langle\psi_{ev}|\langle e|\widehat{\mu_a}|g\rangle|\psi_{g0}\rangle}{\omega_{ev,g1} + (\omega_0 + i\gamma_{ev})}\right] \quad (6.4.3)$$

where g0, ev, g1 are the intial state, intermediate state and final state. In the vibronic coupling approach, the initial and final states are both the ground state, and the vibrational levels are included in states g0, ev and g1 and the number of intermediate states ev also needs to be chosen. In contrast, the vibrational levels of the ground and excited states are not considered in the finite lifetime approach. Therefore, under strong resonance conditions, the vibronic method is expected to provide a good description since it includes the vibrational levels of the ground and excited states (m). Some preliminary calculations were performed with this approach (not shown) and they do not agree well with the experimental data. This is perhaps not surprising since the experimental RRaman and RROA spectra of RR-Ni(II) appear to be not under strong resonance, rather under near resonance, although currently there is no clear understanding on what defines the near resonance condition, especially for RROA.

A further direction explored by our theoretical collaborators is to combine the two approaches described above. It is acknowledged that the near resonance contributions are typically not included in the vibronic approach. At the same time, while the finite lifetime approach includes the near resonance contributions, it is missing the excited state vibrational contributions for states in strong resonance, whose contributions may become more significant if the excited state geometries differ from the ground state geometry. Therefore, combining these two approaches may help to capture all the important factors which govern the RROA pattern of RR-Ni(II).

It is recognized that one cannot just add the finite lifetime Raman polarizability to the vibronic Raman polarizability for the state(s) ev, as the finite lifetime polarizability already includes contributions from the state(s) ev. To avoid such double counting, it was proposed that the contributions from these states can be subtracted off by computing the contribution from the

state(s) ev using the sum over states expression involving the transition moments above. The expression for the Raman polarizability, which includes resonance and near resonance contributions is provided in equation 6.4.4:

$$\tilde{\alpha}_{vibronic+NR} = \sum_{m} \tilde{\alpha}_{vibronic} + \left(\tilde{\alpha}_{finite-lifetime} - \sum_{m} \tilde{\alpha}_{transition-moment} \right) \quad (6.4.4)$$

Currently further theoretical calculations in this direction are being pursued and the final results will be written up in a forthcoming joint publication.[11]

6.5 Conclusion

In conclusion, we extracted the pure RROA signals of the RR-Ni(II) complex from the raw I_R – I_L spectrum, which originally contains a mixture of small RROA and dominant eCP-Raman contributions. Guided by the eCP-Raman equation, we optimized the experimental considerations so that one could extract true RROA by subtracting the contribution of eCP-Raman off. The same RROA spectra of RR-Ni(II) were obtained using two different solvent solutions, confirming that these features belong to the Ni(II) complex, rather than solvents. Interestingly, the RROA features are not mono-signated. Since the existing ROA calculation program offered in the electronic structure calculation packages, such as G16, can not deal with (near) resonance ROA cases, new theoretical approaches were sought after. The finite lifetime approach by Cheeseman was utilized and good and reasonable agreements with the experimental RRaman and ROA spectra were achieved, respectively. The importance of including vibronic coupling was also discussed. A new approach which combines the finite lifetime and the vibronic

coupling approach was proposed to simulate RRaman and RROA spectra. Further theoretical effort in this direction is being pursued.

References

[1] L. A. Nafie, Vibrational Optical Activity: Principles and Applications, John Wiley & Sons, Ltd., UK, **2011.**

[2] (a) W. Hug, Appl. Spectrosc. **2003**, 57, 1-13. (b) J. Kapitán, L. D. Barron, L. Hecht, J. Raman Spectrosc. **2015**, 46, 392-399.

[3] M. Harrand, R. Lennuier, Comptes Rendus Academie des Sciences **1946**, 223, 356-359.

[4] E. V. Efremov, F. Ariese, C. Gooijer, Anal. Chim. Acta, **2008**, 606, 119-134.

[5] (a) Y. Zhang, P. Wang, G. Jia, F. Cheng, Z. Feng, C. Li, Appl. Spectrosc. **2017**, 71(9), 2211-2217. (b) L. A. Nafie, B. E. Brinson, X. Cao, D. A. Rice, O. M. Rahim, R. K. Dukor, N. J. Halas, Appl. Spectrosc. **2007**, 61, 1103-1106. (c) M. Unno, T. Kikukawa, M. Kumauchi, N. Kamo, J. Phys. Chem. B **2013**, 117, 1321-1325.

[6] (a) Z. Dezhahang, C. Merten, M. R. Poopari, Y. Xu, Dalton Trans. **2012**, 41, 10817-10824; (b) Z. Dezhahang, M. R. Poopari, Y. Xu, J. Mol. Struct. **2012**, 1024, 123−131; (c) C. Merten, K. Hiller, Y. Xu, Phys. Chem. Chem. Phys. **2012**, 14, 12884-12891; (d) C. Merten, Y. Xu, Dalton Trans. **2013**, 42, 10572-10578; (e) C. Merten, R. McDonald, Y. Xu, Inorg. Chem. **2014**, 53, 3177-3182.

[7] Z. Dezhahang, M. Poopari, J. Cheramy, Y. Xu, Inorg. Chem. **2015**, 54, 4539-4549.

[8] (a) G. Li, J. Kessler, J. Cheramy, T. Wu, M. R. Poopari, P. Bouř, Y. Xu, Angew. Chem. Int. Ed. **2019**, 58, 16495-16498. (b) T. Wu, G. Li, J. Kapitán, J. Kessler, Y. Xu, P. Bouř, Angew. Chem. Int. Ed. **2020**, 59, 21895-21898.

[9] (a) G. Li, M. Alshalalfeh, Y. Yang, J. R. Cheeseman, P. Bouř, Y. Xu, Angew. Chem. Int. Ed. **2021**, 60, 22004-22009. (b) G. Li, M. Alshalalfeh, J. Kapitán, P. Bouř, Y. Xu, Chem, Eur. J. **2022**, e202104302.

[10] (a) S. Luber, J. Neugebauer, M. Reiher, J. Chem. Phys. **2010**, 132, 044113. (b) F. Krausbeck, J. Autschbach, M. Reiher, J. Phys. Chem. A **2016**, 120, 9740 – 9748. (c) J. Mattiat, S. Luber, J. Chem. Phys. **2019**, 151, 234110/1 – 16. (d) L. Abella, H. D. Ludowieg, J. Autschbach, Chirality **2020**, 32, 741 – 752.

[11] G. Li, Q. Yang, M. Alshalalfeh, A. Baiardi, J. Bloino, J. R. Cheeseman, Y. Xu, to be published.

[12] X. F. Shan, D. H. Wang, C. H. Tung, L. Z. Wu, Tetrahedron **2008**, 64, 5577-5582.

[13] M. J. Frisch, et al., Gaussian development version, Gaussian, Inc., Wallingford, CT, **2020**.

[14] M. J. Frisch, et al., Gaussian 16, Revision C.01, Gaussian, Inc., Wallingford, CT, **2016**.

[15] T. Wu, J. Kapitán, P. Bour, J. Phys. Chem. Lett. **2022**, 13, 3873-3877.

[16] L. A. Nafie, Chem. Phys. **1996**, 205, 309-322.

[17] C. Merten, H. Li, L. A. Nafie, J. Phys. Chem. A **2012**, 116, 7329-7336.

[18] L. N. Vidal, T. Giovannini, C. Cappelli, J. Phys. Chem. Lett. **2016**, 7, 3585-3590.

[19] (a) L Jensen, J. Autschbach, M. Krykunovc, G.C. Schatz J. Chem. Phys. **2007**, 127, 134101. (b) L. A. Nafie, Theor. Chem. Acc. **2008**, 119. 39-55.

[20] T. Holtum, J. Bloino, C. Pappas, V. Kumar, V. Barone, S. Schlücker, J. Raman Spectrosc. **2021**, 52. 2292-2300.

[21] (a) A. Baiardi, J. Bloino, V. Barone, J. Chem. Theory Comput. **2013**, 9, 4097-4115. (b) A. Baiardi, J. Bloino, V. Barone, J. Chem. Phys. **2014**, 141, 114108. (c) A. Baiardi, J. Bloino, V. Barone, J, Chem Theory Comput. **2018**, 14, 6370-6390.

[22] A. Baiardi, C, Latouche, J, Bloino, V. Barone, Dalton Trans **2014**, 43, 17610-17614.

Chapter 7

Conclusions and Future work

7.1 Conclusions

During my PhD research, I have explored mainly novel phenomena associated with Raman and chiral Raman responses under (near) resonance condition. Intense chiral Raman signals, i.e., $I_R - I_L$ signals, of achiral solvent were observed in several sets of experiments carried out using a Raman optical activity spectrometer with a wide range of solvents and with several chiral transition metal complexes. These intense induced solvent chiral Raman responses eventually led to the discovery of a new type of chiral Raman spectroscopy which we termed eCP-Raman, a combination of electronic circular dichroism and circularly polarized Raman spectroscopy. The discovery of eCP-Raman for chiral species under resonance led to the realization that many previously reported resonance Raman optical activity (RROA) spectra may be severely contaminated by eCP-Raman. Furthermore, I addressed the important issue of how to obtain a true RROA spectrum by subtracting the contribution of eCP-Raman under a suitable experimental condition. In addition, novel theoretical treatments of RROA were proposed and pursued, in collaboration with several prominent theorists in this exciting research area. Several different chiroptical spectroscopic techniques which include electronic circular dichroism (ECD), vibrational circular dichroism (VCD) and ROA were utilized, together with extensive theoretical calculations for systematic conformational searches, geometry optimizations, harmonic frequency calculations and spectral simulations.

In Chapter 3, I observed a unique chiral transfer effect from the chiral Ni (II) complex to the achiral solvent molecules. Two possible mechanisms were proposed to explain the strong induced ROA signals observed for achiral solvent molecules. The first mechanism known as the "ring of fire", explains the occurrence of intense chiral Rayleigh scattering where the resonating transition metal complex manifests itself as molecular plasmons. The "ring of fire" model successfully captures the main achiral solvent ROA spectral patterns such as signs and relative intensities. However, this model underestimates the magnitudes of these induced ROA signals and fails to explain the results obtained for the Cu (II) complex. Consequently, after examination of various light matter interactions, a second mechanism was proposed, which is due to the combination of ECD absorption and circularly polarized (CP) Raman, termed eCP-Raman effect. By incorporating the eCP-Raman effect into our simulations, we were able to accurately reproduce not only the signs and relative intensities but also the absolute intensities of the observed ROA bands.

In Chapter 4, I extended the applications of eCP-Raman effects to the chiral solute molecules under resonance. We analyzed the I_R - I_L spectra of two transition metal complexes, namely Ni (II) and Cu (II), along with one organic molecule called S-BN. Interestingly, while the Cu (II) complex and S-BN exhibited a mono-signate I_R - I_L spectra, which is the hallmark of RROA spectra. The theoretical RROA calculations employing the finite lifetime approach do not align with the experimental spectra. However, the theoretical eCP-Raman spectra of all the candidates reproduced the observed I_R - I_L spectral patterns, indicating that the I_R - I_L signals solely stemmed from the eCP-Raman event without no contributions from the inherent RROA. This finding highlights the significance of the eCP-Raman effect in interpreting the experimental I_R - I_L spectra and emphasizes the needs to distinguish it from RROA signals.

In Chapter 5, I investigated the stereochemical properties of two Schiff based transition metal complexes and their corresponding ligand. Multiple spectroscopic tools, including IR/VCD, UV-Vis/ECD, and Raman/eCP-Raman were employed to explore these properties. The comparison between the experimental and simulated IR, VCD, UV-Vis and ECD spectra of the ligand yielded good agreement, enabling the identification of three main ligand conformers in solution. Notably, the remarkable sensitivity of VCD to the conformations associated with the tertbutyl groups played a crucial role in this identification process. The helicity of transition metal complexes was determined to be M for those with the (R, R) ligands and to be P with the (S, S) ligands. Furthermore, eCP-Raman measurements were performed on the two transition metal complexes under (near) resonance. Their induced solvent chiral Raman features were explained, and the potential application of eCP-Raman was discussed.

In Chapter 6, I focused on the extraction of pure RROA signals from the initially mixed I_R - I_L spectra of Ni (II) complex, which were predominantly composed of eCP-Raman contributions. By comparing the experimental results with the corresponding theoretical calculations, I have confidently identified and acquired the pure RROA spectrum of RR-Ni complex. In addition, I have demonstrated two theoretical approaches: finite lifetime method[1] and finite lifetime plus vibronic coupling method.[2] Both methods were employed to simulate RRaman and RROA spectra. The newly generated simulated results provide strong evidence that the consideration of vibronic coupling effect is crucial for accurately reproducing the major spectral patterns of RROA spectrum of system under resonance conditions. We believe that the combined approach of finite lifetime and vibronic coupling approach are necessary to RROA calculations.

7.2 Future work

Throughout the work reported in this thesis, it has become evident that chiroptical spectroscopy offers unique advantages, including high sensitivity in absolute configuration determination and conformational analysis. However, it is important to note the existing limitations, such as the accuracy of theoretical calculations. In particular, simulating ROA spectra under resonance conditions poses significant challenges, as elaborated in Chapters 5 and 6. With the experimental route established in the current thesis work, one can now obtain true experimental RROA spectra. This success has inspired new theoretical treatments of RROA.

Still, to capture the resonance effect properly continues to be highly challenging and much more work will be needed to achieve the final goal. In future work, it is crucial to obtain experimentally more RROA spectra, especially to include RROA spectra of a variety of chiral molecules beyond transition metal complexes, for example organic molecules with various organic chromophores[3] and biomolecules. The extensive experimental data set would be crucial to offer comparison with the theoretical simulation results, assisting the development of new theoretical treatments of RROA.

Second, the experimental RROA spectra reported in this thesis were obtained with the chiral molecules under near resonance condition, rather than resonance condition. How to treat different degree of near resonance is still very much under research currently. Very often, multiple electronic states are under near resonance condition, making it extremely difficult to achieve quantitative simulations which can capture the experimental data properly. The combination of the finite lifetime and the vibronic coupling models seem to be important to capture both on-resonance and near resonance effects.

Additionally, anharmonic frequency calculations can enhance the accuracy of band

positions and intensities in the Raman[4] and ROA[2(c)] spectra. It would be beneficial to include anharmonic effects even though the computational cost associated with them could be high.

As described in this thesis, ROA is a relatively weak process. Strong efforts[5] have been devoted to modifying chiral systems in order to amplify the chiral optical response signals. One goal is to explore metal nanoparticles, for example gold and silver nanoparticle, for enhancement of ROA, in a similar fashion as what has been done with surface enhanced Raman spectroscopy. Good quality experimental data would facilitate meaningful comparisons between experimental and theoretical results.

References

[1] (a) L. Jensen, J. Autschach, M. Krykunovc, G. C. Schatz, J. Chem. Phys. **2007**, 127, 134101. (b) L. A. Nafie, Theor. Chem. Acc. **2008**, 119, 39-55. (c) T. Helgaker, S. Coriani, P. Jørgensen, K. Kristensen, J. Olsen, K. Ruud, Chem. Rev. **2012**, 112, 543-631.

[2] (a) A. Baiardi, J. Bloino, V. Barone, J. Chem. Theory Comput. **2013**, 9, 4097-4115. (b) A. Baiardi, J. Bloino, V. Barone, J. Chem. Phys. **2014**, 141, 114108. (c) A. Baiardi, J. Bloino, V. Barone, J, Chem Theory Comput. **2018**, 14, 6370-6390.

[3] (a) C. Johannessen, P. C. White, S. Abdali, J. Phys. Chem. A **2007**, 111, 32, 7771-7776. (b) R. Sgammato, W. Herrebout, C. Johannessen, J. Raman Spectrosc. **2019**, 50, 1905-1913.

[4] T. Holtum, J. Bloino, C. Pappas, V. Kumar, V. Barone, S. Schlücker, J. Raman Spectrosc. **2021**, 52. 2292-2300.

[5] (a) S. Abdali, C. Johannessen, J. Nygaard, T. Nørbygaard, J. Phys. Condens. Matter **2007**, 19, 285205. (b) S. O. Pouř, L. Rocks, K. Faulds, D. Graham, V. Parchaňský, P. Bouř, E. W. Blanch, Nat. Chem. **2015**, 7, 591 – 596.

Bibliography

[1] L. Pasteur, Ann, Chim. Phys. **1848**, 24, 442-459.

[2] Y. G. Shi, Cell, **2014**, 159, 995-1014.

[3] L. Maveyraud, L. Mourey, Molecules, **2020**, 25, 1030

[4] N. K. Thakral, R. L. Zanon, R. C. Kelly S. Thakral, J. of Pharm. Sci. **2018**, 107, 2969-2982.

[5] N. Berova, L.D. Bari, G. Pescitelli, Chem. Soc. Rev. **2007**, 36, 914-931.

[6] G. Pescitelli, T. Bruhn, Chirality, **2016**, 28, 466-474.

[7] A. S. Perera, J. Thomas, M. R. Poopari, Y. Xu, Front. Chem. **2016**, 4, 1-17.

[8] L. A. Nafie, Vibrational Optical Activity: Principles and Applications, John Wiley & Sons, Ltd., UK, **2011.**

[9] L. D. Barron, Molecular light scattering and optical activity, 2nd edn. Cambridge, **2004**.

[10] R. Sgammato, W. Herrebout, C. Johannessen, J. Raman Spectrosc. **2019**, 50, 1905-1913.

[11] A. S. Perera, J. Cheramy, C. Merten, J. Thomas, Y. Xu, ChemPhysChem. **2018**, 19, 2234-2242.

[12] Y. Yang, J. Cheramy, M. Brehm, Y. Xu, ChemPhysChem. **2022**, doi.org/10.1002/-cphc.202200161.

[13] M. R. Poopari, Z. Dezhahang, Y. Xu, Spectrochim. Acta Mol. Biomol. Spectrosc. **2013**, 136, 131-140.

[14] G. Li, D. Li, M. Alshalalfeh, J. Cheramy, H. Zhang, Y. Xu, Molecules **2023**, 28, 2571.

[15] S. Bellemin-Laponnaz, S. Dagorne, Chem. Rev. **2014**, 114, 8747-8774.

[16] V. W. W. Yam, A. S. Y. Law, Coord. Chem. Rev. **2018**, 367, 127-162.

[17] J. Karges, Angew. Chem. Int. Ed. **2022**, 61, e202112236.

[18] M. Enamullah, M. A. Quddus, M. R. Hasan, G. Pescitelli, R. Berardozzi, G. Makhloufi, V.

Vasylyeva, C. Janiak, Dalton Trans. **2016**, 45, 667-680.

[19] Z. Dezhahang, M. R. Poopari, J. Cheramy, Y. Xu, Inorg. Chem. **2015**, 54, 4539-4549.

[20] C. Merten, K. Hiller, Y. Xu, Phys. Chem. Chem. Phys. **2012**, 14, 12884-12891.

[21] S. Luber, M. Reiher, Chem. Phys. **2008**, 346, 212-223.

[22] C. Mertem. H. Li, X. Lu, A. Hartwig, L. A. Nafie, J. Raman Spec. **2010**, 41, 1563-1565.

[23] L. Nafie, Chem. Phys. **1996**, 205, 309-322.

[24] M. Vargek, T. B. Freedman, E. Lee, L. A. Nafie, Chem. Phys. Lett. **1998**, 287, 359-364.

[25] G. Zajac, A. Kaczor, S. Buda, J. Mlynarski, J. Frelek, J. C. Dobrowolski, M. Baranska, J. Phys. Chem. B **2015**, 119, 12193-12201.

[26] M. Dudek, E. Machalska, T. Oleszkiewicz, E. Grzebelus, R. Baranski, P. Szczśnisk, J. Mlynarski, G. Zajac, A. Kaczor, M. Baranska, Angew. Chem. Int. Ed. **2019**, 58, 8383-8388.

[27] J. Bogaerts, C. Johannessen, J. Raman Spec. **2019**, 50, 641-646.

[28] C. Merten, H. Li, L. A. Nafie, J. Phys. Chem. A. **2012**, 116, 7329-7336.

[29] K. Ruud, T. Helgaker, P. Bour. J. Phys. Chem. A. **2002**, 106, 7449-7455.

[30] S. Luber, J. Neugebauer, M. Reiher, J. Chem. Phys. **2010**, 132, 044113.

[31] L. Jensen, J. Autschbach, M. Krykunov, G. C. Schatz, J. Chem. Phys. **2007**, 127, 134101.

[32] T. Helgaker, S. Coriani, P. Jørgensen, K. Kristensen, J. Olsen, K. Ruud, Chem. Rev. **2012**, 112, 543-631.

[33] M. Losada, Y. Xu, Phys. Chem. Chem. Phys. **2007**, 9, 3127-3135.

[34] S. O. Pour, L. Rocks, K. Faulds, D. Graham, V. Parchaňský, P. Bouř, E. W. Blanch, Nature Chem. **2015**, 7, 591-596.

[35] S. Yamamoto, P. Bouř, J. Comput. Chem. **2013**, 34, 2152-2158.

[36] V. Novák, M. Dendisová, P. Matějka, P. Bouř, J. Phys. Chem. C **2016**, 120, 18275-18280.

[37] V. Novák, J. Šebestík, P, Bouř, J. Chem. Theory Comput. **2012**, 8, 1714-1720.

[38] G. Li, J. Kessler, J. Cheramy, T. Wu, M. R. Poopari, P. Bouř, Y. Xu, Angew. Chem. Int. Ed. **2019**, 58, 16495-16498.

[39] P. Pracht, F. Bohle, S. Grimme, Phys. Chem. Chem. Phys. **2020**, 22, 7169-7192.

[40] F. Xie, N. A. Seifert, M. Heger, J. Thomas, W. Jäger, Y. Xu, Phys. Chem. Chem. Phys. **2019**, 21, 15408-15416.

[41] S. Oswald, N. A. Seifert, F. Bohle, M. Gawrilow, W. Jäger, Y. Xu, M. A. Suhm. Angew. Chem, Int, Ed. **2019**, 58, 5080-5084.

[42] C. D. Carlson, A. S. Hazrah, D. Mason, Q. Yang, N. A. Seifert, Y. Xu, J. Phys. Chem. A **2022,** 126, 7250-7260.

[43] H. Wang, M. Heger, M. H. Al-Jabiri, Y. Xu, Molecules, **2022**, 27, 38.

[44] F. Xie, N. A. Seifert, W. Jäger, Y. Xu, Angew. Chem. Int. Ed. **2020**, 59, 15703-15710.

[45] Y. Yang, J. Cheramy, Y. Xu, ChemPhysChem **2021**, 22, 1336-1343.

[46] T. Kuppens, W. Herrebout, B. Veken, P. Bultinck, J. Phys. Chem. A **2006**, 110, 10191-10200.

[47] F. Xie, M. Fusè, A. S. Hazrah, W. Jäger, V. Barone, Y. Xu. Angew Chem Int. Ed. **2020**, 132, 22613-22616.

[48] Y. Yang, A. Krin, X. Cai, M. R. Poopari, Y. Zhang, J. R. Cheeseman, Y. Xu, Molecules. **2023**, 28, 771. https://doi.org/10.3390/molecules28062571.

[49] F. Xie, N. A. Seifert, A. S. Hazrah, W. Jäger, Y. Xu, ChemPhysChem **2021**, 22, 455-460.

[50] J. Thomas, O. Sukhorukov, W. Jäger, Y. Xu, Angew. Chem. Int. Ed. **2013**, 52, 4402-4405.

[51] C. Merten, Y. Xu, Angew. Chem. Int. Ed. **2013**, 52, 2073−2076.

[52] G. Yang, Y. Xu, Phys. Chem. Chem. Phys. **2008**, 10, 6787−6795.

[53] M. R. Poopari, Z. Dezhahang, G. Yang, Y. Xu, ChemPhysChem **2012**, 13, 2310−2321.

[54] Y. Yang, X. Sun, M. R. Poopari, C. Jian, H. Zeng, T. Tang, Y. Xu, ChemPhysChem **2022**, doi.org/10.1002/cphc.202200608.

[55] G. Yang, Y. Xu, J. Chem. Phys. **2009**, 130, 164506/1-9.

[56] A. S. Perera, C. D. Carlson, J. Cheramy, Y. Xu, Chirality **2023**, 1-14. DOI: 10.1002/-chir.23576.

[57] A. S. Perera, J. Cheramy, M. R. Poopari, Y. Xu, Phys. Chem. Chem. Phys. **2019**, 21, 3574-3584.

[58] M. Losada, P. Nguyen, Y. Xu, J. Phys. Chem. A **2008**, 112, 5621−5627.

[59] M. R. Poopari, P. Zhu, Z. Dezhahang, Y. Xu, J. Chem. Phys. **2012**, 137, 194308/1−7.

[60] L. A. Nafie, T. B. Freedman, R. K. Dukor, "Vibrational Circular Dichroism", In Handbook of Vibrational Spectroscopy, John Wiley & Sons, Ltd., UK, **2002.**

[61] R. K. Dukor, L. A. Nafie, "Vibrational Optical activity of pharmaceuticals and biomolecules", In Encyclopedia of Analytical Chemistry, John Wiley & Sons, Ltd., UK, **2000.**

[62] G. E. Tranter, "Protein Structure Analysis by CD, FTIR, and Raman Spectroscopies", In Encyclopedia of Spectroscopy and Spectrometry, Oxford: Academic Press. UK, **2017.**

[63] G. Placzek in handbuch der Radiologie, Vol. 6 (Ed.: E. Marx), Akademische Verlagsgesellscharft, Leipzig, **1934.** P. 205.

[64] H. G. Kuball "Chiroptical Analysis" In Encyclopedia of Analytical Science, Elsevier Ltd. NL, **2005.**

[65] N. Harada, N. Berova, "Separations and Analysis" In Comprehensive Chirality, Elsevier Ltd. NL, **2012.**

[66] L. D. Long, The Raman Effect: A Unified Treatment of the Theory of Raman Scattering by Molecules. John Wiley & Sons, Ltd., UK, **2002**.

[67] R. Clark, S. R. Jeyes, A. J. McCaffery, R. A. Shatwell, J. Am. Chem. Soc. **1974**, 96. 5586-5588.

[68] G. Li, M. Alshalalfeh, J. Kapitán, P. Bouř, Y. Xu, Chem. Eur. J. **2022**, e202104302

[69] G. Li, M. Alshalalfeh, Y. Yang, J. Cheeseman, P. Bouř, Y. Xu, Angew. Chem. Int. Ed. **2021**, 60, 22004-22009.

[70] T. Wu, G. Li, J. Kapitán, J. Kessler, Y. Xu, P. Bouř, Angew. Chem. Int. Ed. **2020**, 59, 21895-21898.

[71] E. Machalska, G. Zajac, A. J. Wierzba, J. Kapitán, T. Andruniow, M. Spegel, D. Gryko, P. Bouř, M. Baranska, Angew. Chem. Int. Ed. **2021**, 60, 21205-21210.

[72] S. Abdali, E. W. Blanch, Chem. Soc. Rev. **2008**, 3, 980-992.

[73] S. O. Pour, S. E. J. Bell, E. W. Blanch, Chem. Comm. **2011**, 47, 4754-4756.

[74] S. Abdali, C. Johannessen, J. Nygaard, T. Nørbygaard, J. Phys.: Condens. Matter **2007**,19, 285205.

[75] L. D. Barron, A. D. Buckingham, Mol. Phys. **1971,** 20, 1111-1119.

[76] L. D. Barron, M. P. Bogaard, A. D. Buckingham, J. Am. Chem. Soc. **1973**, 95, 603-605.

[77] W. Hug, S. Kint, G. F. Bailey, J. R. Scherer, J. Am. Chem. Soc. **1975**, 97, 5589-5590.

[78] W. Hug, H. Surbeck, Chem. Phys. Lett. **1979**, 60, 186-192.

[80] L. D. Barron, L. Hecht, W. Hug, M. J. Maclntosh, J. Am. Chem. Soc. **1989**, 111, 8731-8732.

[81] L. A. Nafie, T. B. Freedman, Chem. Phys. Lett. **1989**, 154, 260-266.

[82] D. Che, L. Hecht, L. A. Nafie, Chem. Phys. Lett. **1991**, 180, 182-190.

[83] W. Hug, G. Hangartner, J. Raman Spectrosc. **1999**, 30, 841-852.

[84] W. Hug, Appl. Spectrosc. **2003**, 57, 1-13.

[85] J. Cheramy, Master Thesis. **2016**.

[86] R. Sgammato, W. Herrebout, C. Johannessen, J. Raman Spectrosc. **2019**, 50, 1905-1913.

[87] G. Zajac, A. Kaczor, A. P. Zazo, J. Mlynarski, M. Dudek, M. Baranska, J. Phys. Chem. B **2016**, 120, 4028-4033.

[88] M. Dudek, G. Zajac, A. Kaczor, M. Baranska, J. Raman, Spectrosc. **2017**, 48, 673-679.

[89] G. Zajac, J. Lasota, M. Dudek. A. Kaczor, M. Baranska, Spectrochim. Acta A Mol. Biomol. Spectrosc. **2017**, 173, 356-360.

[90] T. Wu, J. Kapitán, P. Bouř, J. Phys. Chem. Lett. **2022**, 13, 3873-3877.

[91] C. Merten, Y. Xu, ChemPhysChem **2013**,14, 213−219.

[92] P. Pracht, F. Bohle, S. Grimme, Phys. Chem. Chem. Phys., 2020,22, 7169-7192.

[93] E. G. Schnitzler, N. A. Seifert, S. Ghosh, J. Thomas, Y. Xu, W. Jäger, Phys. Chem. Chem. Phys. **2017**, 19, 4440-4446

[94] N. A. Seifert, J. Thomas, W. Jäger, Y. Xu, Phys. Chem. Chem. Phys. **2018**, 20, 27630-27637

[95] M. D. Marshall, H. O. Leung, S. R. Domingos, A. Krin, M. Schnell, N. A. Seifert, Y. Xu, W. Jäger, Phys. Chem. Chem. Phys. **2022**, 24, 28495-28505

[96] J. Thomas, I. Peña, C. Carlson, Y. Yang, W. Jäger, Y. Xu, Phys. Chem. Chem. Phys. **2020**, 22, 23019-23027.

[97] Z. Su, Y. Xu, Angew. Chem. Int. Ed. **2007**, 46, 6163−6166.

[98] J. Thomas, X. Liu, W. Jäger, Y. Xu, Angew. Chem. Int. Ed. **2015**, 54, 11711-11715.

[99] A. N. Mort, F. Xie, A. S. Hazrah, C. D. Carlson, Y. Xu, Phys. Chem. Chem. Phys. **2023**, 25, 16264-16272.

[100] B. Wu, N. A. Seifert, A. Insausti, J. Ma, S. Oswald, W. Jäger, Y. Xu, Phys. Chem. Chem. Phys. **2022**, 24, 14975-14984.

[101] F. Weigend, R. Ahlrichs, Phys. Chem. Chem. Phys. **2005**, 7, 3297-3305.

[102] S. Grimme, J. Antony, S. Ehrlich, H. Krieg, J. Chem. Phys. **2010**, 132, 154104.

[103] D. G. A. Smith, L. A. Burns, K. Patkowski, C. D. Sherrill, J. Phys. Chem. Lett. **2016**, 7, 2197-2203.

[104] H. J. Werner, P. J. Knowles, G. Knizia, F. R. Manby, M. Schütz, Molpro: Wires Comput. Mol. Sci. **2012**, 2, 242-253.

[105] M. J. Frisch, G.W. Trucks, H. B. Schlegel, G. E. Scuseria, M. A. Robb, J. R. Cheeseman, G. Scalmani, V. Barone, G. A. Petersson, H. Nakatsuji, et al. Gaussian 16, Revision C.03; Gaussian, Inc.: Wallingford, CT, **2019**.

[106] C. Bannwarth, E. Caldeweyher, S. Ehlert, A. Hansen, P. Pracht, J. Seibert, S. Spicher, S. Grimme, WIREs Comput. Mol. Sci. **2021**, 11, e1493.

[107] A.V. Onufriev, D. A. Case, Annu. Rev. Biophys. **2019**, 48, 275−296.

[108] M. Alshalalfeh, N. Sun, A. H. Moraes, A. P. A. Utani, Y. Xu, Molecules **2023**. 28, 4013. https://doi.org/10.3390/molecules28104013.

[109] A. D. Becke, J. Chem. Phys. **1993**, 98, 5648-5652.

[110] C. Lee, W. Yang, R. G. Parr, Phys. Rev. B. **1988**, 37, 785.

[111] T. Yanai, D. P. Tew, N. C. Handy, Chem. Phys. Lett. **2004**, 393, 51-57.

[112] A.D. Becke and E.R. Johnson, J. Chem. Phys. **2005**, 123, 154101.

[113] Z. Dezhahang, M. R. Poopari, F. E. Hernández, C. Diaz, Y. Xu Phys. Chem. Chem. Phys. **2014**, 16, 12959−12967.

[114] C. Merten, Y. Xu, Dalton Trans. **2013**, 42, 10572−10578.

[115] J. Tomeček, P. Bouř, J. Chem. Theory Comput. **2020**, 16, 2627-2634.

[116] R. Ditchfield, W. J. Hehre, J. A. Pople, J. Chem. Phys. **1971**, 54, 724-728.

[117] R. Krishnan, J. S. Binkley, R. Seeger, J. A. Pople, J. Chem. Phys. **1980**, 72, 650-654.

[118] T. M. Dunning, J. Chem. Phys. **1989**, 90, 1007-1023.

[119] F. Weigend, F. Furche, R. Ahlrichs, J. Chem. Phys. **2003**, 119, 12753-12762.

[120] P. J. Hay, W. R. Wadt, J. Chem. Phys. **1985**, 82, 270-283.

[121] S. Chiodo, N. Russo, E. Sicilia, J. Chem. Phys. **2006**, 125, 104107.

[122] L. Pasteur, Théses de chimie et de physique, Bachelier, Paris, **1847.**

[123] J. Haesler, I. Schindelholz, E. Riguet, C. G. Bochet, W. Hug, Nature **2007**, 446, 526-529.

[124] A. Baiardi, J. Bloino, V. Barone, J. Chem. Theory Comput. **2018**, 14, 6370-6390.

[125] J. Šebestík, J. Kapitán, O. Pačes, P. Bouř, Angew. Chem. Int. Ed. **2016**, 55, 3504-3508.

[126] K. Osinka, M. Pecul, A. Kudelski, Chem. Phys. Lett. **2010**, 496, 86 – 90.

[127] C. Johannessen, P. C. White, S. Abdali, J. Phys. Chem. A **2007**, 111, 7771 – 7776.

[128] R. Shimada, H. Kano, H. Hamaguchi, J. Chem. Phys. **2008**, 140, 204506.

[129] K. A. Willets, R. P. VanDuyne, Annu. Rev. Phys. Chem. **2007**, 58, 267 – 297

[130] S. Y. Ding, E. M. You, Z. Q. Tian, M. Moskovits, Chem. Soc. Rev. **2017**, 46, 4042 – 4076.

[131] Y. Liu, G. Yang, M. Losada, Y. Xu, J. Chem. Phys. **2010**, 132, 234513/1-11.

[132] Z. Liu, J. Ai, P. Kumar, E. You, X. Zhou, X. Liu, Z. Tian, P. Bouř, Y. Duan, L. Han, N. Kotov, S. Ding, S. Che, Angew. Chem. Int. Ed. **2020**, 59, 15226-15231.

[133] J. R. Cheeseman, M. J. Frisch, J. Chem. Theory Comput. **2011**, 7, 3323 – 3334.

[134] L. N. Vidal, T. Giovannini, C. Cappelli, J. Phys. Chem. Lett. **2016**, 7, 3585 – 3590.

[135] K. D. Chapkin, L. Bursi, G. J. Stec, A. Lauchner, N. J. Hogan, Y. Cui, P. Nordlander, N. J. Halas, Proc. Natl. Acad. Sci. USA **2018**, 115, 9134 – 9139.

[136] C. Zong, M. Xu, L. J. Xu, T. Wei, X. Ma, X. S. Zheng, R. Hu, B. Ren, Chem. Rev. **2018**, 118, 4946 – 4980.

[137] A. D. Laurent, D. Jacquemin, Int. J. Quantum Chem. **2013**, 113, 2019 – 2039

[138] H. H. Falden, K. R. Falster-Hansen, K. L. Bak, S. Rettrup, S. P. A. Sauer, J. Phys. Chem. A **2009**, 113, 11995 – 12012.

[139] Y. Zhang, M. R. Poopari, X. Cai, A. Savin, Z. Dezhahang, J. Cheramy, Y. Xu, J. Nat. Prod.

2016, 79, 1012 – 1023.

[140] E. Debie, L. Jaspers, P. Bultinck, W. Herrebout, B. V. D. Veken, Chem. Phys. Lett. **2008**, 450, 426 – 430.

[141] P. Bouř, J. Chem. Phys. **2007**, 127, 136101.

[142] B. G. Janesko, G. E. Scuseria, J. Chem. Phys. **2006**, 125, 124704.

[143] S. Luber, C. Herrmann, M. Reiher, J. Phys. Chem. B **2008**, 112, 2218 – 2232.

[144] T. Wu, J. Kapitán, V. Mašek, P. Bouř, Angew. Chem. Int. Ed. **2015**, 54, 14933–14936.

[145] J. L. Lunkley, D. Shirotani, K. Yamanari, S. Kaizaki, G. Muller, J. Am. Chem. Soc. **2008**, 130, 13814-13815.

[146] L. D. Barron, Biomed. Spectrosc. Imaging **2015**, 4, 223 – 253.

[147] M. Krupová, J. Kessler, P. Bouř, ChemPlusChem **2020**, 85, 561 – 575.

[148] S. Haraguchi, M. Hara, T. Shingae, M. Kumauchi, W. D. Hoff, M. Unno, Angew. Chem. Int. Ed. **2015**, 54, 11555 – 11558.

[149] E. Machalska, G. Zajac, M. Baranska, D. Kaczorek, R. Kawęcki, P. F. J. Lipiński, J. E. Rode, J. Dobrowolski, Chem. Sci. **2021**, 12, 911 – 916.

[150] S. Luber, M. Reiher, ChemPhysChem **2010**, 11, 1876 – 1887.

[151] F. Krausbeck, J. Autschbach, M. Reiher, J. Phys. Chem. A **2016**, 120, 9740 – 9748.

[152] L. Abella, H. D. Ludowieg, J. Autschbach, Chirality **2020**, 32, 741 – 752.

[153] G. L. J. A. Rikken, E. Raupach, Nature **1997**, 390, 493 – 494.

[154] K. M. Nicholas, Inorg. Chim. Acta **1976**, 20, L42.

[155] X. F. Shan, D. H. Wang, C. H. Tung, L. Z. Wu, Tetrahedron **2008**, 64, 5577-5582.

[156] M. J. Frisch, et al., Gaussian development version, Gaussian, Inc., Wallingford, CT, **2020**.

[157] J. Sadlej, J. C. Dobrowolski, J. E. Rode, Chem. Soc. Rev. **2010**, 39, 1478 – 1488.

[158] T. Wu, J. Kessler, P. Bouř, Phys. Chem. Chem. Phys. **2016**, 18, 23803 – 23811.

[159] W. Hug, G. Zuber, A. de Meijere, A. F. Khlebnikov, H.-J. Hansen, *Helv. Chim. Acta* **2001**, 84, 1-21.

[160] L. A. Nafie, *Theor.* Chem. Account, **2008**, *119*, 39-55.

[161] T. Helgaker, S. Coriani, P. Jørgensen, K. Kristensen, J. Olsen, K. Ruud, Chem. Rev. **2012**, 112, 543-631.

[162] J. L. Segura, M. J. Mancheño, F. Zamora, Chem. Soc. Rev. **2016**, 45, 5635-5671.

[163] M. N. Uddin, S. S. Ahmed, S. M. Rahatul Alam, J. Coord. Chem. **2020**, 73, 3109-3149.

[164] M. S. More, P.G. Joshi, Y. K. Mishra, P. K. Khanna, Mater. Today Chem. **2019**, 14 100195.

[165] S. De, A. Jain, P. Barman, ChemistrySelect **2022**, 7, e202104334.

[166] M. K. Goshisht, G. K. Patra, N. Tripathi, Mater. Adv. **2022**, 3, 2612-2669.

[167] F. S. Alamro, S. M. Gomha, M. Shaban, A. S. Altowyan, T. Z. Abolibda, H. A. Ahmed, Sci. Rep. **2021**, 11, 15046. https://doi.org/10.1038/s41598-021-94533-6

[168] S. N. Shariff, S. Saravu, D. Ramakrishna, IntechOpen, London, **2022**. DOI: http://dx.doi.org/ 10.5772/intechopen.107904.

[169] A. Gualandi, F. Calogero, S. Potenti, P. G. Cozzi, Molecules, **2019**, 24, 1716.

[170] Z.-W. Li, X. Wang, L.-Q. Wei, I. Ivanović-Burmazović, G.-F. Liu, J. Am. Chem. Soc. **2020**, 142, 7283-7288.

[171] R. Mazzoni, F. Roncaglia, L. Rigamonti, Crystals **2021**, 11, 483.

[172] A. Trujillo, M. Fuentealba, D. Carrillo, C. Manzur, J. R. Hamon, J. Organomet. Chem. **2009**, 694, 1435–1440.

[173] G. Pescitelli, L.D. Bari, N. Berova, Chem. Soc. Rev. **2011**, 40, 4603–4625.

[174] G. Pescitelli, S. Lüdeke, A. C. Chamayou, M. Marolt, V. Justus, M. Górecki, L. Arrico, L. Di

Bari, M. A. Islam, I. Gruber, Inorg. Chem. **2018**, 57, 13397–13408.

[175] M. Górecki, M. Enamullah, M. A. Islam, M. K. Islam, S. P. Höfert, D. Woschko, C. Janiak, G. Pescitelli, Inorg. Chem. **2021**, 60, 14116–14131

[176] T. Wu, X. Z. You, P. Bouř. Coord. Chem. Rev. **2015**, 284, 1–18.

[177] P. Zhu, G. Yang, M. R. Poopari, Z. Bie, Y. Xu, ChemPhysChem **2012**, 13, 1272–1281.

[178] C. Merten, C. J. Berger, R. McDonald, Y. Xu, Angew. Chem. Int. Ed. **2014**, 53, 9940–9943.

[179] G. Yang, Y. Xu, Top. Curr. Chem. **2011**, 298, 189–236.

[180] E. Machalska, N. Hachlica, G. Zajac, D. Carraro, M. Baranska, G. Licini, P. Bouř, C. Zonta, A. Kaczor, Phys. Chem. Chem. Phys. **2021**, 23, 23336–23340.

[181] E. Machalska, G. Zajac, M. Baranska, P. Bouř, D. Kaczorek, R. Kawecki, J. E. Rode, K. Lyczko, J. C. Dobrowolski, Chem. Comm. **2022**, 58, 4524.

[182] N. Harada, K. Nakanishi, Univ Science Books: Mill Valley, CA, USA, **1983**.

[183] T. Taniguchi, D. Manai, M. Shibata, Y. Itabashi, K. Monde, J. Am. Chem. Soc. **2015**, 137, 12191–12194.

[184] M. A. J. Koenis, L. Visscher, W. J. Buma, V. P. Nicu, J. Phys. Chem. B **2020**, 124, 1665–1677.

[185] Z. Dezhahang, M. R. Poopari, Y. Xu. Chem. Asian J. **2013**, 8, 1205–1212.

[186] A. Becke, Phys. Rev. A **1988**, 38, 3098–3100.

[187] M. J. Frisch, J. A. Pople, J. Chem. Phys. **1984**, 80, 3265.

[188] B. Mennucci, J. Tomasi, R. Cammi, J. R. Cheeseman, M. J. Frisch, F. J. Devlin, S. Gabriel, P. J. Stephens, J. Phys. Chem. A **2002**, 106, 6102–6113.

[189] A. D. Becke, A. D. Johnson, J. Chem. Phys. **2005**, 123, 154101.

[190] R. F. W. Bader, Chem. Rev. **1991**, *91*, 893-928.

[191] C. Riplinger, P. Pinski, U. Becker, E. F. Valeev, F. Neese, J. Chem. Phys. **2016**, 144, 024109

[192] F. Neese, Software Update: The ORCA Program System—Version 5.0. WIREs Comput. Mol. Sci. **2022**, 12, e1606.

[193] M. Enamullah, M. A. Quddus, M. R. Hasan, G. Pescitelli, R. Berardozzi, G. Makhloufi, V. Vasylyeva, C. Janiak, Dalton Trans. **2016**, 45, 667–680.

[194] H. Zhang, L.-L. Zeng, Y.-K. Wang, S. Cao, D. Guo, D. Li, X.-M. Fang, L.-R. Lin, Acta Phys.-Chim. Sin. **2015**, 31, 2229–2250.

[195] A. Haikarainen, J. Sipilä, P. Pietikäinen, A. Pajunen, I. Mutikainen, J. Chem. Soc. Dalton Trans. **2001**, 991–995.

[196] M. Losada, H. Tran, Y. Xu, J. Chem. Phys. **2008**, 128, 014508.

[197] M. Katari, E. Nicol, V. Steinmetz, G. van der Rest, D. Carmichael, G. Frison, Chem. Eur. J. **2017**, 23, 8414–8423.

[198] J. Kapitán, L. D. Barron, L. Hecht, J. Raman Spectrosc. **2015**, 46, 392-399.

[199] M. Harrand, R. Lennuier, Comptes Rendus Academie des Sciences **1946**, 223, 356-359.

[200] E. V. Efremov, F. Ariese, C. Gooijer, Anal. Chim. Acta, **2008**, 606, 119-134.

[201] Y. Zhang, P. Wang, G. Jia, F. Cheng, Z. Feng, C. Li, Appl. Spectrosc. **2017**, 71(9), 2211-2217.

[202] L. A. Nafie, B. E. Brinson, X. Cao, D. A. Rice, O. M. Rahim, R. K. Dukor, N. J. Halas, Appl. Spectrosc. **2007**, 61, 1103-1106.

[203] M. Unno, T. Kikukawa, M. Kumauchi, N. Kamo, J. Phys. Chem. B **2013**, 117, 1321-1325.

[204] Z. Dezhahang, C. Merten, M. R. Poopari, Y. Xu, Dalton Trans. **2012**, 41, 10817-10824.

[205] Z. Dezhahang, M. R. Poopari, Y. Xu, J. Mol. Struct. **2012**, 1024, 123−131.

[206] C. Merten, R. McDonald, Y. Xu, Inorg. Chem. **2014**, 53, 3177-3182.

[207] J. Mattiat, S. Luber, J. Chem. Phys. **2019**, 151, 234110/1 – 16.

[208] G. Li, Q. Yang, M. Alshalalfeh, A. Baiardi, J. Bloino, J. R. Cheeseman, Y. Xu, to be published.

[209] T. Wu, J. Kapitán, P. Bour, J. Phys. Chem. Lett. **2022**, 13, 3873-3877.

[210] L. A. Nafie, Theor. Chem. Acc. **2008**, 119. 39-55.

[211] T. Holtum, J. Bloino, C. Pappas, V. Kumar, V. Barone, S. Schlücker, J. Raman Spectrosc. **2021**, 52. 2292-2300.

[212] A. Baiardi, J. Bloino, V. Barone, J. Chem. Theory Comput. **2013**, 9, 4097-4115.

[213] A. Baiardi, J. Bloino, V. Barone, J. Chem. Phys. **2014**, 141, 114108.

[214] A. Baiardi, C, Latouche, J, Bloino, V. Barone, Dalton Trans **2014**, 43, 17610-17614.

Appendix A: Supporting information for Chapter 3

Materials and Methods

ROA Experiments: Raman and ROA spectra were measured using a ChiralRaman-2X^{TM} spectrometer (BioTools) operating with a 532 nm laser excitation source. Typically, 3.0 mg of the Ni complex was dissolved in 200 μL of solvent, providing a concentration of ~0.02 M. For certain solvents, the Ni complex could not be dissolved at this ratio and saturated solutions were formed. The sample was irradiated using a laser power of 30-50 mW (at the source) for about 25 hours, which corresponds to 65536 accumulation scans. The solvents included acetone, methanol (CH_3OH and CD_3OD), dichloromethane (DCM), chloroform ($CHCl_3$ and $CDCl_3$), dimethyl sulfoxide (DMSO and DMSO-d_6), acetonitrile (ACN-d_3), benzene, 2-butanol (both *R* and *S* enantiomers), and carbon tetrachloride. Raman spectra of the Ni (II) complex in $CDCl_3$ were also measured at the 633 nm and 785 nm excitation wavelengths using an in-Via confocal Raman microscope (Renishaw). For these two wavelengths, the concentration of the Ni complex was the same as for the 532 nm experiment and 10 scans were performed for each.

Synthesis: The Ni (II) complex was synthesized and purified according to procedures described in Ref.[1] All reactant compounds were purchased from Sigma-Aldrich and used without purification. Briefly, 2-pyrole aldehyde and 1,2-diamino cyclohexane yielded the chiral ligand, then the nickel perchlorate salt ($Ni(ClO_4)_2 \cdot 6H_2O$) was added in order to obtain the final Ni (II) complex. The reaction time was over 10 hours, to ensure that the reaction was completed. Both the ligand and the complex are air stable. Mass spectrometry analysis was performed to confirm the purity of the reaction products.

Model Computations: The density functional theory (DFT) calculations were performed using the Gaussian16 software package.[2] The B3LYP[3] and CAM-B3LYP[4] functionals provided very similar results. In trial computations, the aug-cc-pVTZ and 6-311++G(2df,2pd) basis sets provided almost identical results, whereas a basis set size increase from 6-311++G** to 6-311++G(2df,2pd) provided minor improvements in the simulated spectra. Therefore, the 6-311++G(2df,2pd) basis set was used as a default. The observed functional and basis set dependence is consistent with previous studies.[5] The solvent environment was modeled using the polarizable continuum model (PCM).[6] In some computations the LanL2DZ[7] effective core potential and basis set was used for Ni, which again provided very similar results as the full basis set model. The B3LYP/6-311++G(2df,2pd)/PCM ROA polarizabilities (tensors α, G' and A, cf. Ref.[8]) were used as input parameters for the transition polarizability model (TPM) as described in the Figure A8.

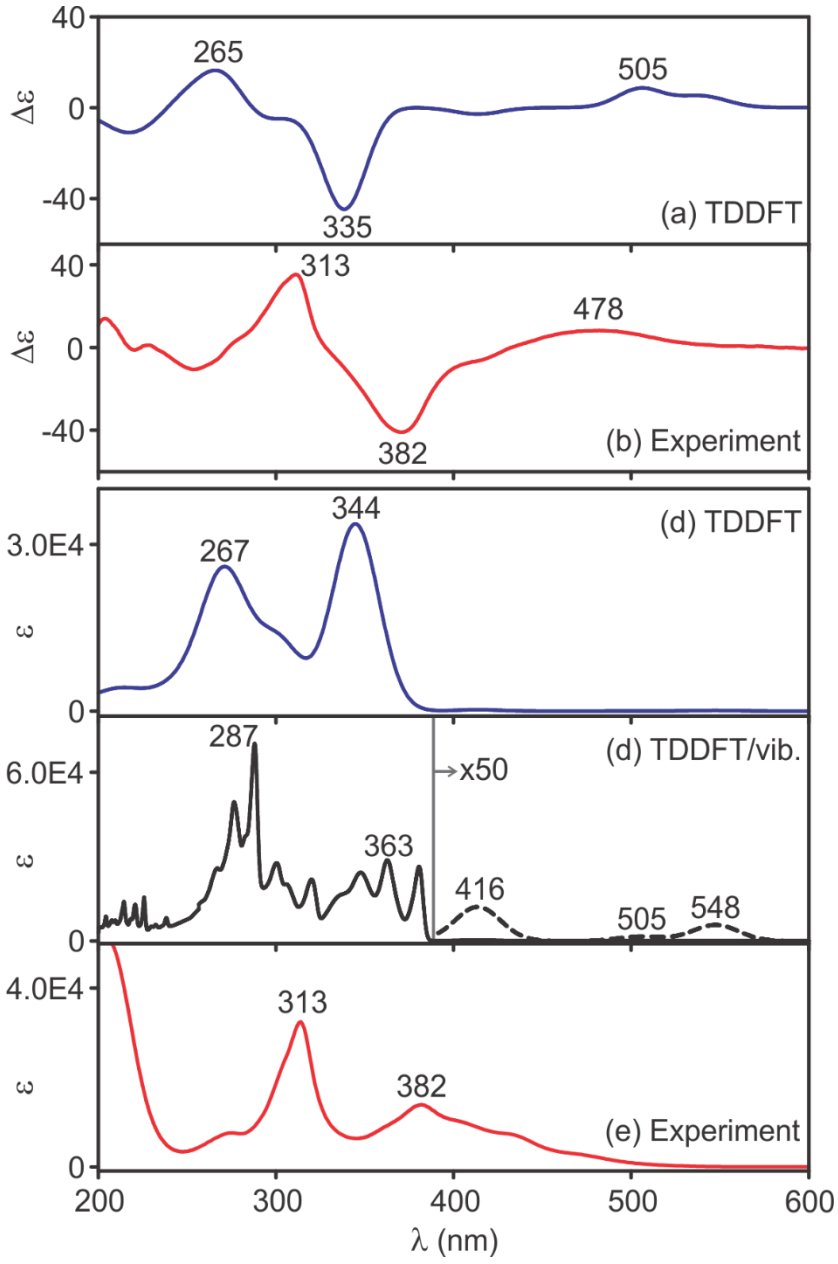

Figure A1. CD (a,b) and absorption (c,d,e) spectra of the (*R,R*)-Ni complex. The TDDFT computations (a,c,d) were performed at the CAM-B3LYP/6-311++G**/PCM($CHCl_3$) level. The vibrational substructure of some bands in the absorption spectrum (d) was calculated at the harmonic level; for electronic bands with very different ground and excited state geometries, Gaussian profiles were used with a 30 nm full width at half maximum.

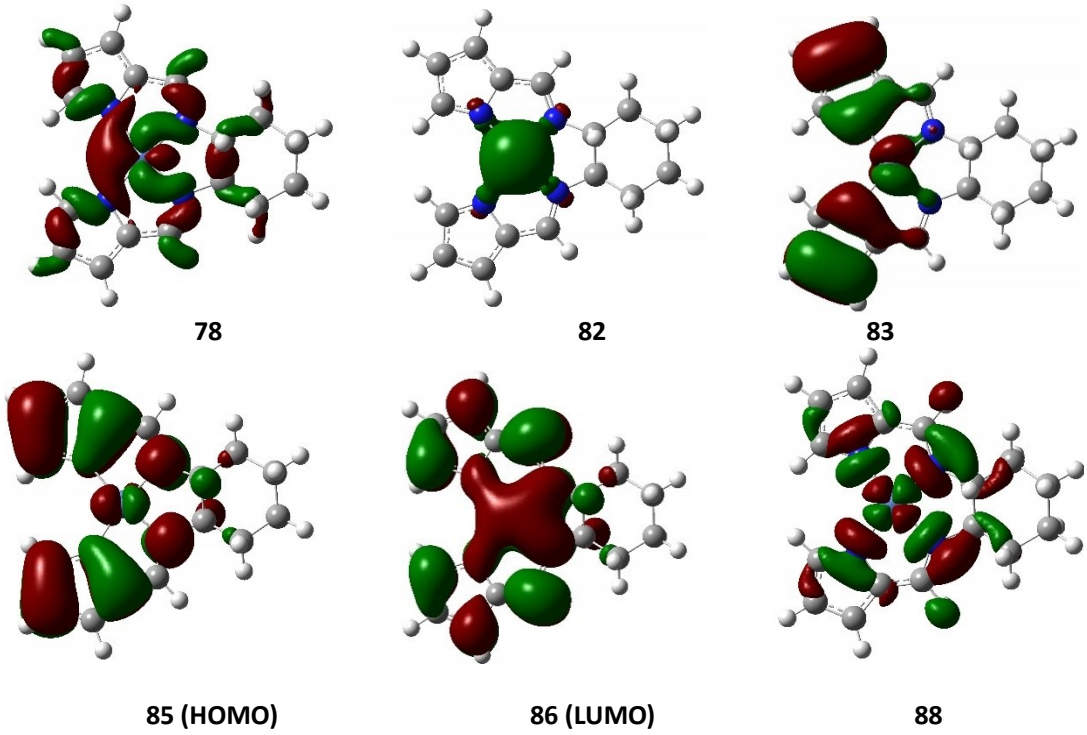

Figure A2. Boundary orbitals of the (*R,R*)-Ni complex at the B3LYP/6-311++G** level of theory.

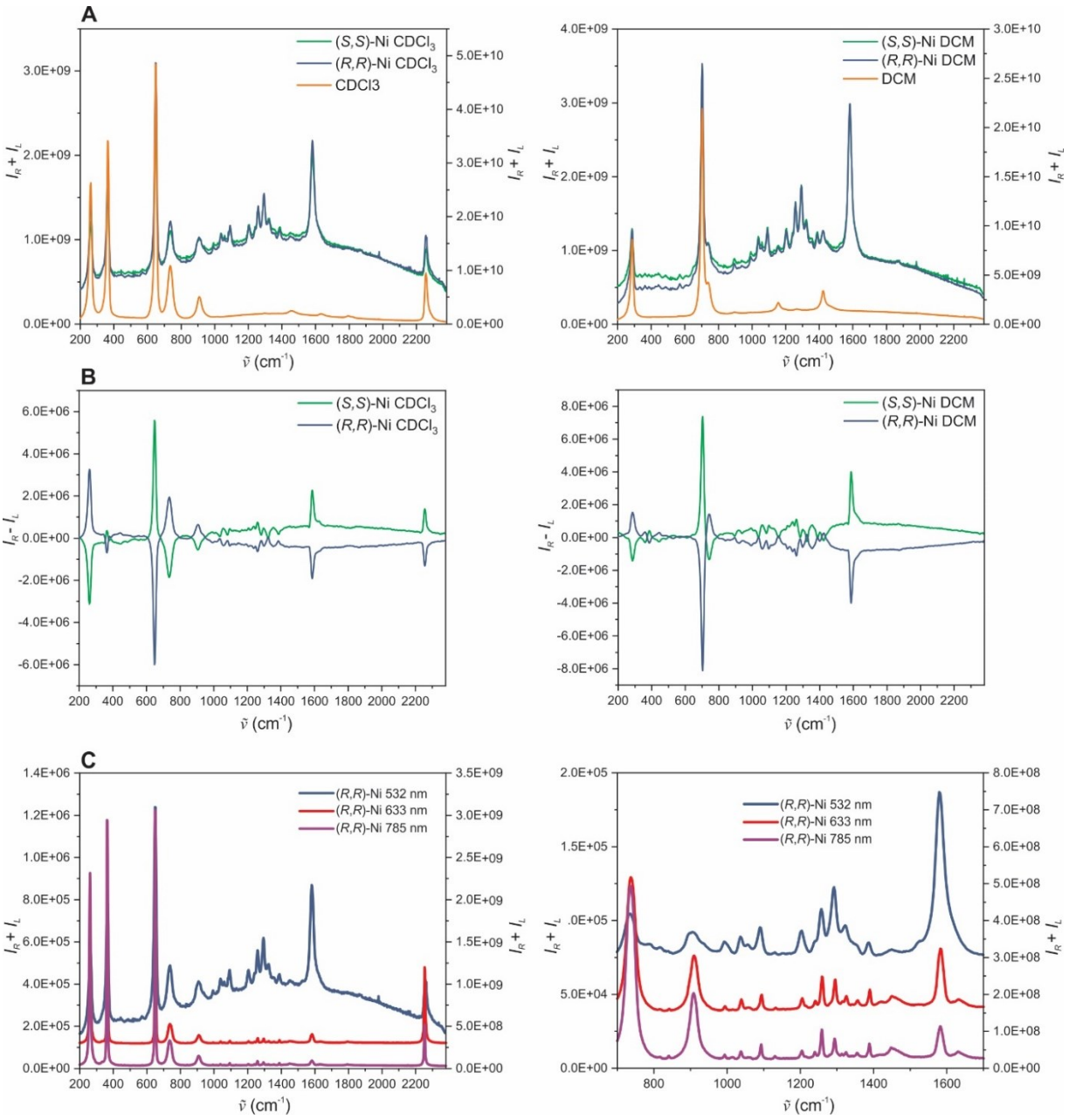

Figure A3. A) Raw experimental Raman spectra of the (*R*,*R*)-Ni and (*S*,*S*)-Ni complex in $CDCl_3$ and in DCM (left $I_R + I_L$ axis) and Raman spectra of the pure solvents (right $I_R + I_L$ axis), measured at the 532 nm laser excitation. B) Raw experimental ROA spectra of the (*R*,*R*)-Ni and (*S*,*S*)-Ni complex in $CDCl_3$ and in DCM measured at the 532 nm laser excitation. C) Raman spectra of the (*R*,*R*)-Ni complex in $CDCl_3$ at the three excitation wavelengths: 532 nm (right $I_R +$

I_L axis), 633 nm and 785 nm (left $I_R + I_L$ axis). In the zoom-in window (right), the 532 nm spectrum is baseline corrected for easier comparison of the recorded spectral features.

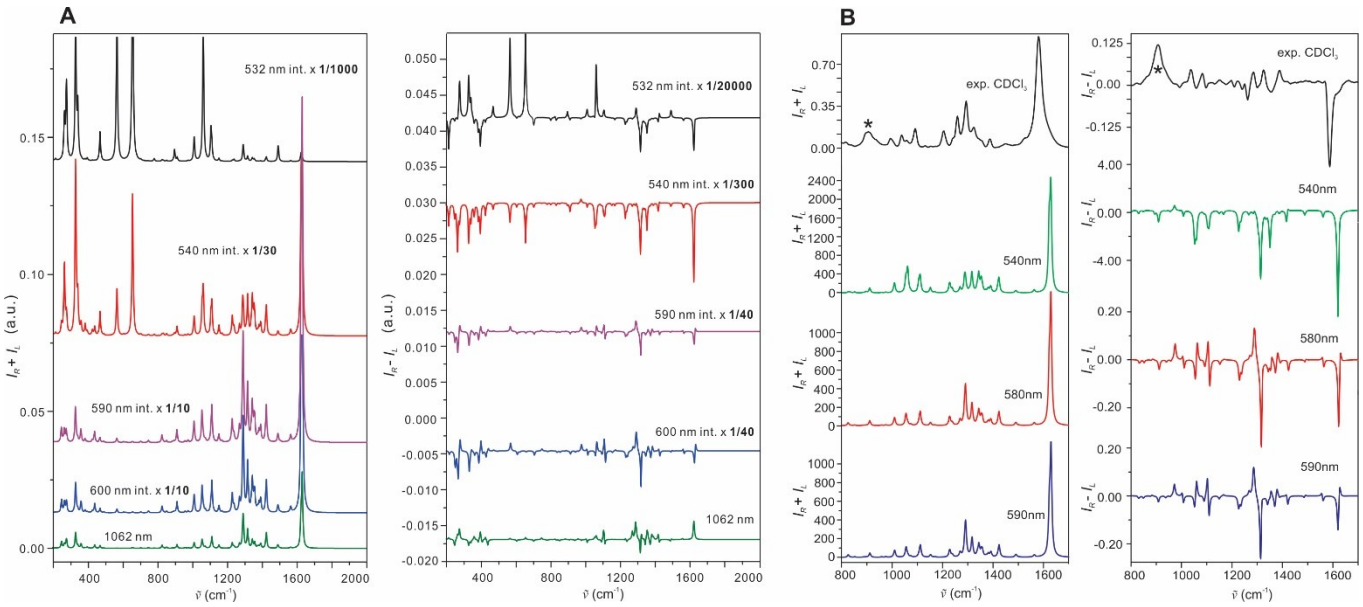

Figure A4. A) Simulated Raman and ROA spectra of (*R*,*R*)-Ni for five excitation wavelengths, from the far-off resonance (1062 nm) to resonance at 532 nm conditions. Note the ~1000-fold increase of Raman and ROA intensities and sign changes of some ROA bands as the excitation wavelength approaches 532 nm. B) Comparison of the experimental Raman and ROA spectra of (*R*,*R*)-Ni at 532 nm in $CDCl_3$ with the simulations for the 540, 590 and 600 nm excitation. Asterisk (*) indicates a solvent band.

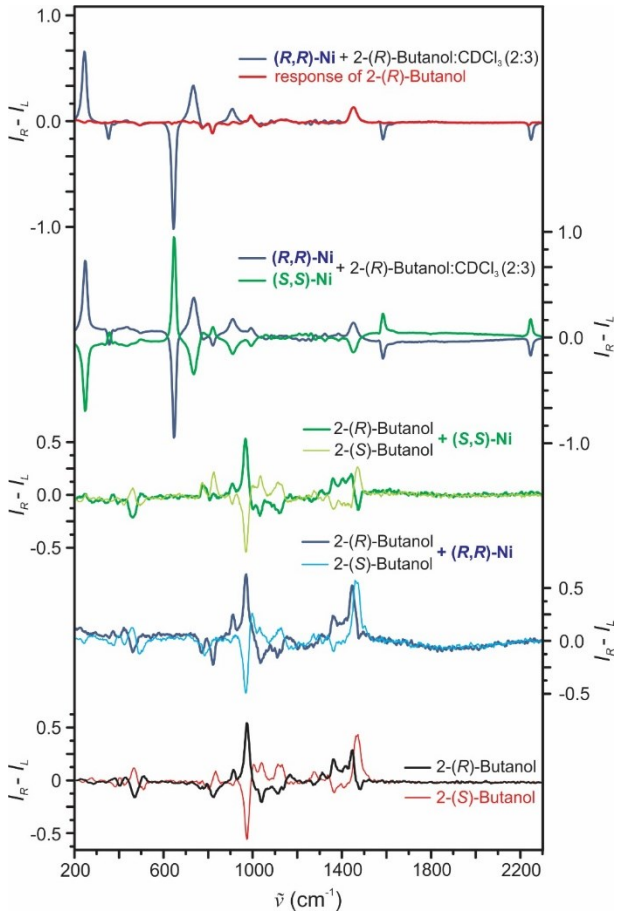

Figure A5. From bottom to top: ROA spectra of neat 2-(*R*) and 2-(*S*)-butanol liquid, (*R*,*R*)-Ni in 2-(*R*)-butanol and 2-(*S*)-butanol, (*S*,*S*)-Ni in 2-(*R*)-butanol and 2-(*S*)-butanol, (*R*,*R*)-Ni and (*S*,*S*)-Ni in a mixture of 2-(*R*)-butanol:$CDCl_3$ (2:3), and 2-(*R*)-butanol with contributions of $CDCl_3$ and the Ni complex subtracted vs. (*R*,*R*)-Ni in a solvent mixture of 2-(*R*)-butanol:$CDCl_3$ (2:3).

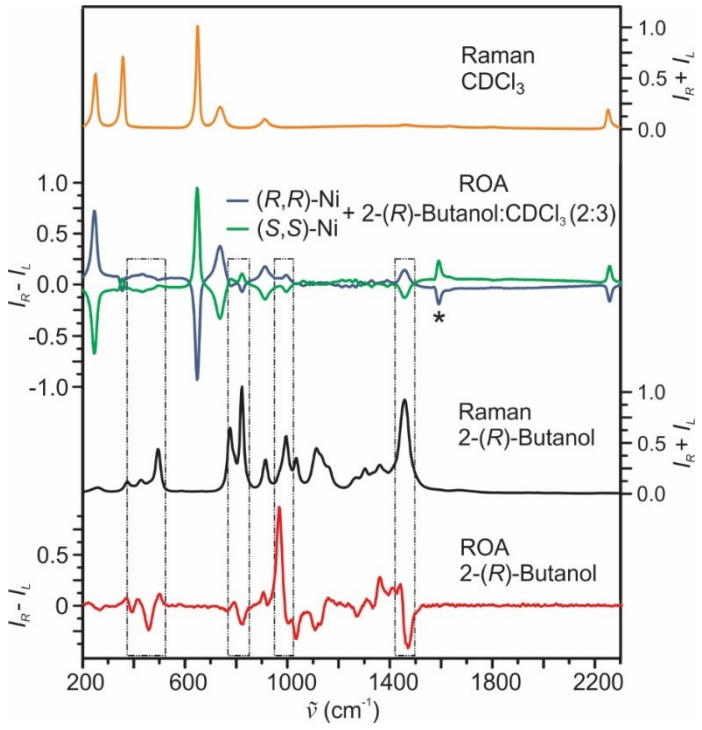

Figure A6. Experimental baseline-corrected ROA spectra of the (*R*,*R*)-Ni (blue) and (*S*,*S*)-Ni (green) complex in a mixture of 2-(*R*)-butanol:$CDCl_3$ (2:3) solvent, Raman spectra of neat $CDCl_3$ (orange) and 2-(*R*)-butanol (black), and ROA spectrum of 2-(*R*)-butanol (red). The strongest Ni complex bands at 1588 cm^{-1} are marked by an asterisk (*). The four rectangular boxes highlight the (*R*)-2-butanol ROA bands, which exhibit mirror-image quality for solutions containing the (*R*,*R*)-Ni and (*S*,*S*)-Ni complex. The induced chiral response of 2-butanol is completely dictated by the chirality of Ni complex.

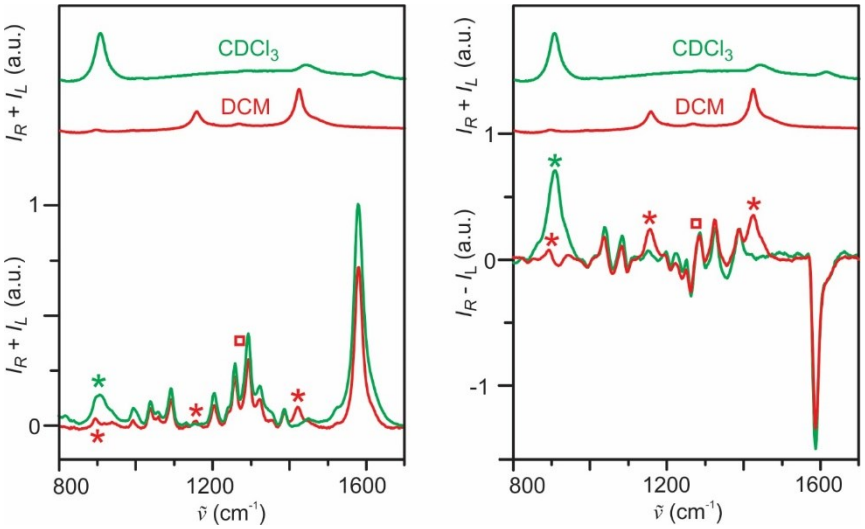

Figure A7. Raman (left) and ROA (right) spectra of the (*R*,*R*)-Ni complex in $CDCl_3$ (green) and in DCM (red). Raman spectra of pure solvents are also shown in both panels. The features related to $CDCl_3$ and DCM are marked with asterisks (*) in green and in red, respectively. The red square indicates that the corresponding DCM features are likely buried beneath those of the Ni complex.

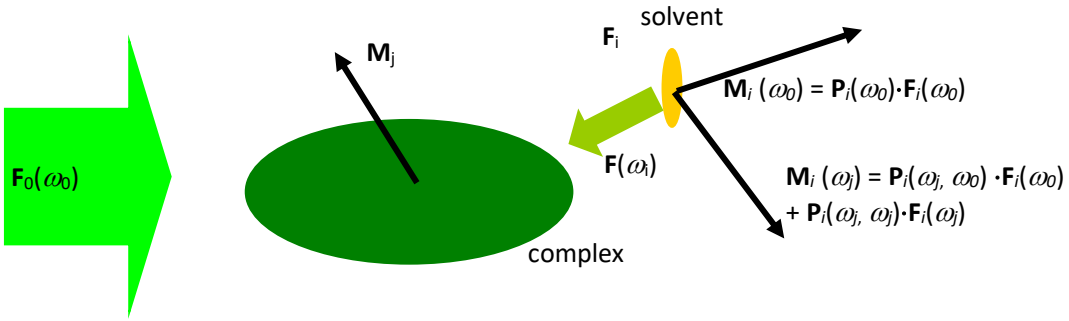

Figure A8. The Transition Polarizability Model (TPM): at each particle, a local field ($\mathbf{F}_i$) of certain frequency induces a moment ($\mathbf{M}_i$) of the same (and for Raman scattering also of a different frequency). Fields from these moments are felt by other particles, where they induce additional moments, and so on. This system polarization is initiated by the excitation laser field ($\mathbf{F}_0$).

Molecules present in the studied system are represented only by their oscillating electric (μi) and magnetic (mi) dipole moments, and electric quadrupole (Θi) moments. By convention, the moments, polarizability and field components are written in the local coordinate systems of each particle. Incident radiation of angular frequency (ω0) consists of the electric (Ei), magnetic

(Bi) and electric gradient (∇Ei) fields. In the linear regime, the moments are[8]

$$\boldsymbol{\mu}_i = \boldsymbol{\alpha}_i.\mathbf{E}_i + \omega^{-1}\mathbf{G'}_i\cdot\dot{\mathbf{B}}_i + \tfrac{1}{3}\mathbf{A}_i\cdot\cdot\nabla\mathbf{E}_i \tag{1a}$$

$$\mathbf{m}_i = -\omega^{-1}\mathbf{G'}_i.\dot{\mathbf{E}}_i \tag{1b}$$

$$\boldsymbol{\Theta}_i = \mathbf{A}_i.\mathbf{E}_i \tag{1c}$$

where α is the electric (dipole-dipole) polarizability, G' is the electric dipole - magnetic dipole polarizability and A is the electric dipole – electric quadrupole polarizability. We are using the dot convention for matrix multiplication (index contraction, two dots for double contraction). To simplify the notation, following Refs. 9 And 10 , for each particle we collect the variables in generalized moment (Mi), polarizability (Pi) and field (Fi) matrices,

$$\mathbf{M}_i = \begin{pmatrix} \boldsymbol{\mu}_i \\ \omega^{-1}\dot{\boldsymbol{\mu}}_i \\ \mathbf{m}_i \\ \omega^{-1}\dot{\mathbf{m}}_i \\ \boldsymbol{\Theta}_i/3 \\ \omega^{-1}\dot{\boldsymbol{\Theta}}_i/3 \end{pmatrix},\ \mathbf{P}_i = \begin{pmatrix} \boldsymbol{\alpha}_i & \mathbf{0} & \mathbf{0} & \mathbf{G}_i' & \mathbf{A}_i/3 & \mathbf{0} \\ \mathbf{0} & \boldsymbol{\alpha}_i & -\mathbf{G}_i' & \mathbf{0} & \mathbf{0} & \mathbf{A}_i/3 \\ \mathbf{0} & -\mathbf{G}_i'^{t} & \mathbf{0} & \mathbf{0} & \mathbf{0} & \mathbf{0} \\ \mathbf{G}_i'^{t} & \mathbf{0} & \mathbf{0} & \mathbf{0} & \mathbf{0} & \mathbf{0} \\ \mathbf{A}_i^{t}/3 & \mathbf{0} & \mathbf{0} & \mathbf{0} & \mathbf{0} & \mathbf{0} \\ \mathbf{0} & \mathbf{A}_i^{t}/3 & \mathbf{0} & \mathbf{0} & \mathbf{0} & \mathbf{0} \end{pmatrix}, \text{ and } \mathbf{F}_i = \begin{pmatrix} \mathbf{E}_i \\ \omega^{-1}\dot{\mathbf{E}}_i \\ \mathbf{B}_i \\ \omega^{-1}\dot{\mathbf{B}}_i \\ \nabla\mathbf{E}_i \\ \omega^{-1}\nabla\dot{\mathbf{E}}_i \end{pmatrix}.$$

Assembled again, these matrices form the total moment (**M**), polarizability (**P**), and field (**F**) tensors, and Eqs. 1a-b can be concisely written as one matrix equation, **M** = **P**·**F**. During Raman scattering, field of certain frequency (ω_j) induces in each particle a moment with different frequency (ω_i), which can be accounted for by introduction of transition polarizabilities[11] $\mathbf{P}(\omega_i,\omega_j)$, so that

$$\mathbf{M}(\omega_i) = \sum_j \mathbf{P}(\omega_i,\omega_j)\cdot\mathbf{F}(\omega_j)\,. \tag{2}$$

Each particle "feels" the incident radiation $\mathbf{F}_0 = \mathbf{F}_0(\omega_0)$ as well as fields coming from the

moments on other particles. For a particular frequency (ω_j) and the whole system we can write

$$\mathbf{F}(\omega_j) = \delta_{j,0}\mathbf{F}_0 + \mathbf{X}\cdot\mathbf{M}(\omega_j) \tag{3}$$

where the "distance" matrix $\mathbf{X}$

$$\mathbf{X} = \begin{pmatrix} 0 & \mathbf{X}_{12} & .. & \mathbf{X}_{1N} \\ \mathbf{X}_{21} & 0 & .. & \mathbf{X}_{2N} \\ .. & .. & .. & .. \\ \mathbf{X}_{N1} & \mathbf{X}_{N2} & .. & 0 \end{pmatrix}, \quad \mathbf{X}_{ij} = \begin{pmatrix} \mathbf{T}_{ij} & \mathbf{0} & \mathbf{0} & \mathbf{0} & -\nabla_i\mathbf{T}_{ij} & \mathbf{0} \\ \mathbf{0} & \mathbf{T}_{ij} & \mathbf{0} & \mathbf{0} & \mathbf{0} & -\nabla_i\mathbf{T}_{ij} \\ \mathbf{0} & \mathbf{0} & \mathbf{T}_{ij}/c & \mathbf{0} & \mathbf{0} & \mathbf{0} \\ \mathbf{0} & \mathbf{0} & \mathbf{0} & \mathbf{T}_{ij}/c & \mathbf{0} & \mathbf{0} \\ \nabla_i\mathbf{T}_{ij} & \mathbf{0} & \mathbf{0} & \mathbf{0} & -\nabla_i\nabla_i\mathbf{T}_{ij} & \mathbf{0} \\ \mathbf{0} & \nabla_i\mathbf{T}_{ij} & \mathbf{0} & \mathbf{0} & \mathbf{0} & -\nabla_i\nabla_i\mathbf{T}_{ij} \end{pmatrix},$$

$T_{ij,\alpha\beta} = \frac{1}{4\pi\varepsilon_0}\frac{3r_{ij,\alpha}r_{ij,\beta} - \delta_{\alpha\beta}r_{ij}^{\,2}}{r_{ij}^{\,5}}$ (for SI units), $\mathbf{r}_{ij} = \mathbf{r}_i - \mathbf{r}_j$, $\nabla_i = \frac{\partial}{\partial\mathbf{r}_i}$, and ε_0 is vacuum permittivity.

Consider a Raman Stokes scattering event with $\omega_j = \omega_0 - \omega_I$, where ω_I is vibrational frequency of a mode I. For both frequencies ω_j and ω_0 we may implant Eq. 3 into Eq. 2, obtaining

$$\mathbf{M}(\omega_0) = \mathbf{P}(\omega_0,\omega_0)\cdot\mathbf{F}_0 + \mathbf{P}(\omega_0,\omega_0)\cdot\mathbf{X}\cdot\mathbf{M}(\omega_0) + \mathbf{P}(\omega_0,\omega_j)\cdot\mathbf{X}\cdot\mathbf{M}(\omega_j) \tag{4a}$$

$$\mathbf{M}(\omega_j) = \mathbf{P}(\omega_j,\omega_0)\cdot\mathbf{F}_0 + \mathbf{P}(\omega_j,\omega_j)\cdot\mathbf{X}\cdot\mathbf{M}(\omega_j) + \mathbf{P}(\omega_j,\omega_0)\cdot\mathbf{X}\cdot\mathbf{M}(\omega_0)\,. \tag{4b}$$

We may omit anti-Stokes scattering, setting corresponding polarizabilities to zero, $\mathbf{P}(\omega_0,\omega_j) = 0$. For brevity, we introduce $\mathbf{P}_I = \mathbf{P}(\omega_j,\omega_0)$ for the Stokes and $\mathbf{P}(\omega_j,\omega_j) \approx \mathbf{P}(\omega_0,\omega_0) = \mathbf{P}_0$ for the Rayleigh (elastic) scattering. By a matrix manipulation we obtain

$$\mathbf{M}(\omega_j) = \mathbf{\Pi}_I\cdot\mathbf{F}_0 \tag{5}$$

where $\mathbf{\Pi}_I = (\mathbf{E} - \mathbf{P}_0.\mathbf{X})^{-1}\cdot\mathbf{P}_I\cdot(\mathbf{E} + \mathbf{X}\cdot(\mathbf{E} - \mathbf{P}_0\cdot\mathbf{X})^{-1}\cdot\mathbf{P}_0)$ and $\mathbf{E}$ is a unit matrix.

$\boldsymbol{\Pi}_I$ can be thought of as an effective polarizability of the whole system. Indeed, at large distances, the elements of $\mathbf{X}$ get smaller, $\|\mathbf{P}_0 \cdot \mathbf{X}\| << 1$, and $\boldsymbol{\Pi}_I \sim \mathbf{P}_I$. That means that the system behaves as a sum of individual particles. For smaller distances, the effective polarizability may differ significantly.

The most interesting case is when $\mathbf{E} - \mathbf{P}_0 \cdot \mathbf{X} \sim 0$, which may occur at certain distances and orientations. Then $\boldsymbol{\Pi}_I$ diverges to infinity. This certainly does not happen in real systems; to simulate the damping mechanisms not included in the simple model and to make practical computations more stable, we introduce an imaginary part of the polarizability, replacing $\mathbf{P}_0$ by $\mathbf{P}_0 + i\Gamma\mathbf{P}_0$, so that

$$\left(\mathbf{E} - \mathbf{P}_0 \cdot \mathbf{X}\right)^{-1} \cong \frac{\left(\mathbf{E} - \mathbf{P}_0 \cdot \mathbf{X}\right)^t}{\left(\mathbf{E} - \mathbf{P}_0 \cdot \mathbf{X}\right) \cdot \left(\mathbf{E} - \mathbf{P}_0 \cdot \mathbf{X}\right)^t + \Gamma^2 \mathbf{P}_0 \cdot \mathbf{X} \cdot \left(\mathbf{P}_0 \cdot \mathbf{X}\right)^t} . \qquad (6)$$

Equations (5) and (6) then provide the effective polarizabilities and Raman and ROA spectral intensities corrected for the mutual polarization effects.[12] As specified above in Materials and Methods, molecular polarizabilities (individual components of $\mathbf{P}(\omega_0,\omega_0)$ and $\mathbf{P}(\omega_0,\omega_j)$ were calculated using DFT. The effective polarizability $\boldsymbol{\Pi}_I$ defined in eq. (5) contains the total "redressed"[12] electric, magnetic and quadrupole polarizabilities defining Raman and ROA intensities (cf., for example, eqs. 8a-c in Ref. 9). From the redressed polarizability components, Raman and SCP ROA intensities for each transition *i* were calculated as[13]

$$I_{I,Raman} = 6\sum_{\beta=1}^{3}\sum_{\alpha=1}^{3}(\alpha_{I,\alpha\alpha}\alpha_{I,\beta\beta} + 7\alpha_{I,\alpha\beta}\alpha_{I,\alpha\beta}), \qquad (4a)$$

$$I_{I,ROA} = 48\sum_{\beta=1}^{3}\sum_{\alpha=1}^{3}(3\alpha_{I,\alpha\beta}G'_{I,\beta\alpha} - \alpha_{I,\alpha\alpha}G'_{I,\beta\beta} + \sum_{\varepsilon=1}^{3}\sum_{\gamma=1}^{3}\varepsilon_{\alpha\beta\gamma}\alpha_{I,\alpha\varepsilon}A_{I,\beta\gamma\varepsilon}), \qquad (4b)$$

Using these line intensities, smooth Raman and ROA spectra were generated within the

harmonic approximation, including a Boltzmann temperature correction as

$$S(\omega) = \sum_I I\left[1 - \exp\left(-\frac{\omega_I}{kT}\right)\right]^{-1}\left[4\left(\frac{\omega - \omega_I}{\Delta}\right)^2 + 1\right]^{-1} \quad (7)$$

where k is the Boltzmann constant, T is temperature, and the full width at half maximum $\Delta = 20$ cm^{-1}.

The induced ROA solvent spectra were simulated for one solvent and one solute molecule (for example, the Ni complex and chloroform). Because the ROA spectral pattern was virtually independent of the distance, the simulations are presented for solvent molecule whose center of mass is 10 Å from the Ni atom. Different solvent and solute orientations were averaged numerically. The solvent was rotated in 12 degree increments (360 / 12 = 30 points) around an axis going through the main moment of inertia, for 50 orientations of the axis. The orientations were chosen using the Lebedev-Laikov formulas for a regular division of sphere surface.[14] This was repeated for 50 positions of the solvent around the solute, using the same Lebedev-Laikov grid. The spectra obtained for the 30 × 50 × 50 = 75 000 points were averaged. In control computations, finer grids did not produce different results.

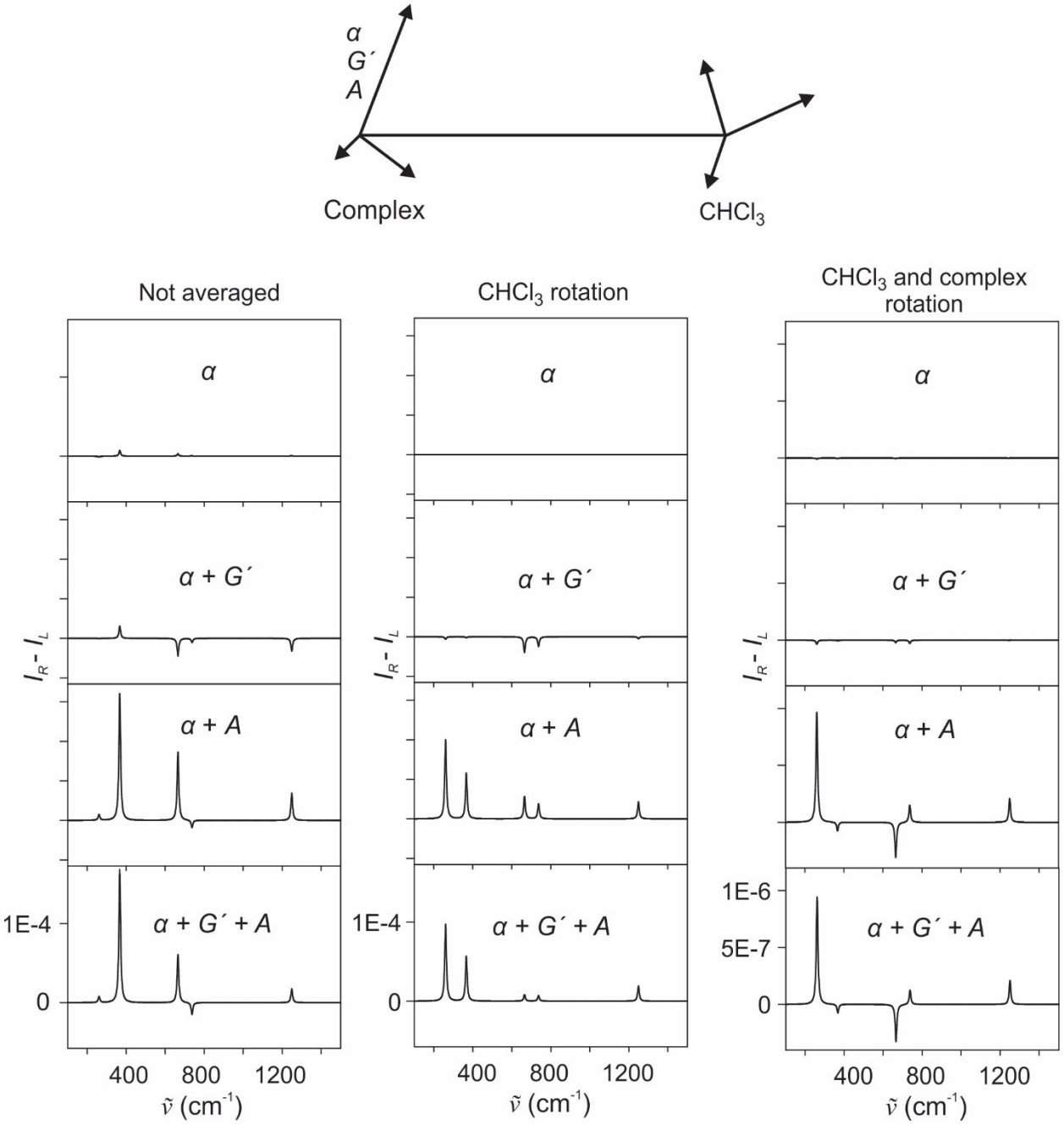

Figure A9. Induced ROA spectra simulated for the (*R*,*R*)-Ni complex with a chloroform molecule for a random orientation (left), and when averaged over chloroform and complex rotational degrees of freedom (middle, right). As indicated, the simulations were done considering separately the electric dipole - electric dipole (α), electric dipole - magnetic dipole (G') and electric dipole - electric quadrupole (A) Rayleigh polarizabilities and/or their

combinations.

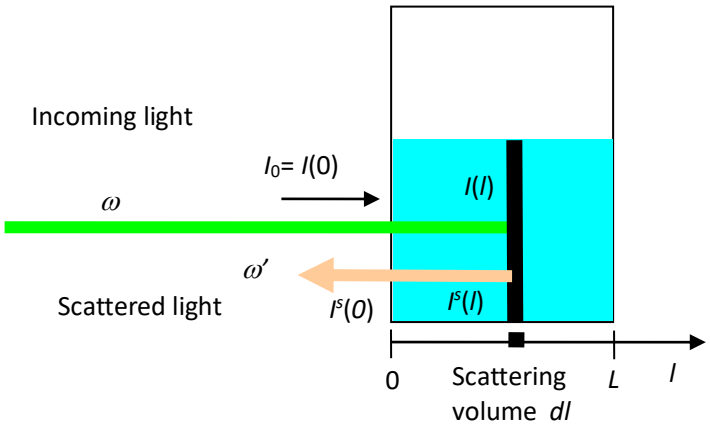

Figure A10. Geometry of the backscattering SCP experiment, incoming unpolarized light of frequency ω enters with intensity I_0 at $l = 0$, the scattered light with intensity I^s and frequency ω' leaves. The incoming light is a sum of left- and right-circularly polarized components, $I_0(0) = I_R(0) + I_L(0)$, where $I_R(0) = I_L(0) = I(0)/2$.

We describe situation in **Figure A10**. Let ε_L and ε_R be the absorption indices for left and right circular polarized light (LCPL, RCPL) of frequency ω, which enters the sample. The absorption index

$$\varepsilon = (\varepsilon_L + \varepsilon_R)/2 \qquad \text{(A1)}$$

and circular dichroism

$$\Delta\varepsilon = \varepsilon_L - \varepsilon_R . \qquad \text{(A2)}$$

Once entering the sample, the intensity diminishes, differently for the different polarizations, originally equally present in the excitation beam:

$$I_R(l) = I_0 e^{-\varepsilon_R c l} / 2, \qquad \text{(A3)}$$

$$I_L(l) = I_0 e^{-\varepsilon_L c l} / 2,$$

c is concentration and l is the path length. An example of the dependence of the intensities following the Lambert-Beer laws (3) on l is in **Figure A11**, plotted with rather unrealistically high $\Delta\varepsilon/\varepsilon$ ratio so that the difference is better seen. The difference $|I_R - I_L|$ is maximal at $l_{\max} = \dfrac{\ln(\varepsilon_L/\varepsilon_R)}{c|\Delta\varepsilon|} \cong \dfrac{1}{c\varepsilon}$, with $\Delta I_{\max} \cong \dfrac{I_0 \Delta\varepsilon}{2e\varepsilon}$, where e = 2.71828. For typical values encountered in experiment, $\varepsilon \sim 10^4$ L·mol^{-1}·cm^{-1}, $\Delta\varepsilon \sim 10$ L·mol^{-1}·cm^{-1} and $c \sim 10^{-4}$ mol/L, we obtain $l_{\max} \sim 1$ cm. This length is well comparable with cell dimensions (few mm) used in typical ROA measurement. The ratio $"CID" = \dfrac{I_R - I_L}{I_R + I_L}$, formally equal to the circular intensity difference, grows nearly linearly with l, $"CID" \sim \Delta\varepsilon c l / 2$, and is positive for $\varepsilon_L > \varepsilon_R$. At $l = l_{\max}$, $"CID" \sim \Delta\varepsilon/(2\varepsilon)$, and it can grow further for $l > l_{\max}$.

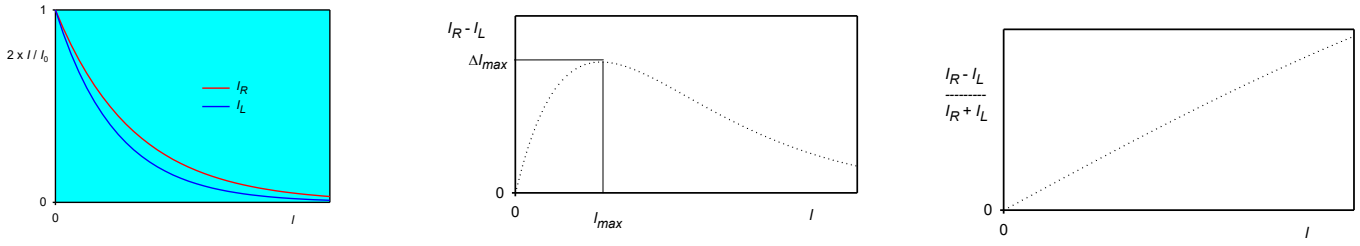

Figure A11. Intensities of the left- and right-circularly polarized light components as dependent

on the path length *l*.

Backscattering from achiral solvent. Each volume element *Sdl* contributes to scattered intensities as

$$dI_R^s = aI_R(l)dl + bI_L(l)dl \qquad \text{(A4)}$$

$$dI_L^s = aI_L(l)dl + bI_R(l)dl\,,$$

where the polarization coefficients *a* and *b* determine polarization changes during the scattering and are related to the degree of circularity.[1] For brevity in (A4) and further on we omit the beam cross section (area) *S*, as this is just a constant. We additionally suppose that all volume contributes equally and neglect finite depth of field of the transfer optics. Re-arranging expressions (A4), we get Raman signal contributions,

$$dI_{Ram}^s(l) = dI_R^s + dI_L^s = (a+b)(I_R(l) + I_L(l))dl \qquad \text{(A5)}$$

The scattered light is also absorbed when passing back through the solvent. According to the Lambert-Beer law the intensity from volume *dl* at $l = 0$ is

$$dI_{Ram}^s(0) = (a+b)[I_R(l)e^{-\varepsilon_R' cl} + I_L(l)e^{-\varepsilon_L' cl}]dl\,, \qquad \text{(A6)}$$

where $\varepsilon_i' = \varepsilon_i(\omega')$ are absorption indices at the Raman scattering frequency. With a negligible error we can set $\varepsilon_L' \cong \varepsilon_R' = \varepsilon'$, $\varepsilon_L \cong \varepsilon_R = \varepsilon$, and combining (A6) with (A3) we get

$$dI^s_{Ram}(0) = (a+b)I_0 e^{-(\varepsilon'+\varepsilon)cl} dl \ . \qquad \text{(A7)}$$

Integration of (A7) over the whole volume gives

$$I_{Ram} = \int_{l=0}^{L} dI^s_{Ram}(0) = \frac{a+b}{c} \cdot \frac{1-e^{-(\varepsilon+\varepsilon')cL}}{\varepsilon+\varepsilon'} I_0 \, . \qquad \text{(A8a)}$$

Formula (A8a) may be better understood when we investigate the limit of short path lengths/weak absorption when $2\varepsilon cL << 1$ and

$$I_{Ram} \sim (a+b)I_0 L \, . \qquad \text{(A8b)}$$

This means that the intensity does not depend on concentration; all volume L is available for the scattering. This is the usual situation for non-resonance Raman experiments. For another extreme, long path lengths/strong absorption, $2\varepsilon cL >> 1$, we get

$$I_{Ram} \sim \frac{(a+b)I_0}{(\varepsilon+\varepsilon')c} \ . \qquad \text{(A8c)}$$

In this case only a effective penetration volume $L_{pen} = \frac{1}{(\varepsilon+\varepsilon')c}$ is available for the scattering, independent of the total volume/path length L.

Detected ROA, SCP. Unlike for Raman, for ROA we must distinguish different absorption indices for left and right CPL. Starting from eq. (A4) and following the Lambert-Beer law, we obtain ROA $dI^s_{ROA}(0) = dI^s_R(0) - dI^s_L(0)$ measurable at $l = 0$ as

$$dI^{s}_{ROA}(0) = [aI_R(l)dl + bI_L(l)dl]e^{-\varepsilon_R' cl} - [aI_L(l)dl + bI_R(l)dl]e^{-\varepsilon_L' cl} \quad \text{(A9)}$$

We use eq. (S3), $\Delta\varepsilon = \varepsilon_L - \varepsilon_R$, $\Delta\varepsilon' = \varepsilon_L' - \varepsilon_R'$, $\varepsilon' \cong \varepsilon_R'$, and $\varepsilon \cong \varepsilon_R$, so that

$$dI^{s}_{ROA}(0) = (a + be^{-\Delta\varepsilon cl} - ae^{-(\Delta\varepsilon+\Delta\varepsilon')cl} - be^{-\Delta\varepsilon' cl})I_0 e^{-(\varepsilon'+\varepsilon)cl} dl/2 \quad \text{(A10)}$$

and obtain the integral value

$$\begin{aligned} I_{ROA} &= \int_{l=0}^{L} dI^{s}_{ROA}(0) \\ &= (a\frac{1-e^{-(\varepsilon'+\varepsilon)cL}}{\varepsilon'+\varepsilon} + b\frac{1-e^{-(\varepsilon'+\varepsilon+\Delta\varepsilon)cL}}{\varepsilon'+\varepsilon+\Delta\varepsilon} - a\frac{1-e^{-(\varepsilon'+\varepsilon+\Delta\varepsilon+\Delta\varepsilon')cL}}{\varepsilon'+\varepsilon+\Delta\varepsilon+\Delta\varepsilon'} - b\frac{1-e^{-(\varepsilon'+\varepsilon+\Delta\varepsilon')cL}}{\varepsilon'+\varepsilon+\Delta\varepsilon'})\frac{I_0}{2c} \end{aligned} . \quad \text{(A11)}$$

In common experiments $\Delta\varepsilon << \varepsilon$, $\Delta\varepsilon' << \varepsilon'$, and $(\Delta\varepsilon'+\Delta\varepsilon)cL << 1$, which provides

$$I^{SCP}_{ROA} = [a(\Delta\varepsilon + \Delta\varepsilon') + b(\Delta\varepsilon' - \Delta\varepsilon)]\frac{1-e^{-(\varepsilon'+\varepsilon)cL}[cL(\varepsilon'+\varepsilon)+1]}{2(\varepsilon'+\varepsilon)^2 c} I_0 . \quad \text{(A12)}$$

Dividing (A12) by (A8a) we obtain measured *CID*,

$$CID = \frac{a(\Delta\varepsilon + \Delta\varepsilon') + b(\Delta\varepsilon' - \Delta\varepsilon)}{a+b}\frac{1-e^{-(\varepsilon'+\varepsilon)cL}[cL(\varepsilon'+\varepsilon)+1]}{2(\varepsilon'+\varepsilon)(1-e^{-(\varepsilon'+\varepsilon)cL})} . \quad \text{(A13)}$$

For weak absorption, $cL(\varepsilon'+\varepsilon) << 1$, and

$$CID \cong \frac{a(\Delta\varepsilon + \Delta\varepsilon') + b(\Delta\varepsilon' - \Delta\varepsilon)}{a+b}\frac{cL}{4}. \qquad \text{(A14a)}$$

In case of strong absorption, $cL(\varepsilon' + \varepsilon) >> 1$, and

$$CID = \frac{a(\Delta\varepsilon + \Delta\varepsilon') + b(\Delta\varepsilon' - \Delta\varepsilon)}{2(a+b)(\varepsilon' + \varepsilon)}. \qquad \text{(A14b)}$$

Relation to molecular properties. For a sample consisting of chiral absorbing dye dissolved in a solvent, the absorption indices ($\Delta\varepsilon$, $\Delta\varepsilon'$, ε and ε') are functions of the dye, whereas the depolarization coefficient *a* and *b* depend on transition polarizabilities of the solvent. To find *a* and *b*, let us consider backscattering of LCPL. Using the Stokes parameters,[1] for the excitation light, up to a constant, $S_0 = I_0$ and $S_3 = I_R - I_L = -I_0$. For the backscattered light (ref. [1], Eq. 3.5.3, considering only real symmetric polarizability α)

$$S_0' = \frac{K}{2}(\alpha_{xx}^2 + 2\alpha_{xy}^2 + \alpha_{yy}^2)I_0 \qquad \text{(A15)}$$

$$S_3' = K(\alpha_{xx}\alpha_{yy} - \alpha_{xy}^2)I_0$$

where *K* is a constant, and the *z* axis goes along *l*. Using isotropic averages

$$\langle \alpha_{xx}\alpha_{yy} \rangle = \frac{1}{15}(2\alpha_{\alpha\alpha}\alpha_{\beta\beta} - \alpha_{\alpha\beta}\alpha_{\alpha\beta})$$

$$\langle \alpha_{xx}^2 \rangle = \langle \alpha_{yy}^2 \rangle = \frac{1}{15}(\alpha_{\alpha\alpha}\alpha_{\beta\beta} + 2\alpha_{\alpha\beta}\alpha_{\alpha\beta})$$

$\langle \alpha_{xy}^2 \rangle = \frac{1}{30}(3\alpha_{\alpha\beta}\alpha_{\alpha\beta} - \alpha_{\alpha\alpha}\alpha_{\beta\beta})$ we get

$$S_0' = \frac{K}{30}(\alpha_{\alpha\alpha}\alpha_{\beta\beta} + 7\alpha_{\alpha\beta}\alpha_{\alpha\beta})I_0 \tag{A16}$$

$$S_3' = \frac{K}{6}(\alpha_{\alpha\alpha}\alpha_{\beta\beta} - \alpha_{\alpha\beta}\alpha_{\alpha\beta})I_0$$

The backscattered intensities are $I_0' = I_R' + I_L' = S_0'$, $I_R' - I_L' = S_3'$, so that

$$I_R' = (S_3' + S_0')/2 = (3\alpha_{\alpha\alpha}\alpha_{\beta\beta} + \alpha_{\alpha\beta}\alpha_{\alpha\beta})\frac{KI_0}{30} \tag{A17}$$

$$I_L' = (S_0' - S_3')/2 = (6\alpha_{\alpha\beta}\alpha_{\alpha\beta} - 2\alpha_{\alpha\alpha}\alpha_{\beta\beta})\frac{KI_0}{30}.$$

Comparing (S17) with (S4), we see that $b \sim 3\alpha_{\alpha\alpha}\alpha_{\beta\beta} + \alpha_{\alpha\beta}\alpha_{\alpha\beta}$ and $a \sim 6\alpha_{\alpha\beta}\alpha_{\alpha\beta} - 2\alpha_{\alpha\alpha}\alpha_{\beta\beta}$. Defining the degree of circularity $DOC = -S_3'/S_0'$ (cf. also eq. 2.123 in ref. [3]), we can write

$$DOC = 5\frac{\alpha_{\alpha\beta}\alpha_{\alpha\beta} - \alpha_{\alpha\alpha}\alpha_{\beta\beta}}{\alpha_{\alpha\alpha}\alpha_{\beta\beta} + 7\alpha_{\alpha\beta}\alpha_{\alpha\beta}} = \frac{a-b}{a+b} \tag{A18}$$

Alternatively, we can relate *a* and *b* to the reversal coefficient (eq. 3.5.15 in ref.8 or eq. 2.122 in ref.13)

$$R = I_L'/I_R' = \frac{a}{b} = \frac{6\alpha_{\alpha\beta}\alpha_{\alpha\beta} - 2\alpha_{\alpha\alpha}\alpha_{\beta\beta}}{3\alpha_{\alpha\alpha}\alpha_{\beta\beta} + \alpha_{\alpha\beta}\alpha_{\alpha\beta}} \tag{A19}$$

Eq. (S14a), for example, can be written as

$$CID \cong \frac{\Delta\varepsilon' + DOC\Delta\varepsilon}{4} cL \,. \qquad \text{(A20)}$$

The most important parameter determining solvent induced chirality is thus the degree of circularity.

To think about the result, it might be useful to consider solvent of a spherical symmetry (e.g. tetrachloromethane) where $\alpha_{\alpha\beta} = \alpha\delta_{\alpha\beta}$, $R = 0$ and $DOC = -1$. In this case, LCPL is after scattering totally converted to RCPL. From (A20) we see that observed *CID* is then just proportional to ECD difference between the scattered and incoming light. For $\Delta\varepsilon = \Delta\varepsilon'$ we get the obvious result that circular polarization due to the ECD of the excitation beam is annulated by ECD of the scattered radiation, because the path length and concentrations are the same.

Table A1. Calculated (B3LYP/ 6-311++G**) spectral parameters of the five lowest-energy electronic transitions in the (*R,R*)-Ni complex.[a]

Transition symmetry	λ / nm	D / debye^2	R / debye^2	$g = R / D$	Main orbital contribution
1A	557.39	0.010	0.0008	0.0762	85 → 88
2B	538.20	0.124	0.0005	0.0040	82 → 88
3B	514.34	0.033	0.0015	0.0457	83 → 88
4B	418.12	0.047	0.0000	-0.0008	78 → 88
5A	442:.34	4.273	-0.0004	-0.0001	85 → 86

[a] Wavelength (λ), dipole (D) and Rotational (R) strengths.

Table A2. Wavelengths of five lowest-energy transitions (λ in nm) as calculated by different methods.

Functional	B3LYP	B3LYP	B3LYP	CAM-B3LYP
basis set	6-31G**	6-311++G**	6-311++G**	6-311++G**
solvent	vacuum	vacuum	PCM/$CHCl_3$	PCM/$CHCl_3$
1A	554	557	542	557
2B	510	538	528	551
3B	500	514	502	513
4B	396	418	411	419
5A	442	442	409	355

Table A3. Assignment of selected induced ROA solvent bands.[a]

Band		Calculation ω		Experiment ω		Mode, symmetry
$CHCl_3$	1	261	+	246	+	δ(CCl), *E*
	2	367	-	354	-	δ (CCl), A_1
	3	665	-	666	-	ν(CCl), A_1
	4	737	+	746	+	ν(CCl), *E*
	5	1249	+	1214	+	δ (CH), *E*
$CDCl_3$	1	260	+	242	+	δ(CCl), *E*
	2	364	-	356	-	δ (CCl), A_1
	3	646	-	648	-	ν(CCl), A_1
	4	717	-	732	-	ν(CCl), *E*
	5	925	+	905	+	δ (CD), *E*
	6	2349	+	2255	-	ν(CD) , A_1
DMSO	1	286	+	287	+	δ (C-S-C), *A'*
	2	320	+	313	+	δ (C-S=O), *A"*
	3	642	-	663	-	ν(CS), *A'*
	4	675	+	693	+	ν(CS), *A"*
	5	960	-	1034	-	ν (SO), *A'*
	6	1341	-	1307	-	δ(CH), *A'*
	7	1448	+	1418	+	δ (CH), *A"*
DMSO-d_6	1	246	+	237	+	δ (C-S-C), *A'*
	2	295	+	287	+	δ (C-S=O), *A"*
	3	592	-	604	-	ν(CS), *A'*
	4	608	+	623	+	ν(CS), *A"*
	5	757	+	746	+	δ(CD), *A"*
	6	1032	-	1002	-	ν (SO), *A'*
	7	1041	+	1037	+	δ(CD), *A"*
	8	2180	-	2127	-	ν(CD), sym., *A'*
	9	2331	+	2248	+	ν(CD), sym., *A"*
DCM	1	283	+	258	+	δ (Cl-C-Cl), A_1
	2	701	-	699	-	ν(CCl), A_1
	3	727	+	733	+	δ (H-C-H), in plane rocking, B_1
	4	904	+	884	+	ν(CCl), B_2
	5	1183	+	1148	+	δ (H-C-H), out of plane twisting, A_2
	6	1304	+	1282	+	δ (H-C-H), out of plane wagging, B_2
	7	1473	+	1420	+	δ (H-C-H), in plane scissoring, A_1
C_6H_6		1018	-	992	-	ν(CC) breathing, A_{1g}
AcN-d_3		2195	-	2111	-	ν(CN), A_1

[a] Frequencies (ω) in cm^{-1}, δ-bending, ν - stretching, totally symmetric modes in blue, others in red.

Reference

[1] X. F. Shan, D. H. Wang, C. H. Tung, L. Z. Wu, Tetrahedron **2008,** 64, 5577-5582.

[2] M. J. Frisch, et al. Gaussian 16, Wallingford, CT, **2016.**

[3] A. D. Becke, J. Chem. Phys. **1993,** 98, 5648-5652.

[4] T. Yanai, D. Tew, N. C. Handy, Chem. Phys. Lett. **2004,** 393, 51-57.

[5] J. R. Cheeseman, M. J. Frisch, J. Chem. Theory Comput. **2011,** 7, 3323-3334.

[6] J. B. Foresman, T. A. Keith, K. B. Wiberg, J. Snoonian, M. J. Frish, J. Phys. Chem. **1996,** 100, 16098-16104.

[7] P. J. Hay, W. R. Wadt, J. Chem. Phys. **1985,** 82, 299-310.

[8] L. D. Barron, Molecular Light Scattering and Optical Activity, Cambridge University Press, Cambridge, UK, **2004.**

[9] V. Novák, J. Šebestík, P. Bouř, J. Chem. Theory Comput. **2012,** 8, 1714-1720.

[10] P. Bouř, J. Chem. Phys. **2007,** 127, 136101.

[11] S. Yamamoto, P. Bouř, J. Comput. Chem. **2013,** 34, 2152-2158.

[12] B. G. Janesko, G. E. Scuseria, J. Chem. Phys. **2006,** 125, 124704.

[13] L. Nafie, Vibrational optical activity: Principles and applications, Wiley, Chichester, **2011**.

[14] V. I. Lebedev, D. N. Laikov, Dokl, Akad. Nauk **1999,** 366, 741-745.

Appendix B: Supporting information for Chapter 4

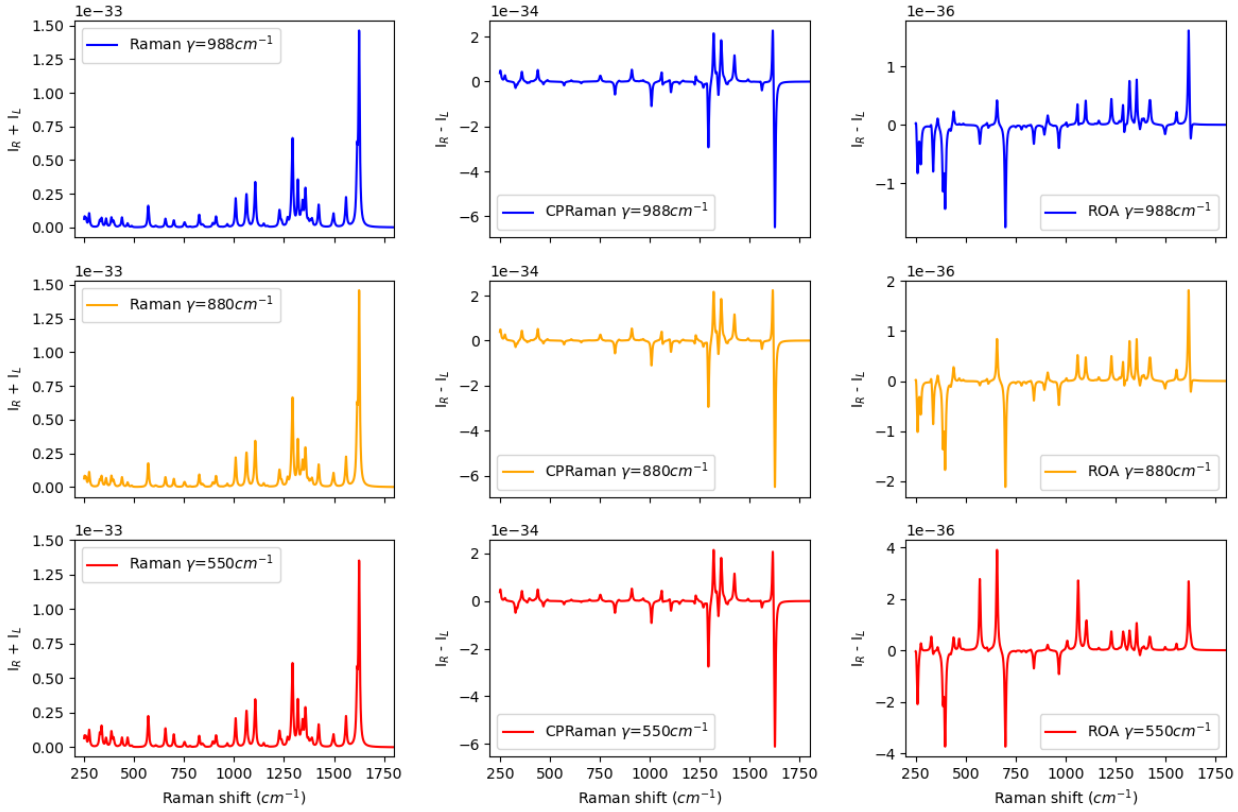

Figure B1. Calculated Raman, CP-Raman and ROA of *R*-**Ni** at 532 nm with different values for the damping parameter, γ. Calculated $I_R + I_L$ and $I_R - I_L$ are in m^2 cm/sr where m is meter and sr is steradian.

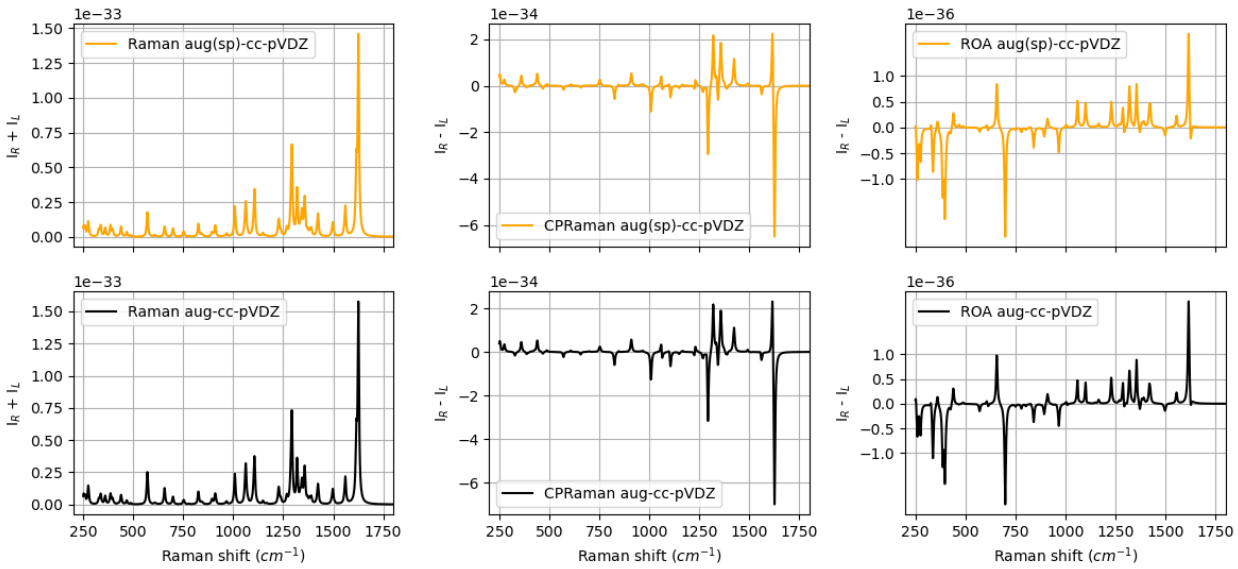

Figure B2. Calculated Raman, CP-Raman and ROA of *R*-**Ni** at 532 nm with two different basis sets. Calculated $I_R + I_L$ and $I_R - I_L$ are in m^2 cm/sr.

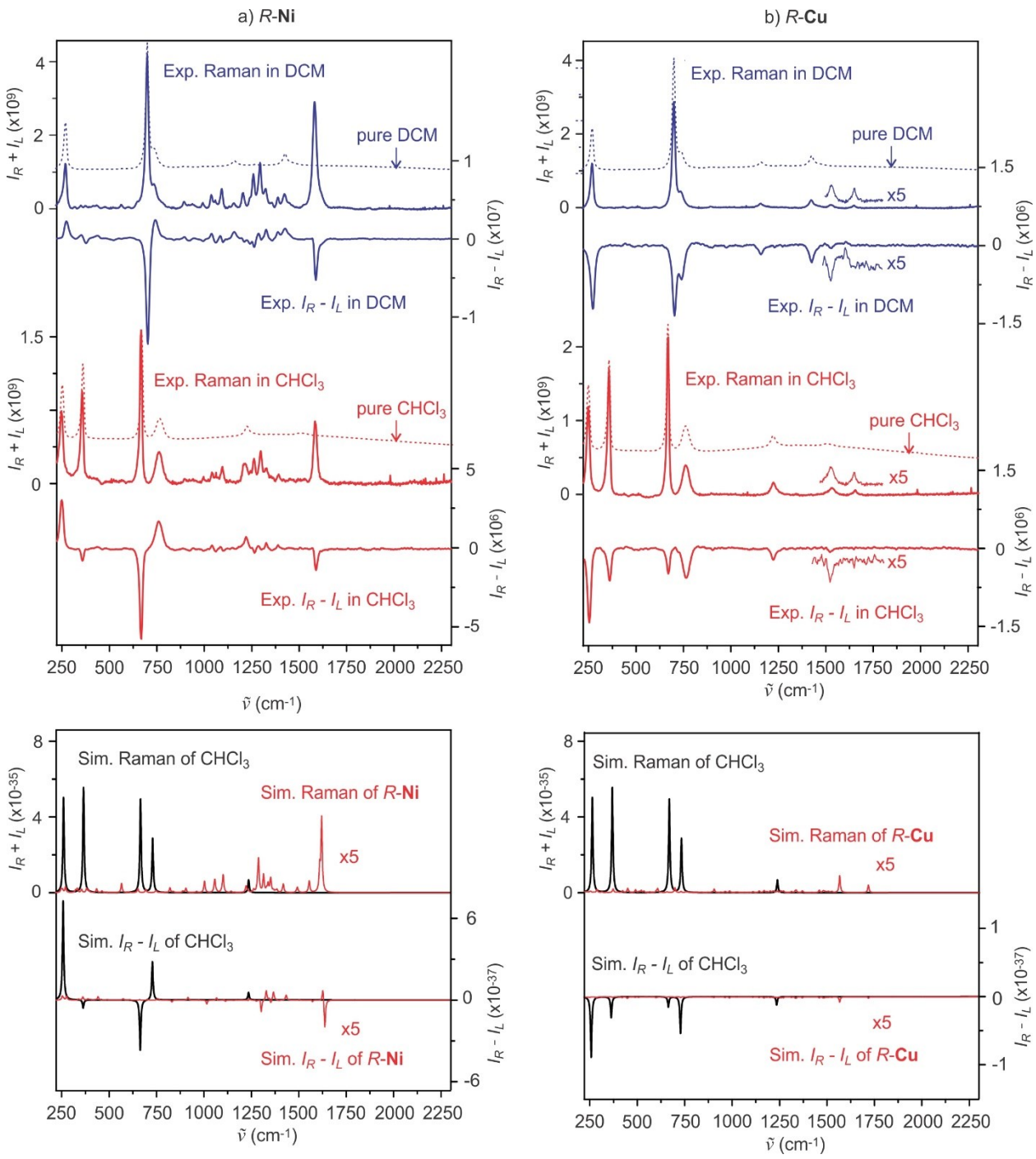

Figure B3. Top: comparison of experimental IR + IL and IR - IL spectra of a) R-Ni and b) R-Cu in DCM (blue) and CHCl3 (red). The experimental IR + IL spectra (dotted line) of pure solvent DCM and CHCl3 are also provided for easy identification of the solvent bands. Bottom:

simulated solute IR + IL (Raman) and IR - IL (eCP-Raman) spectra (pink) which are amplified by a factor of 5, and the related solvent spectra (black). The simulated IR + IL and IR - IL intensities are in m2 cm/sr and are scaled with the respective solvent or solute concentration and path length.

a) *R*-**Ni**

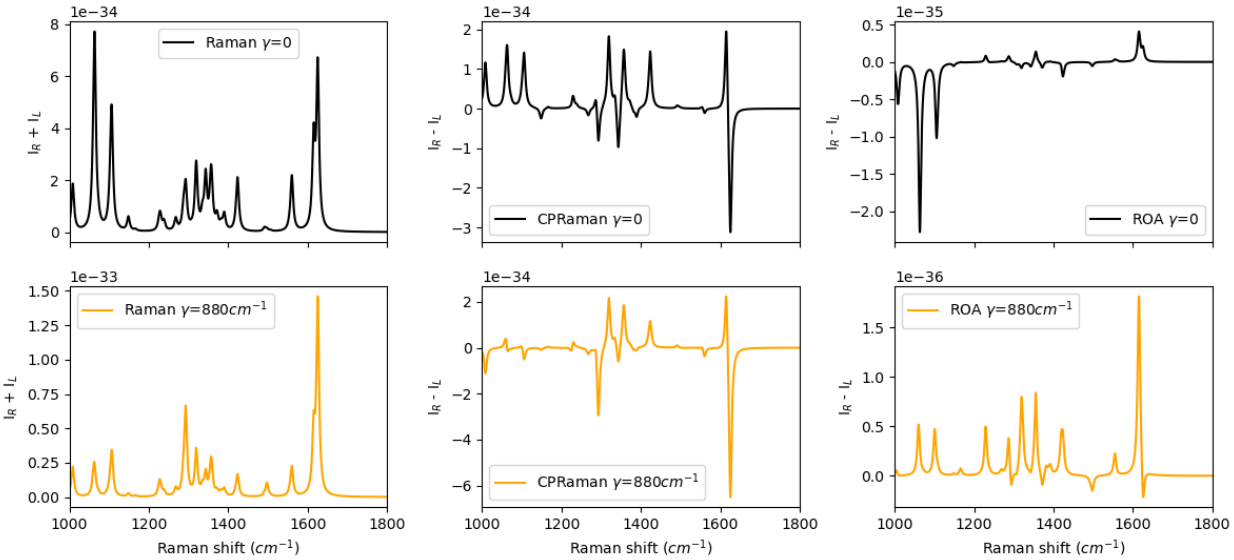

b) *R*-**Cu**

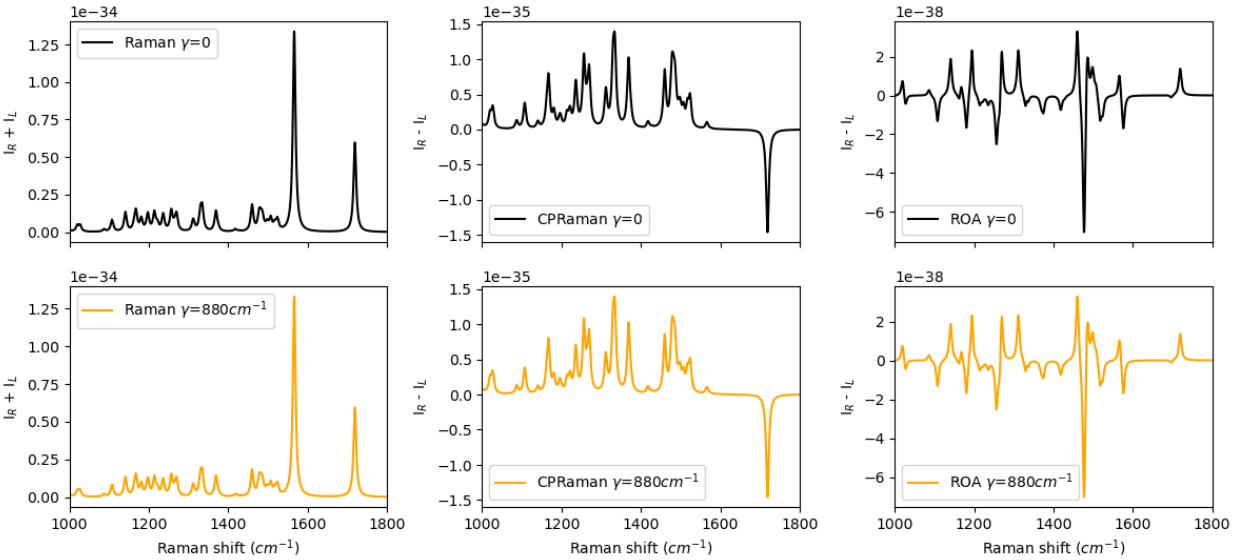

Figure B4. Comparison of the simulated Raman, CP-Raman and ROA spectra of a) *R*-**Ni** and b) *R*-**Cu** without (γ=0) and with (γ=880 cm^{-1}) the finite-lifetime approach. The simulated $I_R + I_L$ and $I_R - I_L$ intensities are in m^2 cm/sr. For *R*-**Ni,** the optimized geometry and harmonic frequencies were computed at the B3LYP/aug-cc-pVTZ level of theory.

Table B1. The experimental and theoretical *CID* values of *R*-**Ni**, *R*-**Cu** and their $CHCl_3$ solvent and *S*-**BN** and its $CHCl_3$ and CH_3CN solvents.

[a] This is not predicted with the harmonic calculation.

RR-Ni	**Experimental**		**Theoretical**		**Vib. mode**
	v (cm^{-1})	*CID* ($X10^{-3}$)	V (cm^{-1})	*CID* ($X10^{-3}$)	
solute	1039 1263 1326 1388 ~1570 (shoulder) 1588	3.25 -0.95 2.87 2.68 N/A -2.60	1059 1293 1356 1424 1615 1625	2.30 -4.61 7.10 7.90 3.94 -4.77	C-H scissoring C-H scissoring C-H wagging C-C stretching C=N sym stretching C=N antisym stretching
$CHCl_3$ solvent	246 354 666 761	4.40 -0.81 -3.80 5.88	255 360 662 726	14.46 -1.05 -7.45 10.04	C-Cl asym. bending CHCl sym. bending CCl sym. stretching CCl asym. stretching
R-Cu	**Experimental**		**Theoretical**		**Vib. mode**
	v (cm^{-1})	*CID* ($X10^{-4}$)	V (cm^{-1})	*CID* ($X10^{-4}$)	
solute	1520	-5.70	1565	-8.86	C=C stretching
$CHCl_3$ solvent	246 354 666 761	-12.06 -3.72 -2.24 -14.40	255 360 662 726	-17.75 -5.60 -3.11 -19.32	C-Cl asym. bending CHCl sym. bending CCl sym. stretching CCl asym. stretching
S-BN	**Experimental (Ref. 11)**		**Theoretical**		**Vib. mode**
	v (cm^{-1})	*CID* ($X10^{-4}$)	V (cm^{-1})	*CID* ($X10^{-5}$)	
solute	1419 1608	-2.76 -4.3	1467 1686	-3.79 -6.83	C=C stretching C=C stretching
$CHCl_3$ solvent	260 365 667 763	-6.31 -1.1 N.A. -5.76	255 360 662 726	-22.8 -4.6 0.76 -21.64	C-Cl asym. bending CHCl sym. bending CCl sym. stretching CCl asym. stretching
CH_3CN solvent	379 924 1378 1446 2256 2300	-3.2 0.55 -1.00 -1.53 1.38 1.21	412 919 1410 1459 2326 N/A[a]	-16.8 3.11 -5.48 -12.65 3.58 N/A[a]	CCN bending CC stretching CH_3 bending CH_2 bending CN stretching CH_3 bend. +CC str.

Completion of references 19 and 20

[19] Gaussian Development Version, M. J. Frisch, G. W. Trucks, H. B. Schlegel, G. E. Scuseria, M. A. Robb, J. R. Cheeseman, G. Scalmani, V. Barone, G. A. Petersson, H. Nakatsuji, X. Li, A. V. Marenich, M. Caricato, J. Bloino, B. G. Janesko, J. Zheng, R. Gomperts, B. Mennucci, H. P. Hratchian, J. V. Ortiz, A. F. Izmaylov, J. L. Sonnenberg, D. Williams-Young, F. Ding, F. Lipparini, F. Egidi, J. Goings, B. Peng, A. Petrone, T. Henderson, D. Ranasinghe, V. G. Zakrzewski, J. Gao, N. Rega, G. Zheng, W. Liang, M. Hada, M. Ehara, K. Toyota, R. Fukuda, J. Hasegawa, M. Ishida, T. Nakajima, Y. Honda, O. Kitao, H. Nakai, T. Vreven, K. Throssell, J. A. Montgomery, Jr., J. E. Peralta, F. Ogliaro, M. J. Bearpark, J. J. Heyd, E. N. Brothers, K. N. Kudin, V. N. Staroverov, T. A. Keith, R. Kobayashi, J. Normand, K. Raghavachari, A. P. Rendell, J. C. Burant, S. S. Iyengar, J. Tomasi, M. Cossi, J. M. Millam, M. Klene, C. Adamo, R. Cammi, J. W. Ochterski, R. L. Martin, K. Morokuma, O. Farkas, J. B. Foresman, and D. J. Fox, Gaussian Inc., Wallingford CT, **2020**.

[20] Gaussian 16, Revision C.01, M. J. Frisch, G. W. Trucks, H. B. Schlegel, G. E. Scuseria, M. A. Robb, J. R. Cheeseman, G. Scalmani, V. Barone, G. A. Petersson, H. Nakatsuji, X. Li, M. Caricato, A. V. Marenich, J. Bloino, B. G. Janesko, R. Gomperts, B. Mennucci, H. P. Hratchian, J. V. Ortiz, A. F. Izmaylov, J. L. Sonnenberg, D. Williams-Young, F. Ding, F. Lipparini, F. Egidi, J. Goings, B. Peng, A. Petrone, T. Henderson, D. Ranasinghe, V. G. Zakrzewski, J. Gao, N. Rega, G. Zheng, W. Liang, M. Hada, M. Ehara, K. Toyota, R. Fukuda, J. Hasegawa, M. Ishida, T. Nakajima, Y. Honda, O. Kitao, H. Nakai, T. Vreven, K. Throssell, J. A. Montgomery, Jr., J. E. Peralta, F. Ogliaro, M. J. Bearpark, J. J. Heyd, E. N. Brothers, K. N. Kudin, V. N. Staroverov, T. A. Keith, R. Kobayashi, J. Normand, K. Raghavachari, A. P. Rendell, J. C. Burant, S. S. Iyengar, J. Tomasi, M. Cossi, J. M. Millam, M. Klene, C. Adamo, R. Cammi, J. W. Ochterski, R. L. Martin, K. Morokuma, O. Farkas, J. B. Foresman, and D. J. Fox, Gaussian Inc., Wallingford CT, **2016**.

Appendix C: Supporting information for Chapter 5

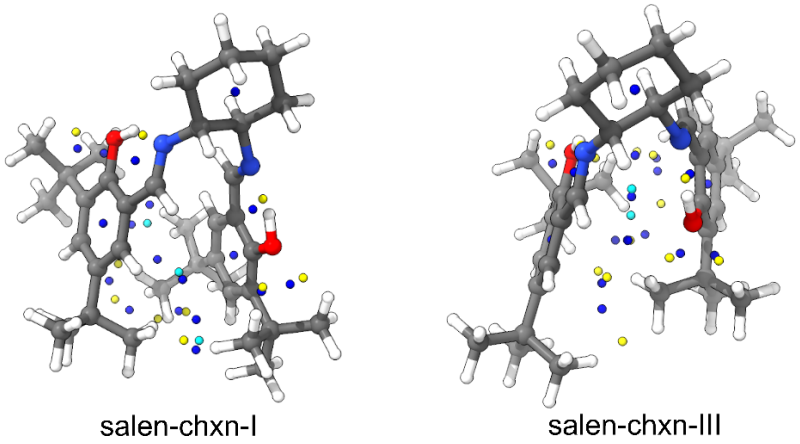

Figure C1. The QTAIM analysis of salen-chxn-I and -III with their bond critical points indicated: yellow = bond critical point, blue = ring critical point, and cyan = cage critical points. Salen-chxn-I has one more cage critical point than -III, stabilizing its geometry.

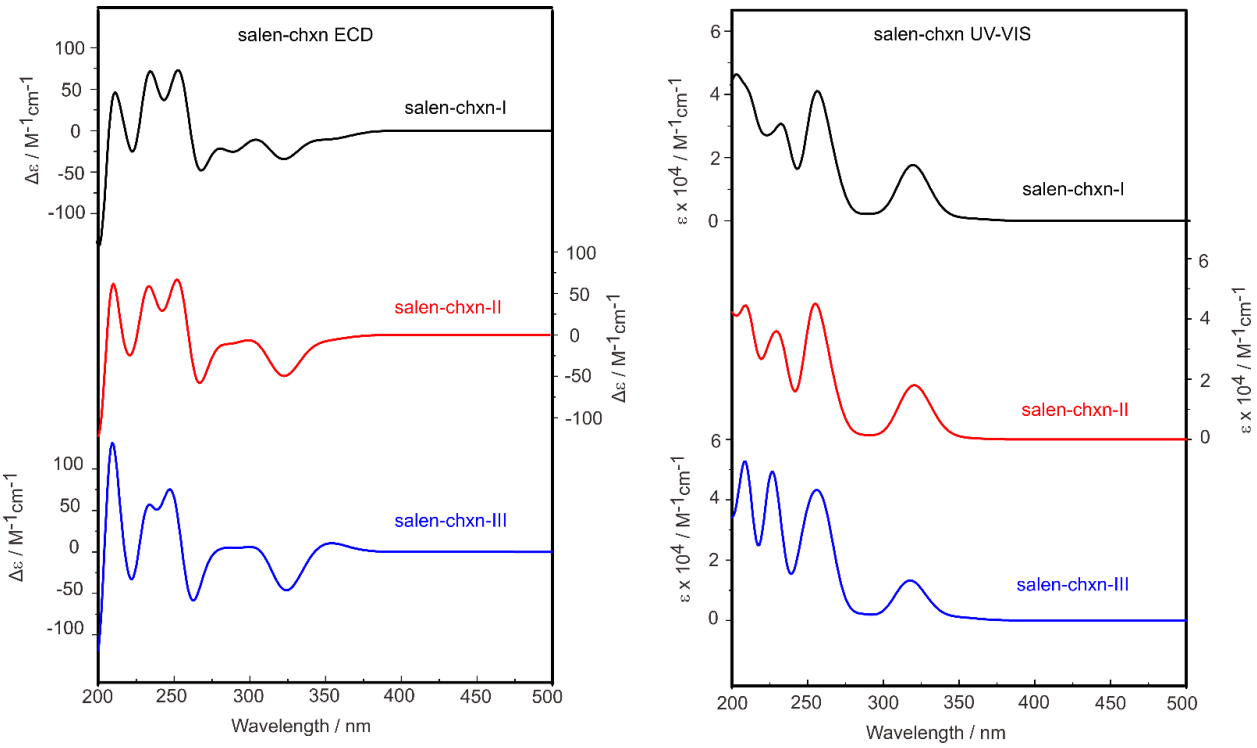

Figure C2. The theoretical UV-Vis and ECD spectra of three salen-chxn ligand conformers in acetonitrile solution at the MN12L/def2-TZVP level. The first 200 electronic states were included in the calculations.

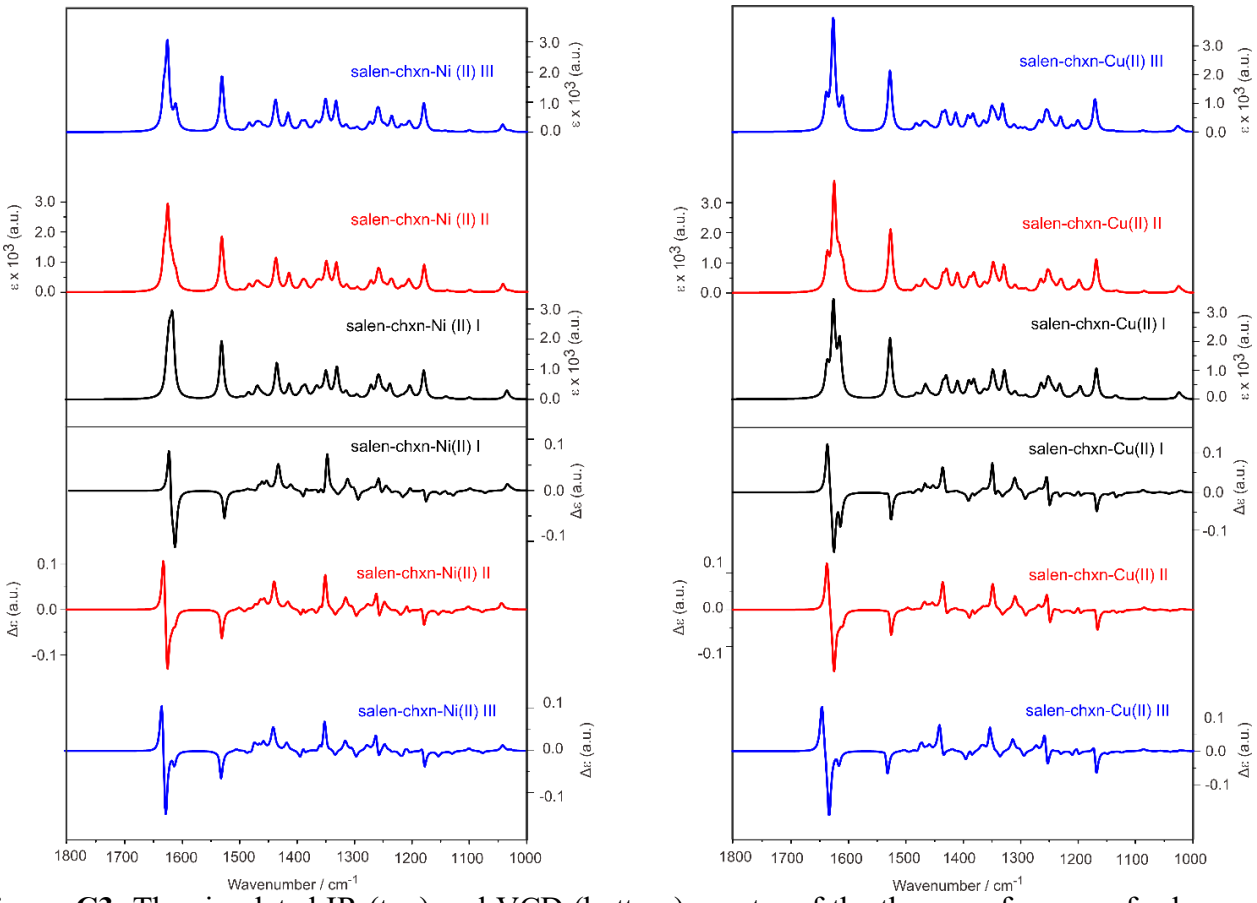

Figure C3. The simulated IR (top) and VCD (bottom) spectra of the three conformers of salen-chxn-Ni(II) and salen-chxn-Cu(II) at the B3LYP-D3BJ/6-311++G(d,p) level with the PCM of chloroform.

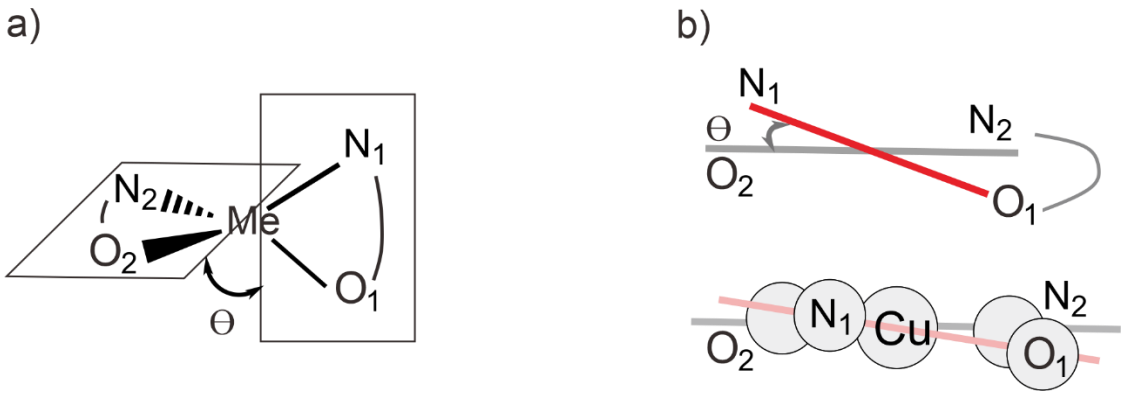

Figure C4. a) Definition of the helicity-determining angle θ. For square planar, θ=0°, whereas θ=90° for tetrahedral. N_1 and O_1 are atoms of one aromatic branch, and N_2 and O_2 are atoms of

the other branch. b) Illustration of the *M*-helicity in the near square planar metal complexes with the (R,R) ligand, viewing the coordination arrangement in a) from the right side. Note that N_2 and N_4 are connected by the cyclohexane ring. We use (R,R)-salen-chxn-Cu(II) as an example. Note that all other atoms are removed for clarity.

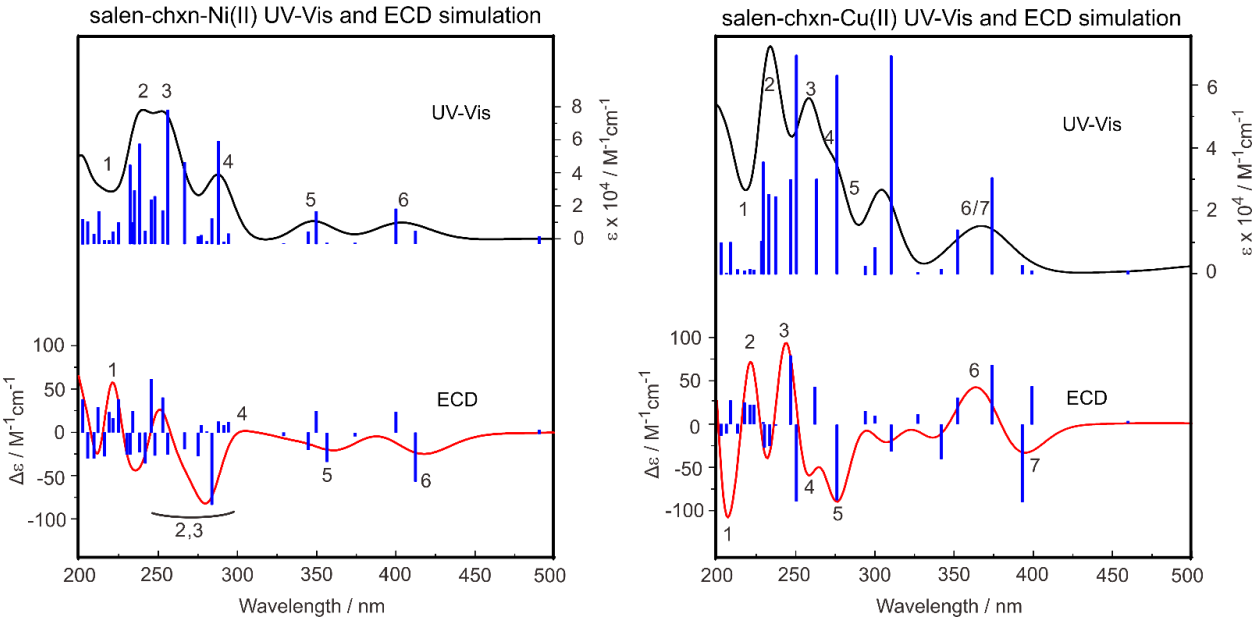

Figure C5. The simulated UV-Vis (top) and ECD (bottom) spectra of salen-chxn-Ni(II) and salen-chxn-Cu(II) with the detailed contributions of individual electronic transitions indicated by sticks. The calcaultions were done at the B3LYP-D3BJ/6-311++G(d,p) and 250 electronic states were included in the calculation.

Point C1. The mass spectrometry and NMR data of salen-chxn-Ni(II) and -Cu(II). salen-chxn-Ni(II): TOS MS: m/z 603.3 (M+H)+ . 1H NMR (s400 MHz, CDCl3, 25ºC, TMS): δ 1.26 (s,18H, tBu), δ 1.31 (d,4H, cyclohexane), δ 1.42 (s,18H, tBu), δ 1.88 (s,2H, CH2-cyclohexane), δ 2.42 (s,2H, CH2-cyclohexane), δ 3.04 (s,2H, CH-cyclohexane), δ 6.87 (d,2H, Benzene H), δ 7.30

(d,2H, Benzene H), δ 7.39 (s,2H, imine H, N=C-H). salen-chxn-Cu(II): TOS MS: m/z 608.3 (M+H)+ . 1H NMR (s400 MHz, CDCl3, 25ºC, TMS): δ 1.06 (s,18H, tBu), δ 1.65 (d,4H, cyclohexane), δ 2.03 (s,18H, tBu), δ 2.17 (s,2H, CH2-cyclohexane), δ 7.25 (d,2H, Benzene H), δ 8.04 (s,2H, imine H, N=C-H).

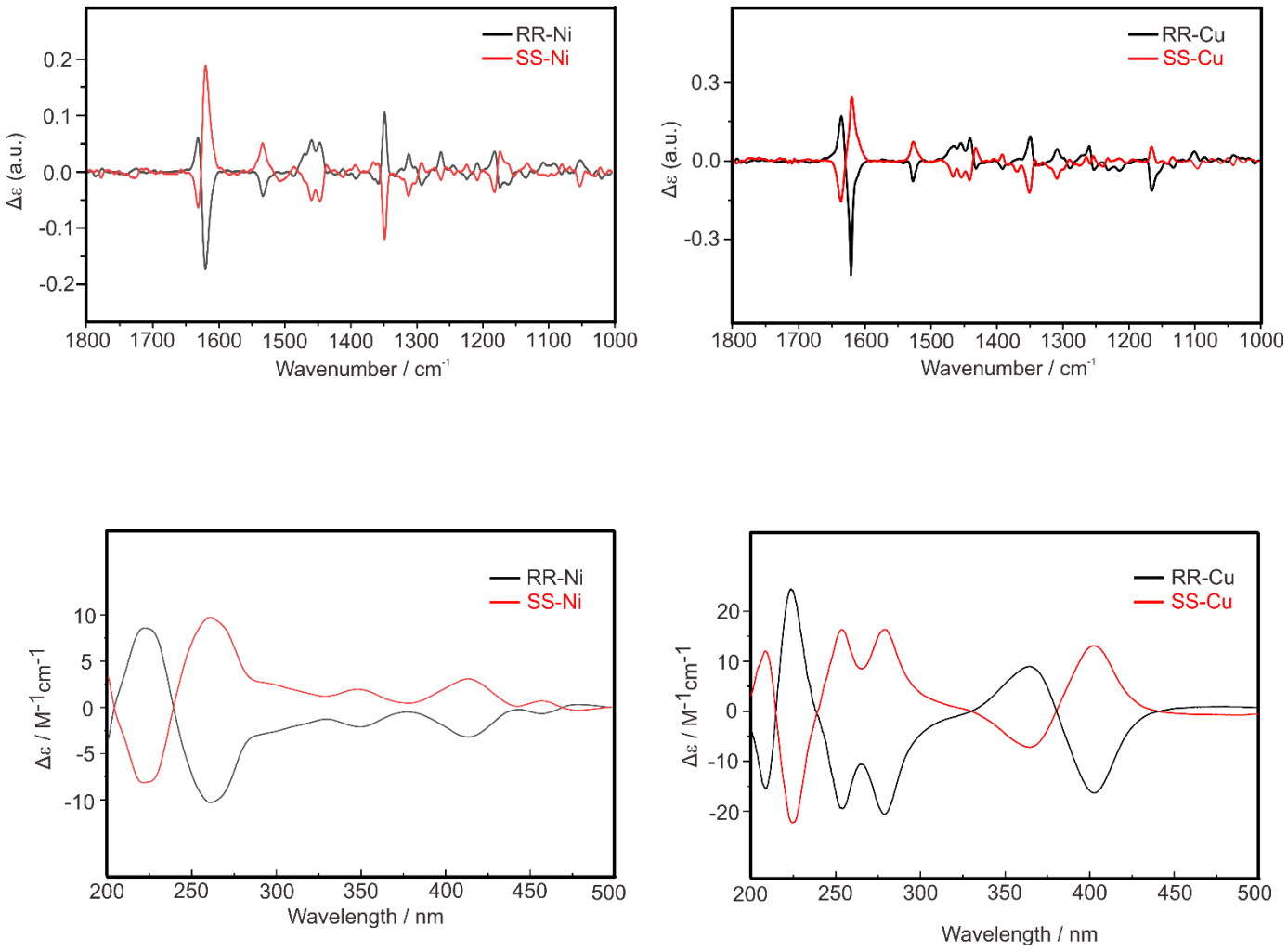

Figure C6. The raw experimental VCD (top) and ECD (bottom) spectra of (R,R) and (S,S)-salen-chxn-Ni(II) and -Cu(II)